Diss. ETHZ No. 14774 and
ETHZ-IPP Internal Report 2002-05

ETH Institute for Particle Physics

A Measurement of D-Meson Production at HERA by Decay Vertex Identification

A dissertation submitted to the
Swiss Federal Institute of Technology Zurich
for the degree of
Doctor of Natural Sciences

presented by
Johannes Gassner
Dipl. Phys. ETH
born on February 10, 1973
in Graz / Austria

accepted on the recommendation of
Prof. Dr. Ralph Eichler, examiner and
Prof. Dr. André Rubbia, co-examiner

August 2002

Abstract

The production of charmed mesons in deep inelastic ep scattering is studied with the H1 detector at HERA. Inclusive production cross sections in the visible range, defined by $p_t(D) \geq 2.5$ GeV/c, $|\eta(D)| \leq 1.5$, $2 \text{ GeV}^2 \leq Q^2 \leq 100 \text{ GeV}^2$ and $0.05 \leq y \leq 0.7$, are measured for the vector D^{*+} and for the pseudo scalar mesons D^0, D_s^+ and, for the first time at HERA, also D^+. The measurements are based on an integrated luminosity of 47 pb^{-1} taken during the e^+p running conditions of the years 1999 and 2000. The finite lifetimes of 0.4 to 1 ps for the pseudoscalar mesons lead to a separation of their production and decay vertices which is exploited to distinguish signal and background processes and to substantially improve the signal qualities. The reconstruction of separation distances of some 1/10 mm is made possible by exploiting the high-precision tracking capabilities of the central H1 silicon detector. Differential distributions are measured for all D-mesons and compared with predictions of Monte Carlo simulations based on leading, and in case of the D^{*+} meson, also next-to-leading order QCD calculations. A good agreement is found in shape as well as in the absolute normalization. The measured production cross sections are used to test the isospin invariance of the fragmentation process and to extract the strangeness suppression factor γ_s and the fraction P_V^d of bound $(c\bar{d})$ states produced in excited spin states. The assumed universality of the fragmentation process can be, for the first time at HERA, tested comprehensively by comparing these ep results to values measured at the LEP e^+e^- collider. All measurements tend to be slightly higher than the e^+e^- values, but are within their errors compatible with them: in R, which tests the isospin invariance of the fragmentation process, the disagreement accounts for 1.2 standard deviations favoring $(c\bar{u})$ over $(c\bar{d})$ states. In P_V^d the measurement is higher than the ALEPH value by 1.4 standard deviations. The measured γ_s value is within its error in agreement with the combined LEP and with ZEUS results. Therefore the assumed universality of the charm fragmentation process can be confirmed.

Zusammenfassung

Die vorliegende Arbeit untersucht die Produktion von Mesonen mit Charm Inhalt in tiefinelastischer Positron-Proton Streuung mit Daten des H1 Experimentes am HERA Speicherring. Die Wirkungsquerschnitte der Erzeugung von vektoriellen D^{*+} und pseudoskalaren D^0, D_s^+ und, zum ersten Mal bei HERA, auch D^+ Mesonen werden im sichtbaren kinematischen Bereich gemessen, welcher durch $p_t(D) \geq 2.5$ GeV/c, $|\eta(D)| \leq 1.5$, 2 GeV$^2 \leq Q^2 \leq 100$ GeV^2 und $0.05 \leq y \leq 0.7$ definiert ist. Die Messungen beruhen auf einer integrierten Luminosität von 47 pb^{-1}, welche in den e^+p Datennahmeperioden der Jahre 1999 und 2000 aufgezeichnet wurden. Die endlichen Lebensdauern der pseudoskalaren Mesonen von einigen Pikosekunden führt zu einer räumlichen Trennung ihrer Erzeugungs- und Zerfallspunkte. Diese Eigenschaft wird zur Unterdrückung von Untergrundereignissen und damit zur Signalverbesserung ausgenützt. Die Messung von Distanzen im 1/10 mm Bereich wird durch die ausgezeichnete Ortsauflösung des H1 Silizium Vertex Detektors ermöglicht. Für alle aufgeführten D-Mesonen werden differentielle Verteilungen gemessen und mit Vorhersagen in erster, im Falle der D^{*+} Mesonen auch in nächst höherer Ordnung durchgeführten QCD Störungsrechnungen verglichen. Die gefundenen Übereinstimmungen zwischen Messung und Vorhersage sind gut, sowohl in den absoluten Grössen als auch in den untersuchten Abhängigkeiten der Wirkungsquerschnitte. Diese Ergebnisse ermöglichen eine Überprüfung der Unabhängigkeit des Charm Fragmentationsprozesses von der Isospin Ausrichtung und erlauben auch eine Messung des Unterdrückungsfaktors γ_s, welcher das geringere Auftreten von gebunden Zuständen mit Strange Inhalt beschreibt, sowie die Bestimmung des Anteils P_V^d von gebundenen $(c\bar{d})$ Zuständen, welche in angeregten Spinzuständen erzeugt werden. Die Resultate werden mit Ergebnissen von e^+e^- Annihilationsexperimenten am LEP Speicherring verglichen. Dadurch kann, zum ersten Mal bei HERA, die als allgemein gültig angenommene Beschreibung des Fragmentationsprozesses umfassend überprüft werden. Alle Messungen tendieren im Vergleich zu den LEP Ergebnissen zu leicht höheren Werten, sind aber im Rahmen ihrer Fehler mit ihnen verträglich: In R, ein Mass für die Isospin Unabhängigkeit der Fragmentation, beträgt der Unterschied 1.2 Standardabweichungen, wobei gebundene $(c\bar{u})$ Zustände häufiger als $(c\bar{d})$ Zustände auftreten. In P_V^d liegt der gemessene Wert 1.4 Standardabweichungen über dem ALEPH Resultat. In γ_s stimmt die Messung innerhalb ihres Fehlers mit dem kombinierten Resultat der LEP Experimente und mit dem von der ZEUS Kollaboration gemessenen Wert überein. Dies besätigt die allgemeine Gültigkeit der Beschreibung des Fragmentationsprozesses.

Contents

Introduction

The production of charm quarks at HERA is anticipated to be well described by perturbative Quantum Chromodynamics (pQCD) due to the relatively large quark mass. However, these calculations are performed at the parton level, while experimentally only bound states, charmed hadrons, are accessible due to confinement. The lack of a large scale in the transition from the parton to the hadron level prohibits a perturbative approach and therefore this fragmentation process has to be described by phenomenological models.

These models have to be tuned with measurements that up to now have been performed almost exclusively at e^+e^- annihilation experiments, where the correlation of the hadron and parton levels is possible: the initial states of the pairwise produced charm quarks are in e^+e^- collisions experimentally accessible due to the fixed center-of-mass energy. This correlation is highly nontrivial in positron-proton or proton-anti-proton collisions due to the composed nature of the proton which complicates the reconstruction of the initial charm state.

Under the assumption of factorization, i.e. the separation of short and long distance phenomena in the QCD calculation, the fragmentation is predicted to be independent of the charm production process, i.e. universal. The application of the models tuned to e^+e^- data to positron-proton (ep) collisions is therefore widely accepted. Still the fragmentation process remains a significant source of uncertainty which obscures the comparison of experimental data and theoretical predictions and therefore an improved understanding is highly desirable.

Different processes may exhibit distinctively different sensitivity to the aspects of fragmentation, wherefore the application of e^+e^- results to ep collision data might be doubtful. Thus testing the hypotheses of universality and factorization in different processes has become compulsory.

This thesis describes a measurement which allows testing the universality by comparing relative production rates of different D-meson types, bound charm states, in ep collisions with results from e^+e^- annihilation experiments. The D-mesons signals are identified consistently by means of a lifetime tag: the D-mesons' finite lifetimes of some picoseconds lead to a separation of their production and decay vertices which is exploited by means of the H1 Central Silicon Tracker (CST) to distinguish them from far more frequent background processes that contain no such lifetime information.

This thesis proceeds as follows. The theoretical background of charm production at HERA and of the fragmentation process is reviewed in chapter 1. The measurements

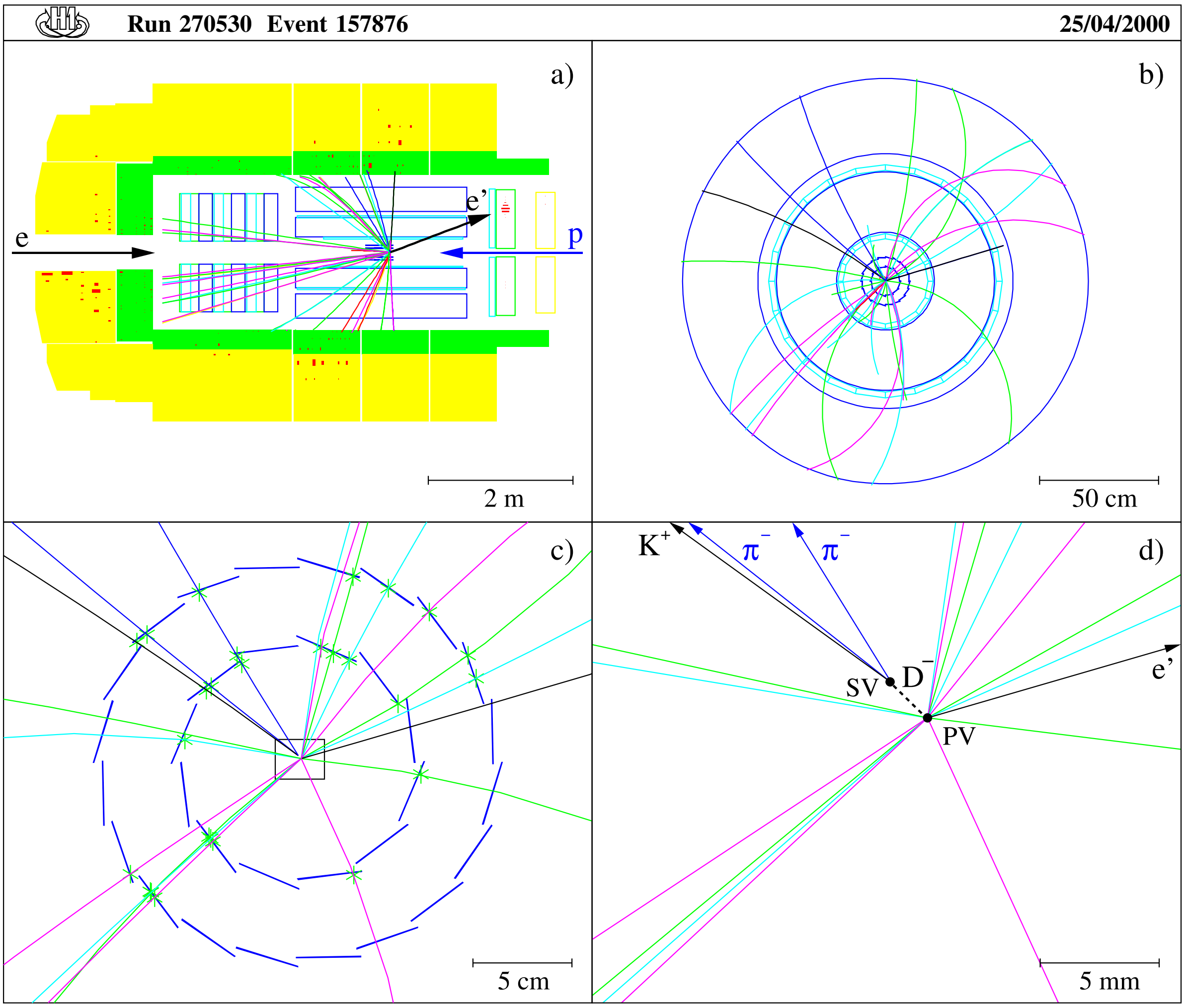

Figure 1: *The deep inelastic positron-proton scattering event recorded with the H1 detector at HERA contains a candidate for a* $D^- \to K^+\pi^-\pi^-$ *decay with a secondary vertex clearly separated from the event's primary vertex (see text).*

are performed in the regime of deep inelastic ep scattering (DIS), exact definitions of the kinematical range and of the measured physical quantities are given in chapter 3, where also the measuring method is specified.

In figure 1a the experimental signature of a DIS event recorded with the H1 experiment at the HERA collider, both described in more detail in chapter 2, is shown: the incoming positron (e) and proton beams (p) are indicated by arrows in the side view of the H1 detector. The bound state of the proton is broken in the scattering process. The outgoing positron (e') is detected by the SpaCal calorimeter in the backward region of the detector which allows the reconstruction of the scattering kinematics discussed in chapter 4.

The tracks, the flight paths of charged particles produced in the interaction indicated in the figure by lines, are measured in the tracking chambers which are surrounded by the H1 main calorimeter, shown in figure 1a as shaded areas. The reconstruction in the central region, discussed in chapter 5, begins from the outside in the Central Jet Chamber (CJC)

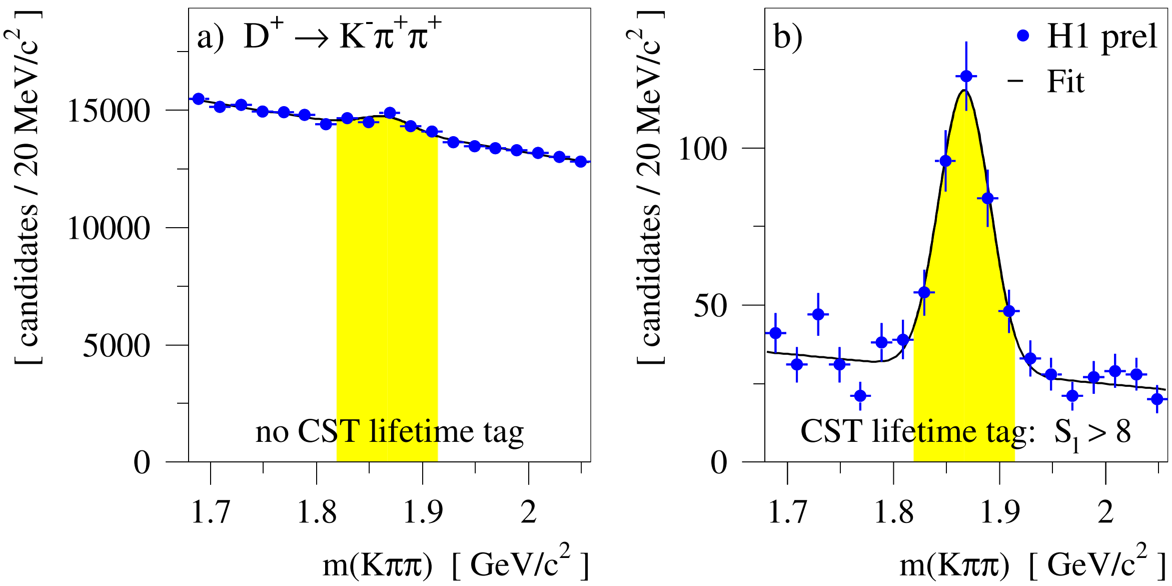

Figure 2: *A comparison of the $m(K\pi\pi)$ mass distributions for $D^+ \to K^-\pi^+\pi^+$ decay candidates is shown (a) before and (b) after a cut on the decay length significance $S_l = l/\sigma_l > 8$. The background contribution is suppressed by $\mathcal{O}(300)$ and the signal to background ratio is improved by a factor $\mathcal{O}(50)$ when vertexing information measured with the H1 central silicon vertex detector CST is exploited.*

which is shown separately in figure 1b in a front view: beside of the track identification and reconstruction, their bending in the applied magnetic field allows a measurement of the particles' momenta.

The CJC encloses the H1 silicon vertex detector CST, shown in a closer view in figure 1c: The high precision CST position measurements, shown in the figure as bright stars, significantly improve the resolution of the CJC tracks. The precision of such CST improved tracks is sufficient to resolve the event topology in the area indicated in the center which is magnified in figure 1d: the decay vertex (SV) of a D^- candidate, reconstructed by intersecting the tracks of its decay products ($K^+\pi^-\pi^-$) as explained in chapter 5, is clearly separated from its production vertex (PV), the point of the *ep* interaction.

Random combination of particles produced at the interaction point itself with an invariant mass similar to the mass of the D-meson are the dominate background for the signal extraction. The power to distinguish signal events characterized by a vertex separation from this background is demonstrated in figure 2: while in the reconstructed mass spectrum of D^+ candidates without a lifetime requirement an excess in the region of the nominal D^+ mass can only be suspected, a clear D^+ signal emerges when requiring a significant decay length. The decay length significance is defined as the quotient of the reconstructed radial decay length l and its calculated error σ_l, $S_l = l/\sigma_l$, and is the major selection criteria of the lifetime tag discussed in chapter 6.

Besides the optimization of the discrimination between signal and background events, the major task is to prove the accuracy of the detector simulation to describe the data with respect to the lifetime tag: by improving the signal quality as shown in figure 2 not only background is largely suppressed, but also a significant fraction of the signal events is rejected. This fraction has to be known for the measurements and it is estimated with simulated events. The procedure is justified by extensive comparisons of data and simulated D-meson decays, where especially the D^0 meson sample tagged in the D^{*+} channel provides a rich testing field, because it is the only channel in which, due to the Δm tagging technique, the signal extraction does not rely crucially on the lifetime tag.

The discussion of the results in chapter 7 proceeds along the following lines: first the established measurement of the D^{*+} production cross section is repeated using only the CJC information and shown to be consistent with previous publications. Once the CJC analysis chain has been established, the D^{*+} cross section measurement is redone by means of the CST as a final comprehensive test for the lifetime tagging method.

Then the determination of the cross sections based on the lifetime tag is presented for the different decay channels. Because the results of the different channels are extracted consistently within the same visible kinematic regime, they allow a determination of production ratios sensitive to the fragmentation process in which most systematic uncertainties of the experimental method cancel. For the first time at HERA a comprehensive test of the assumed universality of the fragmentation process is possible by comparing these ep results with ratios measured at e^+e^- experiments. In chapter 8 conclusions from the measurements are drawn and in an outlook possible improvements of the measurements are discussed.

Chapter 1

Theoretical Framework

The fragmentation process, the formation of bound states from initial partons, is the link between the theoretical predictions on the parton level and the experimental accessible hadrons. The process can not be derived from first principles in the framework of pQCD due to confinement. Therefore it has to be described by phenomenological models which are up to now tuned almost exclusively with e^+e^- data. The application of these models to *ep* scattering relies on several assumptions generally referred to as the universality of the fragmentation process.

Charm production in *ep* scattering provides a rich field to test pQCD, because many aspects of the theory are involved. Herein the fragmentation process of charm quarks into D-mesons is studied an understanding of which is compulsory for such tests. The measurement is the first comprehensive study at HERA in this field.

In the following the performed measurements are embedded inside a broader theoretical framework: First a general review of some of the basic concepts necessary to describe deep inelastic lepton hadron interactions is given. In section 1.2 the mechanisms of heavy flavor production at HERA are discussed. Thereafter the description of the fragmentation process is reviewed with a focus on D-mesons, the experimental signature of charm exploited herein, and the assumptions necessary for an universality of the process are discussed. In section 1.4 follows a brief review of relevant D-meson properties and definitions of variables describing their kinematics are given. The chapter concludes with a description of the Monte Carlo generators used herein to calculate the pQCD predictions.

1.1 Deep inelastic scattering at HERA

The kinematics of deep inelastic *ep* scattering (DIS) is defined by a few Lorentz invariant variables discussed in section 1.1.1. But the dynamics of the process depends on the internal structure of the proton and therefore structure functions are introduced to describe the hadronic part of the interaction (see sec. 1.1.2). A consistent interpretation of these structure functions is possible within the framework of QCD which most important features will be reviewed in section 1.1.3.

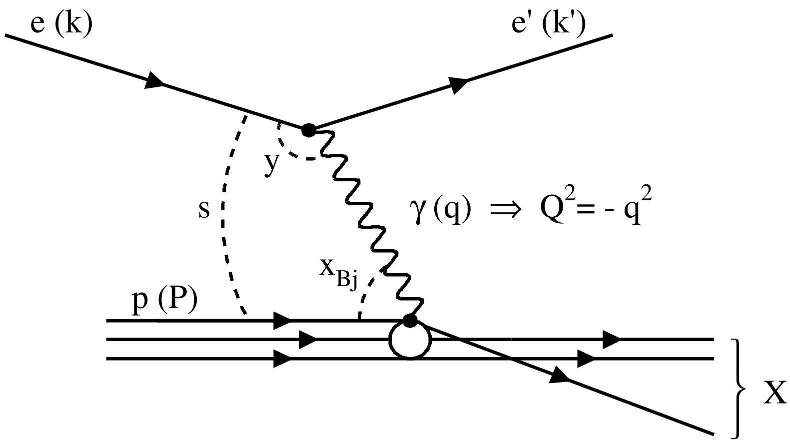

Figure 1.1: *The dominate deep inelastic ep scattering process at HERA is shown: a positron (e), coming in from the left, emits a photon (γ) which scatters on a constituent of the proton (p). Characters in brackets give the notation of the particles' four-momenta used in the text to define the kinematical variables s, Q^2, y and x_{Bj} which have been places in the figure to fit with their intuitional meanings.*

1.1.1 DIS kinematics

At HERA positrons[1] and protons are collided at high energies. The scattering process is called elastic, if the proton stays intact, inelastic otherwise. The elasticity of the scattering depends on the momentum transfer from the positron to the proton. Breakups of the proton are interesting to study, because they reveal its internal structure: the incoming lepton can be viewed as a source of gauge bosons that resolve the composed hadron.

The scattering process can be characterized by the type of the exchanged gauge boson: in neutral current events γ or Z bosons are exchanged, where due to interferences effects no clear separation is possible, while in charged current events the positron emits a W^+ boson and therefore transmutes into an undetected neutrino.

Figure 1.1 shows the dominate deep inelastic *ep* scattering process at HERA. The squared four-momentum transfer from the positron to the proton is calculated via

$$Q^2 = -\boldsymbol{q}^2 = -(\boldsymbol{k} - \boldsymbol{k'})^2, \tag{1.1}$$

where $\boldsymbol{q}$, $\boldsymbol{k} = (E_e, \vec{p}_e)$ and $\boldsymbol{k'} = (E_{e'}, \vec{p}_{e'})$ denote the four-momenta of the exchanged gauge boson and of the incoming and outgoing positron.

In optics the resolution depends linearly on the wave length of the light source. Equivalently the de Broglie wave length ($\lambda\!\!\!^- = \hbar \cdot c / |\boldsymbol{q}|$) of the exchanged gauge boson describes the resolution available for probing the proton's internal structure. Thus Q^2 gives a physical scale to distinguish three different regimes at HERA:

[1]In fact, both charge conjugates of the electron can be stored in HERA. The measurement is performed with e^+p data, but the term "positron" can be used interchangeably to label positrons and electrons.

- $Q^2 < 1$ GeV^2 (photoproduction):
  Because the propagator of the gauge bosons is inversely proportional to $(M^2 + Q^2)$, the exchange of the massive $W^\pm$ and Z bosons ($\mathcal{O}(M) = 100$ GeV/c^2) is heavily suppressed. The $1/Q^2$ dependence for the exchange of massless photons makes photoproduction the dominate scattering process at HERA. Photoproduction events can be used to study the hadronic structure of the photon arising from $\gamma \rightarrow q\bar{q}$ fluctuations (resolved processes).

- 1 GeV$^2 < Q^2 < 100$ GeV^2 (DIS at moderate Q^2):
  This is the regime where most HERA measurements concerning the structure of the proton are performed, because the scattering cross section is still reasonable large and there is already a good resolution power available. Also the present analysis is performed in this regime. The exchange of photons is still dominant and thus Z exchange is omitted henceforth. The scattered positron is measured in the SpaCal calorimeter (cf. chap. 2) which serves as a clear experimental signature. Resolved processes are suppressed, because the high virtuality of the photon sets an upper time limit for $q\bar{q}$ fluctuations. In the range analyzed herein they contribute less than 2% to the total cross section [2].

- $Q^2 > 100$ GeV^2 (DIS at high Q^2):
  The cross section expected from the Standard Model in this regime is small. Therein lies some of the discovery potential for new physics at HERA. Besides the search for new physics, this data is extremely valuable to examine the existing theories in this environment accessible only at HERA. For $Q^2 \approx \mathcal{O}(M_Z^2)$ charged and neutral currents attain comparable strength. The scattered positron is measured in the main calorimeter.

The squared center of mass energy s of the reaction is given by the initial state:

$$s = (\boldsymbol{P} + \boldsymbol{k})^2 \approx 4 \cdot E_e \cdot E_p, \tag{1.2}$$

where $\boldsymbol{P}$ and E_p denote the four-momentum and the energy of the incoming proton. The approximation neglects the masses of the proton and the positron.

Besides Q^2 and s the kinematics of the scattering process is fully defined by just one additional variable, usually a dimensionless Lorentz scalar. Convenient choices are either the lepton inelasticity y or the Bjorken x_{Bj} variable. They are defined and related via

$$y = \frac{\boldsymbol{q} \cdot \boldsymbol{P}}{\boldsymbol{k} \cdot \boldsymbol{P}} \qquad x_{Bj} = -\frac{1}{2} \cdot \frac{\boldsymbol{q} \cdot \boldsymbol{q}}{\boldsymbol{q} \cdot \boldsymbol{P}} \qquad Q^2 = s \cdot x_{Bj} \cdot y. \tag{1.3}$$

In the photoproduction limit y represents the fraction of the positron momentum carried by the exchanged photon, while x_{Bj} can be interpreted in the Parton Model as the fraction of the proton momentum carried by the struck proton constituent (see sec. 1.1.2).

There are several methods to reconstruct the ep scattering kinematics, some of which will be discussed in chapter 4.

1.1.2 Inclusive cross section and structure functions

Because the proton is a composed object with a priori unknown structure, *ep* scattering differs considerably from the e^+e^- annihilation process. Still, without further knowledge of the involved theory, but some assumptions on its basic symmetries like Lorentz invariance, momentum and current conservation (see e.g. [3]), the inclusive double differential *ep* scattering cross section can be derived:

$$\frac{d^2\sigma(ep \to e'X)}{dx_{Bj}\; dQ^2} = \frac{4 \cdot \pi \cdot \alpha_{em}^2}{x_{Bj} \cdot Q^4} \cdot \left[\; y^2 \cdot x_{Bj} \cdot F_1(x_{Bj}, Q^2) + (1-y) \cdot F_2(x_{Bj}, Q^2) \; \right], \quad (1.4)$$

where α_{em} denotes the electromagnetic coupling constant. The ignorance of the proton structure is absorbed in the two proton structure functions $F_1(x_{Bj}, Q^2)$ and $F_2(x_{Bj}, Q^2)$. They describe the dynamics of the scattering process and thus depend on x_{Bj} and Q^2.

An intuitive interpretation of the structure functions is possible in the Parton Model suggested by Bjorken and Paschos in 1969 [4]. In this model the proton is supposed to be composed of non-interacting, point like spin 1/2 partons and the photon-proton scattering can thus be seen as photon-parton scattering. The internal structure of the proton can then be derived from parton density functions $f_{i/p}(x_{Bj})$ which denote the probability to find a parton i inside the proton carrying a fraction x_{Bj} of the proton's momentum. An important result of this model is the structure functions' independence on Q^2. This behavior is called scaling invariance or Bjorken scaling [5].

In the Quark Model[2] the proton is composed of three valence quarks. Historical it was questioned, if the partons introduced by Bjorken are equivalent to these quarks. This question has partially been confirmed, but there were two major experimental hints that the world is more complicated than the Parton Model suggests: on the one hand the measured momentum sum of all valence quarks accounts for only about half of the proton's momentum and on the other hand the proton structure functions are being found to be Q^2 dependent, a behavior called the scaling violation of F_2. These failings are overcome in the theory of Quantum Chromodynamics, introduced in the following.

1.1.3 Quantum Chromodynamics

Quantum Chromodynamics (QCD) is a gauge field theory that describes the strong interaction which is the dominant force between the constituents of the proton. In the framework of QCD the partons introduced in the last section are indeed partially identified with the quarks suggested by Gell-Mann, but also gluons, the gauge bosons of the strong interaction, contribute to the internal structure of the proton.

Quarks are massive spin 1/2 particles with one or two thirds of the elementary electrical charge. There are six quark flavors which are, sorted ascending in their masses: up, down, strange, charm, beauty and top. Flavors are often abbreviated by their first letter,

[2]The Quark Model has been proposed by Gell-Mann and Zweig to describe the results of hadron spectroscopy. Gell-Mann has been awarded with the Nobel Price for Physics in 1969 for this work [6].

e.g. c for charm. Quarks carry the charge of the strong interaction which has three basic states: in analogy to color theory the charge is called color charge and its positive charge states are red, green and blue, while negative charges are denoted with the corresponding anti-colors.

Gluons are the gauge bosons of the strong interaction and thus glue together the hadrons. They are massless and electrically neutral spin 1 particles. In contrast with QED, where the gauge bosons (photons) are neutral with respect to the interaction, gluons carry the charge of the strong force: they are charged with one color and one anti-color and can therefore couple to each other. There are eight gluons according to the eight different combinations which form the asymmetric[3] basis of the color charge doublet.

As long as the coupling constant of the strong interaction α_s is reasonable small ($\alpha_s \ll 1$), a perturbative treatment of the theory, i.e. an evolution in orders of α_s is applicable. This framework is called perturbative QCD (pQCD). A fixed order calculation, e.g. in leading order $\mathcal{O}(\alpha_s)$ (LO) or next-to-leading order $\mathcal{O}(\alpha_s^2)$ (NLO), neglects contributions of terms in higher orders of α_s.

Problems arise in the calculation of the scattering amplitude from the contribution of virtual gluon emissions: integrals over the energy fraction x transfered from the initial parton to the virtual gluon diverge for large and for small values of x. These divergencies are called ultraviolet or collinear for $x \to 1$ and infrared or soft for $x \to 0$. Because physical observables are always finite, the divergencies are only an artefact of theory. The work of Hooft and Veltman has shown, how they can be tamed and interpreted, and has been awarded with the Nobel Prize for Physics in 1999 [7]. The basic ideas are discussed below on the examples of the running coupling constant and the dynamic evolution of the proton structure functions.

The running coupling constant $\alpha_s(\mu_R)$

According to the uncertainty principle ultraviolet emissions take place at very short time and distance scales. The solution to avoid the corresponding divergencies in the calculations is known under the name of renormalization: the essential idea is to avoid looking too closely at the divergent processes, but to absorb them into parameters defined and measured at an evolution point.

For the coupling constant α_s of the strong interaction the mass M_Z of the Z boson, the heaviest known gauge boson, is a reasonable choice for the evolution point. Interactions taking place at time scales $t < \hbar/M_Z$ are absorbed into the bare coupling constant $\alpha_s(M_Z)$ the value of which has to be determined experimentally (see e.g. [8]). The corresponding integrals are then aborted at the cutoff M_Z and become finite with respect to the collinear divergencies.

Processes happening between the cutoff, $t > \hbar/M_Z$, and the time scale $t = \hbar/\mu_R$ of the interaction, where μ_R is a relevant hard scale of the process, e.g. a large mass or a high momentum, are absorbed into the coupling constant which becomes therefore dependant

[3] In the symmetric state colors and anti-colors cancel, wherefore this neutral gluon does not interact.

on the (renormalization) scale μ_R. This dependence, described by renormalization group equations, is known as the running of the coupling constant: $\alpha_s = \alpha_s(\mu_R)$. The solution for α_s in leading order is

$$\alpha_s(\mu_R) = \frac{12 \cdot \pi}{(33 - 2 \cdot N_\mathrm{f}) \cdot \ln(\mu_R^2/\Lambda_{QCD}^2)} \text{ with } \Lambda_{QCD}^2 = M_Z^2 \cdot e^{-\frac{12\cdot\pi}{(33-2\cdot N_\mathrm{f})\cdot\alpha_s(M_Z)}}, \tag{1.5}$$

where N_f denote the numbers of quark flavors considered in the virtual loop corrections to the gluon propagator. The value of the introduced Λ_{QCD} parameter is of the order $\mathcal{O}(200\text{ MeV})$[9] and depends not only on the cutoff M_Z, but also on the orders in α_s and the number of flavors N_f considered in the calculations.

$\alpha_s(\mu_R)$ becomes large with decreasing $\mu_R \to \Lambda_{QCD}$ which corresponds to long distance and time scales. The increasing strength of the strong force with rising distance is known as confinement and is responsible for the binding of quarks into color neutral objects, hadrons. The perturbative approach fails in this regime, because evolutions in $\alpha_s(\mu_R) \to 1$ become divergent. On the other hand the interaction becomes weak at short distances, $\alpha_s(\mu_R) \ll 1$ for $\mu_R \gg \Lambda_{QCD}$, which is therefore called the regime of asymptotic freedom in which a perturbative treatment is applicable.

Parton density functions in QCD

The infrared divergencies involve processes on large time scales in the confinement regime and can therefore not be treated inside the framework of pQCD. There are two solutions to arrive at infrared save observables: either the divergencies cancel by summing over indistinguishable final states or the long and short distance phenomena are separated. The latter, the factorization theorem of QCD, will be discussed in the following on the example of the parton density functions introduced in the Parton Model (see sec. 1.1.2).

In the framework of QCD the proton contains beside of its three valence quarks also gluons as gauge bosons which themselves may fluctuate into gg or $q\bar{q}$ pairs, the latter are called sea quarks. Valence quarks, sea quarks and gluons, the partons, contribute all to the proton's structure functions.

The factorization follows closely the formalism of the renormalization introduced in the previous section: contributions of slow processes, $t > \hbar/\mu_F$, are taken from the perturbative calculations and are packed into "running" parton density functions. Similar to the renormalization scale μ_R, the factorization scale μ_F is given by a hard scale relevant for the scattering process, e.g. Q^2. The renormalization group equations for (massless) parton density functions $f_{i/p}$, the DGLAP[4] evolution equations [10], are given by

$$\frac{df_{i/p}(x, \mu_F)}{d\ln\mu_F^2} = \frac{\alpha_s(\mu_R)}{2 \cdot \pi} \sum_{partons\ j} \int_x^1 P_{ij}(x/z) \cdot f_{j/p}(z, \mu_F) \cdot \frac{dz}{z}, \tag{1.6}$$

where the splitting functions $P_{ij}(z)$ denote the probability that an initial parton j emits a secondary parton i with a fraction z of its initial momentum. The functions P_{ij} depend on the order in α_s considered in the calculations.

[4]Dokshitzer, Gribov, Lipatov, Altarelli, Parisi

With the concepts of renormalization and factorization the perturbative treatment of hard scattering processes have been protected against ultraviolet and infrared divergencies. The inclusive cross section of ep scattering in deep inelastic scattering (cf. eq. 1.4) can therefore be related to the perturbatively calculable partonic cross sections $\hat{\sigma}_i$ which describe the scattering of the positron on a parton i inside the proton with

$$d\sigma(ep \to e'X) = \sum_{partons\ i} \int_0^1 f_{i/p}(x, \mu_F) \cdot d\hat{\sigma}_i(\hat{s}, \alpha_s(\mu_R), \mu_R, \mu_F) \cdot dx, \tag{1.7}$$

where $\hat{s}$ denotes the center of mass energy of the boson-parton system, $\hat{s} = (x \cdot P + q)^2$.

The equation is the pivotal point of an unfolding procedure to measure the parton density functions $f_{i/p}$. Equivalent to the measurement of the coupling constants at a certain cutoff, they are measured at a certain factorization scale μ_F, usually a small Q^2 value. These measurements serve as the necessary boundary condition for equation 1.6 which can then be used to predict the dynamical behavior of the parton density functions. Because they depend in the framework of QCD on the scale μ_F of the scattering process, the scaling violation of F_2 can be explained by setting $\mu_F^2 = Q^2$. An intuitive interpretation of the scaling violation is that with rising resolution μ_F more and more of the vibrant inner life of the proton is reveal.

Usually μ_R and μ_F are set equal: $\mu_F = \mu_R = \mu$. As already indicated there is some freedom in the choice of μ, because most often the scattering process involves more than just one single hard scale. Ideally a variation of the scale just changes the place at which some processes are considered in the calculations and therefore leave the results unchanged. But in the perturbative treatment at a fixed order this is fulfilled only partially. The residual dependence can be estimated by comparing calculations with different choices.

A more complete introduction to QCD can be found in e.g. [3, 11].

1.2 Heavy flavor production at HERA

While the light u, d and s quarks have masses of the order of the Λ_{QCD} parameter, the masses of the heavy flavors are already sufficient to serve as a hard scale for perturbative calculations. The top quark being just out of reach, charm and beauty are the heavy flavors produced at HERA. The following discussion will focus on charm production, but most arguments are equally valid for beauty.

In figure 1.2 the photon-gluon fusion graph (PGF), of leading order in α_s, is shown which is the main production mechanism of charm at HERA: a photon coupling to the incoming positron interacts with a gluon in the proton to form a charm anti-charm pair. Because the proton serves as a gluon source, charm production at HERA is sensitive to the gluon density inside the proton and allows a direct measurement of it [12, 13]. Especially at small x_{Bj} values the gluons contribute significantly to the proton structure (cf. fig. 1.3).

There are two schemes available to describe heavy flavor production in DIS. In the massive scheme the charm mass is taken fully into account in the calculations of the partonic

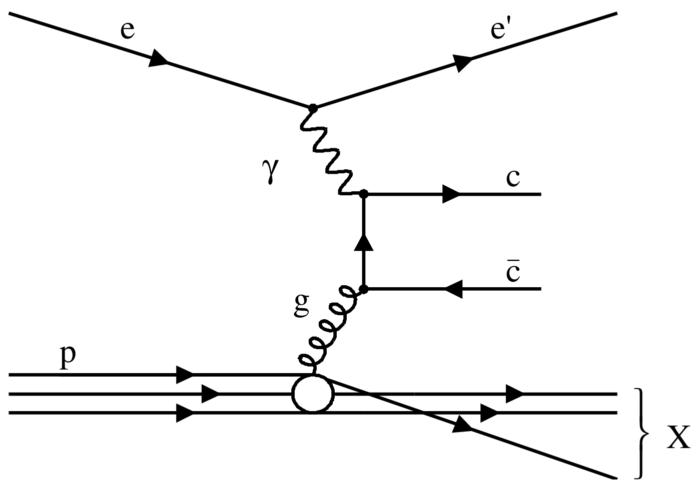

Figure 1.2: *The dominant charm production mechanism at HERA is shown: a photon (γ) emitted by the positron (e) and a gluon (g) out of the proton (p) scatter on a $c\bar{c}$ pair. The diagram is called the photon-gluon fusion graph (PGF).*

cross sections, while the lighter quarks are treated massless as required by the DGLAP formalism (cf. eq. 1.6). The charm contribution to the proton structure is neglected. In the massless approach the charm is regarded as massless too and treated as an active flavor in the proton structure functions.

The massive calculation is expected to be reliable in the low momentum regime of charm production, where the charm mass m_c is a relevant scale. For high charm momenta, $p_c \gg m_c$, the mass becomes negligible and the scale is dominated by $\mu \approx p_c$. In this regime terms in $(\alpha_s \cdot \ln(p_c^2/M_Z^2))$ are due to the large logarithm not necessary small enough to guarantee a convergency of the perturbative evolution. The massless approach is expected to yield a better description in this regime. Because heavy flavors are produced at HERA mainly at threshold the massive scheme is favored for this analysis.

Alternative sources of charm at HERA

- A small fraction of the analyzed D-mesons are produced in beauty decays. Beauty is also produced dominantly in the PGF process, but due to its higher mass, its production cross section is about two orders smaller than for charm [16]. Beauty decays via the weak interaction almost exclusively into charm (the branching ratio for charmless decays is less than 1% [17]). Especially due to the applied experimental technique this source of charm is taken fully into account for the measurement.
- The proton or the photon might contain a non-negligible amount of charm. An analysis by the H1 collaboration [18] came to the conclusion that such intrinsic charm can be neglected in the analyzed kinematic range.
- The charm production cross section in the photon-photon fusion process are predicted to be serval orders smaller than in photon-gluon fusion [19] and its contribu-

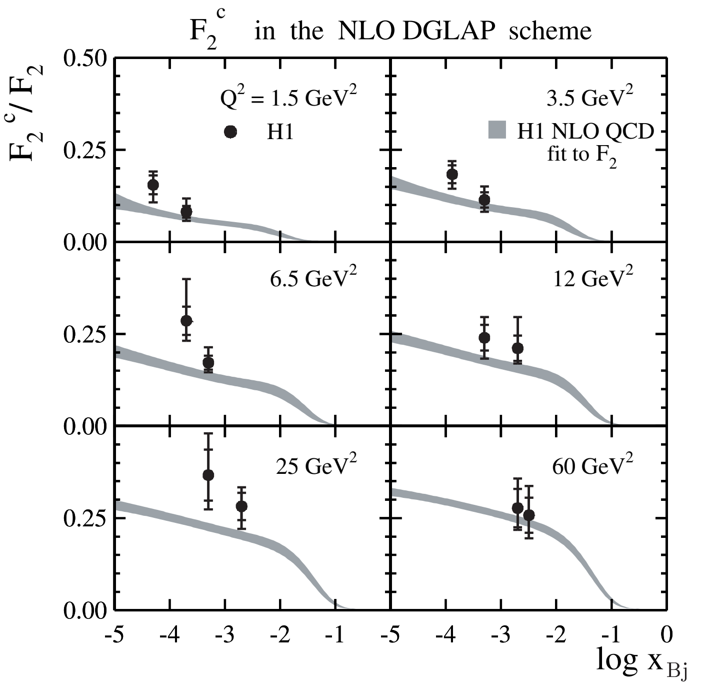

Figure 1.3: *The x_{Bj} dependence of the charm contribution F_2^c to the total proton structure function F_2 is shown for different values of Q^2 [14]. The fraction rises in all Q^2 bins towards small values of x_{Bj} and becomes especially significant with rising Q^2. The charm contribution F_2^c is sensitive to the gluon density $f_{g/p}$ in the proton.*

tion is therefore neglected.

- Single charm quarks could be produced by scattering W^+ bosons emitted by the positron on s or d quarks in the proton. This process has herein no relevance, because the analyzed events are tagged by the scattered positron.
- Charm quark pairs can also be produced in the fragmentation process. But as it will be discussed in the next section this process is highly suppressed due to the large charm mass.

1.3 Heavy flavor fragmentation

Because of confinement colored quarks form colorless bound states, the hadrons. They are classified in the Quark Model into baryons with three valence quarks, e.g. protons or neutrons, and into mesons consisting of a quark anti-quark pair. The process of the hadron formation is called fragmentation[5].

Due to confinement experiments can not access isolated quarks, but only hadrons. On the other hand a perturbative treatment of the hadron formation is not possible for exactly the same reason. It is necessary to fill this gap between experiment and theory to preserve

[5]In some models the formation process is also called hadronization.

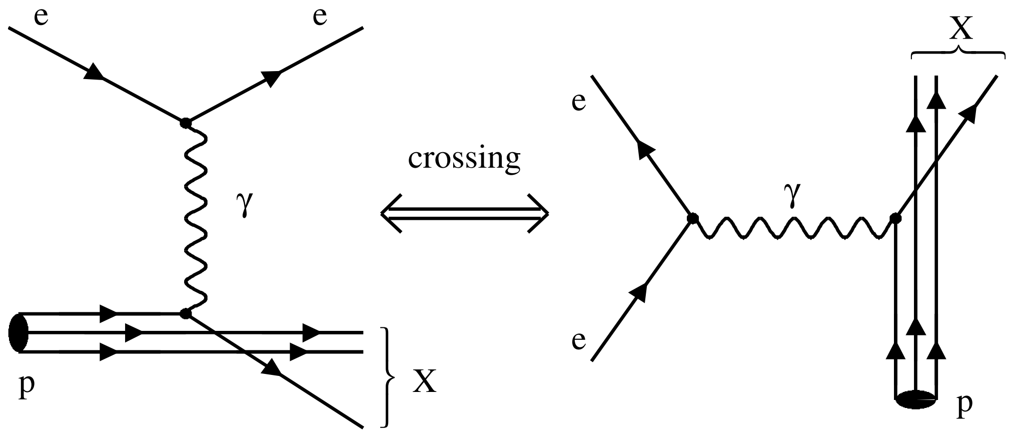

Figure 1.4: *The dominant diagram of deep inelastic ep scattering (cf. fig. 1.1) and its associated u-channel diagram are shown. The crossed diagram represents an e^+e^- scattering with an outgoing anti-proton and a hadronic final state X.*

the desired ability to test theoretical predictions. Thus phenomenological models have been developed to describe the fragmentation process.

Charm quarks can be detected either as hidden charm, where the $c\bar{c}$ pair itself forms a bound state such as a J/ψ meson, or as open charm, where the charm quarks "pick up" lighter quarks to form D-mesons or charmed baryons. In the following the focus will be on D-mesons which are the task at hand. The discussion of the hidden charm sector is omitted completely.

The fragmentation function formalism in which the short and long distance phenomena are separated is reviewed in the following. The perturbative part of the formalism has inspired the Parton Shower model. The Lund String and the Peterson fragmentation models, two of the most common models describing the long distance part of the fragmentation, are reviewed thereafter. The topic is concluded with a discussion of the assumed universality of the fragmentation process.

1.3.1 Fragmentation functions and Parton Showers

The fragmentation function formalism is very similar to the treatment of the parton density functions discussed in section 1.1.3. Considering the crossed diagram of the dominant deep inelastic *ep* scattering diagram shown in figure 1.4 the analogy becomes evident: its associated u-channel diagram represents an e^+e^- annihilation process into a hadronic final state X and an outgoing anti-proton produced in a fragmentation process from the initial parton. Even if this similarity invites the development of analog formalisms, results from the two processes can not be compared, because their allowed phase space regions have no overlap.

Similar to the inclusive *ep* cross section (cf. eq. 1.7) short and long distance processes are factorized to compute the cross section $d\sigma_h(p)$ of the observable hadron h with momentum p from the perturbatively calculated cross sections $d\hat{\sigma}_i(p/z, \mu_F)$ which describe the production of a parton i with momentum p/z at the factorization scale μ_F:

$$d\sigma_h(p) = \sum_{partons\ i} \int_0^1 \mathcal{D}_i^h(z,\mu_F) \cdot d\hat{\sigma}_i(p/z,\mu_F) \cdot dz. \tag{1.8}$$

The fragmentation functions $\mathcal{D}_i^h(z,\mu_F)$ describe the probability for an initial parton i to produce a hadron h with momentum fraction z. The ansatz implies the independence of $\mathcal{D}_i^h$ from the hard scatter process which is completely defined by $d\hat{\sigma}_i$. This is usually referred to as the universality of the fragmentation process.

The functions $\mathcal{D}_i^h(z,\mu_F)$ are not calculable for light quarks, but for a heavy enough quark a perturbative treatment is partially possible and calculations in leading and next-to-leading order are available [20]. Thereto $\mathcal{D}_Q^H(z,\mu_F)$, the probability to produce a hadron H from a primordial heavy quark Q, is further split into short and long distance parts:

$$\mathcal{D}_Q^H(z,\mu_F) = \int_z^1 D_Q(x,\mu_F) \cdot D_{np}^H(z/x) \cdot dx. \tag{1.9}$$

The perturbative fragmentation function $D_Q(x,\mu_F)$ describes via subsequent gluon emissions the transition of Q produced at the scale μ_F to a quark on its mass shell. The confinement ruled formation of the bound hadron state is then described by the non-perturbative fragmentation function $D_{np}^H(z)$. Because $D_{np}^H(z)$ can not be derived within the framework of pQCD, phenomenological models have been developed and the two most common are discussed hereafter.

The dependence of $D_Q(x,\mu_F)$ on the scale μ_F is described by the DGLAP evolution equation (see eq. 1.6). This evolution compensates for higher order corrections omitted in the fixed order calculation of the partonic cross section (cf. eq. 1.8). Because no evolution is necessary for a quark already produced at its mass shell the boundary condition for the evolution equation simply reads

$$D_Q(x,\mu_F) = \delta(1-x) \quad \text{for} \quad \mu_F = m_Q, \tag{1.10}$$

where $\delta(1-x)$ denotes a delta-function peaking at $x = 1$ and m_Q is the mass of Q. This inherent boundary condition is a major difference to the parton density functions which have to be measured at a certain evolution point.

The DGLAP formalism for the perturbative fragmentation functions has inspired the Parton Shower Model [21] which is used to simulate the evolution of the partons on a statistical basis in Monte Carlo programs. Therein the $1 \to 2$ splitting functions $P_{ij}(z)$ introduced in equation 1.6 model secondary parton emission and thus a shower evolution. The shower is developed until the partons reach a scale, where the perturbative treatment becomes unreliable, typically of the order $\mathcal{O}(1\ \text{GeV})$.

1.3.2 Lund String Model

The Lund String Model [23] describes the confinement ruled part of the fragmentation process on a broad basis. It is inspired by the string dynamics of Lattice QCD: the strong force between the isolated partons is implemented by connecting their color charges with one dimensional color flux tubes called strings.

The energy of the strings is determined under the assumption of a linear confinement potential, $E_{string} = \kappa \cdot \Delta x$, where Δx denotes the distance between the color charges and κ is a constant parameter interpreted as the string tension or the mass density in the string: $\kappa = \mathcal{O}(1 \text{ GeV/fm})$. Gluons are treated in the model as energy and momentum carrying kinks in the color strings.

The production of new quark pairs is described by string breakups. String breaking can be understood as a tunneling phenomenon. The tunneling probability,

$$\mathcal{P} \propto \exp(-\frac{\pi \cdot m_q^2 \cdot c^4}{\kappa \cdot \hbar \cdot c}) \cdot \exp(-\frac{\pi \cdot p_t^2 \cdot c^2}{\kappa \cdot \hbar \cdot c}), \tag{1.11}$$

provides a Gaussian spectrum in the transverse momentum p_t and describes the suppressed production of quarks with large masses m_q: a flavor mix of $u : d : s : c \approx 1 : 1 : 0.3 : 10^{-11}$ is expected from the quark masses [24]. Thus up and down quarks are produced equivalently due to their similar masses which is called the isospin invariance of the fragmentation process, while strangeness is suppressed due to the higher s quark mass. Because of the large c quark mass, charm production in the fragmentation is negligible.

The strings are evolved until the quarks are on their mass shells. Adjacent quarks are then combined to colorless mesons. The production of baryons is described as quark-diquark combinations, where the diquarks are also produced pairwise in string breakups.

The association of a mass to the quarks is difficult inside the renormalization scheme, because masses are similar to α_s dependent on the scale μ_R. Thus instead of using equation 1.11 the flavor mix is mostly determined experimentally: the isospin invariance is usually assumed which leaves the strangeness suppression γ_s to be measured (cf. sec. 7.2).

In addition the model does not predict the spin states of the formed hadrons. The pseudo scalar to vector meson ratio is therefore set either to a measured ratio (cf. sec. 7.2) or to theoretical predictions: beside the naive expectation from spin state counting[6], resulting in a ratio of 1:3, the ratio is predicted by two models, the thermodynamical approach [25] and the string fragmentation approach [26], to be closer to 2:3.

1.3.3 Peterson fragmentation for heavy quarks

The Peterson model [28] is an independent fragmentation model. It describes the transition of a heavy quark Q to a bound meson state H. Independent fragmentation models neglect the influence of the recoil system on the final hadron, i.e. the properties of the initial quark define the fragmentation process completely. The quark and meson momenta are further assumed to be the only relevant parameters for the process. This assumption is known as Feynman scaling and is legitimated by the confined nature of the process dominated by the exchange of soft gluons.

[6]There are $(2s+1)$ possible spin orientation for a state with spin s, i.e one for s=0 and three for s=1.

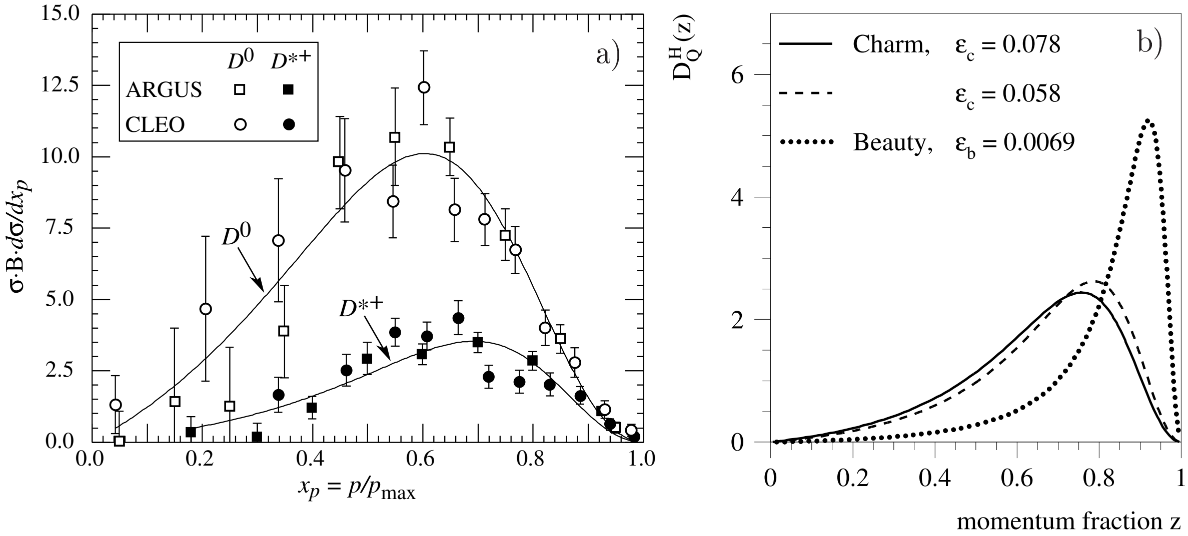

Figure 1.5: **(a)** *The inclusive D^0 and D^{*+} cross section spectra measured at the CLEO and ARGUS e^+e^- experiments ($\sqrt{s} = 10.5$ GeV) in the momentum fraction x_p are fitted with Peterson fragmentation functions to extract the ε_Q parameter [29].* **(b)** *The Peterson functions are shown for the values of ε_Q extracted in [31] for charm and beauty fragmentation in LO. Both figures are further discussed in the text.*

The bound meson state $(Q\bar{q})$ is formed by creating a light $q\bar{q}$ quark pair from the vacuum. The Peterson fragmentation function $D_Q^H(z)$ is derived from the probability for the transition which is inversely proportional to the squared energy difference between the initial and the final states. It is found to be

$$D_Q^H(z) = \frac{N_H}{z}\left(1 - \frac{1}{z} - \frac{\varepsilon_Q}{1-z}\right)^{-2}, \tag{1.12}$$

where z denotes the momentum fraction transfered from the initial quark Q to the final state meson H. The factor N_H normalizes the total probability for a hadron formation to one. The Peterson parameter ε_Q introduced describes the hardness of the fragmentation process and is defined by

$$\varepsilon_Q = (m_q/m_Q)^2, \tag{1.13}$$

where m_Q stands for the mass of the initial heavy quark and m_q denotes the mass of the light quark produced in the process.

Due to the difficulty to define a quark mass ε_Q is determined rather experimentally than with equation 1.13. Two examples are shown in figure 1.5a: The D^{*+} and D^0 spectra are both well described by the fitted Peterson functions. The D^0 mesons spectrum is clearly softer and therefore the extracted Peterson parameter $\varepsilon_c = 0.135 \pm 0.010$ is significantly higher than the value $\varepsilon_c = 0.078 \pm 0.008$ obtained from the fit to the D^{*+} spectrum [29].

The softer D^0 spectrum is not a consequence of a softer fragmentation process, but origins in the large fraction of D^0 mesons produced in cascade decays of spin excited D^{*+} and D^{*0} mesons (cf. sec. 1.4). Thus $D_Q^H(z)$ can not be directly extracted from the D^0 spectrum,

Peterson parameter	Experiment	$\sqrt{s}$ $[GeV]$	LO	NLO
ε_c	ARGUS	10.5	0.058	0.035
ε_c	OPAL	91.2	0.078	0.040
ε_b	ALEPH	91.2	0.0069	0.0033

Table 1.1: *The table quotes results from an extraction of the Peterson parameter from data of the e^+e^- experiments ARGUS, OPAL and ALEPH at different center of mass energies $\sqrt{s}$. The extraction has been done with leading (LO) and next-to-leading (NLO) order QCD calculations and has been performed for the fragmentation of charm as well as for beauty quarks [31].*

but is usually determined from the spectrum of vector mesons which are formed almost exclusively in the fragmentation process itself.

The Peterson model does not predict the probability to form a certain meson type H_i. Thus a generic Peterson function $D_Q^H(z)$ is assumed and the fragmentation function $D_Q^{H_i}(z)$ for a H_i meson is then defined as

$$D_Q^{H_i}(z) = f_{dir}(Q \to H_i) \cdot D_Q^H(z), \tag{1.14}$$

where the probabilities $f_{dir}(Q \to H_i)$ to form a certain meson type H_i have to be determined experimentally. The sum over all $f_{dir}(Q \to H_i)$ denotes then the fraction of heavy quarks which fragment into meson states, but it does not include the fraction of baryons produced.

The use of a generic $D_Q^H(z)$ function implies a similar ε_Q parameter for all meson types which might be questioned especially for the D_s^+ meson due to the higher s quark mass. The CLEO collaboration has determined the Peterson parameter with D_s^{*+} and D_s^+ spectra and the results, $\varepsilon_c = 0.056 \pm 0.008$ and $\varepsilon_c = 0.10 \pm 0.02$ respectively [30], are well comparable with the values quoted above and therefore justify this approach.

The value of the Peterson parameter depends on the perturbative treatment applied. In [31] the Peterson parameters have been extracted from data measured at the e^+e^- experiments ARGUS, OPAL and ALEPH within LO and NLO frameworks and some results are quoted in table 1.1. Because additional gluon radiation processes are considered in the NLO calculations which are omitted in LO, the values obtained in NLO are smaller. It is also interesting to note that the value extracted from the ARGUS data at a lower center of mass energy $\sqrt{s}$ are smaller which may indicate a harder fragmentation.

In figure 1.5b the Peterson function for the ε_Q values extracted from the D- and B-meson spectra in LO are shown: the fragmentation of the b quark is significantly harder than for the c quark, because the hadron formation is less sensitive to the production of the light quark pair due to the larger b mass (cf. eq. 1.13).

But while the Lund String model yields a description of the full hadronic final state, the Peterson model is only applicable for independent heavy flavor fragmentation. To profit still from the good description obtained in the heavy flavor sector, it has been optionally added to the Lund String Model: in this modus the Peterson function is used to describe string breakups and the longitudinal momentum distribution of heavy quarks. The treatment of the momentum component perpendicular to the string and the fragmentation of light quarks remains unchanged by this implementation.

1.3.4 Universality of Fragmentation

The parameters of the phenomenological models discussed are up to now tuned with measurements which have been performed almost exclusively at e^+e^- annihilation experiments, where the correlation of the hadron and parton levels is possible. The initial states of the pairwise produced charm quarks are experimentally accessible in e^+e^- scattering due to the fixed center-of-mass energy. This correlation is highly nontrivial in positron-proton or proton-anti-proton collisions due to the composed nature of the proton which complicates the reconstruction of the initial quark state.

But the factorization ansatz made in equation 1.8 implies that the fragmentation functions $\mathcal{D}_i^h$ do not depend on the type of the hard process. This universality justifies the application of the models tuned to e^+e^- data to ep scattering. But the factorization is an assumption only and residual dependences on the hard process might be present in $\mathcal{D}_i^h$ which are compensated by the tuned non-perturbative fragmentation function $D_{np}^H(z)$.

Different processes may exhibit distinctively different sensitivity to the aspects of fragmentation [32]: assuming out of simplicity that the dependence of the heavy flavor production cross section on the quark's momentum p is given by

$$\frac{d\hat{\sigma}_Q(p)}{dp} = \frac{A}{p^N}. \tag{1.15}$$

The spectrum of the produced hadrons H can then be written by using equation 1.8 as

$$\frac{d\sigma_H(p)}{dp} = \frac{A}{p^N} \cdot \int z^{N-1} \cdot \mathcal{D}_Q^H(z) \cdot dz, \tag{1.16}$$

where the integral expression is the definition of the N-th Mellin moment. Thus the form of the spectrum basically determines which Mellin moments of the fragmentation function are most easily accessed. But the heavy quark spectrum is steeper in ep than in e^+e^- collisions. Therefore the large moments of the fragmentation function most relevant for ep scattering are only poorly determined by fits to e^+e^- data.

In addition the ansatz of a generic Peterson function as defined in equation 1.14 could be questioned. The presented cross section measurements are sensitive to the value of the ε_Q parameter, because not the full momentum range of the mesons can be accessed: ε_Q influences the steepness of the momentum spectrum and the fraction of detected mesons above a certain threshold depends on this steepness.

The importance of a correct description of the fragmentation process is shown in [33] on the example of the beauty production cross section: measurements at TEVATRON in $p\bar{p}$ collisions previously indicated an access by a factor two and more with respect to NLO calculations. The authors show that an accurate use of up-to-date information on the B fragmentation functions reduces the observed excess to an acceptable level.

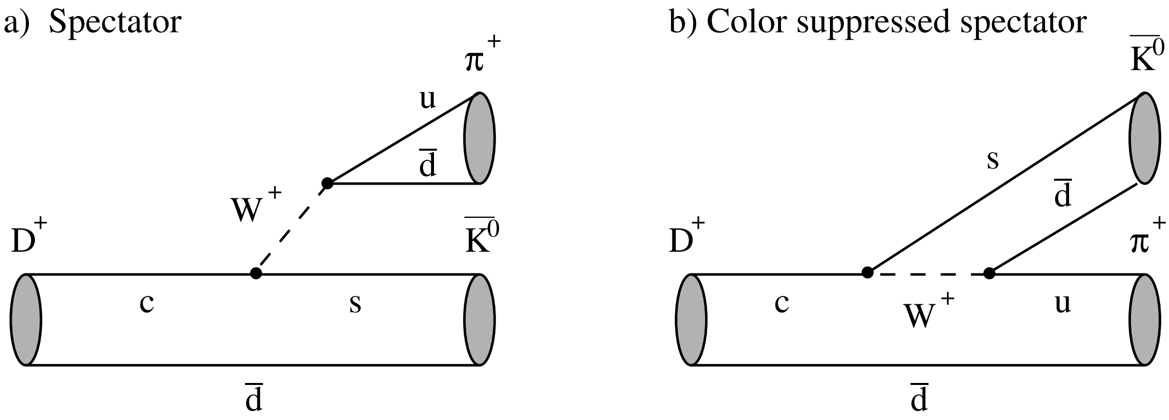

Figure 1.6: *(a) The spectator and (b) the color suppressed spectator diagrams of a $D^+ \to \overline{K^0}\pi^+$ decay are shown. Because they have an identical final state, the two diagrams can interfere.*

1.4 D-meson properties

In the Quark Model picture D-mesons[7] are bound states of a charm and a light up, down or strange anti-quark. According to their transformation properties D-mesons with zero spin are called pseudo scalar mesons (PS) and in the first excited spin state D^* vector mesons (VM). Their masses $m(D)$, mean lifetimes $c\tau$ and branching ratios can not be predicted accurately from theory and are therefore measured experimentally. In table 1.2 some D-meson properties relevant for this thesis are summarized and in addition the decay channels exploited herein are listed.

The pseudo scalar D-mesons are stable with respect to the strong interaction and therefore decay via the weak interaction by emitting a $W^\pm$ boson. This leads to their finite mean lifetimes of some 100 μm. The lifetime is longer by a factor 2.5 for D^+ than for D^0 and D_s^+ mesons. Even if not deducible from first principles, this can be understood qualitatively from the diagrams shown in figure 1.6: beside of the spectator diagram shown for a $D^+ \to \overline{K^0}\pi^+$ decay, there exists also a color suppressed diagram with an identical final state. These diagrams can interfere and a negative interference would explain a net increase of the D^+ lifetime. No such interference effects are possible for D^0 and D_s^+ mesons wherefore they have shorter lifetimes of a similar size (see also [35]).

In table 1.2 the D-meson fragmentation factors $f(c \to D)$ and $f(b \to D)$ are listed. They includes not only D-mesons directly formed in the fragmentation process, i.e. the fractions $f_{dir}(Q \to H_i)$ introduced in equation 1.14, but also indirect D-mesons originating from decays of spin excited states.

The different contributions to the $f(c \to D)$ factors of the pseudo scalar mesons have been pictured in the charm fragmentation tree shown in figure 1.7. The absolute values of all $f(c \to D)$ depend on the fraction of c quarks fragmenting into mesons indicated by the first branching. The splitting into pseudo scalar and vector mesons is usually parameterized with $P_V = \frac{VM}{PS+VM}$ denoting the fraction of mesons produced in a spin

[7]Hereafter, the charge conjugated states are always implicitly included.

D-**meson properties**	D^+	D^0	D_s^+	D^{*+}
valence quarks spin J^{Parity} mass [MeV/c^2] $c\tau$ [μm]	$(c\bar{d})$ 0^- 1869.3 ± 0.5 315 ± 4	$(c\bar{u})$ 0^- 1864.5 ± 0.5 123.7 ± 0.8	$(c\bar{s})$ 0^- 1968.6 ± 0.6 148.6 ± 3.0	$(c\bar{d})$ 1^- 2010.0 ± 0.5 -
$f(c \to D)$ [%] $f(b \to D)$ [%]	23.2 ± 1.0 23.7 ± 2.3	54.9 ± 2.3 60.5 ± 3.2	10.1 ± 0.9 18 ± 5	23.5 ± 0.7 17.3 ± 2.0
decay channel branching ratio [%]	$K^-\pi^+\pi^+$ 9.0 ± 0.6	$K^-\pi^+$ 3.83 ± 0.09	$\Phi\pi^+$ $\hookrightarrow K^+K^-$ 1.8 ± 0.5	$D^0\pi^+$ $\hookrightarrow K^-\pi^+$ 2.59 ± 0.06

Table 1.2: *The table summarizes the D-meson properties relevant for the presented analysis. The measured values are taken from [17] with exception of the charm fragmentation factors $f(c \to D)$, where values from [34] are quoted[a]. The factors $f(b \to D)$ stand for the probabilities for a beauty quark to decay into a D-meson of the corresponding type. In addition the decay channels analyzed herein and their branching ratios are listed.*

[a] Because the $f(c \to D)$ factors have been measured in the same decay channels as studied herein, the uncertainties in the corresponding branching ratios have been excluded from their quoted errors.

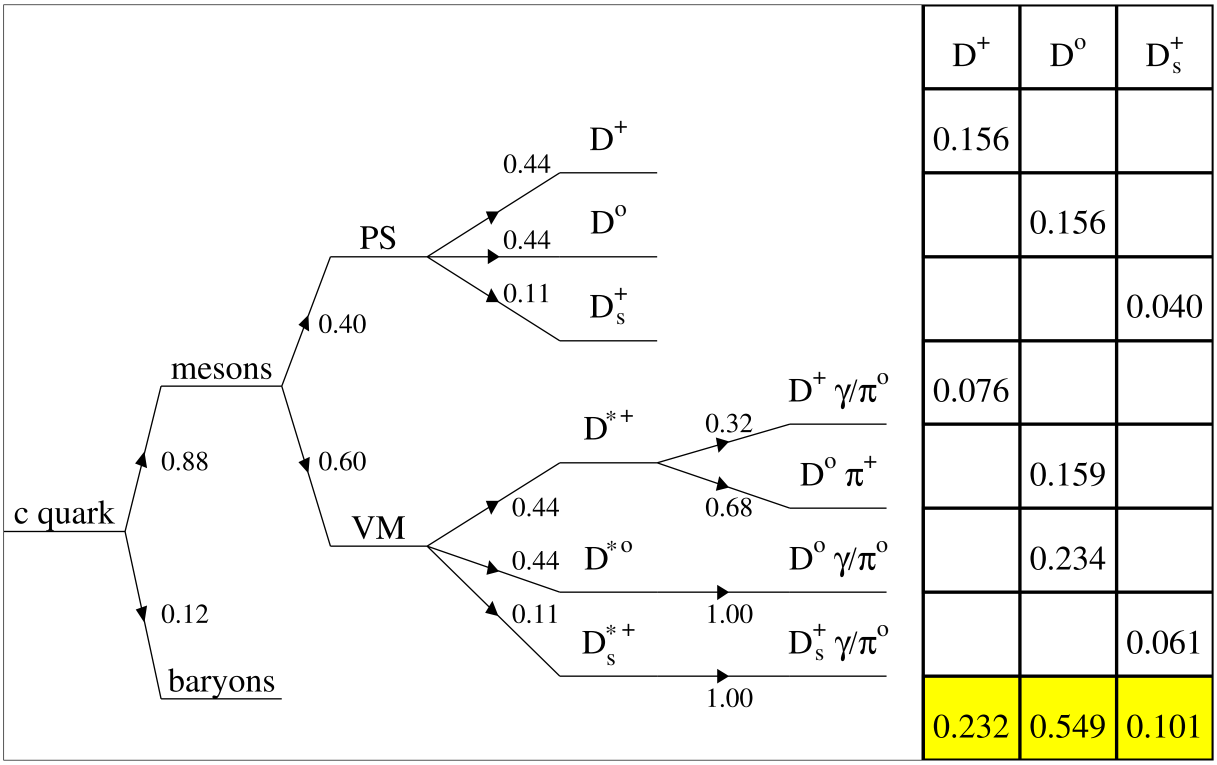

Figure 1.7: *The charm quark fragmentation tree into D- and D^*-mesons is shown. In addition the decay channels of the spin excited D^*-mesons are given. The values for the branchings are derived from the value in [34] and the branching ratios of the D^*-mesons are quoted from [17]. The table to the right sums the contributions of the directly and indirectly produced pseudo scalar D-mesons to their $f(c \to D)$ factors.*

excited state. The similar branchings into D^+ and D^0, D^{*+} and D^{*0} respectively, reflect the isospin invariance of the fragmentation process. The smaller fraction of the D_s^+ and D_s^{*+} mesons produced is parameterized by γ_s with respect to the states with up and down quark content (cf. sec. 7.2).

Interesting to note is also the decay channels of the vector mesons: while D^{*0} and D_s^{*+} mesons decay exclusively into pseudo scalars with the same valence quark content, the D^{*+} mesons favor the decay into D^0 mesons over the D^+ channel. The $f(c \to D)$ factors have therefore a different sensitivity to the P_V ratio: while more than 2/3 of D^0 mesons origin from decays of spin excited states, more than 2/3 of the D^+ are produced directly in the fragmentation process. In the D_s^+ channel the fraction is given directly by the P_V value.

D-meson kinematics

In the following the variables used to describe the kinematics of the D-meson are defined. For these definitions it is necessary to anticipate some knowledge of the H1 coordinate system (cf. chap. 2): The positive z-axis of the coordinate system is defined by the flight direction of the incoming protons and polar angles θ are measured relative to it. The transversal plane is defined as the plane perpendicular to the z-axis.

In this coordinate system the transverse momentum $p_t(D)$ of the D-meson is given by its total momentum $p(D)$ and polar angle θ_D via

$$p_t(D) = p(D) \cdot \sin(\theta_D). \tag{1.17}$$

Because of the symmetric experimental setup the angular dependence of the D-meson production is defined by just one variable, e.g. the pseudo rapidity $\eta(D)$ defined by

$$\eta(D) = \frac{1}{2} \cdot \ln\left(\frac{p(D) + p_z(D)}{p(D) - p_z(D)}\right) = -\ln\left(\tan\left(\frac{\theta_D}{2}\right)\right), \tag{1.18}$$

where the D-meson's longitudinal momentum $p_z = p(D) \cdot \cos(\theta_D)$ has been introduced. The last relation correlates $\eta(D)$ with the D-meson's polar angle.

A variable interesting for the extraction of the proton's gluon density is the charm quark's elasticity z_c which is related to the momentum fraction transfered from the photon to the charm quark:

$$z_c = \frac{\boldsymbol{P} \cdot \boldsymbol{c}}{\boldsymbol{P} \cdot \boldsymbol{q}} = \frac{E_c - c_z}{E_\gamma - q_z}, \tag{1.19}$$

where P, q and c denote the four-momenta of the incoming proton, the exchanged photon and the produced charm quark (cf. sec. 1.1.1). In the second relation E_c and c_z stand for the energy and longitudinal momentum of the charm quark, E_γ and q_z for the same quantities of the exchanged photon.

The elasticity z_c is Lorentz invariant and needed for the reconstruction of the x_g variable, which gives the fraction of the proton's momentum carried by the gluon participating in

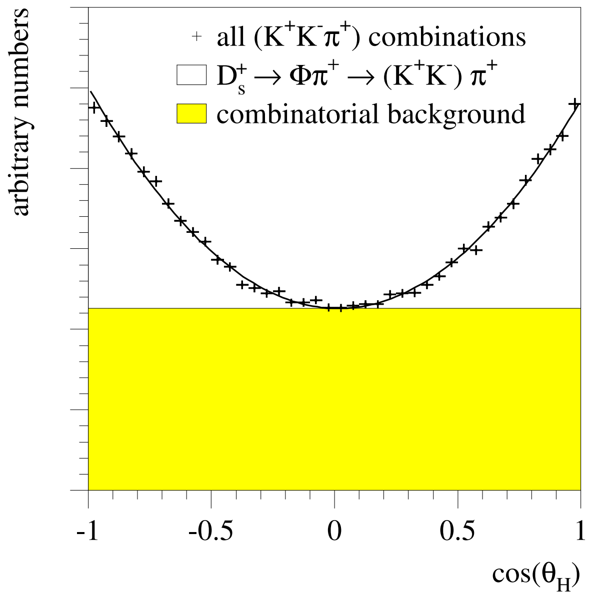

Figure 1.8: *The distribution of the cosines of the helicity angle θ_H is described by a parabola for $D_s^+ \to \Phi\pi^+ \to (K^+K^-)\pi^+$ decays, while it is flat for the background. The indicated parabola has been fitted to the distribution of the simulated D_s^+ decays.*

the scattering process. Because the four-momentum of the charm quark is not directly accessible at HERA, the related D-meson elasticity $z_e(D)$ is measured instead. It is defined by

$$z_e(D) = \frac{E(D) - p_z(D)}{E_\gamma - q_z} = \frac{E(D) - p_z(D)}{2 \cdot y \cdot E_e}, \tag{1.20}$$

where y stands for the lepton's inelasticity and E_e for the energy of the incoming positron (cf. sec. 1.1.1). The transition from $z_e(D)$ back to z_c depends on the characteristics of the fragmentation process.

In $D_s^+ \to \Phi\pi^+ \to (K^+K^-)\pi^+$ decays all participating particles are pseudo scalars but the spin one Φ meson. This leads to a correlation in the decay particles' angular distributions reflected in the distribution of the helicity angle θ_H. Its cosines is defined by the scalar product

$$\cos(\theta_H) = \frac{\vec{p}_K^{\,*} \cdot \vec{p}_\pi^{\,*}}{|\vec{p}_K^{\,*}| \cdot |\vec{p}_\pi^{\,*}|}, \tag{1.21}$$

where $\vec{p}_K^{\,*}$ and $\vec{p}_\pi^{\,*}$ are the spacial momenta of the kaon[8] and the pion in the rest frame of the Φ meson. The distribution of the cosines is shown in figure 1.8: it has a parabolic shape for signal events and is flat for the background.

1.5 QCD calculations

Herein the `AROMA` 2.24 [36] and the `HVQDIS` 1.3 [37] programs are used for the fixed order QCD calculations which are compared to data. The `AROMA` program includes the leading

[8]The result does not depend on the chosen kaon, because they are back-to-back in the Φ rest frame.

Parameter settings for QCD calculations	**AROMA (LO)** central values	**AROMA (LO)** variations	**HVQDIS (NLO)** values
proton structure function	GRV 98 LO [38]	CTEQ 5L [39]	GRV 98 HO [38]
$\Lambda^{[4]}_{QCD}$ [MeV]	200	192	200
Q^2_{min} [GeV^2]	0.4	1.0	0.4
charm mass m_c [GeV/c^2]	1.5	1.4 - 1.6	1.5
beauty mass m_b [GeV/c^2]	4.75	-	4.75
renorm./factor. scale $\mu^2 = \mu_R^2 = \mu_F^2$	$Q^2 + M_t^2 + \overline{M_t^2}$	$\hat{s}$	$Q^2 + 4 \cdot m_c^2$
Peterson fragmentation [31]		Lund String	
ε_c	0.078	0.048	0.036
ε_b	0.0069	-	-
beauty scale factor [40]	4.3 ± 1.4	-	-

Table 1.3: *The parameter settings used to calculate the QCD predictions for the measurements are summarized. The programs and parameter variations are further discussed in the text.*

order (LO) BGF graph in the massive scheme. It can be used as a full Monte Carlo event generator, i.e. the full hadronic final state is simulated: thereto `AROMA` is interfaced to the `PYTHIA` program package [24] which includes the Parton Shower and Lund String models and a full simulation of subsequent particle decays into stable particles. The branching ratios and fragmentation factors quoted in table 1.2 are used.

The `HVQDIS` program includes the full next-to-leading order (NLO) matrix element for heavy flavor production in ep scattering. Because in such NLO calculations interference terms are considered by counter-events with negative weights, a statistical simulation of the hadronic final state is so far not possible. To account for the fragmentation process the momentum spectrum of the final state quarks is weighted with the Peterson fragmentation function. Such a treatment neglects the hard evolution of the fragmentation functions and is therefore only legitimated for relative low quark momenta, where it is left intentionally open, what "relative low" means.

In addition there is no description for cascade decays available in `HVQDIS`: thus the contributions of D-mesons produced in b decays and of pseudo scalar D-mesons originating from decays of spin excited D-meson states can not be calculated with `HVQDIS`. In spite of these failings the data is still compared to results of the `HVQDIS`. One point of interest is to see, how much LO and NLO calculations differ. Thereto `HVQDIS` is used to predict the charm contribution to the production cross section of vector D^{*+} mesons which are dominantly produced directly in the fragmentation process.

The theoretical uncertainties are estimated only for the LO calculations, because they are expected to be of the same order for LO and NLO. Thereto the parameters of the calculations are varied as listed in table 1.3:

- The uncertainties in the proton structure functions is estimated by using two dif-

Model dependences [%]	D^+	D^0	D_s^+	D^{*+}
proton structure function	-1.8	-0.2	-1.4	-1.5
charm mass $m_c = 1.4$ GeV/c^2	+6.9	+8.0	+7.8	+7.8
charm mass $m_c = 1.6$ GeV/c^2	**-7.1**	**-6.2**	**-7.2**	**-7.9**
Peterson parameter $\varepsilon_c = 0.048$	**+8.3**	**+9.3**	+7.6	+8.1
Lund String fragmentation	+4.8	+8.4	**+10.4**	**+8.8**
renorm./factor. scale $\mu^2 = \hat{s}$	-0.8	-1.2	-0.4	-1.8

Table 1.4: *The relative theoretical uncertainties of the charm contributions to the visible D-meson production cross sections (cf. chap. 3) are listed as obtained by varying the parameter settings in the leading order Monte Carlo generator* `AROMA` *(cf. tab. 1.3). The values give the relative differences to the cross sections calculated with the central parameter settings. The largest differences, in bold, are quoted henceforth as the model dependences.*

ferent parameterizations, GRV 98 [38] and CTEQ 5L [39]. The values for $\Lambda_{QCD}^{[4]}$, where the superscript stands for four considered flavors, and the lower limit Q^2_{min} for the applicable Q^2 range are quoted in the table.

- The mass m_c of the charm quark is strongly correlated to the choice of the renormalization scale μ_R, because m_c has to be interpreted within this framework and is therefore scale dependent. Being the more physical parameter it has been preferred to vary the mass itself and not the scale by some factor. Still a different scale definition is considered: the squared center-of-mass energy $\hat{s}$ of the γg system. The central values are determined with the program authors' choice, where the squared tranverse mass M_t^2 ($\overline{M_t^2}$) is given by the sum of m_c^2 and the squared (anti-)charm's transverse momentum.
- The influence of the uncertainties in the fragmentation process is estimated by setting the Peterson parameter ε_c to a lower value, motivated by the harder fragmentation seen at low center of mass energies (cf. sec. 1.3.3). The variation has been chosen according to the lowest extracted ε_c value in [31]. Alternatively also the standard Lund String Model without the Peterson fragmentation implementation has been used.

The influences of the different parameter variations is shown in table 1.4. The largest uncertainties arise from the charm mass and the fragmentation. Because the quadratic sum of these uncorrelated effects would certainly overestimate the total theoretical uncertainty, the maximal difference to the central values is quoted henceforth as the model dependences. In the table these maximal differences are printed in bold characters.

D-mesons from beauty decays contribute to the measured cross section in second order. As several recent measurements have shown, the beauty production cross section is underestimated by LO and NLO calculations by factors 2-4 (see [42] for a review). A measurement in a similar kinematic range as studied herein has been performed recently by H1 and the factor of (4.3 ± 1.4) between data and LO prediction found [40] is being used to scale up the expected beauty contribution and the factor's relative error of about

30% is considered as a theoretical uncertainty. Besides the model dependences found for charm production are also used for beauty, because they are expected to be similar due to the same production process, i.e. of the order of 10% and therefore small in comparison to the error of the scale factor.

Chapter 2

The H1 Detector at HERA

The presented measurement is based on positron-proton (ep) collision data taken by the H1 experiment. H1 is one of the two multipurpose detectors which study such ep collisions at the Hadron Electron Ring Accelerator (HERA) at the Deutsches Elektron Synchrotron laboratory (DESY) in Hamburg.

In section 2.1 a short overview of HERA is given. Thereafter the components of the H1 experiment relevant for the measurement are briefly reviewed. The chapter closes with a short description of the detector simulation.

2.1 The HERA collider

HERA is the first and so far unique storage ring in the study of ep collisions and its center of mass energy ($\sqrt{s} = 318$ GeV) is in comparison to fixed target lepton nucleon scattering experiments larger by one order of magnitude. The main purposes of HERA are probing the structure of the proton and testing the standard model of particle physics. Figure 2.1 shows the layout of the HERA collider.

After passing a chain of pre–accelerators, positrons and protons are injected in opposite directions into two separate rings of 6.3 km circumference, where they are accelerated to their final energies of $E_e = 27.5$ GeV and $E_p = 920$ GeV. The particle beams are stored for several hours which is referred to as a luminosity fill.

Positrons and protons are brought into collision in the interaction regions of the H1 and ZEUS experiments. The particle beams are not continuous, but consist of about 175 bunches each. Every 96 ns two bunches intersect inside H1 and ZEUS, corresponding to a collision rate of 10.4 MHz.

The lateral dimension of the beams, $200\ \mu\text{m} \times 53\ \mu\text{m}$ and $190\ \mu\text{m} \times 50\ \mu\text{m}$ [43], define the radial extent of the interaction region, the beam spot, with $137\ \mu\text{m} \times 37\ \mu\text{m}$ (all values denote one sigma extensions in x and y). The longitudinal length of the interaction is constrained by the length of the proton bunches to $\sigma(z) = 113$ mm.

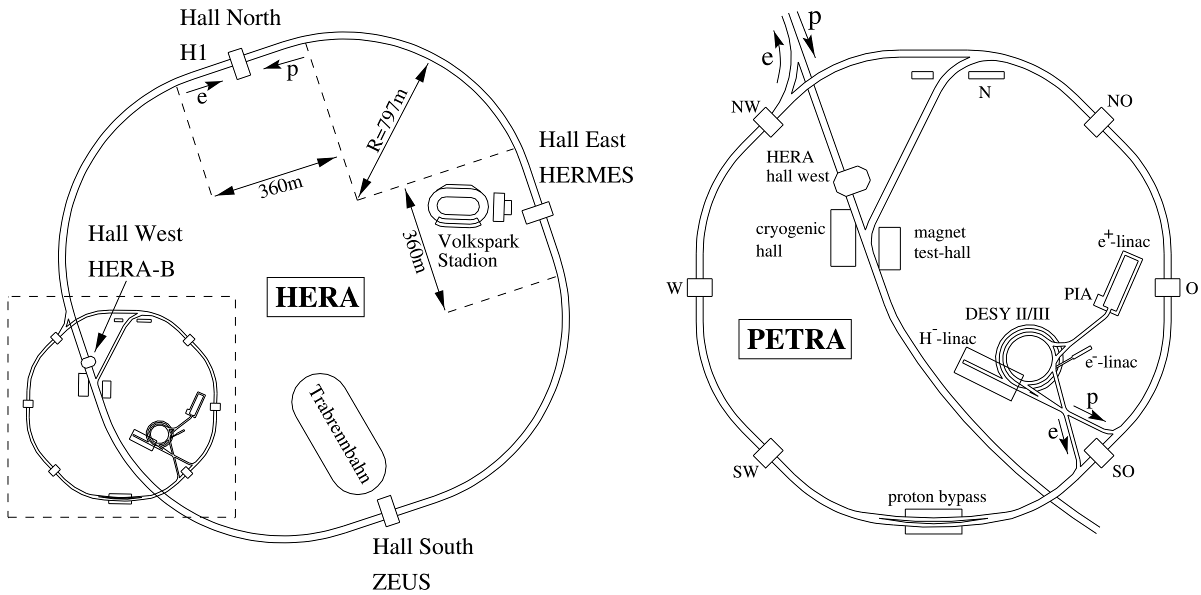

Figure 2.1: *The HERA collider (left) and its pre–accelerators (right) at DESY are shown. The ep scattering experiments H1 and ZEUS are located in the interaction regions in the north and south halls of the HERA ring.*

2.2 The H1 Experiment

The H1 experiment is a general purpose detector composed of several detector components, the subdetectors, optimized for the measurement of various physical quantities. Herein only the subdetectors relevant for the analysis will be briefly reviewed. A detailed description of the H1 detector can be found in reference [44].

Figure 2.2 gives an overview of the H1 detector. In the top right corner of the figure the H1 coordinate system is indicated: with the origin at the nominal interaction point (indicated in the figure by a small cross at $\boxed{1}$), the positive z-axis is defined by the proton beam direction, the x-axis extends towards the center of the HERA ring and the y-axis points upwards. Polar angles θ are measured with respect to the positive z-axis, while azimuthal angles ϕ extend clockwise from the x-axis upwards. The projection transverse to the z-axis is referred to as $r\phi$-plane. The term forward will be used for directions close to the proton beam direction, backward accordingly.

The following list of H1 subdetectors is ordered according to their distances from the interaction region. The numbering of the points refer to figure 2.2.

$\boxed{1}$ The interaction region is surrounded by a carbon fiber beam pipe with aluminum liner with a radius of 4.5 cm.

$\boxed{2}$ The central tracking system consisting of the Central Silicon Tracker (CST), the Central Jet Chamber (CJC), the Central z-chambers (CxZ) and the Central Proportional Chamber (CxP).

The CST is at the heart of the H1 detector and of the presented analysis and its design and performance are described in detail in appendix F.

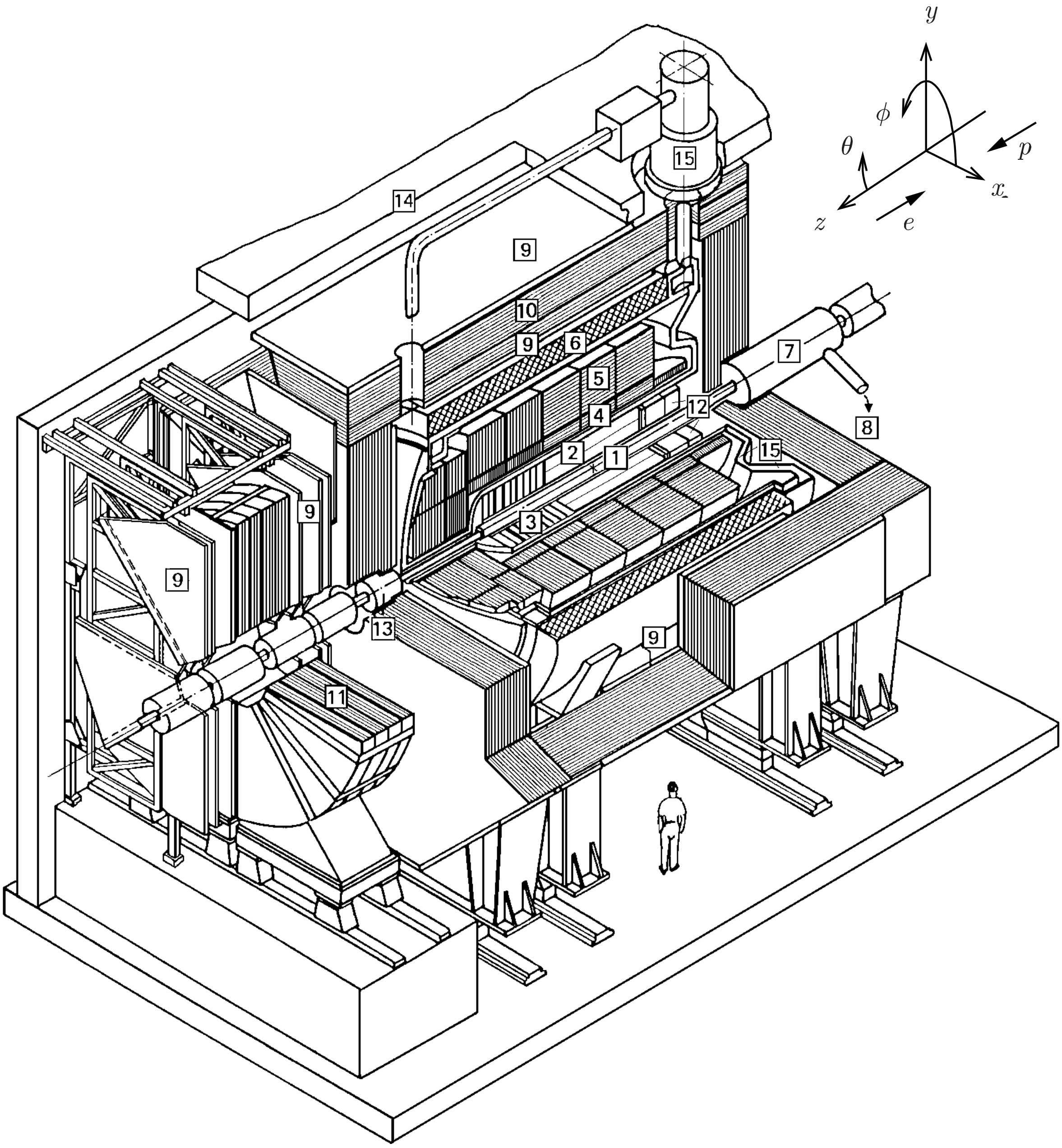

Figure 2.2: *The overview of the H1 experiment shows the main detector components. The flight directions of the incoming proton and positron beams and the H1 coordinate system are indicated in the top right corner.*

The CJC, backbone of the tracking in the central region, identifies the flight trajectories and measures the momenta of charged particles [45]. It consists of two cylindrical chamber rings, mounted concentrically around the beam line. In the azimuthal direction the inner (outer) chamber ring is subdivided by planes of cathode wires into 30 (60) identical drift cells which contain planes with 24 (32) anode sense wires each. A charged particle ionizes atoms of the chamber gas and the produced electron cloud drifts in the applied electrical field towards the sense wires. By drift time measurements the distances of the particle flight path from the sense wires are reconstructed. The z coordinate is measured by charge division of the signals measured at the two wire ends.

Mounted inside of each chamber ring are two polygonal z drift chamber intended to improve the θ resolution and two multi-wire proportional chambers with pad readout for triggering purposes [46].

$\boxed{4}$ The electromagnetic and

$\boxed{5}$ hadronic part of the liquid argon calorimeter (LAr) [47], the main calorimeter of H1, measure energies of particles with polar angles between $4°$ and $154°$. Lead, respectively steel plates are used as absorber materials which account for 20-30 radiation lengths in the electromagnetic part and a total thickness of 4-8 nuclear interaction lengths. The energy measurement of the LAr is used herein to verify the method by which the event kinematics are reconstructed (cf. sec. 4.5).

$\boxed{6}$ The superconducting coil generates a homogeneous magnetic field of 1.15 T which allows the momentum determination for charged particles through their curvature measured in the CJC.

$\boxed{12}$ The lead scintillator "Spaghetti" calorimeter (SpaCal) [48] in the backward region of the H1 experiment ($153^o < \theta < 177.8^o$) is optimized for the detection of the scattered positron in the kinematic range of deep inelastic scattering under consideration here. The final method used for the reconstruction of the event kinematics is based on its energy and position measurements. It consists of an electromagnetic and a more coarsely segmented hadronic section and achieves for positrons an energy resolution of $\sigma(E)/E \approx 7.5\ \%/\sqrt{E[\text{ GeV}]} \oplus 1\ \%$ and a spacial resolution of about 4 mm. A four-layer drift chamber (BDC) [49] is mounted on its front.

Not shown in the figure are the two electron taggers (ETAG) and the photon detector located along the beam pipe at $z = -33$ m, $z = -44$ m and $z = -103$ m. They are used for the luminosity measurement discussed in section 4.4.

Trigger system and data acquisition

In just one out of a million bunch crossings an "interesting" ep interaction occurs. The task of the H1 trigger system is to discriminate these events from the large backgrounds [50]. The pipelined multi-level trigger system is designed to minimize the dead time emerging from the read-out of the detector signals for which the data acquisition has to be stopped. Relevant for the presented analysis are:

- The Level 1 trigger decides within 2.4 μs on the basis of logical combinations of quickly available detector signals, if an event contains interesting information. On a positive decision the data acquisition is stopped and the detector signals, stored due to the decision time of 25 bunch crossings in pipelines, are read-out within about 1-2 ms.

Examples of Level 1 subsystems are the DCRPhi trigger which searches for charged particle crossings with selected CJC signals, the z-Vertex trigger giving a rough estimate of the interaction's z-position using the $zVtx$ histogram based on measurements of the central and forward proportional chambers and the Inclusive Electron Trigger (IET) sensitive to significant energy depositions in the SpaCal calorimeter. In addition several Time-of-Flight (TOF) and VETO systems allow to reject events outside the interaction time window.

- Level 4 is a software trigger running in parallel on a multi processor farm made up of 30 PowerPC boards. With the full detector information available, a fast version of the event reconstruction is performed which allows a more sophisticated selection and classification of interesting physical processes (cf. chap. 4). In addition a first set of detector calibration constants is determined. Events are accepted by Level 4 with a rate of 5-10 Hz and stored on magnetic tapes.

- On the Level 5 computer farm all recorded events are fully reconstructed using the calibration constants determined at Level 4 and stored on data summary tapes (DSTs) in a compressed format which are the basis of physics analyzes.

2.3 Detector simulation

The detector response on events generated by Monte Carlo programs (cf. sec. 1.5) is simulated in detail within the `GEANT` framework [51] by the `H1SIM` program. The `GEANT` package includes descriptions of many physical phenomena relevant for the responses of complex HEP detectors on basis of fundamental formulas describing particle interactions with matter, e.g. energy loss, multiple scattering and secondary particle production.

The generated long living particles are propagated through the volumes of a virtual H1 experiment and their interactions with the detector materials are simulated. The energy deposited by the particles in the sensitive volumes is translated into signals according to measured performance figures of the detector. On the basis of these simulated signals the events are reconstructed similar to real data.

Events simulated in this vain are used to study the performance of the detector in terms of efficiencies and purities. The measurement relies crucially on an accurate description of the data by the simulation (cf. chap. 3) and it is one of the major tasks to prove the high level by which this is achieved.

Chapter 3

Definitions and Methodology

In this chapter the physical quantities measured within this thesis are defined and the strategy chosen to ensure the reliability of the measurement is given. The measuring method and the essential points to be substantiated are explained as motivation for the subsequent chapters.

3.1 Cross sections

The inclusive D-meson production cross sections $\sigma_{vis}(ep \to e'DX)$, defined as sum of both particle and antiparticle states, are measured with a consistent method for D^+, D^0, D_s^+ and D^{*+} mesons in the visible kinematic range defined as

$$\begin{aligned} 2\ \mathrm{GeV}^2 \leq\ & Q^2 \ \leq 100\ \mathrm{GeV}^2\,, & & p_t(D) \ \geq 2.5\ \mathrm{GeV}/c\,, \\ 0.05 \leq\ & y \ \leq 0.7 & \text{and} \quad & |\eta(D)| \ \leq 1.5\,. \end{aligned} \tag{3.1}$$

The $D^{*+} \to D^0\pi^+ \to (K^-\pi^+)\pi^+$ channel serves as a pivotal point for the analysis: The established measurement of D^{*+} production based on the Δm-tagging technique [52] is repeated on basis of the CJC measurement alone without using any CST or lifetime information and the result is compared with previously published results [12, 14, 15].

D^0 mesons produced in D^{*+} decays, called tagged D^0 mesons henceforth, have a clear signature due to the Δm-tag. Because of their finite lifetime they provide a precious sample to prove the understanding of the newly developed lifetime tagging technique. As a final comprehensive test the D^{*+} production cross section measurement is repeated using the CST lifetime information for the D^0 meson in addition to the Δm-tag.

Because the characteristics of all studied channels are very similar, the lifetime tagging methods established in tagged D^0 decays are applicable to the D-meson channels which are accessible only through this information. Therefore those cross sections measured for the first time at HERA are put on solid grounds.

The measured cross sections are compared to predictions of QCD calculations. Measurements of the single differential cross sections in variables describing the event and the D-meson kinematics are used to test the predicted dynamics of the production process.

3.2 Fragmentation ratios

Having measured different D-meson channels with a consistent method in nearly equal kinematical regimes invites the determination of fragmentation ratios for which most of the systematic uncertainties cancel. The following ratios are measured herein:

- The R ratio tests the isospin invariance of the charm fragmentation process. Isospin invariance is given, if the probabilities to form a bound D-meson state with an up or a down quark are equal which is, due to their similar masses, expected. In this case the R ratio is equal to one.

- The strangeness suppression factor γ_s expresses the smaller probability for the initial charm quark to form a bound state with a strange quark when compared to states formed with the lighter up and down quarks ($u : d : s = 1 : 1 : \gamma_s$). From the quark mass differences a value of $\gamma_s \approx 0.3$ is expected [24].

- The $P_V = \frac{VM}{PS+VM}$ ratio denotes the fraction of vector mesons (VM) with respect to all vector and pseudo scalar D-mesons (PS+VM) produced. There are $(2s+1)$ available orientation for a state with spin s. Thus the three orientations possible in the first excited spin state compare to a single one in the pseudo scalar state which leads to an expected value of $P_V = 0.75$ for the ratio.

These ratios can not be derived directly from the measured cross sections, because the fraction of mesons in the visible range with respect to all produced D-mesons differs according to the meson type by some $\pm 5\%$ due to the criteria on the D-meson properties which enter the visible range definition: especially the $p_t(D)$ spectrum has a slight channel dependence, because the type dependent fraction of D-mesons produced in cascade decays of spin excited states has a softer $p_t(D)$ distribution than mesons directly produced in the fragmentation process. Furthermore the slightly different masses of the D-mesons change the phase space available for their production and therefore also their $p_t(D)$ spectra. In addition the fraction of D-mesons originating from beauty decays, which has to be subtracted form the measurements, depends on the D-meson type (cf. tab. 7.3).

Therefore fragmentation factors $f(c \to D)$ introduced in chapter 1 are deduced from the measured D-meson production cross sections and the QCD leading-order prediction. The $f(c \to D)$ describe the probability that an initial charm quark forms a D-meson of a certain type.

Assuming the validity of the factorization theorem the $f(c \to D)$ factors are independent of the charm production process, but are sensitive to the fragmentation process alone. They can be compared directly to results from e^+e^- experiments. But while latter are normalized to the measured total charm production cross section, the $f(c \to D)$ factors derived in this thesis are normalized to QCD calculations.

3.3 Measurement method

In general the rate r of a scattering process is given by the luminosity l multiplied with the cross section σ of the process: $r = l \cdot \sigma$. The luminosity can be derived from machine properties, but it is more convenient to use a scattering process with a well understood cross section σ for its determination (cf. sec. 4.4).

Thus the visible D-meson production cross sections can be measured by counting the number of D-mesons which are produced in the visible range during a certain data taking period and by measuring the integrated luminosity $\mathcal{L}$ for which l is integrated over the time of the data taking period. The relation used for the cross section measurements is

$$\sigma_{vis}(ep \to e'DX) = \frac{N_{vis}}{\mathcal{L} \cdot \mathrm{BR} \cdot (1 + \delta_{rad})}. \tag{3.2}$$

In this definition N_{vis} denotes the number of D-mesons produced in the visible range which decay into the analyzed channel. The analyzed decay channels and their branching ratios BR are given in table 1.2. The parameter δ_{rad} corrects the measurement for initial state radiation, i.e. for events where the incoming positrons have already lost some of their energy due to photon emissions (cf. sec. 4.5).

Not all produced D-mesons N_{vis} can be detected. The number of D-mesons N_{rec} which are successfully reconstructed and can therefore be used for the measurement depends on many factors:

- the selection cuts applied for the signal extraction,
- the geometry, efficiency and resolution of the detector and
- the performance of the algorithms used for the reconstruction.

The fraction $\mathcal{F}_{rec} = N_{rec}/N_{vis}$ could be derived in principle from some basic detector properties like hit efficiencies or resolutions. But in practice the dependences of $\mathcal{F}_{rec}$ on these basic properties are mostly rather complicated. Thus a detailed simulation of the detector (cf. sec. 2.3), tuned to measurements of basic detector properties, is used for the determination of $\mathcal{F}_{rec}$.

3.3.1 Definition of acceptances, efficiencies and purities

The fraction $\mathcal{F}_{rec}$ is determined in several consecutive steps with simulated D-meson decays: beginning with all visible decays N_{vis} the fraction of events that fulfill a single condition, e.g. a minimal cut on the momenta of the decay particles, is determined. In all subsequent steps only decays meeting this requirement are considered. The terminology used to discuss these consecutive steps is as follows.

- The acceptance A is defined as the fraction of all decays N_a that meet a requirement with their simulated parameters: $A = N_s/N_a$. The acceptance determination does not need the detector simulation.

- The efficiency ε describes the transition from the simulated to the reconstructed variables and is defined as the fraction of accepted decays N_s which fulfill the requirement in addition with their reconstruction properties: $\varepsilon = N_{s+r}/N_s$.

- The purity p of the reconstruction is a measure for its quality and is defined as the fraction of the reconstructed decays N_r which satisfy the specific cut also in the simulated quantities $p = N_{s+r}/N_r$.

The fraction of decays N_r which fulfill the specific cut on the level of the reconstruction with respect to all considered decays N_a is the parameter relevant for the measurement and with the definitions above it is given by $N_r/N_a = A \cdot (\varepsilon/p)$.

These definitions ensure that the individual factors are always smaller than one which is not only desirable for the discussions, but also facilitates the error calculation. But errors are at this stage of statistical nature only and they are kept small by choosing the number of simulated events adequately, i.e. large.

The definitions of the single consecutive steps are arbitrary, because only their total product $\mathcal{F}_{rec}$ is relevant which is completely determined by the detector simulation. The choice in definitions as listed below is an attempt to constrain the influence of a certain detector property into one single step, because this facilitates the study of the systematic effects caused by the uncertainties in them. The chosen step are the following:

- the kinematic acceptance A_{kine}, e.g. cuts on decay particles' momenta;

- the geometrical acceptances A_{geo} of subdetectors used for the event reconstruction;

- the efficiencies and purities of the SpaCal calorimeter $(\varepsilon/p)_{SPC}$,
  the Central Jet Chambers $(\varepsilon/p)_{CJC}$ and
  the Central Silicon Tracker $(\varepsilon/p)_{CST}$;

- the efficiency of the mass reconstruction ε_m,
  the lifetime tag ε_{vtx} and
  the subtrigger requirement ε_{ST}.

The efficiencies quoted in the last item are outside the introduced terminology, because for these effects a correlation between the simulated and the reconstructed variables is not meaningful. In the notation introduced above these efficiencies are defined by $\varepsilon = N_r/N_a$.

With these definitions the number of D-meson decays N_{vis} produced in the visible range can be deduced from the number of reconstructed decays N_{rec} with the equation

$$N_{vis} = \frac{N_{rec}}{\mathcal{F}_{rec}} = \frac{N_{rec}}{A_{kin} \cdot A_{geo} \cdot (\varepsilon/p)_{SPC} \cdot (\varepsilon/p)_{CJC} \cdot (\varepsilon/p)_{CST} \cdot \varepsilon_m \cdot \varepsilon_{vtx} \cdot \varepsilon_{ST}} \,. \tag{3.3}$$

3.3.2 Measuring strategy

The crucial role of the simulation for the measurement motivates the following strategy:

- The detector simulation is tuned with measurements of basic detector properties such as hit efficiencies and resolutions.
- The quality of the simulation is verified by comparison with data in the relevant observables. The applied CST lifetime tag is an analysis technique new at H1. Therefore the focus of these verifications is put on the simulation of the CST detector and the description of the variable distributions used for the lifetime tag. Especially the D^0-mesons tagged in the D^{*+} channel provide a rich testing field.
- Once the high quality of the simulation has been proven, the values of the acceptances, efficiencies and purities necessary for the measurements are determined with the help of the simulation.
- The simulation serves also for the estimation of the systematic effects that uncertainties of basic detector properties bear on the final measurements. The quadratic sum of these estimates is then quoted as the systematic experimental error of the measurement.

Chapter 4

Event Selection

This chapter describes the selection of the analyzed data set. The first part discusses the requirements on the detector status, the selected trigger conditions and the measurement of the integrated luminosity. In the second part the reconstruction of the event kinematics is discussed which is used for the definition of the visible range of the measurements and for the studies of the dynamics of the D-meson production process.

4.1 Analyzed data set

The CST is the essential detector component for this analysis. It has been fully operational since 1997. The data taken by the H1 experiment in the e^+p running period of the years 1999 and 2000 are considered for this analysis. These data are characterized by a uniform quality. The data taken in the previous years have significantly different characteristics with respect to their calibration and are discarded, because they account for only one quarter of the chosen data sample. A uniform quality of the complete data set can be established only after the reprocessing with improved calibration constants which was unfortunately still ongoing at the time of this analysis.

The data taken at the very beginning of 1999 e^+p running was rejected because of corrupt CST information in the data which will be only recovered after the reprocessing of the data. The last period of the 1999 data taking is dismissed due to major CJC inefficiencies (cf. sec. 5.4.3). Runs with a different trigger setup and runs taken with a shifted z-position of the interaction region are also discarded. The selected H1 run ranges can be found in table 4.5.

For the events to be selected for analysis all detector components relevant for the measurement are required to be fully operational in terms of their high voltage (HV) and their read-out chain. These relevant components are the CST and CJC for the track reconstruction, the SpaCal and BDC for the measurement of the scattered positron, the luminosity system, and the CIP, COP, TOF and VETO systems for the event triggering. The run quality classification is a scheme also based on the operational status of the H1 detector. For technical reasons only runs of good or medium quality are considered which

ST 61 =	`(SCPLe_IET>2 || SCPLe_IET_Cent_3) && DCRPh_THig && zVtx_sig && (d:0) && (v:8) && (f:0)`
`(d:0)` =	`DCRPh_NL_many && DCRPh_NH_many && DCRPh_PL_many && DCRPh_PH_many`
`(v:8)` =	`! SPCLh_AToF_E_1 && ! SPCLh_ToF_E_2 && ! VETO_inner_BG && ! VETO_Outer_BG && ! VLQToF_BG`
`(f:0)` =	`(FToF_IA || FIT_IA) || (! FToF_BG && ! FIT_BG)`

Table 4.1: *The trigger element composition of ST 61 during the analyzed data taking period is given. The logical operators used in the definition are "`&&`" for "and", "`||`" for "or" and "`!`" for a logical "not".*

discards less than 0.3% of the luminosity, because the only additional detector component required is the LAr calorimeter.

Advantage has been taken of the event classification performed on Level 4 to reduce the number of analyzed events further. Only events classified as moderate Q^2 events (`FPACK` class 20 and head bank classification bit 20) are retained. The selection criteria $E_{e'} \geq 4$ GeV and $R_{clu} \leq 4$ cm of this class on Level 4 are well within the quality requirements made for the analysis (cf. sec. 4.5).

4.2 Required trigger condition

At HERA a wide range of physical processes is accessible. At the first level of the H1 trigger system a classification of events into physical classes is done by combining different trigger elements into conditions called subtriggers. An optimal use of the available band width of the read-out is achieved by an autoprescale scheme [53].

The prescale strategy sets priorities to the different physics classes. According to these priorities events are rejected by the Level 1 trigger system. The rejection is steered by prescale factors assigned to the different subtriggers. A prescale factor N means that only one out of N triggered events is preserved. The production rates of all processes decrease together with the luminosity during a HERA fill. Therefore more band width becomes available for physical classes with low priorities and their prescale factors are successively reduced.

The autoprescale scheme has the consequence that the effectively taken luminosity depends on the subtrigger and its mean prescale factor. The integrated luminosity is needed for the cross section measurement and therefore the analysis is constrained to events accepted by a specific subtrigger.

The subtrigger 61 (ST 61) is designed for selecting possible heavy flavor events in the analyzed Q^2 range and therefore only events triggered by this subtrigger are considered. The Level 1 condition of ST 61 is given in table 4.1. The main trigger elements of ST 61 are

Q^2 range [GeV^2]	event weight	Q^2 range [GeV^2]	event weight
$Q^2 < 5$	20	$10 < Q^2 < 20$	4
$5 < Q^2 < 10$	8	$20 < Q^2$	2

Table 4.2: *The prescaling scheme of Level 4 rejects events according to event weights depending on the squared momentum transfer Q^2. An event might still be saved by a final state finder. In this case the event weight is reset to one.*

- `(SCPLe_IET>2 || SCPLe_IET_Cent_3)` requires a cluster with more than 6 GeV energy deposition in the SpaCal setting off the Inclusive Electron Trigger (IET),
- `DCRPh_THig` demands a track with a transverse momentum above 800 MeV/c identified by the DCRPhi drift chamber trigger and
- `zVtx_sig` asks for a significant entry in the $zVtx$ histogram of the proportional chambers.

The global options `(d:0)`, `(v:8)` and `(f:0)` are included in several subtriggers and are designed to suppress noisy CJC events and to reject background events from outside the interaction time window which are identified by time of flight (ToF) and the VETO systems. In the analyzed period the mean prescale factor of ST 61 is 1.17 (cf. tab. 4.5). The subtrigger had no additional Level 2 requirement.

On Level 4 events are once again prescaled according to their Q^2 value. The applied prescale factors are called event weights and they are listed in table 4.2. An event might still be saved by a final state finder such as `HQSEL` which looks, among others, for D-meson candidates in the analyzed decay channels. Therefore either the efficiency of the Level 4 reconstruction and the applied final state finders has to be determined or decays have to be counted according to their event weight in the distributions used for the signal extraction. As the former is a quite difficult task for several reasons the latter method has been chosen.

4.3 Subtrigger efficiency measurement

The probability that an event fulfills a subtrigger condition depends on the specific event properties and thus the total subtrigger efficiency depends on the sample composition. The efficiency of the ST 61 has been determined with simulated D-meson decays meeting the final selection criteria. The quality of the trigger simulation is verified by comparing the efficiencies measured in data and simulated event samples. In the following an overview of the performed measurements is given.

The efficiency can be measured with events triggered independently of ST 61. Thus an independent reference trigger has to be chosen which does not include the elements used in ST 61 or elements closely related to them. The selection of a sufficiently large independent sample is difficult, because ST 61 is based on the trigger informations of three

$D^+ \to K^-\pi^+\pi^+$	reference	Efficiency of trigger element		$\Delta\varepsilon$ [%]
trigger element	trigger	ε_{data} [%]	ε_{sim} [%]	$(\varepsilon_{sim} - \varepsilon_{data})$
`DCRPh_THig`	035	98.74 ± 0.03	98.05 ± 0.10	-0.69 ± 0.10
`zVtx_sig`	035	93.08 ± 0.07	93.61 ± 0.18	0.53 ± 0.19
`SPCLe_IET`	071	99.96 ± 0.01	100.00 ± 0.00	0.04 ± 0.01
`(v:8)`	039	99.95 ± 0.01	(100.00)	0.05 ± 0.01
`(d:0) && (f:0)`	112	99.95 ± 0.02	(100.00)	0.05 ± 0.02
subtrigger efficiency ε_{ST}		91.78 ± 0.08	91.78 ± 0.20	0.01 ± 0.21

Table 4.3: *The table summarizes the trigger element efficiencies of ST 61 measured in data and simulated samples in the decay channel $D^+ \to K^-\pi^+\pi^+$.*

subdetectors which are included in many subtrigger definitions. Therefore the efficiencies of the trigger elements included in ST 61 are measured separately with different reference triggers. The reference triggers used are listed in table 4.3.

The measurements are done with preselected event samples as follows. For the track related DCRPhi and z-Vertex trigger elements at least one D-meson candidate fulfilling all kinematic and track quality requirements are selected (cf. tab. 5.3 and 5.6), while for the IET trigger elements a cluster in the SpaCal calorimeter fulfilling all quality requirements applied on the positron candidates is demanded (cf. tab. 4.6). Both requirements are relaxed for the determination of the efficiencies of the purely background rejecting global options.

The efficiency is then determined by counting the events in the reference sample which have fired the examined element. A double counting of the prescale factor is avoided by regarding only the raw subtrigger decision for the latter. A summary of the efficiencies measured in the D^+ decay channel is presented in table 4.3. The trigger simulation reproduces the efficiencies of all main trigger elements reasonably well. The simulation does not include all trigger elements used in the global options, but their efficiencies in data are essentially one anyhow and therefore only the simulated main trigger elements are required for the subtrigger efficiency determination.

Similar summary tables of the measurements performed for the other analyzed decay channels can be found in appendix B. The table 4.4 gives the results for the total subtrig-

decay channel	ε_{data} [%]	ε_{sim} [%]	$\Delta\varepsilon$ [%]
$D^+ \to K^-\pi^+\pi^+$	91.78 ± 0.08	91.78 ± 0.20	0.01 ± 0.21
$D^0 \to K^-\pi^+$	90.52 ± 0.14	89.73 ± 0.21	-0.78 ± 0.25
$D_s^+ \to \Phi\pi^+ \to (K^+K^-)\pi^+$	93.01 ± 0.20	92.76 ± 0.37	-0.24 ± 0.42
$D^{*+} \to D^0\pi^+ \to (K^-\pi^+)\pi^+$	92.40 ± 0.81	92.82 ± 0.80	0.41 ± 1.14

Table 4.4: *The table summarizes the subtrigger efficiencies measured in the analyzed decay channels and compares the results with the efficiencies found with the detector simulation.*

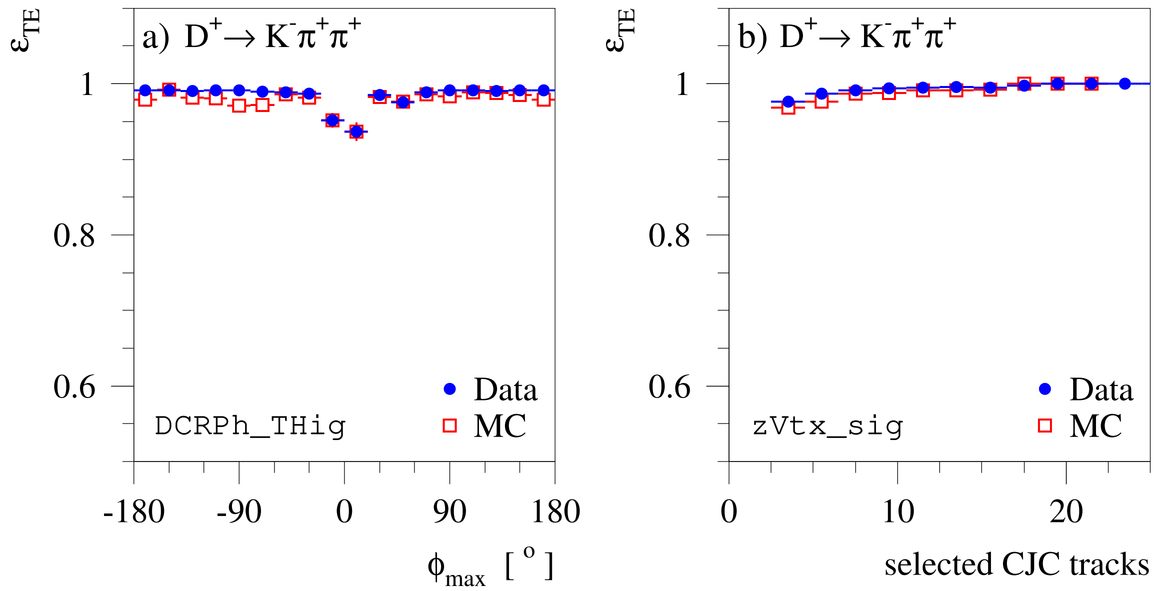

Figure 4.1: *The description of trigger efficiency dependencies in data (dots) achieved by the detector simulation (open boxes) is shown on two examples:* **(a)** *The azimuthal angle ϕ_{max} of the track with the highest transverse momentum in the event is a relevant parameter for the efficiency of the* `DCRPhi_THig` *trigger element based on the signals of the partially inefficient CJC.* **(b)** *The number of tracks available for the determination of the interaction's z-position is a major criteria for the achieved resolution and therefore interesting for the efficiency of the* `zVtx_sig` *trigger element.*

ger efficiencies found by these measurements. In all channels a good agreement between the data and the simulation has been found.

In addition to these inclusive measurements, the dependence of the trigger efficiencies on relevant event parameters has been studied and used to verify the description achieved by the detector simulation furthermore. In figure 4.1 two examples for such comparisons are shown.

Good agreement has been found in all comparisons between the data and the simulation. Therefore it is regarded as save to use the trigger efficiency of the simulation for the measurement. The systematic error introduced by this proceeding is estimated to be one percent.

4.4 Integrated luminosity

Bethe-Heitler scattering events $ep \rightarrow e\gamma p$ are used for the luminosity measurement because their cross section is well understood. The simultaneous detection of the scattered positron and the radiated photon allows different measurement methods. In this way systematic uncertainties can be controlled with high precision [54]. The values quoted in table 4.5 are

Integrated luminosity $\mathcal{L}$ [pb^{-1}]	1999	2000	1999+2000
$\mathcal{L}$ delivered by HERA	20.2	66.8	87.0
H1 $\mathcal{L}$ on tape	17.3	59.4	76.7
$\mathcal{L}$ in run selection*	11.4	52.4	63.8
$\mathcal{L}$ after HV requirements	10.5	48.3	58.8
$\mathcal{L}$ after all corrections †	9.5	38.4	47.8
relative error in $\mathcal{L}$ [%]	1.50	1.45	1.46
* selected run ranges	246891-257636	262144-278666	
		278995-279215	
† average prescale factor	1.06	1.20	1.17
† satellite bunch correction	0.96	0.96	0.96

Table 4.5: *The table summarized the integrated luminosities of the* e^+p *collision data taken in the years 1999 and 2000. The luminosity used for the presented measurement is* $\mathcal{L} = 47.8 \pm 0.7$ pb^{-1} *after all corrections.*

measured with the single electron method which relies on the detection of the scattered positron alone.

The satellite bunch corrections quoted in the table arise from protons which migrate during a luminosity fill into satellite bunches separated from the main bunch structure. These protons interact with the positrons outside the nominal interaction region. Because these interactions contribute to the luminosity measurement but are rejected in the data taking by the trigger systems, the former has to be corrected by 4%.

4.5 Reconstruction of event kinematics

The fundamental measured variables used to reconstruct the kinematics of the deep inelastic scattering process are the energy $E_{e'}$ deposited by the scattered positron in the SpaCal calorimeter and the position of its impact point which defines the polar angle $\theta_{e'}$. As the energy is usually spread over several cells of the calorimeter, a cluster finding algorithm is applied. The chosen algorithm is the `ELAN` algorithm of the H1 internal `QESCAT` package. For the measurements the most energetic cluster in the SpaCal is identified as the scattered positron.

In table 4.6 the selection criteria applied to ensure a good reconstruction quality of the scattered positron are summarized. The measured energy $E_{e'}$ of the cluster is closely related to the lepton inelasticity y and the minimal requirement of 8 GeV defines the upper limit $y \leq 0.7$ of the visible range (cf. eq. 4.1). This upper limit is reached for positrons with large polar angles $\theta_{e'} \approx 177^o$. The polar angle $\theta_{e'}$ is determined through the vertex position and the radial position R_{cog} of the cluster's center of gravity. The restrictions on the polar angle and the radial position are motivated by the geometrical acceptance of the SpaCal and define the visible Q^2 range.

Selection criteria for positron candidates								
			$E_{e'}$	$\geq$	8 GeV			
$\theta_{e'}$	$\geq$	153°	R_{cog}	$\geq$	8.7 cm	R_{clu}	$\leq$	3.5 cm
	$\leq$	177°		$\leq$	78.0 cm	Δ_{BDC}	$\leq$	2.5 cm

Table 4.6: *The quality requirements posed on SpaCal clusters identified with a scattered positron are summarized.*

Hadrons produce wider showers as the scattered positrons and hadronic background, e.g. from high energetic pions, can therefore be discriminated by a cut on the lateral shower size R_{clu}. The BDC is used to suppress background from high energetic photons which produce no signals in the drift chamber, but which have the same signature as positrons in the calorimeter. They are rejected by requiring a maximal distance Δ_{BDC} between the calorimeter cluster and the next associated track in the BDC.

The photoproduction background, where a hadron fakes a scattered positron, has been estimated in [12] for equivalent positron quality criteria and in the same kinematical range with simulated events of direct and resolved charm photoproduction to be less than 1%. Therefore no correction are applied in the measured cross sections.

The acceptance, efficiency and purity of the SpaCal calorimeter are determined with simulated DIS events and are found to be 97.7 %, 94.0 % and 96.0 % respectively.

4.5.1 Reconstruction methods

There are various methods to reconstruct the kinematics of the deep inelastic scattering process [55]. In this analysis the e-, Σ- and $e\Sigma$-methods have been studied. The choice of the method must take into consideration the resolutions achieved in the kinematic variables and the reliability of the calibration of the detectors necessary for their determination.

In addition the influence of initial state radiation (ISR) has to be taken into account. In events with initial state radiation the positron emits a photon before participating in the scattering process. The positron looses some of its energy by this emission. A determination of the kinematics based on the assumption that the energy of the incoming positron equals the beam energy is therefore systematically wrong. The emitted photons are collinear, remain in the beam pipe and therefore leave the experiment undetected. The error introduced becomes significant for the emission of high energetic photons.

On the other hand final state radiation of the scattered positron is of minor importance: If a photon is emitted with significant energy, it is measured in the same calorimeter cells as the scattered positron and its energy is therefore included in the calorimeter cluster.

The e-method is based only on the measurement of the energy $E_{e'}$ and the polar angle $\theta_{e'}$ of the scattered positron. In the analyzed Q^2 range both quantities are measured with

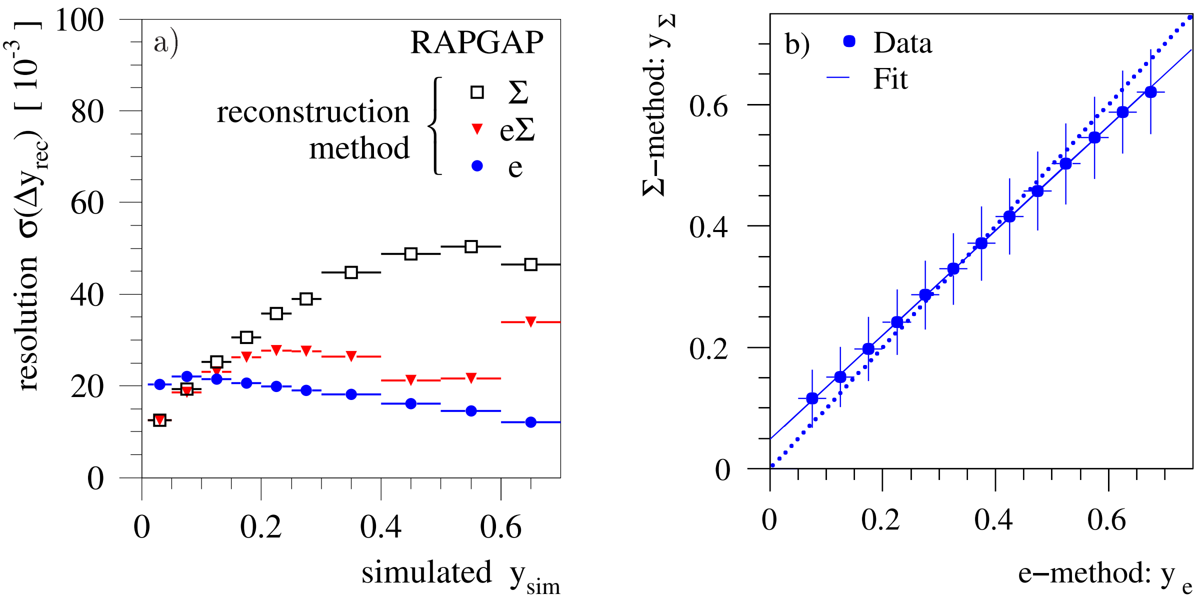

Figure 4.2: **(a)** *The y resolutions of the different methods used to reconstruct the DIS kinematics is shown for events simulated with the RAPGAP program [57]. The symbols give the standard deviations of bin wise Gaussian fits of the differences Δy_{rec} between the simulated and reconstructed values of y.* **(b)** *The correlation between the lepton inelasticities reconstruction with the Σ- and e-method is shown for data. The solid dots are the means and the horizontal error bars are the root mean squared values of the y_Σ distributions in bins of y_e.*

the SpaCal calorimeter. The kinematic variables Q^2 and y, defined in chapter 1, can be expressed in terms of these measurements with

$$Q^2 = 4 \cdot E_e \cdot E_{e'} \cdot \cos^2\left(\frac{\theta_{e'}}{2}\right) \qquad \text{and} \qquad y_e = 1 - \frac{E_{e'}}{E_e} \cdot \sin^2\left(\frac{\theta_{e'}}{2}\right) , \tag{4.1}$$

where the energy of the incoming positron of the scattering process is assumed to be the beam energy E_e. Thus the e-method is sensitive to ISR. The value of the x_{Bj} variable is derived from the two measurements and the center of mass energy s with the relation

$$x_{Bj} = \frac{Q^2}{s \cdot y} . \tag{4.2}$$

The Σ-method uses a measurement of the full hadronic state to avoid the beam energy assumption for the incoming positron and is therefore not sensitive to ISR. Besides $E_{e'}$ and $\theta_{e'}$ the measurement of the Δ variable is used in the Σ-method. Δ is defined by

$$\Delta = \sum_{particles\, i} (E - p_z)_i , \tag{4.3}$$

where the sum runs over all detected particles i and $(E - p_z)_i$ denote differences of their energies and longitudinal momenta. Due to energy and momentum conservation Δ is

$D^{*+} \to D^0\pi^+ \to (K^-\pi^+)\pi^+$			$D^+ \to K^-\pi^+\pi^+$		
method	$N(D)$	$\Delta N/N$	method	$N(D)$	$\Delta N/N$
e	468 ± 32		e	350 ± 31	
Σ	457 ± 32	-2.3%	Σ	358 ± 32	$+2.4\%$
$e\Sigma$	459 ± 32	-1.7%	$e\Sigma$	348 ± 31	-0.5%
$D^0 \to K^-\pi^+$			$D_s^+ \to \Phi\pi^+ \to (K^+K^-)\pi^+$		
method	$N(D)$	$\Delta N/N$	method	$N(D)$	$\Delta N/N$
e	408 ± 31		e	78.0 ± 18.9	
Σ	404 ± 31	-1.0%	Σ	79.1 ± 19.4	$+1.3\%$
$e\Sigma$	398 ± 30	-2.5%	$e\Sigma$	73.6 ± 19.5	-5.7%

Table 4.7: *The extracted numbers of D-mesons in the visible range are given for different methods of reconstructing the event kinematics. The quoted relative differences are calculated with respect to the samples reconstructed with the e-method. The extracted numbers have not been corrected for ISR.*

preserved in the scattering process. By neglecting the masses of the proton and the positron Δ can be easily calculated in the initial state: while the incoming proton does not contribute to Δ, the positron's longitudinal momentum has a negative sign and Δ equals therefore twice the incoming positron's energy. The measurement of Δ in the final state therefore determines the energy of the incoming positron. Δ is derived from the momenta and energy measurements of the trackers and calorimeters.

The $e\Sigma$-method is a hybrid of the two methods. It combines the good resolution achieved with the e-method (cf. fig. 4.2) with the independence on the ISR process of the Σ-method. While Q^2 is determined in the same way as in the e-method, the inelasticity is a combination using the measurement of Δ as well as the beam energy assumption. It is therefore less sensitive to initial state radiation than the pure e-method [56].

4.5.2 Comparison of reconstruction methods

The resolutions of the different methods have been determined in events simulated with the `RAPGAP` program [57]. The program has been chosen because it includes the ISR process. The resolution is determined by comparing the reconstructed kinematics with the simulated values. The results obtained for the inelasticity are shown in figure 4.2a.

The e-method has an almost constant y resolution in the whole visible range, because it is direct proportional to the nearly constant energy resolution. It is superior to the results achieved with the Σ- and the $e\Sigma$-methods for all but the lowest y values. This can be understood from the hadronic energy resolution which is inherently worse than the resolutions achieved for positrons. The y resolution of the Σ- and $e\Sigma$-methods becomes proportional to y toward small inelasticities, i.e. the relative error in y is constant. For the e-method this relative error becomes larger, because the relatively small energy loss

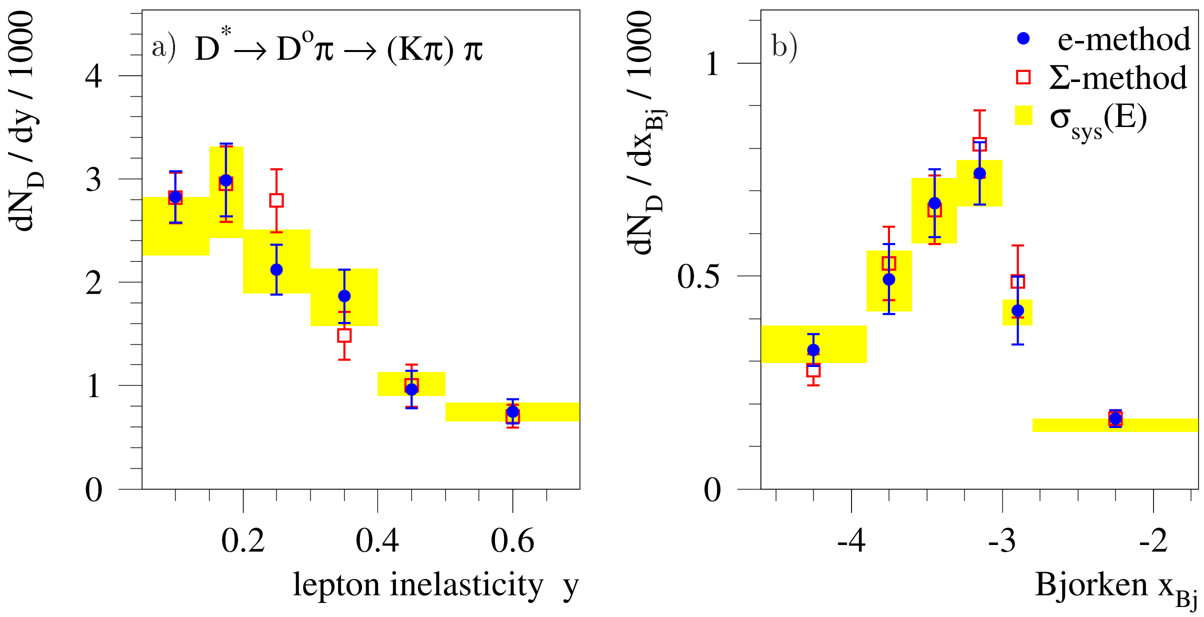

Figure 4.3: *The influence of the method used for the reconstruction of the event kinematics is studied (a) in bins of y and (b) in bins of x_{Bj}. The e-method (solid dots) and the Σ-method (open boxes) agree well considered the estimated uncertainty of the SpaCal energy calibration indicated by the shaded bands. The results using the e-method have been corrected for ISR.*

of the positron at such small y values can not be accurately measured due to the constant energy resolution.

The energy calibration of the calorimeters is the main source of the systematic error in all methods. Calibration constants for the SpaCal calorimeter have been determined for a running period with a dedicated trigger setup in the end of 1999. This set is used for the reconstruction with the e-method. The relative accuracy of the calibration is about two percent [58]. Because it is applied to a different data sample, a conservative error of four percent is estimated for the energy calibration. An improved set of calibration constants for the LAr calorimeter will be available only after the reprocessing of the data. Therefore the reconstruction with the Σ-method uses the calibration set which was available for the reconstruction on Level 5.

In figure 4.2b the inelasticities reconstructed with the e- and Σ-methods are compared. A mismatch between the two measurements can be seen. But from such a comparison it can not be concluded which of the two methods suffers from an improper calibration. In addition the methods are not uncorrelated because both use the energy measurements of the SpaCal calorimeter. Therefore the sensitivity of the measurement to the reconstruction method is further investigated.

The D-meson signals are extracted in samples reconstructed with the three different methods and the results are summarized in table 4.7. The measurements change only on a percent level which may be considered as rather small compared to the systematic error from the SpaCal calibration estimated to be $^{+4}_{-9}\,\%$ (cf. tab. 7.4).

This comparison considers only fluctuations on the boundaries of the visible range. In addition the independence of the distributions in the measured kinematical variables on the chosen reconstruction method has been tested with the D^{*+}-sample reconstructed with the CJC. This comparison is sensitive to fluctuations between the different bins. The results of the comparison in y and x_{Bj} are shown in figure 4.3. Considering the size of the estimated errors due to the SpaCal energy calibration (shaded bands), the results of the two methods agree very well.

4.5.3 Selected reconstruction method

For the cross section measurement the kinematic variables were determined by means of the e-method, because its resolution is superior to the Σ- and $e\Sigma$-methods in the visible range. The systematic error on the reconstructed variables introduced by the energy calibration is estimated with the simulation by multiplying the measured energies with factors 0.96 and 1.04. The systematic error on the measurements is about $^{+4}_{-9}\,\%$ and is listed for the different channels in table 7.4.

The e-method is sensitive to initial state radiation and the measured cross sections are corrected accordingly. The correction δ_{rad} introduced in equation 3.2 is estimated with the `HECTOR` program [55]. This program corrects the measured cross section not only for the systematically wrong reconstructed kinematics, but considers also the different center of mass energies of the ep scattering process in the cross section calculation.

The correction determined for the inclusive measurements in the visible range is $\delta_{rad} = 2.5\,\%$. The measurements done in bins of the kinematic variables Q^2, y and x_{Bj} have been corrected with the values listed in table 4.8. All other bin wise measurements have been corrected with the mean correction factor determined for the full visible range. This value has also been used as an estimate for the systematic error introduced by the correction.

Q^2 [GeV^2]	δ_{rad}[%]	y	δ_{rad}[%]	$\log(x_{Bj})$	δ_{rad}[%]
[2, 4]	1.6	[0.05, 0.15]	-3.7	[-4.6, -3.9]	5.9
[4, 7]	1.9	[0.15, 0.20]	3.3	[-3.9, -3.6]	5.0
[7, 12]	3.1	[0.20, 0.30]	6.1	[-3.6, -3.3]	2.4
[12, 22]	3.0	[0.30, 0.40]	8.4	[-3.3, -3.0]	0.8
[22, 35]	4.0	[0.40, 0.50]	8.3	[-3.0, -2.8]	0.6
[35, 100]	4.7	[0.50, 0.70]	6.3	[-2.8, -1.7]	-1.3

Table 4.8: *The radiative corrections used for the cross section measurement are listed in bins of the kinematic variables of the scattering process. The corrections have been determined with the* `HECTOR` *program [55].*

Chapter 5

D-Meson Reconstruction

The distributions used for the signal extractions are the reconstructed mass spectra of the selected D-meson candidates. The signal over background ratio in these distributions is enhanced by a lifetime tagging method. In this chapter the reconstruction chain is explained. The lifetime tagging method itself will be discussed separately thereafter.

The various tracking detectors measuring charged particles' flight trajectories, the tracks, have been discussed in chapter 2. Each of these subdetectors is optimized for a specific measurement the combination of which, commonly referred to as linking, is at the heart of the overall track reconstruction.

The reconstruction chain is pictured schematically in figure 5.1 which also represents the outline of the chapter. The CJC is the backbone of the tracking in the central region. The information of the other central tracking detectors is consecutively combined with these CJC tracks.

The association of CST hits and the combined CJC-CST track fit, which determines the CST improved track parameters, is crucial for the lifetime tag. In addition the fit is used to enhance the purity of the CJC-CST linking procedure and also serves as a tool to determine the track resolution of the drift chamber.

To distinguish signal and background events on the basis of their lifetime information the decay topology is reconstructed: the event's primary vertex is used to define the D-meson's production point, while its decay point is determined by intersecting the D-meson's decay tracks. The lifetime information of a candidate is reflected by its radial decay length l which denotes the distance between the primary and secondary vertex positions.

The fitted momenta are used for the mass reconstruction of the D-meson candidate which is discussed in the section 5.3. The chapter closes with a discussion of the kinematical and geometrical acceptances of the D-meson selection and the detector's efficiencies and purities are given.

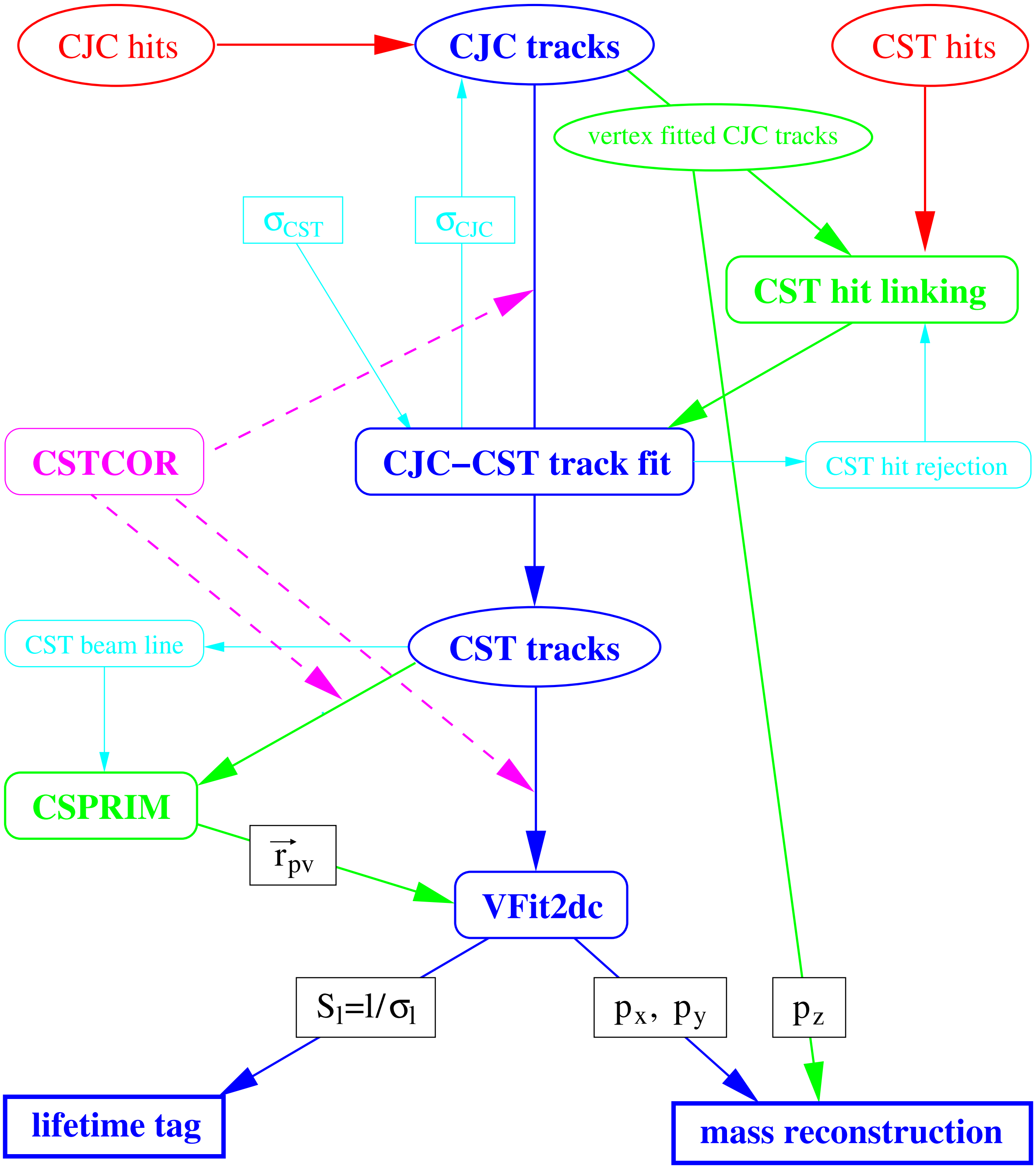

Figure 5.1: *The diagram represents the applied reconstruction chain: Beginning from the top at the hit level the particles' flight trajectories, the tracks, are measured with improving accuracy. As a final step the decay topology needed for the lifetime tag is reconstructed. The measured particles' momenta are used to determine the mass of the D-meson candidates. The* `CSTCOR`*,* `CSPRIM` *and* `VFit2dc` *algorithms are discussed in the text.*

5.1 Track reconstruction

The homogeneous magnetic field B parallel to the z-direction bends a charged particle in the transverse plane proportional to the transverse momentum p_t of the particle and the strength of the magnetic field. The flight path is described by a helix and is parameterized in H1 coordinates as a function of the arclength s by

$$\begin{aligned} x(s) &= +(d_{ca} - \tfrac{1}{\kappa}) \cdot \sin(\phi_0) + \tfrac{1}{\kappa} \cdot \sin(\phi_0 + \kappa s) \\ y(s) &= -(d_{ca} - \tfrac{1}{\kappa}) \cdot \cos(\phi_0) - \tfrac{1}{\kappa} \cdot \cos(\phi_0 + \kappa s) \qquad s \geq 0 \; . \\ z(s) &= z_0 + s \cdot \cot(\theta) \end{aligned} \tag{5.1}$$

The five track parameters $(\kappa, \phi_0, \theta, d_{ca}, z_0)$ describe the helix with respect to the origin of the H1 coordinate system and are displayed in figure 5.2. The absolute value of the curvature κ equals the inverse bending radius. Its sign is chosen opposite to the electric charge of the particle. The azimuthal angle ϕ_0 gives the flight direction in the radial plane at the point of closest approach to the z axis which is seen as the starting point of the helix: $s = 0$. The distance of this point from the z axis is given by the absolute value of the parameter d_{ca}. The sign of d_{ca} is chosen equal to the sign of κ, if the z axis is included in the circle which describes the track in the radial plane, otherwise it is chosen opposite to it. In the zs plane the track is described by a straight line with an z-axis intercept at $z = z_0$ and a slope $cot(\theta)$, where the polar angle θ gives the flight direction with respect to the positive z-axis.

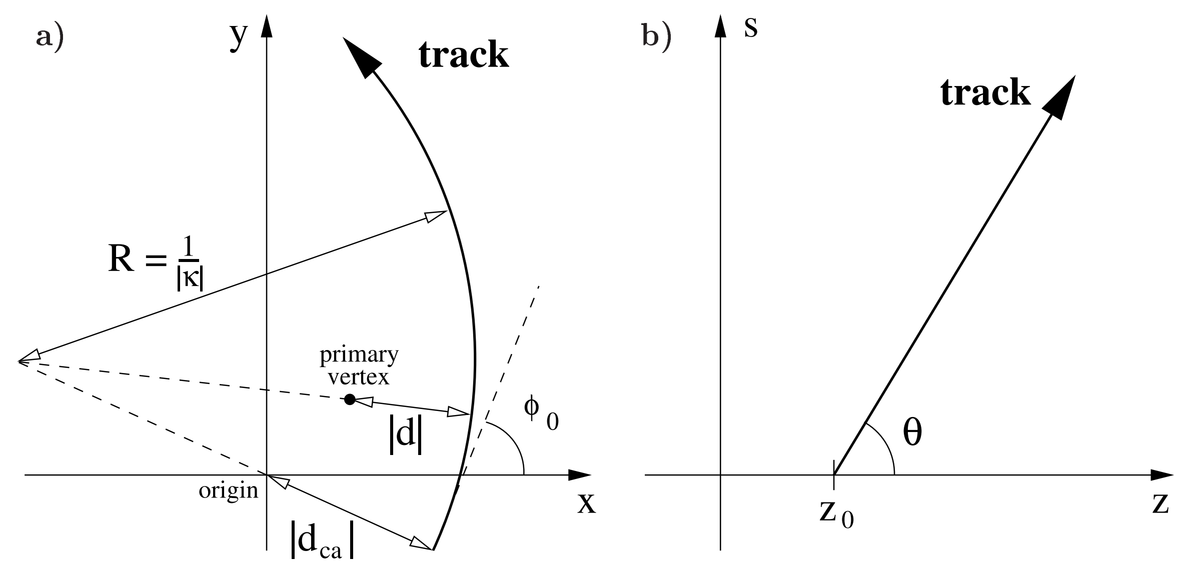

Figure 5.2: *The track parameters $(\kappa, \phi_0, \theta, d_{ca}, z_0)$ describe the helix (a) in the $r\phi$ and (b) in the zs plane with respect to the origin of the coordinate system (see text). The absolute value of the impact parameter d denotes the minimal distance of the track to the event's primary vertex.*

The description of the trajectory by a helix is insofar an approximation as the flight direction is distorted by multiple scattering in the material of the detector. In addition the particle's momentum is reduced by energy loss in matter which leads to a subsequent decreases of the particle's bending radius (spiraling tracks). And finally the magnetic field has position dependent inhomogeneities, of the order of 2% in the central region which also leads to a variation of the track's curvature.

All these effects become relevant, if the flight trajectory has to be extrapolated outside of the measurement volume. In the reconstruction chain this is the case for the extrapolation of tracks measured in the CJC to the CST and still further to the particles' production points inside the beam pipe. The track extrapolation routine `CSTCOR`[1] corrects the track parameters respectively their covariance matrix for all the mentioned effects.

5.1.1 CJC tracks

The hit measurements of the Central Jet Chambers are the basis for the identification and reconstruction of the flight trajectories [44] which is briefly reviewed in the following. In figure 5.3 an exemplary event with the reconstructed CJC hits and tracks is shown.

The reconstruction algorithm first determines the track parameters (κ, ϕ_0, d_{ca}) of the particle trajectory in the transverse plane, because the hit resolution in $r\phi$ is with $\mathcal{O}(200\ \mu\text{m})$ superior to the z resolution by two orders of magnitude. For the track fit a circular trajectory is assumed.

The pattern recognition looks first for hit triplets on adjacent sense wires. Triplets found in a chamber cell compatible with the fit model are connected to track segments. The reconstruction algorithm then looks first for matching track segments in the cells of each ring separately and only then tries to combine the measurements of the inner and outer chamber rings. By combining the measurements of different cells the ambiguity on the hit level arising from the unknown drift direction is resolved because so called mirror tracks miss a prolongation in the neighboring cell. As a last step of the $r\phi$ reconstruction remaining unlinked hits along the track are added to the track's circle fit.

The parameters (θ, z_0) describing the longitudinal track component are determined from a straight line fit in the zs plane. For the fit z position measurements only on wires with linked $r\phi$ hits are considered. The arclength values s used for the fit are determined from the wire positions and the $r\phi$ track parameters.

A precise calibration of the drift chamber is essential for the proper matching of the track segments. The important parameters are the measured reference time t_0 of the particle passage, the electrons' drift velocity v_D, the Lorentz angle α_L [2] and the precise knowledge of the wire positions given by the detector's alignment constants. Residual uncertainties in these calibration constants must be reflected in the covariance matrix describing the errors of the track parameters.

[1] `CSTCOR` is described in more detail in appendix C.

[2] The Lorentz angle α_L describes the angle between field and drift direction caused by the applied magnetic field B and is of the order of $\mathcal{O}(30^o)$.

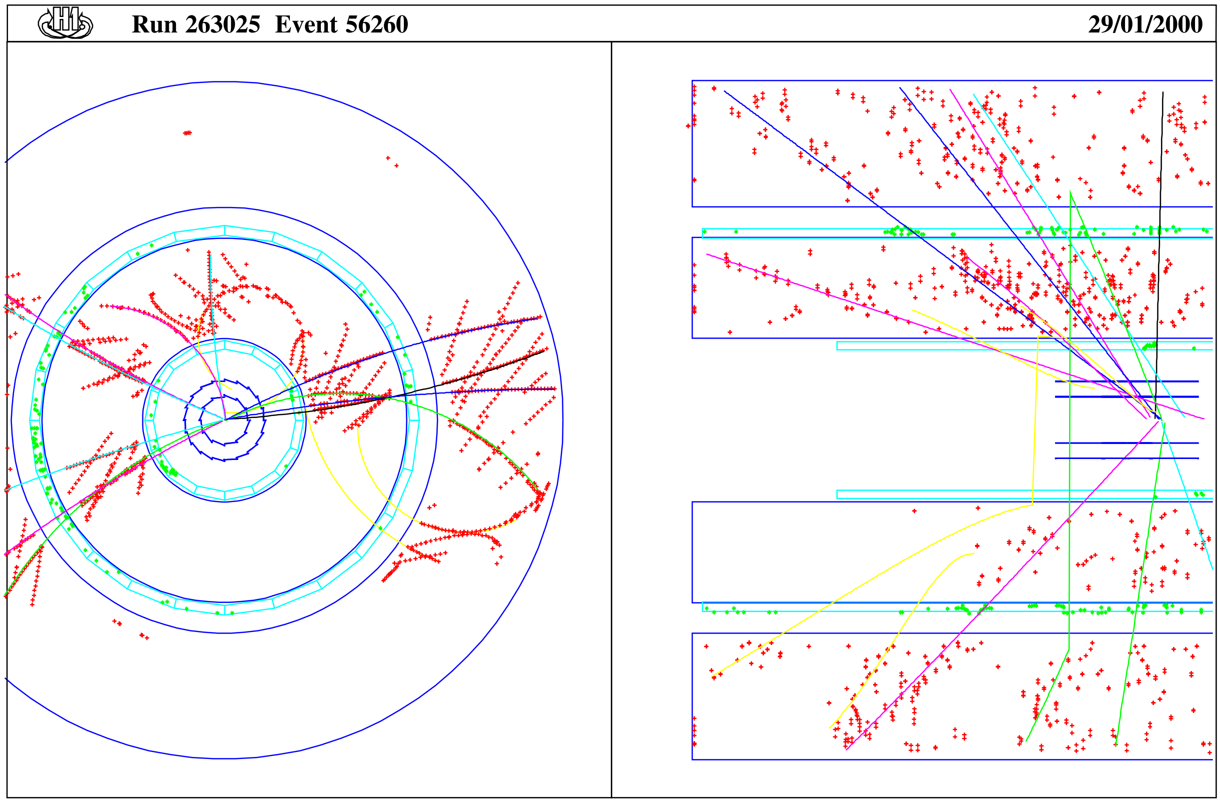

Figure 5.3: *The figure shows the result of the CJC pattern recognition in the $r\phi$- (left) and the zR- projection (right). The measured hits including their mirror hits are displayed as dots, while the lines represent the reconstructed CJC tracks.*

The different precision of the hit measurements in $r\phi$ and z is reflected in the resolutions achieved for the different track parameters: while the azimuthal angle ϕ_0 is known on the level of $\mathcal{O}(3\text{ mrad})$ the resolution of the polar angle θ is one order worse. The resolutions of the d_{ca} and z_0 parameters are even two orders of magnitude different. The former is shown in figure 5.7 as a function of the particle's transverse momentum. The relative error in the track's curvature, $\sigma(\kappa)/\kappa = \mathcal{O}(2\,\%)$, expresses the resolution of the transverse momentum achieved at this stage.

The z-chambers mounted in front of each CJC ring are designed to improve the resolution in the (θ, z_0) parameters significantly. But the accuracy achieved in these parameters by the CJC alone is not sufficient to allow a reliable linking of z-chamber hits. Therefore the resolution of the CJC tracks is first enhanced by fitting the tracks of an event to a common point of origin, the "primary vertex".

Vertex fitted CJC tracks

The majority of the particles in ep scattering are produced at the interaction point itself. The primary vertex fit performed with the CJC tracks takes advantage of this fact. In addition the measured mean position of the interaction region is used to further confine the position of the primary event vertex. The algorithm proceeds in the following steps:

- determine the mean radial beam position with the time averaged beam line and a coarse estimate of the interaction's z position,
- constrain the CJC tracks to this beam position in $r\phi$,
- average the z_0 measurements of tracks successfully fitted in $r\phi$,
- assign z-chamber hits to these vertex fitted CJC tracks,
- re-determine the interaction's z position,
- repeat the procedure with the mean radial beam position at the new z position.

The size of the interaction region is defined by the overlap of the colliding beams (see chap. 2) and its mean position is determined on Level 4 with well measured CJC tracks. The procedure averages over the positions of the interactions during a H1 data taking run which usually lasts for about one hour. The result is described by a straight line usually referred to as "run vertex". Due to the larger extension in z it is commonly parameterized to give the mean radial position as a function of the interaction's z position.

Tracks compatible with the common origin hypothesis in $r\phi$ are constrained to the mean radial position determined in this first iteration at the z position coarsely estimated with the central and forward proportional chambers by means of the $zVtx$ histogram. Successfully fitted tracks are then constrained to a common origin in z. By averaging the z measurements of several tracks the resolution in the (θ, z_0) parameters improves enough to allow the linking of z-chamber hits. After including these hits in the track fit the interaction's z-position measurement is improved and its new value is used for another iteration of the $r\phi$ primary vertex fit.

The improvement in the resolution of the (θ, z_0) parameters depends on the event's track multiplicity and the number of linked z-chamber hits. The resolutions of the $r\phi$ track parameters depend crucial on the measured track length L_{CJC} [59], where L_{CJC} is defined as the radial distance between the first and last CJC hits on the track. A measured distribution of L_{CJC} is shown in figure 5.4b. Interpreting the run vertex as an additional measured point on the track, the distance between the first and the last measured point is enhanced from L_{CJC} to $L_{CJC} + R_{start}$, where R_{start} denotes the radius of the innermost CJC hit. The resolutions decrease accordingly: In d_{ca} and ϕ_0 the improvement can be estimated by $(L_{CJC} + R_{start})/L_{CJC}$, in the curvature κ even by $(L_{CJC} + R_{start}/L_{CJC})^2$.

5.1.2 CST tracks

The position measurements of the CST hits have the accuracy necessary to resolve the rather small distances separating the production and decay vertices of selected D-mesons. The lifetime tagging method relies on the measurements in the $r\phi$-projection alone, therefore the zs-projection will be referred to only where necessary.

Two orthogonal coordinates of the point at which a charged particle transverses the sensitive area of a silicon wafer are measured independently with the strips implemented on the p- and n-side of the sensor (cf. app. F). Three dimensional space points are

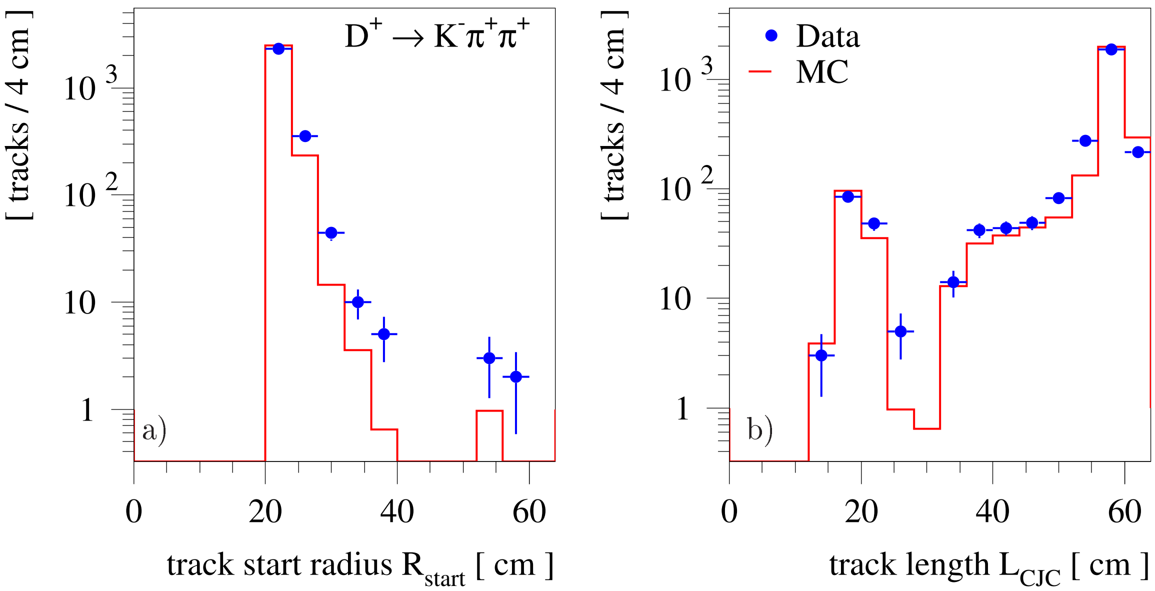

Figure 5.4: *(a) The radius R_{start} of the innermost linked CJC hit and (b) the measured CJC track length L_{CJC} are shown for decay tracks of D^+ candidates. The data distributions (dots) are fairly well described by the simulated Monte Carlo events (histograms, normalized to data).*

reconstructed from all possible combination of p- and n-side hits and the precise knowledge of the strip positions with respect to the origin of the H1 coordinate system.

The p-side strips are designed to be parallel to the z-axis and thus the $r\phi$-position would be defined by the p-side measurement alone. The mechanical assembly of the CST modules has a precision with respect to this strip orientation along z of $\mathcal{O}(1 \text{ mrad})$ which can be seen from the detector's alignment constants measured with data. Therefore the z-position of the intersect can influence the $r\phi$-position by as much as 100 μm. Thus a precise $r\phi$-reconstruction must consider also the n-side measurement which implies a reconstruction on the basis of space points.

CST space point linking

In the following the "standard linking" which associates CST space points to vertex fitted CJC tracks is discussed. Its idea is rather simple: a track measured in the CJC is extrapolated onto the silicon layers and the CST space points closest to these CJC crossings are associated with the track. The efficiency and purity of the linking depend on the size of the search window and the CST noise hit density: the search window is limited to five units of the track extrapolation error, the noise hit density defines the probability to find a noise hit closer to the intersection point than the real signal hit.

The CST p-side occupancy is shown in figure 5.5b for data and simulated events. The mean occupancy summed over all 64 halfladders is about 60 p-side hits/event. It is dominated by noise as indicated by the track multiplicity distribution shown in figure 5.5a:

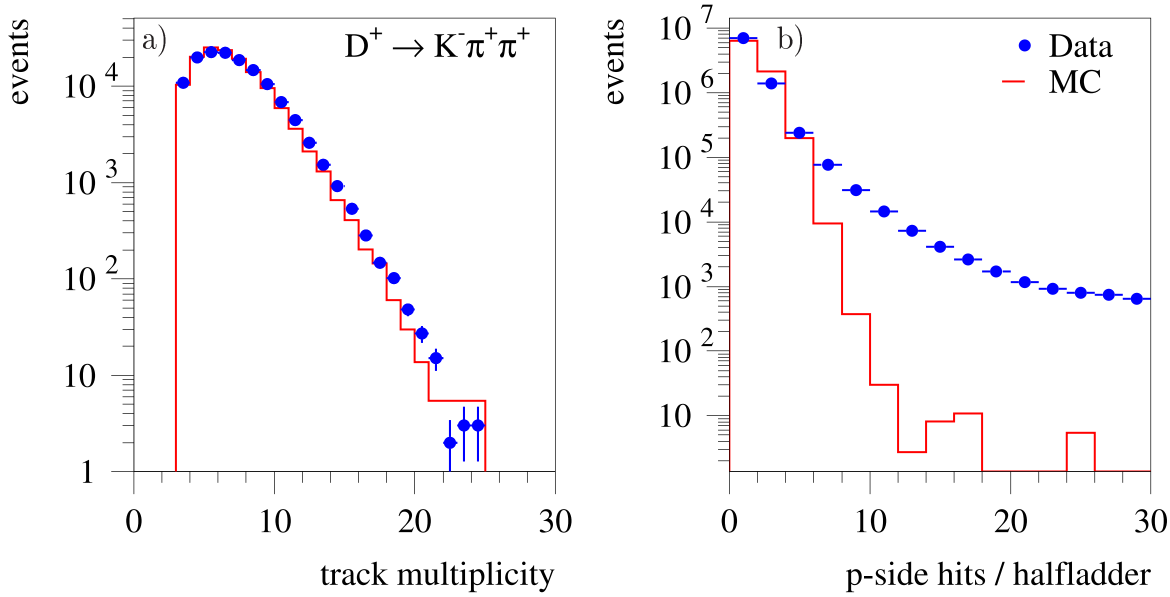

Figure 5.5: **(a)** *The multiplicity spectrum of selected CJC tracks within the CST acceptance in data (dots) is well described by the simulated distribution (histogram).* **(b)** *The CST p-side occupancy is not well reproduced by the simulation which fails to describe the non Gaussian tail: in about 2% of the events in data single halfladders have more than 6 p-side hits.*

only about 14 signal hits are expected from the mean multiplicity of about 7 tracks/event. Even though the simulation is tuned to reproduce the mean CST halfladder occupancy by using a double Gaussian to simulate the noise distribution, the non-Gaussian tail of the CST occupancy distribution is not accurately reproduced by the detector simulation. There is room to improve this implementation, but on the other hand less than 2% of the events in data do have single halfladders with more than 6 p-side hits.

The linking procedure is rather unproblematic in $r\phi$, because the CJC resolution in $r\phi$ is good and the CST p-side noise density is low due to a good signal-to-noise ratio (cf. app. F). Problems arise for the linking in the zs-plane: not only is the CJC resolution hardly sufficient to resolve the three folded ambiguities of the CST n-side hits[3], but also a mean noise density of about one noise hit per 1.5 cm complicates the n-side linking additionally.

Therefore the CST linking is done with vertex fitted CJC tracks which have a resolution of $\sigma(z_0) = \mathcal{O}(2 \text{ mm})$ due to the vertex constraint and the additional z-chamber hits. This procedure has a clear disadvantage for the lifetime tag, because the linking efficiency deteriorates for large impact parameters. The absolute value of the impact parameter d

[3]The exact z-position of a n-side hit on a halfladder is only know modulo 5.93 cm (cf. app. F).

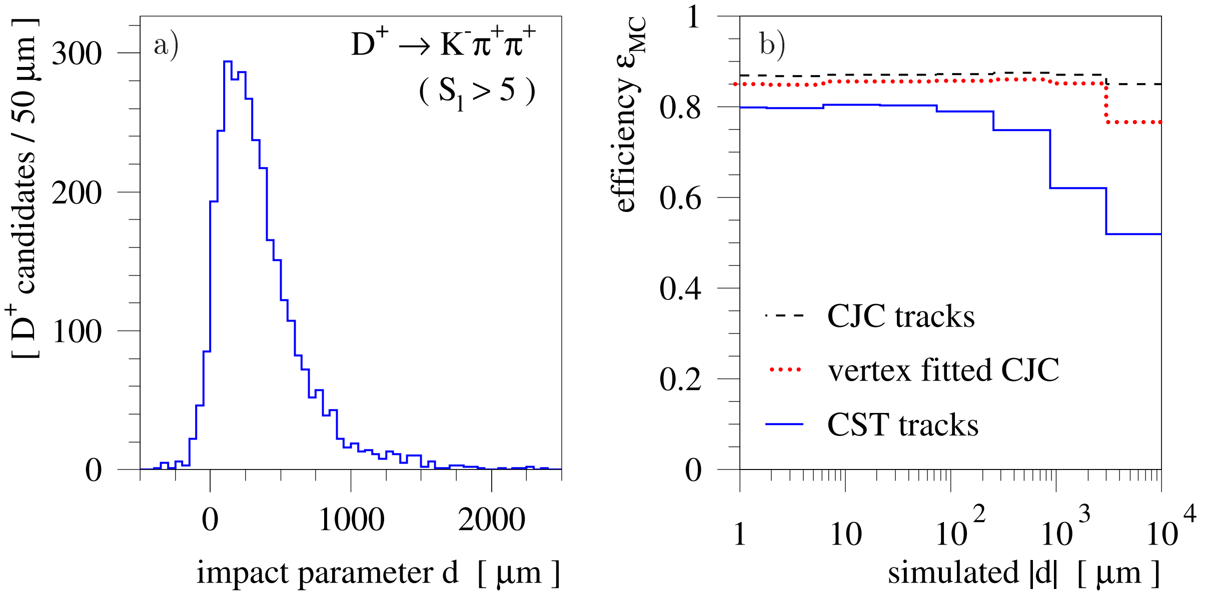

Figure 5.6: (a) *The impact parameter distribution for decay tracks of lifetime tagged D^+ candidates is shown.* **(b)** *The dependence of the track efficiency on the impact parameter has been studied with simulated Monte Carlo events for CJC tracks (dashed), vertex fitted CJC tracks (dotted) and CST tracks (solid). The results are further discussed in the text.*

denotes the minimal distance of a track to the primary vertex (cf. fig. 5.2) and is given by

$$|d| \quad = \left| \frac{1}{\kappa} - \frac{\kappa}{|\kappa|} \cdot \left(\left(-(\tfrac{1}{\kappa} - d_{ca}) \cdot \sin\phi_0 - x_{pv} \right)^2 + \left(+(\tfrac{1}{\kappa} - d_{ca}) \cdot \cos\phi_0 - y_{pv} \right)^2 \right)^{1/2} \right| \tag{5.2}$$

where (x_{pv}, y_{pv}) denotes the radial position of the event's primary vertex and κ, d_{ca} and ϕ_0 are the previously introduced track parameters. The sign convention of the impact parameter will be discussed in the next chapter.

Figure 5.6a shows the impact parameter distribution for the decay tracks of lifetime tagged D^+ candidates ($S_l > 5$, cf. chap. 6), where the influence of the impact parameter dependent linking efficiency, shown in figure 5.6b for simulated decays, is largest due to long lifetime of the D^+ meson. The inefficiencies at large impact parameters have two sources: because the CJC tracks are incompatible with the primary vertex hypothesis their vertex fit fails and they are therefore lost for the CST linking. Even if the fit succeeds the vertex fitted track is shifted systematically by the size of its impact parameter. Thus the extrapolated CJC intersection points on the CST sensors are wrong by the same amount and the CST signal hits might be outside of the search window or a noise hit might be closer.

The quality of the simulation has been investigated with respect to these effects. To test the dependency of the linking efficiency on the size of the search window, the window

impact parameter cut	ε_{data} [%]	ε_{sim} [%]	$(\varepsilon_{data} - \varepsilon_{sim})$ [%]
$d \leq$ 800 μm	72.1 ± 2.7	71.6 ± 1.1	-0.5 ± 2.9
$d \leq$ 1000 μm	83.4 ± 2.5	84.2 ± 0.9	-0.8 ± 2.6
$d \leq$ 1200 μm	88.7 ± 2.1	90.7 ± 0.7	-1.9 ± 2.2
$d \leq$ 1500 μm	98.7 ± 1.5	95.8 ± 0.5	2.9 ± 1.6

Table 5.1: *The table summarizes the efficiency of various upper cuts on the impact parameter d of D^+ decay tracks derived from the corresponding lifetime tagged D^+ signals in data and simulated events (cf. tab. 6.1). In the last column the results are compared and a good agreement can be seen.*

is enlarged from 5 to 10 units of the track extrapolation error. The D^+ signal gain of $(1 \pm 2)\%$ observed in data is well comparable with the value of 2% found for simulated decays.

The linking inefficiencies found with simulated events become relevant for impact parameters $d \gtrsim 800$ μm. To test the description of this dependency the D^+ signals are extracted for different upper cuts on the impact parameters of the decay tracks. The results are summarized in table 5.1 and a good agreement is found between data and simulated D^+ decays.

CJC-CST track fit

The space points measured with the two CST layers are not sufficent for a stand alone track reconstruction. Therefore the CST information is added to CJC tracks with a combined CJC-CST track fit which determines CST improved track parameters. In analogy to the CJC reconstruction the fit is done separatly in the $r\phi$- and zs-plane. The CST space points and the measured CJC track parameters are used as input. This procedure is equivalent to a fit with all CJC and CST hits as long as the track's covariance matrix describes the CJC resolution accurately. For the frequently applied track fit the considerably faster procedure is favoured.

A circle fit in $r\phi$ minimizes the following χ^2 function to determine the new track parameters $\vec{T}$:

$$\chi^2 = (\vec{T} - \vec{T}_{CJC})^t \, V_{CJC}^{-1} \, (\vec{T} - \vec{T}_{CJC}) + \sum_{hits\ j} \frac{\Delta(\vec{T}, hit_j)^2}{\sigma_\Delta^2}, \tag{5.3}$$

where $\vec{T}_{CJC}$ and V_{CJC} denote the track parameters and their covariance matrix measured with the CJC. $\Delta(\vec{T}, hit_j)$ and σ_Δ stand for the Euclidian distance between the track and the j-th CST space point and its calculated error. The sum runs over all CST hits linked to the CJC track. If the circle fit convergences, it is followed by a straight line fit which determines the parameters in the zs-plane.

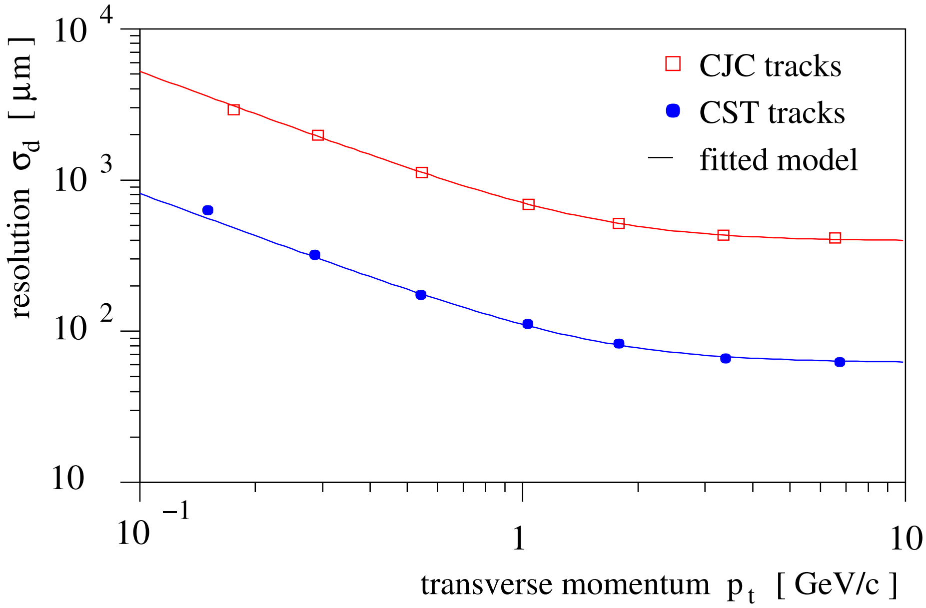

Figure 5.7: *The impact parameter resolution σ_d of CJC (open boxes) and CST tracks (solid dots) horizontal in ϕ is shown as a function of the transverse momentum p_t. The resolution is dominated by multiple scattering at low momenta and it reaches asymptotically the intrinsic detector resolutions of $\sigma_{int} = 57\ \mu\mathrm{m}$ for CST and $\sigma_{int} = 400\ \mu\mathrm{m}$ for CJC tracks as found by the fitted curves discussed further in the text. The beam spot size has not been unfolded from σ_d.*

CST resolution

The intrinsic CST hit resolution has been measured and values of $\sigma_{r\phi} = 12\ \mu$m for the p- and $\sigma_z = 22\ \mu$m for the n-side have been reached (cf. app. F). The resolution averaged over all CST modules is about 20% (p), respectively 10% (n) worse due to residual misalignment effects. The detector simulation does not include any misalignment and to account for these residual effects the simulated resolution is deteriorated by an additional Gaussian smearing of 10 μm in the p- and n-side hit positions.

The additional CST information improves the accuracy of all track parameters. Most relevant for the lifetime tag is the impact parameter resolution σ_d. It is shown in figure 5.7 for CJC and CST tracks as a function of the transverse momentum p_t. The measurement is done with respect to the center of the beam spot. The size of the beam spot enters the resolution and only horizontal tracks are considered, because they see the beam spot's smallest extension ($\sigma_y \approx 40\ \mu$m). Unfolding the beam spot from the measurement an intrinsic impact parameter resolution of $\sigma_d \approx 37\ \mu$m is achieved with the CST (cf. app. F) which is ten times more accurate than the CJC measurement alone.

The strong dependence of the resolution on the transverse momentum arises from multiple scattering in the material in front of the detector, in case of CST tracks the beam pipe and the first silicon layer. The curves fitted to the data points of figure 5.7 parameterize the resolution with

$$\sigma_d^2 = \sigma_{int}^2 + (A_{MS}/p_t)^2, \tag{5.4}$$

where σ_{int} denotes the intrinsic resolution and the parameter A_{MS} describes the multiple scattering contribution as a function of the transverse momentum p_t. The asymptotic value σ_{int} achieved for high momentum tracks depends only on the detector's intrinsic hit resolution and the length of the extrapolation's lever arm from the detector to the interaction region. $A_{MS} \approx 80\ \mu\text{m/GeV/c}$ is proportional to the square root of the material thickness x traversed, measured in units of the mean radiation length X_0: $A_{MS} \sim \sqrt{x/X_0}$.

The effect of the remaining uncertainty in the CST hit resolution on the cross section measurements is estimated with the simulation. Thereto its simulated value is varied by $\pm 20\%$ motivated by the size of the space point smearing itself. The relative differences in the extracted numbers of D-mesons are added to the experimental systematic error.

CJC track resolution

An accurate description of the resolution is essential for the lifetime tag. An intermediate solution is needed to take the incomplete calibration of the CJC into account. The method discussed in the following uses the precise CST information to measure the actual CJC resolution and is based on the CJC-CST track fit.

The shape of a χ^2 distribution is given by the number of degrees of freedom (ndf) alone. In case of the CJC-CST track fit the ndf is equal to the number of CST hits used. In the definition given in equation 5.3 the accuracy of the differences $(\vec{T} - \vec{T}_{CJC})$ and $\Delta(\vec{T}, hit_j)$ is dominated by the CJC resolution. Thus the distribution of the fit's χ^2 results is described by a χ^2 function only, if the CJC covariance matrix accurately reflects its resolution. Therefore the degree of agreement can be used to actually measure the achieved CJC resolution.

A nice way to do so uses the fit's (upper tail) probability $\mathcal{P}_{r\phi}$ which gives the probability to have a larger χ^2 value as achieved by the minimization algorithm and is based on the χ^2 distribution expected for the available ndf. The probability distribution of a χ^2 function is therefore flat between 0 and 1. Thus the slope of the distribution is a direct measure for the accuracy of the CJC covariance matrix.

The effect of the residual CJC miscalibration is parameterized by a global scale factor f_{cjc} applied on the $r\phi$-components of the CJC covariance matrix. The slope of the probability distribution is measured as a function of f_{cjc} and a linear dependence is found. An example for such a measurement is shown in figure 5.8. The scale factor averaged over several samples of the analyzed data period is found to be $f_{cjc} = 1.42$ with a spread of less than 10%.

The simulation does not include the improper calibration observed in data. The effect is covered by smearing the reconstructed track parameters of simulated decays by the amount of the scale factor determined in data and applying the same correction on the covariance matrix. To do so the reconstructed track parameters are compared with their simulated values and the former are modified to enlarge their residua according to the chosen factor.

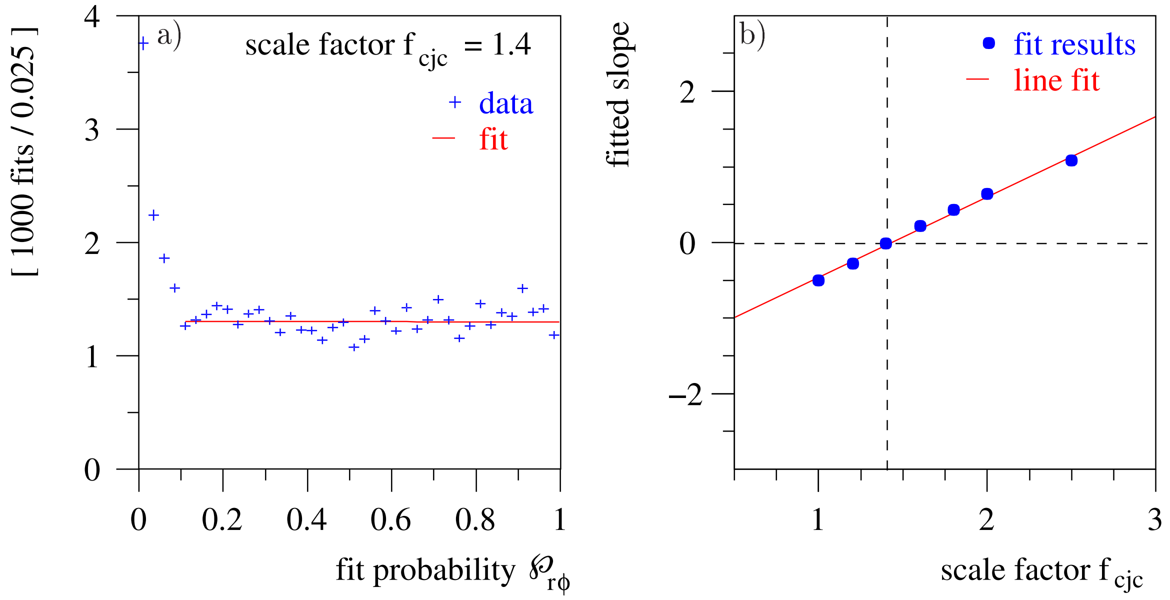

Figure 5.8: **(a)** *The probability distribution of the CJC-CST track fit in $r\phi$ is shown for a scale factor of $f_{cjc} = 1.4$ applied on the $r\phi$-components of the CJC covariance matrix. The rise of the distribution towards low probabilities originates from incompatible CJC and CST measurements. The slope of the distribution is determined only from probability values above 0.1.* **(b)** *The fitted slopes of distributions obtained for different values of f_{cjc} are shown. A linear fit to the data points determines the scale factor for which the distribution becomes flat (no slope) with $f_{cjc} = 1.42 \pm 0.03$.*

The influence of the uncertainty in the CJC resolution is also estimated with the simulation by varying the scale factor by ±10% which is motivated by the spread of the scale factors determined with different data samples. The relative differences in the extracted numbers of D-mesons are added to the experimental systematic error.

Additional CST hit rejection

The search window used for the space point linking is rather generous with five units of the CJC track extrapolation error and thus a non-negligible amount of noise hits are assigned to the CJC tracks. Especially for the lifetime tag such impurities deteriorate the signal and background separation power, because they fake large impact parameters with small errors due to the good CST resolution.

The CJC-CST track fit represents a powerful tool to identify impurities of the CST linking, because it correlates the measurements from the two CST layers and compares the flight directions measured with the CST and the CJC. The comparison of directions is more powerful than just the position sensitive layer wise linking, because the radial extension of the drift chamber allows a precise direction measurement in the $r\phi$-plane. The $r\phi$ CJC-CST track fit is used herein as a quality criteria for the hit assignment and as a tool to improve this assignment by rejecting space points from the track fit.

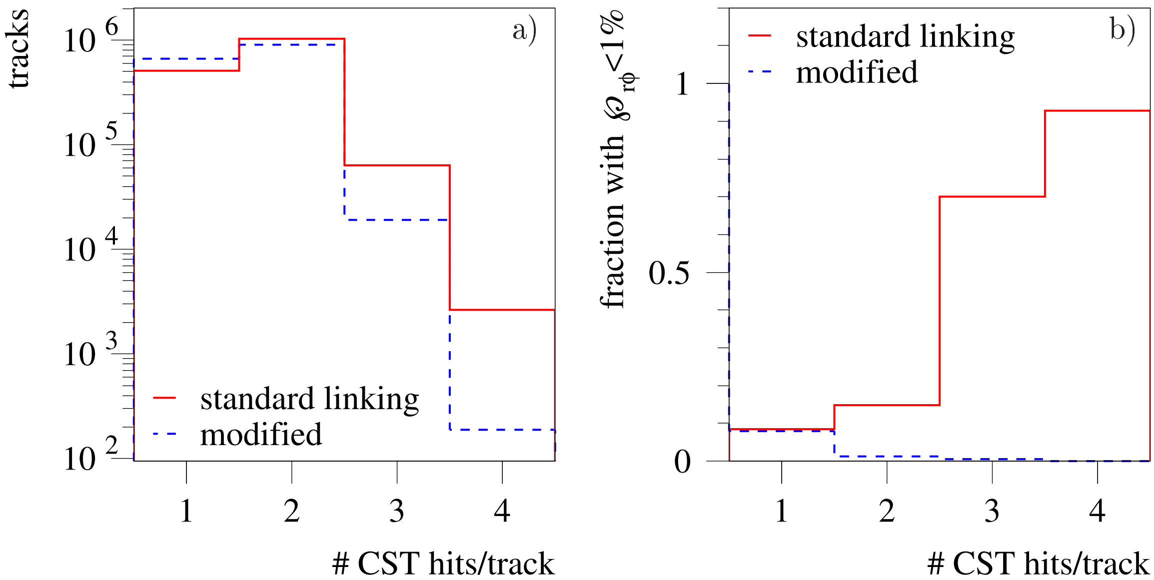

Figure 5.9: (a) *The number of linked space point per track is shown for the standard and for the modified version of the CST linking procedure (see text).* **(b)** *The fraction of tracks with a fit probability less than 1% is shown as a function of the number of linked hits.*

Hits are only rejected, if the track fit does not converge or if the fit probability is below 1%. That holds for about 15% of the track fits which use the hit assignment found by the CST space point linking. In these cases the track fit is redone with all possible combinations of the assigned CST hits, but at least one CST hit is required. Alternative CST hits not assigned by the linking are not considered in the procedure. The fit with the highest probability, even if it is below 1%, determines the best assignment and the final CST track parameters. The fraction of failed or bad track fits is reduced by this procedure to less than 5%.

The impact of the hit rejection is most obvious for tracks with more than two linked CST hits as can be seen in figure 5.9. Assignments with more than one hit per CST layer are possible, because the active regions of silicon sensors adjacent in the $r\phi$-plane have a small overlap of about 3%. The generous linking finds a larger fraction, but the purity of these potential overlap candidates is low as can be seen in figure 5.9b from the large fraction of fits with low probability. The track fit identifies these impurities and the incompatible space points are discarded.

The benefit of the method for the D-meson reconstruction has been investigated in the three body decay $D^+ \to K^-\pi^+\pi^+$: the background in the mass spectrum used for the cross section measurement is reduced by 15%. The method reduces the mean number of space points used per CST track from 1.73 to 1.58. Through this procedure also 4% of the signal events are lost which don't fulfill the criteria posed on the number of linked CST hits any more (cf. tab. 5.8).

5.2 Vertex reconstruction

The lifetime tag distinguishes signal and background events on the basis of their decay topology: the selected D-mesons decay due to their momentum and their finite lifetime of some 100 μm at secondary vertices separated from the ep interaction point in space, while the combinatorial background origins mostly at the interaction point itself. The decay length l gives a measure of this separation in the radial plane. It is reconstructed the event's primary and the candidate's secondary vertex. The methods used for this reconstruction are discussed in the following.

The event's primary vertex is assumed herein to be the D-meson's production point[4]. `CSPRIM` is an H1 internal tool to determine its position using the precise CST track measurements. In addition to this event based information, the time averaged mean position of the ep collision region inside the H1 detector is used to further confine the event's primary vertex position.

The position of the candidate's decay vertex is determined with the CST tracks of its decay particles by the two dimensional track-vertex fitter `VFit2dc`. It includes a constraint which forces the vertex positions to be conform with the transverse momentum directions and therefore yields a consistent picture of the decay topology.

5.2.1 Primary vertex fitter `CSPRIM`

Similar to the primary vertex fit of the CJC, `CSPRIM` determines the position of the ep interaction point with tracks compatible with a common origin hypothesis and it uses the average beam position to confine its position further. While CJC tracks are essentially constrained to the latter, high precision CST tracks can resolve the interaction region and improve the accuracy of primary vertex position measurement.

Beside the CJC run vertex already discussed (cf. sec. 5.1.1), the results of short term CST beam line measurements are used herein, because the CJC run vertex has two disadvantages: the run wise determination becomes unreliable for short H1 runs and in long runs (about one hour) the method averages over beam movements which are continuously made to optimize the luminosity (cf. fig. 5.10).

The short term CST beam line is determined offline. It is based on an event wise primary vertex reconstruction with CST tracks. No further constraint to an average beam position is made. The mean position of the interaction region, defined as the "beam line", is measured with the primary vertex positions of some hundred events and is therefore independent of the run length and follows beam movements on a time scale of minutes.

The short term CST beam line measurement is not available for the data taken after the H1 run 273798. This period accounts for about a fourth of the analyzed luminosity, but the H1 and HERA running conditions in this period have been fairly stable and therefore the CJC run vertex is reasonably reliable.

[4] D-mesons produced in cascade decays of b quarks do not origin at the event's primary vertex.

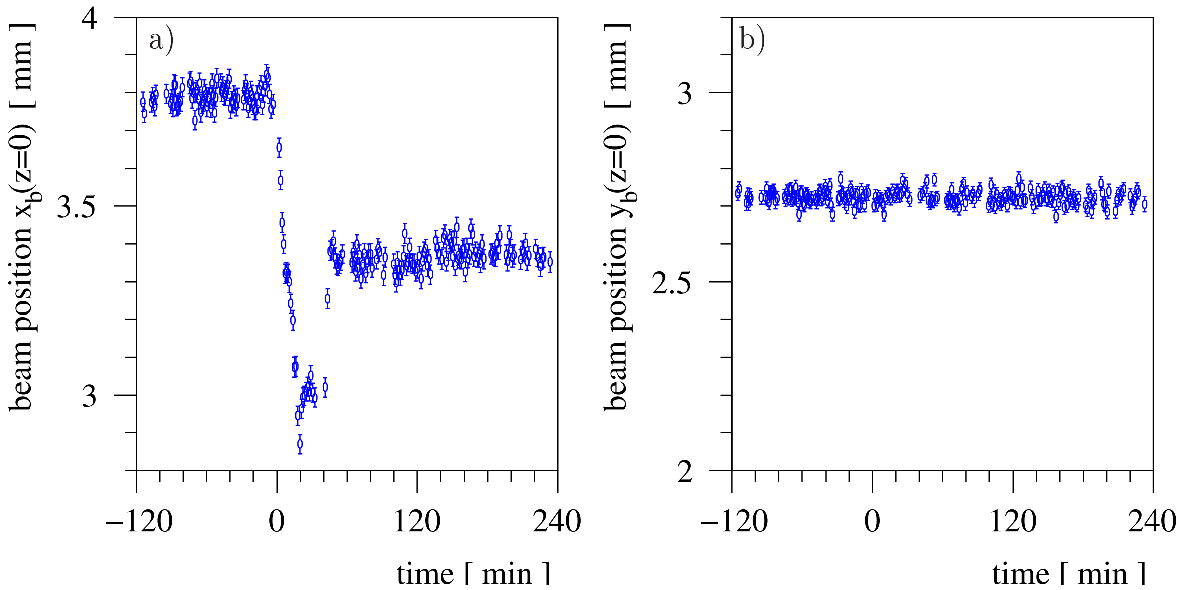

Figure 5.10: *The figure shows the short term CST beam line positions x_b (a) and y_b (b) at $z = 0$ as a function of time. The measurement follows the exceptional large HERA beam movements in x on a time scale of minutes. With such beam movements the luminosity is permanently optimized during a luminosity fill.*

In `CSPRIM` the $r\phi$- and z-positions of the event's primary vertex are determined consecutively. The radial beam position is taken at the z-position of the CJC primary vertex. CST tracks are selected for the $r\phi$-fit with the following criteria:

track length	$L_{CJC} \geq 10$ cm,	start radius	$R_{start} \leq 35$ cm,
impact parameter	$\|d\| \leq 2$ cm	and its significance	$\|S_d\| = \|d\|/\sigma_d \leq 2$.

For this preselection the impact parameter d and its significance $S_d = d/\sigma_d$ is calculated with respect to the mean beam position. The tracks associated with a D-meson decay are explicitly excluded from the fit. The radial position of the event's primary vertex $\vec{r}_{pv} = (x_{pv}, y_{pv})$ is then determined by minimizing the χ^2 function

$$\chi^2 = \sum_{tracks} S_d(\vec{r}_{pv})^2 + (\vec{r}_{pv} - \vec{r}_b)^t \; V_b^{-1} \; (\vec{r}_{pv} - \vec{r}_b), \tag{5.5}$$

where $\vec{r}_b$ and V_b denote the beam position and its covariance matrix which is essentially given by the radial size of the interaction region. The track parameters are not altered by the fit. If S_d^2 of a track becomes larger than 3 with respect to the fitted vertex position, the track is discarded and the $r\phi$-fit is repeated.

The consecutive fit of the z-position takes only tracks into account which have been used in the $r\phi$-fit. If the new z-position of the vertex differs by more than 1 cm from the value measured with the CJC alone, the $r\phi$-fit is repeated using the new z-position.

In figure 5.11 the calculated errors on the radial position of the event's primary vertex are shown. The maximal size of the errors are limited by the size of the elliptic beam

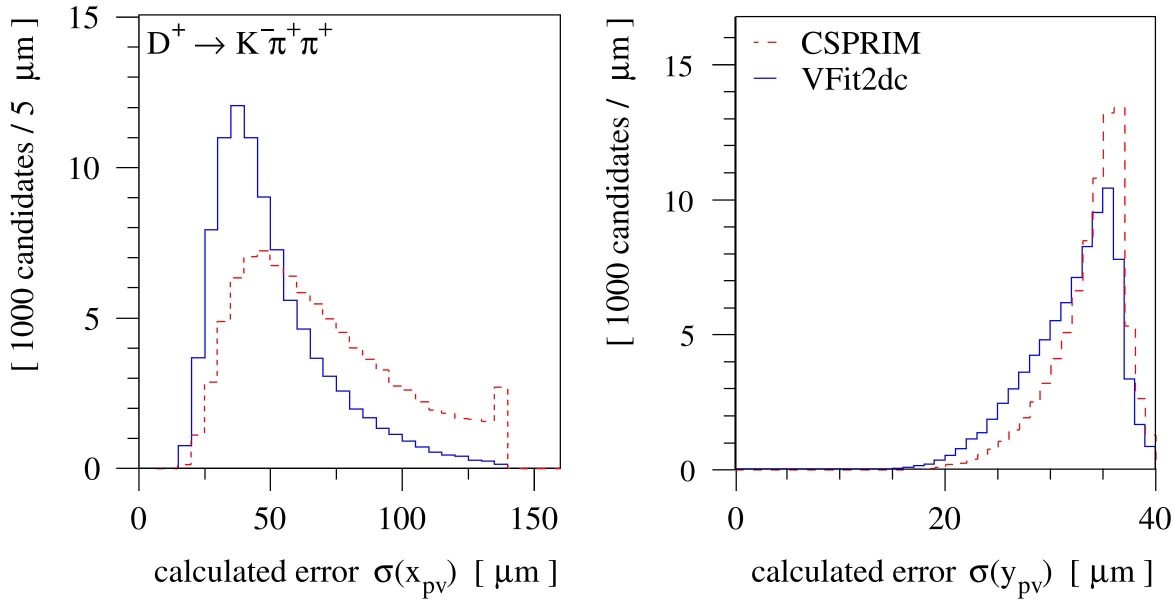

Figure 5.11: *The calculated errors on the primary vertex position (x_{pv}, y_{pv}) of lifetime tagged D^+ candidates (cf. tab. 6.1) are shown. The accuracy achieved with* `CSPRIM` *(dashed) is improved by the directional constraint applied in the* `VFit2dc` *fit (solid).*

spot. In y the already small beam spot extent of $\sigma_y = 37\ \mu$m can hardly be resolved with the CST and a mean error in the y_{pv} position of $\langle\sigma(y_{pv})\rangle = 33.6\ \mu$m is achieved. The accuracy of the x_{pv} position is significantly improved by the additional CST information from $\sigma_y = 137\ \mu$m to an average value of $\langle\sigma(x_{pv})\rangle = 68.7\ \mu$m. The mean values quoted hold for the position determined with the `CSPRIM` fitter. The measurement is further improved by a directional constraint applied in the `VFit2dc` fit which is discussed in the following.

5.2.2 Secondary vertex fitter `VFit2dc`

The D-meson's decay point is reconstructed with the two dimensional track-vertex fitter `VFit2dc`. It determines the most likely common point of origin of a set of N tracks in the $r\phi$-plane and uses in addition the measured decay particles' momenta to constrain both vertex positions further[5]. In the following the general idea of the fitter and its consequences on the final measurements are discussed.

In figure 5.12 the reconstructed topology of an event with a $D^+ \to K^-\pi^+\pi^+$ decay candidate is shown. The positions of the reconstructed primary and secondary vertex are denoted with $\vec{r}_{pv} = (x_{pv}, y_{pv})$ and $\vec{r}_{sv} = (x_{sv}, y_{sv})$. The decay length vector $\vec{l}$ is then defined by

$$\vec{l} = \begin{pmatrix} l_x \\ l_y \end{pmatrix} = \vec{r}_{sv} - \vec{r}_{pv} = \begin{pmatrix} x_{sv} - x_{pv} \\ y_{sv} - y_{pv} \end{pmatrix}. \tag{5.6}$$

[5] A detailed description of the mathematical model used in `VFit2dc` can be found in appendix D.

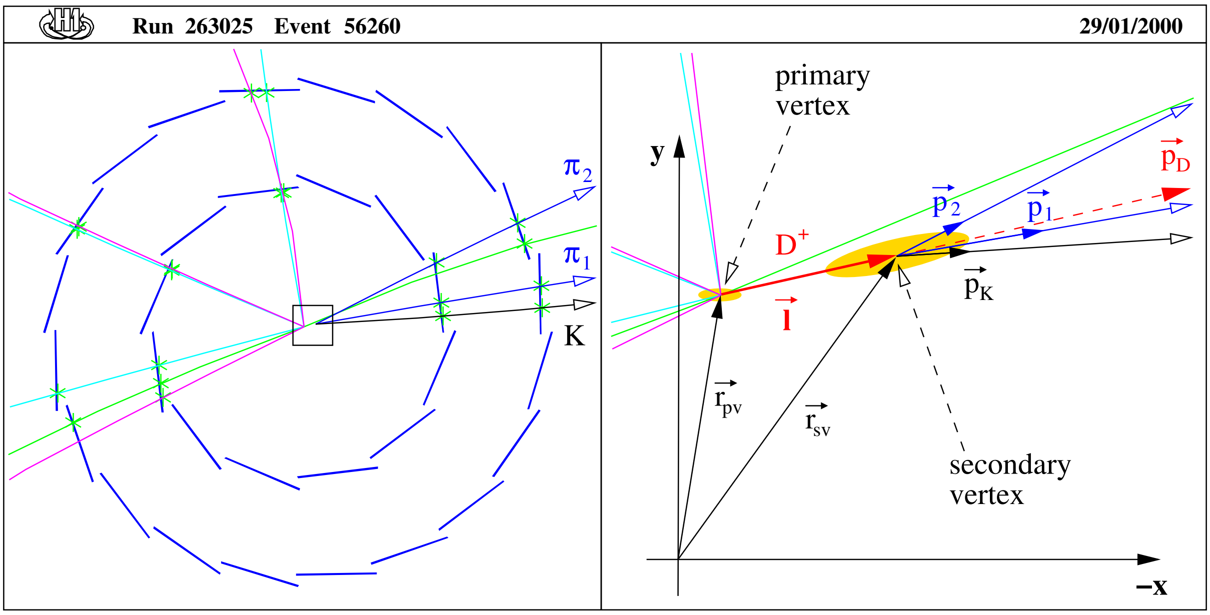

Figure 5.12: *An event with a $D^+ \to K^-\pi^+\pi^+$ decay candidate is shown (cf. fig. 5.3). To the left a schematic $r\phi$-view of the CST including hits (stars) and tracks (lines) is displayed. The area magnified to the right is indicated by the box in the center. The errors of the primary and secondary vertex positions (shaded ellipses) have been blown up by a factor of 10 for illustrative reasons. The reconstructed transverse momentum of the D^+ candidate is* $p_t(D) = |\vec{p}_D| = 3.34 \pm 0.02$ GeV$/c$ *and its radial decay length is measured to be* $l = |\vec{l}| = 4.8 \pm 0.3$ mm.

The direction of $\vec{l}$, referred to as decay direction, is for D-mesons equivalent to the direction of their momentum, i.e. the flight direction. Its value is for the selected D-meson candidates of the order of some 100 μm. Due to this small lever arm the decay direction is only poorly resolved. On the other hand the D-meson's flight direction is known far more accurately, because it can be reconstructed from the momenta of its decay particles. Their directions are measured precisely over the large radial extent of the drift chamber. Thus constraining $\vec{l}$ parallel to the D-meson's flight direction yields a more accurate description of the event topology.

The radial projection $\vec{p}_D = (p_x, p_y)$ of the D-meson candidate's momentum vector is calculated by summing the fitted momentum vectors $\vec{p}_\mu$ of the decay particles:

$$\vec{p}_D = \begin{pmatrix} p_x \\ p_y \end{pmatrix} = \sum_{\mu=1}^{N} \vec{p}_\mu. \tag{5.7}$$

In case of the exemplar $D^+ \to K^-\pi^+\pi^+$ decay shown in figure 5.12 the sum runs over the indicated momenta $\vec{p}_K$, $\vec{p}_1$ and $\vec{p}_2$ of the Kaon and Pion candidates. The directional constraint applied in `VFit2dc` is then expressed by the requirement

$$l_x \cdot p_y - l_y \cdot p_x \stackrel{!}{=} 0. \tag{5.8}$$

Due to this constraint not only the secondary vertex position $\vec{r}_{sv}$ and the momenta $\vec{p}_\mu$ are fit parameters, but also the primary vertex position $\vec{r}_{pv}$ is treated as free within its errors.

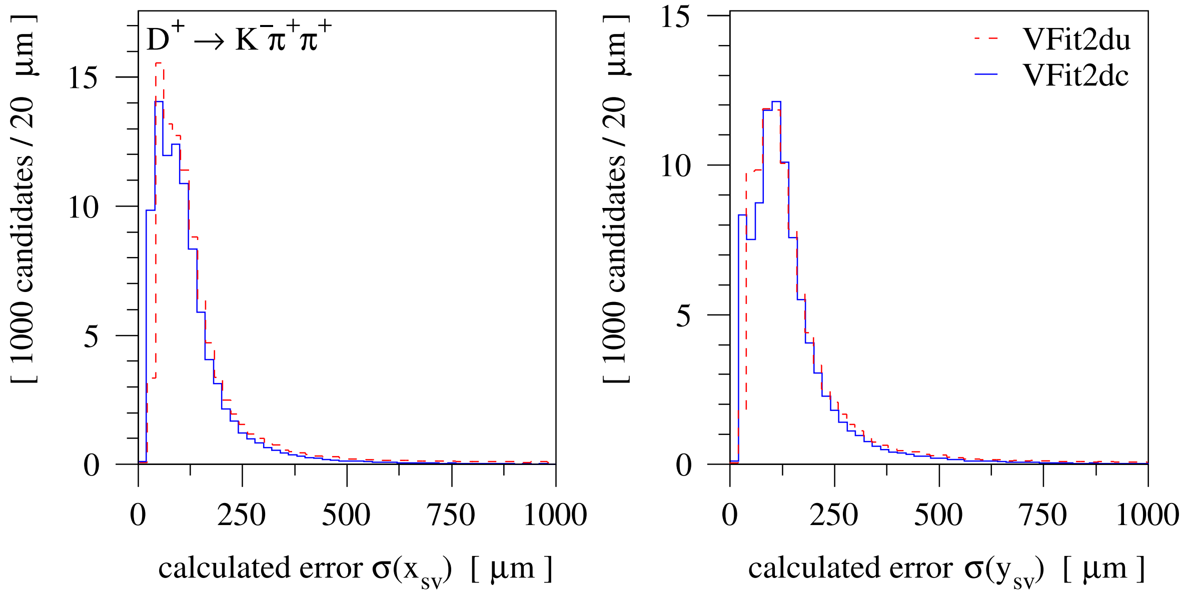

Figure 5.13: *The calculated errors on the secondary vertex position (x_{sv}, y_{sv}) of lifetime tagged D^+ candidates (cf. tab. 6.1) are shown. The accuracy achieved with the unconstrained track-vertex fitted* `VFit2du` *(dashed) is slightly improved by the directional constraint applied in the* `VFit2dc` *fit (solid).*

The solution of `VFit2dc` is found by iteratively minimizing a linearized χ^2 function. The directional constraint is included by means of Lagrangian multipliers. This methods allows a factorization of the algorithm: to find the solution of an fit iteration, first the solution $\hat{x}'$ to the unconstrained fit `VFit2du` is determined and the solution $\hat{x}$ of the constrained χ^2 function is then found in terms of $\hat{x}'$ (cf. app. D).

The vectors $\vec{l}$ and $\vec{p}_D$ are used to define the signed radial decay length l:

$$l = \frac{\vec{l} \cdot \vec{p}_D}{|\vec{l} \cdot \vec{p}_D|} \, |\vec{l}\,|, \tag{5.9}$$

where "·" denotes the scalar product. The absolute value of l is given by the separation distance between the fitted primary and secondary vertices. Its sign is positive for decays with consistent decay and momentum directions and it is negative for decays with opposite decay and flight directions which therefore are inconsistent with a physical D-meson decay.

The decay length significance S_l, defined as $S_l = l/\sigma_l$, is the most important variable for the lifetime tagging. The calculation of the error σ_l considers the correlation between the primary and secondary vertex positions and also their correlations with the fitted momentum of the D-meson candidate.

To demonstrate the benefit of the directional constraint implemented in `VFit2dc`, its performance is compared to an uncorrelated reconstruction of the primary and secondary vertex positions with `CSPRIM` and the unconstrained track-vertex fitter `VFit2du`.

For the comparison a pointing requirement similar to the directional constraint in `VFit2dc` has been formulated for `VFit2du` in the following way: The pointing angle α is defined

Mean resolutions [μm]	CSPRIM+VFit2du	CSPRIM+VFit2dc	$\Delta\sigma/\sigma$
$< \sigma(x_{pv}) >$	68.7	50.5	-27%
$< \sigma(y_{pv}) >$	33.6	32.0	-5%
$< \sigma(x_{sv}) >$	133	121	-9%
$< \sigma(y_{sv}) >$	154	142	-8%
$< \sigma_l >$	218	204	-6%

Table 5.2: *The table summarized the means of the calculated errors in the vertex positions and the signed decay length l of lifetime tagged D^+ candidates (cf. tab. 6.1). The resolutions achieved by uncorrelated primary and secondary vertex fits with* `CSPRIM` *and* `VFit2du` *are compared to the results achieved with* `VFit2dc` *which includes an additional directional constraint.*

as the angle between the decay and the flight direction of the D-meson candidate. In the calculation of the fit probability $\mathcal{P}_{\text{vf}}$ its significance $S_\alpha = \sin\alpha/\sigma_{\sin\alpha}$ is added quadratically to the minimal χ^2 value and the number of degrees of freedom ndf is incremented by one: $\mathcal{P}_{\text{vf}} = \mathcal{P}(\chi^2 + S_\alpha^2, ndf + 1)$. The decay length is calculated slightly differently by projecting the decay length vector onto the momentum vector of the D-meson candidate: $l = \vec{l} \cdot \vec{p}_D/|\vec{p}_D|$.

The equivalent selection criteria are applied for both reconstruction methods[6]. Thus the only difference is the consistent description of the event topology in terms of vertex positions and particle momenta achieved by `VFit2dc`.

Figures 5.11 and 5.13 show the comparison of the calculated error distributions of the primary and secondary vertex positions for lifetime tagged $D^+ \to K^-\pi^+\pi^+$ decay candidates achieved by `VFit2dc` with the results obtained with only `CSPRIM`, respectively `VFit2du`. In table 5.2 the mean resolutions are summarized. The improvements seen in the primary as well as the secondary vertex resolution do not propagate fully into the error of the decay length σ_l, because the constraint mostly confines the vertex positions in the direction orthogonal to the decay direction.

The more important benefit of `VFit2dc` can be seen, when comparing the signal to background ratio in the mass spectra achieved with the two reconstruction methods. Such a comparison is shown in figure 5.14 for lifetime tagged D^+ decay candidates. While physical D-meson decays comply with the directional constraint made in the fit, uncorrelated flight and decay directions in the combinatorial background enlarge the fit's minimal χ^2 value. Thus a quality requirement on the `VFit2dc` fit result in terms of a minimal fit probability $\mathcal{P}_{\text{vf}}$ rejects a significant fraction of the background. In case of the shown D^+ signals the 2-σ background below the signal is reduced with `VFit2dc` by 18% compared to the unconstrained fit with `VFit2du`, even though the latter contains a similar pointing requirement.

[6]The applied lifetime tagging cuts are $S_l > 5$, $\mathcal{P}_{\text{vf}} > 0.05$, $\sigma_l < 300$ μm and $|l| < 5$ mm (cf. tab. 6.1). The impact of the $(2 \times S_d)$ cut is studied separately in section 6.2.

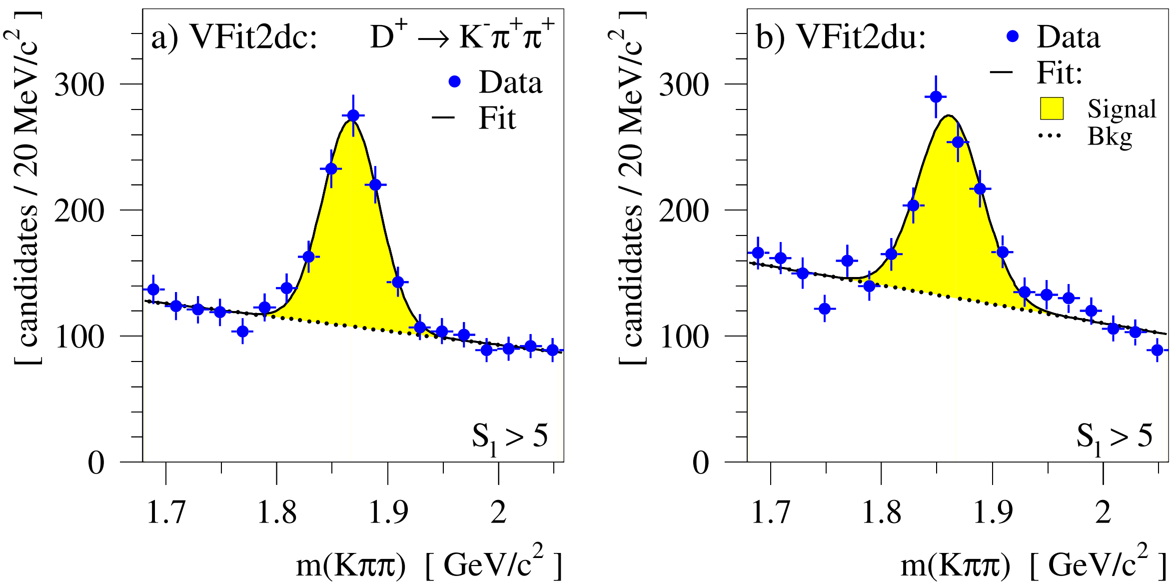

Figure 5.14: *The mass spectra of lifetime tagged D^+ candidates reconstructed with* `VFit2dc` *(a) and* `VFit2du` *(b) are compared for similar selection criteria (cf. sec. 5.2.2). The mass calculation in (b) is based on the CJC vertex fitted tracks, in (a) the $r\phi$ track parameters fitted with* `VFit2dc` *are used instead of the CJC measurements. The additional CST information improves the D^+ mass resolution by 12% to $\sigma_m = 25.6$ MeV/c^2. In total the 2-σ background below the Gaussian signal is reduced by 30% by the more accurate description of the event topology obtained with* `VFit2dc` *without losing any signal events.*

5.3 Signal extraction

The numbers of signal events are extracted from the reconstructed mass spectra of the D-meson candidates. In these spectra the signal events accumulate around the nominal D-meson mass and can therefore be distinguished from the randomly distributed background on a statistical basis. In the following the mass reconstruction, the candidate selection and the signal extraction in the different decay channels are discussed.

D-meson candidates are formed by combining preselected charged particle tracks according to the charge configuration of the decay channel. The preselection of the tracks is based on track quality and momentum requirements discussed in the next section. Because no particle identification is applied at any stage, Kaon or Pion masses are assigned to the tracks on the basis of their charge alone.

The final state of the D-meson decay is fully reconstructed. Due to conservation laws the candidate's momentum $\vec{P}_D$ and its energy E_D can be reconstructed from the measured momenta $\vec{P}_\mu$ and the associated masses m_μ of its decay particles by

$$E_D = \sum_{\mu=1}^{N} \sqrt{m_\mu^2 + |\vec{P}_\mu|^2} \quad \text{and} \quad \vec{P}_D = \sum_{\mu=1}^{N} \vec{P}_\mu \ , \tag{5.10}$$

where the sums run over all N decay particles. The invariant mass m of the candidate is then reconstructed by

$$m = \sqrt{E_D^2 - |\vec{P}_D|^2}. \tag{5.11}$$

The momentum $\vec{P}_\mu$ of the μ-th decay particle is derived from the track parameters via

$$\vec{P}_\mu = p_t^\mu \begin{pmatrix} \cos\phi_\mu \\ \sin\phi_\mu \\ \cot\theta_\mu \end{pmatrix}, \quad \text{with} \quad p_t^\mu\,[\,\mathrm{GeV/c}\,] = \left|\frac{0.003 \cdot B\,[\,\mathrm{T}\,]}{\kappa_\mu\,[\,\mathrm{cm}^{-1}\,]}\right|, \tag{5.12}$$

where p_t^μ stands for the particle's transverse momentum and B denotes the z-component of the magnetic field. The two dimensional track-vertex fitter `VFit2dc` determines only the values of the curvature κ_μ and the azimuth angle ϕ_μ. The polar angle θ_μ is taken from the CJC vertex fitted track, because impurities of the association of CST n-side hits to CJC tracks lead to a limited reliability of the CST z measurements. But the mass resolution is already improved by using the fitted $r\phi$ parameters as can be seen from figure 5.14 on the example of the D^+ signal, where the mass resolution is enhanced by 12%.

5.3.1 D^+ mesons

The $D^+ \to K^-\pi^+\pi^+$ decay chain is reconstructed by considering triplets of charged tracks with total charge ± 1. The pion mass m_π is assigned to the two particles with the same charge, and the kaon mass m_K to the remaining one. The fit model for the signal extraction is a Gaussian function for the D-meson signal and a straight line for the combinatorial background (cf. fig. 5.14). The fitted width σ_m of the Gaussian gives the mass resolution which depends on the detector's momentum resolution and the decay kinematics. For a well calibrated detector the mean $m(D^+)$ of the Gaussian is expected to be in agreement with the world average of the D^+-meson mass. The offset of the straight line is chosen to give the number of background events within a ± 2-σ_m window around the fitted $m(D^+)$ mass.

5.3.2 D^0 mesons

D^0 meson are selected through their decay mode $D^0 \to K^-\pi^+$. The association of the kaon and pion mass to the selected track pairs with opposite charges is ambiguous: for each $D^0 \to K^-\pi^+$ hypothesis the charge conjugated $\overline{D}^0 \to \pi^-K^+$ decay with the opposite mass assignment is also possible. Both assignments are considered which leads in addition to the correctly assigned signal to a "wrong charge background" in the mass spectrum.

The shape of the mass spectrum with the wrong mass assignment is essentially defined by the selected decay kinematics. Therefore a determination with simulated D^0 decays

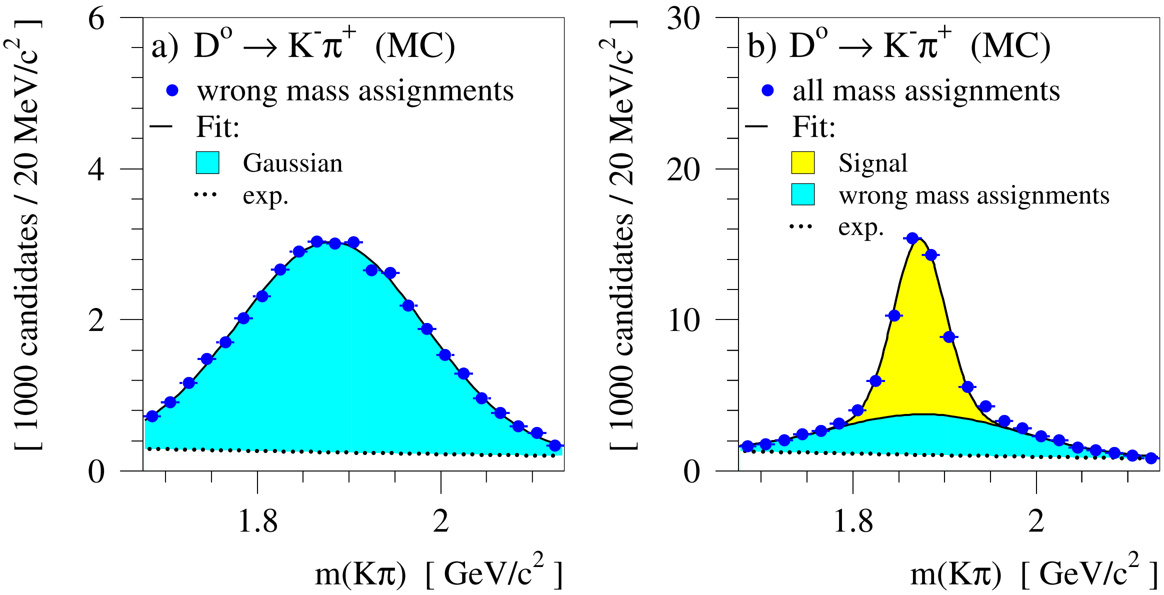

Figure 5.15: **(a)** *The reconstructed mass distribution (dots) of simulated $D^0 \to K^-\pi^+$ decays is shown for a wrong assignment of the pion and kaon masses. Its shape is fitted with a Gaussian (dark shaded) and an exponential function (dotted line). The fitted parameters of the Gaussian are used to fix the shape and normalization of this background in the fit model used for the signal extraction.* **(b)** *The result of this signal extraction with the spectrum of all selected D^0 candidates reproduces the number of events in the signal (light shaded) within 2%.*

as shown in figure 5.15a is regarded as accurate. The spectrum is fitted with a Gaussian G_{wc} and an exponential function. The width $\sigma_{wc} = 99.2$ GeV/c^2 and mean $m_{wc} = 1878.9$ GeV/c^2 of G_{wc} is used for the fit model of the signal extraction. In addition its normalization N_{wc} is determined relative to a Gaussian G_{cc} fitted to the reconstructed mass spectrum of the correctly reconstructed D^0 decays. The ratio between the two normalizations is found to be $N_{wc}/N_{cc} = 0.874$.

It should be noted that by coupling the functions for signal and wrong charge background data points outside the signal peak also contribute to the signal extraction. The combinatorial background in the mass spectrum is described in the fit model with an exponential function. The small exponential contribution seen in the fit to the spectrum with the wrong mass assignments is absorbed in this background function.

The fit model is tested with the spectrum of all D^0 candidates found in the simulated sample as shown in 5.15b. The extracted number of signal events is consistent with the fit result obtained with the correctly reconstructed decays alone within 2%. The untagged D^0 signal in data is shown in figure 7.6.

5.3.3 D_s^+ mesons

The D_s^+ is reconstructed in the decay chain $D_s^+ \to \Phi\pi^+$ with a subsequent $\Phi \to K^+K^-$ decay. The mass of the kaon pair is required to be within ± 11 MeV/c^2 of the nominal Φ

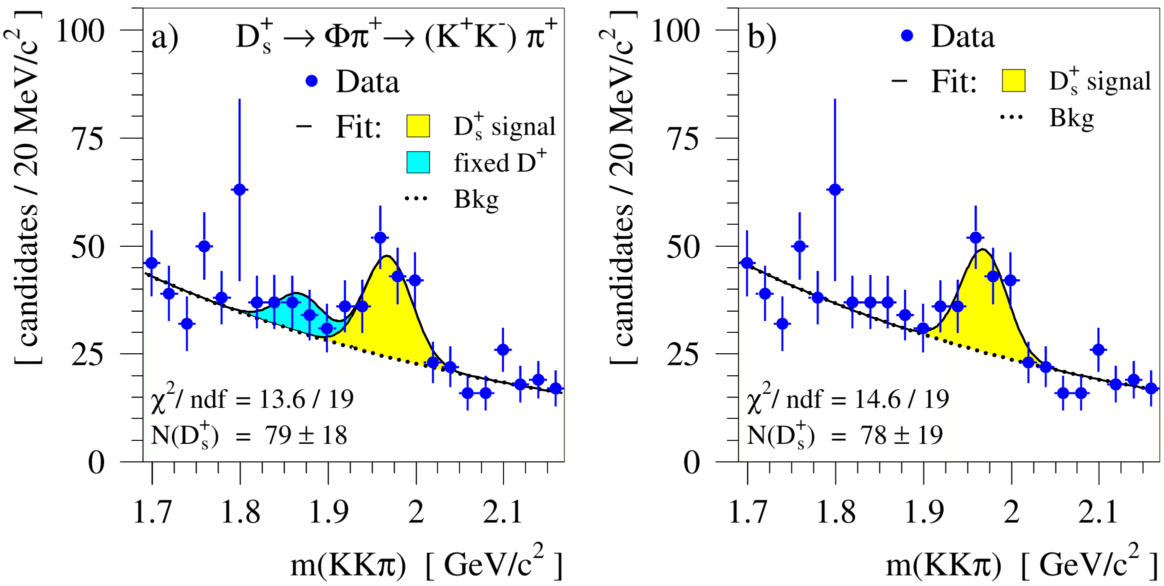

Figure 5.16: *The D_s^+ signal is extracted from the $m(KK\pi)$ spectrum (a) with and (b) without consideration of the signal from D^+ mesons decaying in the same channel. The fit model (a) uses $N(D^+) : N(D_s^+) = 0.38$ as expected from simulated decays, a fixed mass difference $m(D_s^+) - m(D^+) = 99.2$ MeV/c [17] and the two signal Gaussians are assumed to have the same width.*

mass which accounts for two standard deviations of the fitted Φ mass peak. As already discussed in chapter 1 a cut on the helicity angle[7], motivated by the P-wave nature of the Φ decay, is used to reduce the combinatorial background. The latter is described in the fit model with an exponential function.

D^+ mesons decay in the same channel but with a six times smaller branching ratio. On the other hand, strangeness is suppressed in the fragmentation process. In addition the D^+ to D_s^+ ratio is enlarged by the tagging due to the larger D^+ lifetime. The expected ratio in the mass spectrum used for the cross section measurement is estimated with simulated charm and beauty decays to be $N(D^+) : N(D_s^+) = 0.38$. The fit model used for the D_s^+ signal extraction neglects the D^+ signal, because its statistical significance is low as can be seen in figure 5.16: the numbers of D_s^+ decays extracted with and without consideration of the D^+ signal are well compatible.

5.3.4 D^{*+} mesons

D^{*+} mesons are reconstructed in the decay mode $D^{*+} \to D^0\pi^+ \to (K^-\pi^+)\pi^+$ and the same mass association as in the D^+ channel is made. The phase space for the $D^{*+} \to D^0\pi^+$ decay is very limited, because the D^{*+} mass is only slightly higher than the sum of the D^0 and the pion mass. Consequences of this small mass difference are an inherently low

[7]The helicity angle θ_H is defined as the angle between the kaon and pion momenta in the Φ rest frame.

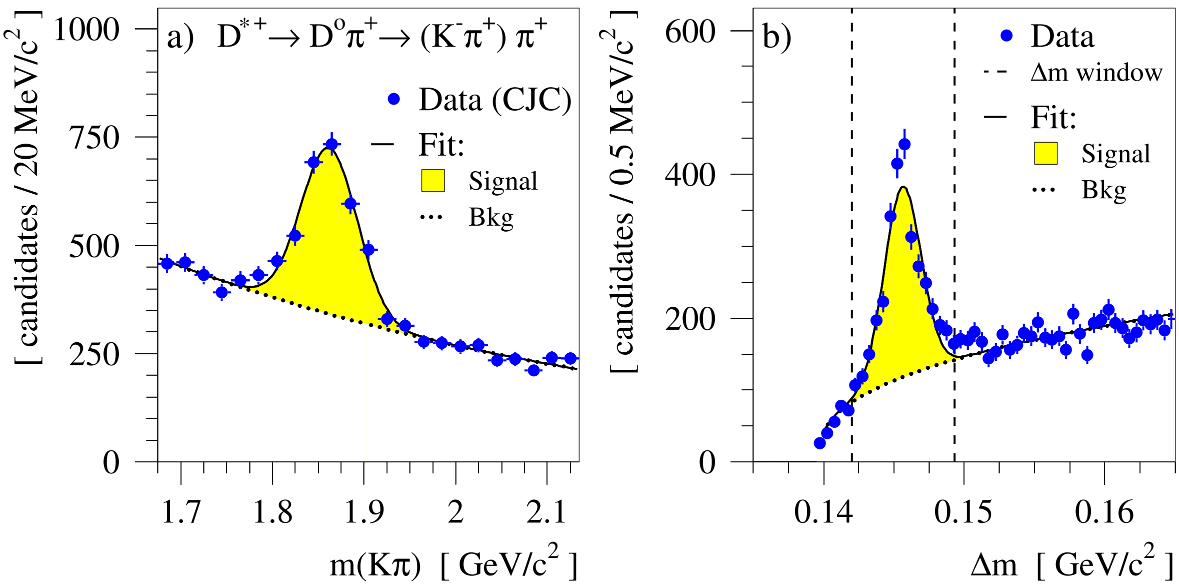

Figure 5.17: *(a) The $m(K\pi)$ spectrum of D^{*+} candidates reconstructed with the CJC (dots) is shown with a 3-σ cut in Δm indicated by the dashed lines in (b) the Δm spectrum. In the $m(K\pi)$ spectrum the fit (solid line) describes the signal (shaded) and background shapes (dotted line) very well, while the fitted Gaussian describes only poorly the Δm signal shape.*

background in this channel and a rather small momentum of the pion which is called for this reason the slow pion π_s.

In the Δm-tagging technique [52] the mass difference $\Delta m = m(K\pi\pi_s) - m(K\pi)$ is reconstructed, because several measurement errors cancel: The resolution achieved in Δm is about 20 times better than in the D-meson masses.

In figure 5.17 the mass spectra of D^{*+} candidates reconstructed with the CJC are shown. The Δm signal is apparently not well described by a Gaussian function. Therefore the $m(K\pi)$ spectrum is used for the signal extraction with a Gaussian for the signal and an exponential function to model the combinatorial background. The candidates are requested to have a Δm within 3.6 MeV/c^2 window ($\pm 3\sigma$) around the nominal value $m_{D^{*+}} - m_{D^0} = 145.44 \pm 0.02$ MeV/c^2 [17].

D^0 mesons produced in the D^{*+} channel are a subset of the inclusive D^0 sample. To distinguish them D^0 mesons with Δm-tag are called henceforth “tagged D^0”.

5.3.5 Systematic errors

Impurities in the decay particle's momentum measurement can lead to a systematically wrong reconstruction of the D-meson mass which is not covered by the Gaussian shape used to describe the signals and therefore such events are lost for the signal extraction. A main source of such impurities is the CST hit linking. The efficiency of the mass reconstruction ε_m is determined with the detector simulation. Thereto the signal is extracted with a Gaussian fitted to the reconstructed mass spectrum and the result is compared to the number of simulated D-meson decays.

The efficiencies found for the different decay channels are given in table 5.9 and are about $\varepsilon_m \approx 96\%$. The systematic error of the method is determined by varying the D-meson sample used for the estimation. In addition the events within two standard deviations of the fitted Gaussian are counted and the result is compared to the number of simulated decays times 0.954 as expected for a Gaussian mass resolution. The maximal variation is of the order of one percent and is included in the systematic error.

To estimate the systematic error arising from fixing the wrong charge background in the untagged $D^0 \to K^-\pi^+$ channel, the fraction N_{wc}/N_{cc} used in the fit model is varied from 0.83 to 0.92 ($\pm 5\%$) and the relative differences in the extracted signal numbers are included in the experimental error.

The mass resolution in the Δm spectrum of D^{*+} candidates is not well described by a Gaussian function. Still it provides the possibility to verify the signal extraction in the $m(K\pi)$ spectrum. Therefore the excess above the fitted background is counted in a ± 3.6 MeV/c^2 window around the nominal Δm value. The number of signal events is found to be 10% larger than in the fit to the $m(K\pi)$ spectrum. This relative difference is added to the positive systematic error.

For D^{*+} candidates reconstructed by means of the CST the Δm signal is far better described by a Gaussian (cf. fig. 7.1) and the results of the fits to the two spectra and the counting method are in very good agreement. Therefore no additional contribution to the systematic error is made.

In case of D-meson differential distributions, the inclusive data sample is divided into bins and the number of signal events is extracted in each bin separately. To determine the signals used for the cross sections' central values the position and width of the Gaussian signal shape are fixed to the values found in the inclusive sample. The normalizations of the signal and the background are left as free parameters in the various fits.

Other methods of determining the number of candidates have also been applied and its maximal variation enter into the systematic error: Possible uncertainties due to assumptions on the background shapes have been estimated by changing the background shape in the fits to the inclusive and differential spectra from linear to exponential and vice versa. In addition the differential signals are extracted with free position and width parameters of the signal Gaussian and by fixing only one of them to the value of the inclusive spectrum.

Contributions to the signals due to other charm decays (so called reflections) are estimated from Monte Carlo simulations to be at most 3% [60], and are included in the systematic errors.

5.4 D-meson selection

In the following the selection of D-meson decays in the different channels is discussed. For the cross section measurements the number of decays in the visible range has to be determined from the number of reconstructed D-mesons. This is done with the help of D-meson decays simulated with the leading-order Monte Carlo program `AROMA`. The definitions of acceptance, efficiency and purity have been introduced in chapter 3.

The kinematical acceptance A_{kine} denotes the fraction of events which satisfy the requirements posed on the decay particles' momenta with respect to number produced in the visible range which is defined by the D-meson and event kinematics. The geometrical acceptance A_{geo} is derived from the layout of the detector and the generated momenta. The efficiency and purity of the detector and the reconstruction depends on the track quality requirements. It is determined with a detailed detector simulation. The efficiency of the lifetime tag is discussed separately in the next chapter.

5.4.1 Kinematical acceptance A_{kine}

Heavy flavor production in ep scattering is a threshold process, i.e. D-mesons are produced predominantly with small momenta. Their momentum spectrum dictates also the momentum distributions of their decay particles. Nevertheless there are the following arguments against very weak kinematical requirements which would maximize the size of the observed signals:

- The particles produced in ep scattering have a rather steeply falling momentum spectrum. The high multiplicity at low momenta causes a very high combinatorial background. Thus the signal over background ratio improves by requiring high momenta of the decay products. In figure 5.18a the kaon transverse momentum spectra in untagged D^0 decays is shown as an example: at small kaon momenta it is dominated by background events, because its distribution in selected D^0 decays is significantly harder.
- The track resolution and therefore also the accuracy of the vertex reconstruction depends strongly on the momentum, because flight directions measured inside the CST are distorted by multiple scattering in the beam pipe and the first CST silicon layer (cf fig. 5.7 and sec. 6.1).
- Multiple scattering in the material between the CJC and the CST affects the performance of the CST hit linking, because the CJC prediction of the particle's impact point in the CST becomes less accurate at low momenta.

Therefore rather high transverse momenta of the D-meson's decay particles are selected. In table 5.3 the requirements posed on the decay kinematics in the different channels are summarized.

These requirements indirectly select high $p_t(D)$ D-mesons as can be seen in figure 5.19, where the acceptance found in simulated D^+ decays is shown as a function of the major kinematical variables. The strong dependence on $p_t(D)$ motivates the rather high cut of $p_t(D) > 2.5$ GeV/c made in the visible range definition, because at lower D-meson momenta the necessary extrapolation from the observed to the number of D-mesons

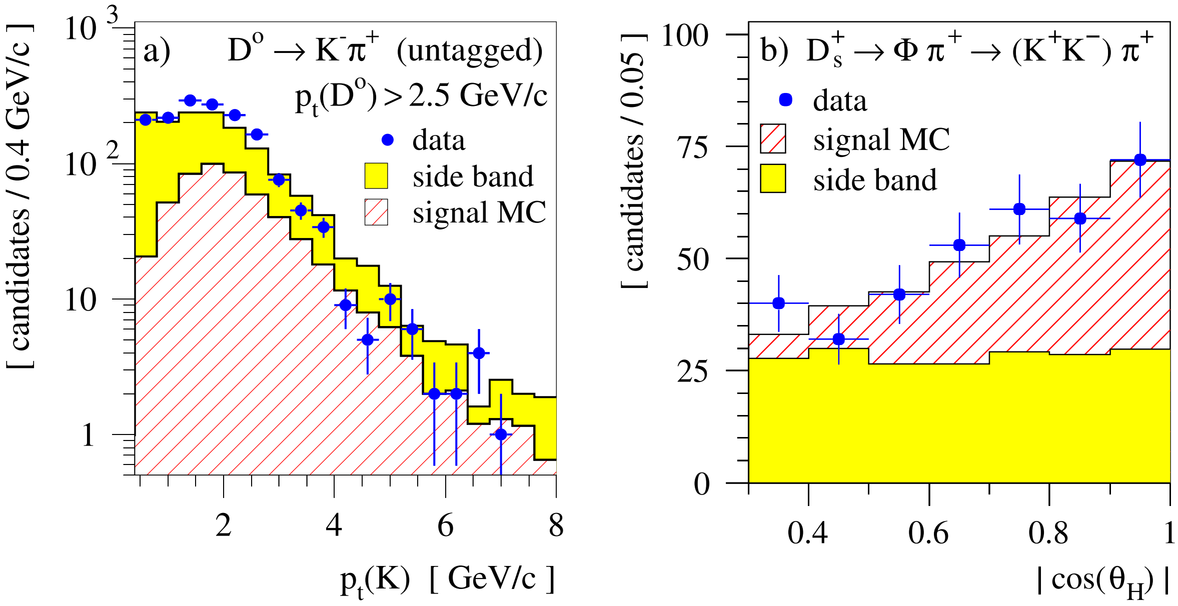

Figure 5.18: *(a) The spectrum of the kaon transverse momentum $p_t(K)$ in untagged D^0 decays and (b) the distribution of the helicity angel's cosine in D_s^+ decays are shown for candidates in the signal region of the mass spectra (dots). The shape of the distributions in these variables differ for signal and background events which can be seen from the fit to the data with the shapes of simulated D-meson decays (hatched) and of events from the side bands of the mass spectrum (shaded). The free parameters in the fit are the normalizations of the two distributions only.*

produced in the visible range becomes large and therefore a reliable measurement is hardly possible.

The minimal requirement on the maximal transverse momentum $\max(p_t)$ of the decay particles used to build the D-meson candidate is motivated by the DCRPhi trigger condition for a high momentum particle. Because of the high $p_t(D)$ of the selected D-meson candidates the requirement is implicitly fulfilled and does not represent an actual cut.

The range of the polar angle θ required for all decay products is motivated by the geometrical acceptance of the CJC and CST detectors and ensures a reliable track reconstruction. In addition the thickness of the material in a particle's flight path is inversely proportional to $\sin(\theta)$ and therefore the distortion by multiple scattering becomes large for particles in the excluded θ range.

The distribution of the helicity angle's cosine $\cos(\theta_H)$ in the D_s^+ channel has a parabolic shape due to the P-wave nature of the Φ decay (see chap. 1). The distribution is flat for the combinatorial background, where the spin argument is not valid. The helicity distribution found for D_s^+ candidates within the signal region of the $m(KK\pi)$ spectrum is shown in figure 5.18b. Its decomposition into signal and background distributions will be discussed in more detail in the section 6.3.

The parabolic shape leads to a high acceptance of the applied $|\cos(\theta_H)| \geq 0.4$ requirement. It can be estimated with 93.6 %, while about 40 % of the combinatorial background is rejected. Therefore the signal over background ratio improves approximately by a factor 1.6.

Selected decay kinematics			D^+	D^0	D_s^+	D^{*+}
$p_t(D)$	[GeV/c]	$\geq$	2.5			
$\|\eta(D)\|$		$\leq$	1.5			
$p_t(K)$	[MeV/c]	$\geq$	500	800	400	250
$p_t(\pi)$	[MeV/c]	$\geq$	400	800	400	250
$p_t(\pi_s)$	[MeV/c]	$\geq$	-	-	-	140
$\max(p_t)$	[MeV/c]	$\geq$	800			
$\theta(K/\pi)$	[^{o}]	ϵ	[20, 160]			
$\|\cos(\theta_H)\|$		$\geq$	-	-	0.4	-

Table 5.3: *The table sums the selection criteria applied on the D-meson decay kinematics for the different channels. For completeness sake also the definition of the visible range concerning $p_t(D)$ and $\eta(D)$ is added.*

The kinematical acceptances found with D-meson decays simulated with the leading order QCD program AROMA are listed in the summary table 5.4. The systematic error of this method depends mainly on the reliability of the simulated momentum spectra. It is estimated by varying the model parameters entering the QCD calculations as discussed in section 1.5. The errors are found to be less than 2% in all decay channels.

5.4.2 Geometrical acceptance

The geometrical acceptance A_{geo} is determined with these simulated D-meson decays and the constants describing the detector layout. Thereto the decay particle's generated momentum at its production point is used to estimate the particle's flight trajectory. The position and size of the interaction region has been simulated according to the distributions observed in the analyzed data set.

The flight path of the high energetic positron from the interaction point to the SpaCal is approximated with a straight line. The trajectories of the D-meson decay particles in a homogeneous magnetic field along the z-axis with strength $B = 1.16$ T are modeled by helices.

The acceptance of the SpaCal A_{SPC} is determined by requiring the quality criteria in the energy $E_{e'}$, the polar angle $\theta_{e'}$ and the radial position R_{cog} of the scattered positron as listed in table 4.6.

For the CJC acceptance A_{CJC} the radius at which the particle exits the sensitive CJC volume either in z or in the radial direction is calculated (cf. tab. 5.5). The measurable track length in the sensitive volume is derived from the radius of the first sense wire and this exit point. D-mesons within the CJC acceptance are required to have decay particles with a measurable track length which satisfies the track length criteria of the track selection ($L_{CJC} \geq 15$ cm, cf. next section).

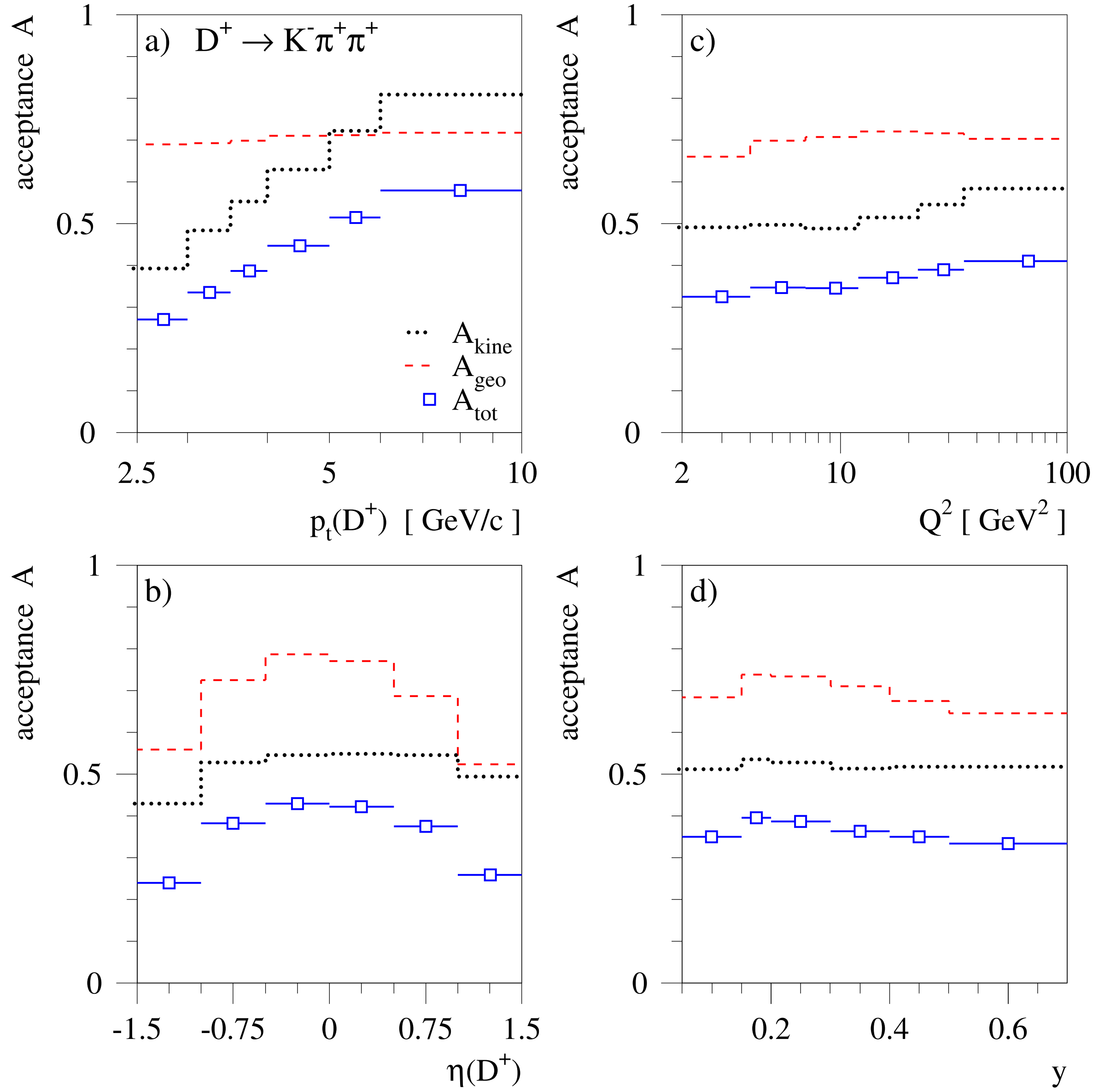

Figure 5.19: *The kinematical, geometrical and total acceptance found with D^+ decays simulated with the* `AROMA` *program (cf. sec. 1.5) is shown as a function of the major kinematical D-meson and event variables: (a) the transverse momentum $p_t(D^+)$, (b) the pseudo rapidity $\eta(D^+)$, (c) the events squared momentum transfer Q^2 and (d) the lepton's inelasticity y.*

Acceptances [%]	D^+	D^0	D_s^+	D^{*+}
A_{kine}	51.9	58.2	71.1	83.1
A_{SPC}	97.7	97.7	97.6	97.6
A_{CJC}	99.6	99.7	99.8	99.6
A_{CST}	71.9	77.2	71.1	76.5
A_{geo}	70.0	75.1	69.3	74.4
$A = A_{kine} \cdot A_{geo}$	36.4	43.8	49.2	61.9
Model dependences	+0.8	+1.2	+1.7	+0.4
$\Delta A/A$ [%]	−0.8	−0.7	−1.7	−0.6

Table 5.4: *The kinematic and geometrical acceptances are determined with D-meson decays simulated with the* `AROMA` *program. They depend on the simulated spectra of the D-mesons. Thus their systematic uncertainties have been determined by varying the model parameters of the QCD calculation program as described in section 1.5.*

The CST acceptance A_{CST} is determined according to ideal detector geometry. The intersection points of the particles with the CST layers are calculated, where the two silicon layers are approximated with concentric cylinders. The crossings with these cylinders are then required to be within the active area of the sensors. Because the detector covers the whole ϕ range, it is sufficient to determine the z-position of the crossing. An active length of the sensor in z of $640 \cdot 88\mu m = 5.632\,cm$ is used and the z-gaps of $0.298\,cm$ between the sensors are considered (cf. app. F).

The number of crossing within the sensitive area is asked to be at least equal to the number of CST hits required per D-meson candidate, i.e. 3 out of 4 possible layer crossings of the two decay particles in D^0 and 5 out of 6 possible of the three decay particles in D^+ and

Nominal CJC sense wire positions		CJC1	CJC2
number of cells N_{cells}		30	60
number of sense wires per cell N_{wires}		24	32
innermost sense wire:	radius R_{in}	21.83 cm	54.48 cm
	azimuth ϕ_{in}	22.90^o	13.92^o
outermost sense wire:	radius R_{out}	42.58 cm	82.32 cm
	azimuth ϕ_{out}	2.59^o	1.29^o
active z range of the chamber		[−112.5 cm, 107.5 cm]	

Table 5.5: *The nominal positions of the inner- and outermost wires in the planes of equidistant sense wires are quoted for the first cells in the inner (CJC1) and outer rings (CJC2) of the Central Jet Chamber. The positions of the sense wires in the (i+1)-th cell are obtained by adding $i \cdot 360^o/N_{cells}$ to the azimuthal angles and leaving the radii unchanged. In addition the active z range of the chamber is given.*

D_s^+ decays (cf. next section). An exception is the slow pion in D^{*+} decays for which no crossing is required.

Especially the CST acceptance leads to a strong dependency of the total acceptance on the pseudo rapidity $\eta(D)$ of the D-meson as can be seen on the example of D-meson decays in figure 5.19b. The geometrical acceptances used for the inclusive cross section measured by the means of the CST are quoted in table 5.4.

The D^{*+} measurement done without any CST information is performed within a similar acceptance to be comparable to the measurement by means of the CST. Therefore the D^0 decay tracks are requested to be within the acceptance of both CST layers, but the z-gaps are not considered. The geometrical CST acceptance for this requirement is found to be $A_{CST} = 0.659$ instead of the value 0.765 quoted in table 5.4.

5.4.3 Detector efficiency and purity

In the following the selection criteria posed on the reconstructed CJC and CST tracks are given. The efficiencies and purities used for the cross section measurements have been determined with simulated events. The methods by which the simulation is adjusted to describe the data are discussed. In table 5.9 at the end of the section the results found for the different decay channels are listed.

CJC track quality and efficiency

The CJC track quality criteria for forming D-meson resonances are summarized in table 5.6: The requirement on the z-position of the CJC primary vertex z_{pv} and the selected θ range is motivated by the geometrical CST acceptance. The condition imposed on the measured track length L_{CJC} rejects short track segments for which a precise momentum measurement (cf. sec. 5.1.1) and a reliable CST linking is not possible.

Decay products of long living particles like K^0 and Λ^0 are rejected by the loose cut on the impact parameter d of the non-vertex fitted CJC track. A reasonable quality of the CJC z-measurement is ensured by the requirement posed on the z_0 parameter of the non-vertex fitted track. These criteria are applied only for particles which are used to determine the

CJC track quality criteria			
primary vertex position	$\|z_{pv}\|$	$\leq$	20 cm
track length	L_{CJC}	$\geq$	15 cm
polar angle	θ	ϵ	[20^o, 160^o]
impact parameter †	$\|d\|$	$\leq$	2 cm
z-measurement †	$\|z_0 - z_{pv}\|$	$\leq$	20 cm

Table 5.6: *The CJC track quality requirements are summarized.* † *The requirements on the impact parameter and the z-measurement are not applied on π_s candidates.*

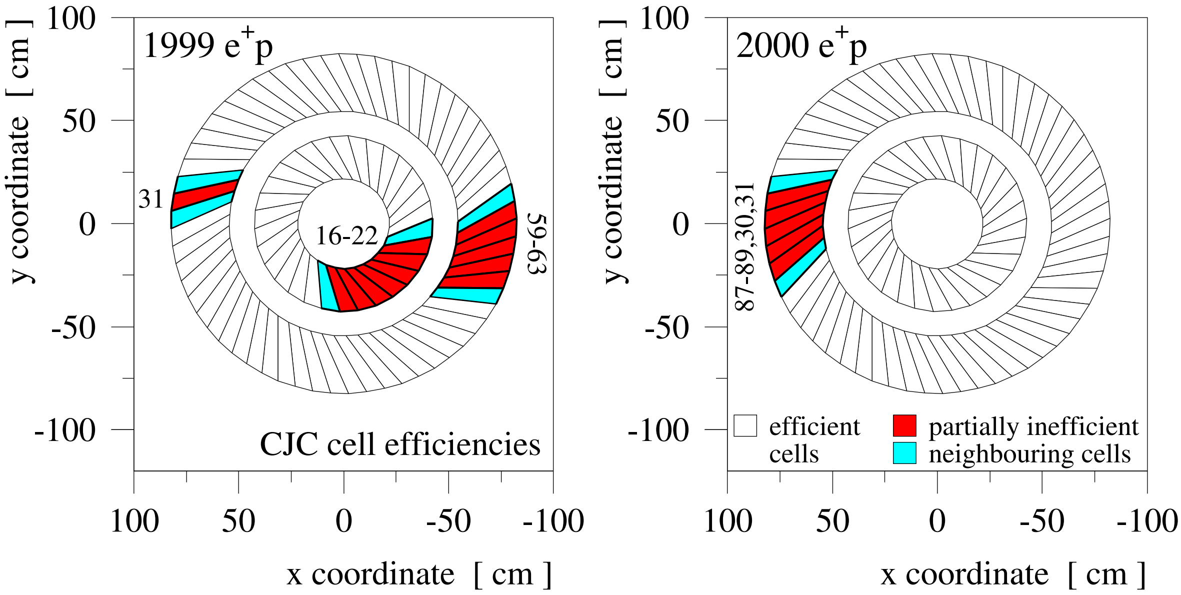

cell number(s)	chamber ring	run range of inefficiency	data taking period
16-22	CJC1	[257637, 262144]	1999 e^+p
30	CJC2	[265173, 279215]	2000 e^+p
31	CJC2	[249102, 262144] [263235, 279215]	1999 e^+p 2000 e^+p
59-63	CJC2	[255407, 262144]	1999 e^+p
87-89	CJC2	[265173, 279215]	2000 e^+p

Table 5.7: *CJC cells operated at reduced or zero voltage in the analyzed data set and the affected run ranges are listed. The cell positions are indicated by the dark shaded areas in the figure above. In addition the neighboring cells are marked in a brighter shading. Tracks passing these cells are discarded in the analysis.*

secondary vertex position, i.e. they are not requested from the slow pion π_s candidates in D^{*+} decays.

The track efficiency depends on the efficiency of the detector and the performance of the reconstruction. The former is measured on a hit basis with long tracks defined by many CJC hits. Inefficient wires along the flight path can be identified, because they produce no detectable signal charge. The measured wire efficiencies are then implemented into the detector simulation which is also used herein to determine the efficiency of the CJC track reconstruction.

In the analyzed data period some CJC cells were disconnected from high voltage or were operated at lower voltages due to broken wires. Such high voltage settings also distort the drift fields in the neighboring cells. Therefore the track efficiency of a whole region is affected by such operational conditions. The inefficient CJC cells and the run ranges concerned are listed in table 5.7 and the cell positions are indicated. Due to the large

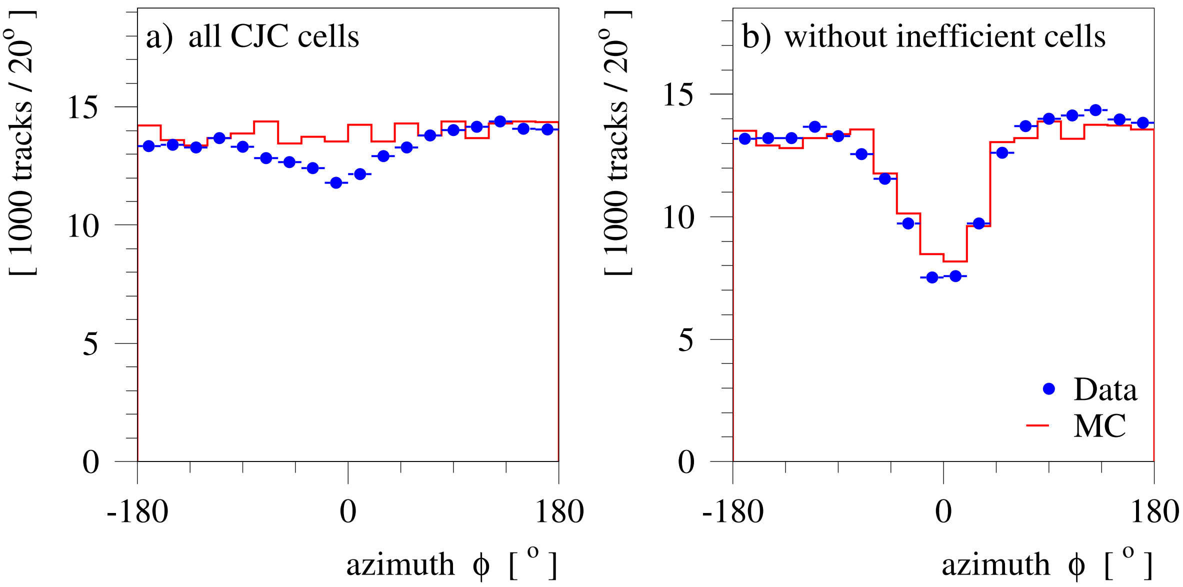

Figure 5.20: *The azimuthal spectra of selected CJC tracks is shown for data (dots) and simulated events (histograms) in all CJC cells (a) and after rejecting tracks traversing inefficient CJC cells (b). The Monte Carlo histograms are normalized to the highest data bin in (a) and to the integral of the data in (b).*

number of inefficient cells at the end of the 1999 data taking period, the run range between 257637 to 262144 is excluded (cf. chap. 4).

Even though the measured wire efficiencies take these operation conditions into account, the detector simulation does not accurately describe their effect on the track efficiency. This can be seen in the azimuthal distributions of selected CJC tracks shown in figure 5.20a, where the simulation fails to describe the data.

To minimize the discrepancy between data and simulation tracks which traverse an inefficient CJC cell are not considered in the formation of D-meson candidates. This includes also cells adjacent to cells operated at reduced or zero voltage. Thereto the positions of 20 equidistant reference points on the measured track are calculated. If one of them is within the volume of an inefficient cell, the track is discarded. The cell borders, in the middle between two sense wire planes, are determined from the constants quoted in table 5.5.

In figure 5.20b the azimuthal track distribution is shown after rejecting tracks in CJC cells with lower efficiency. The simulation describes the spectrum seen in data rather well. The requirement discards about 8% of the selected tracks. The most significant signal loss is observed in the D^{*+} channel due to the strongly bent track of the slow pion: the extracted signals are reduced by 14% in data and by 20% in simulated D-meson decays. The resulting CJC D-meson efficiencies and purities for the different decay channels can be found in table 5.9.

Methods to measure the CJC track efficiency for high momentum particles in data can be found in [61, 62]. A measurement concerning the efficiency for low momentum tracks, which is more relevant for the D-meson reconstruction, is discussed in [63]. No such measurement was performed for the analyzed data set which is the reason for the large systematic error of $^{+1}_{-5}\,\%$ per track assigned to the CJC efficiency. The asymmetry of the error reflects the tendency of the simulation to overestimate the track efficiency.

CST efficiency

The CST information is essential for the precise reconstruction of the D-meson decay vertex. The efficiency of this vertex reconstruction depends on the CST detector efficiency and the performances of the hit finding algorithm, the CST space point linking, the CJC-CST track fit and the vertex fit. Thus not only detector properties like signal-to-noise ratio or dead read-out channels are relevant, but also the momentum and angular distributions and the particle composition of the sample influence the efficiency. Due to these complicated dependences the efficiency is determined with simulated events which are expected to have the same composition as the signals in data.

The CST signal-to-noise ratio is measured in data [1] and the simulation is adjusted accordingly. There are several methods to measure the CST hit efficiency, e.g. with cosmic muons as discussed in [1] or with well measured CJC tracks which can be used to predict the positions of particle crossings in the CST.

Herein the simulated CST hit efficiency is calibrated with the CST D^0 efficiency $\varepsilon_{CST}(D^0)$ which is measured with a tagged D^0 sample reconstructed by means of the CJC alone. $\varepsilon_{CST}(D)$ is defined as the fraction of D-meson decays reconstructed with the CJC inside the CST acceptance which have a minimal number of associated CST hits and for which a reasonable result of the `VFit2dc` fit could be obtained. This efficiency includes all relevant effects and the measurement is done by construction with the correct sample composition.

In table 5.8 the CST hit requirements are listed for the different decay channels: one track with only one associated CST hit is allowed per D-meson candidate, while the other decay particles are requested to have two linked hits. Including candidates, where one decay particle traverses the active area of just one CST layer, enlarges the number of decays within the CST acceptance by 40% (D^0) to 50% (D^+/D_s^+).

D-meson decay channel	required CST hits per track	required CST hits per candidate	mean number of linked CST hits
$D^+ \to K^-\pi^+\pi^+$	1	5	5.6
$D^0 \to K^-\pi^+$	1	3	3.6
$D_s^+ \to K^+K^-\pi^+$	1	5	5.4

Table 5.8: *The table lists the number of linked CST hits per decay track and per D-meson candidate required in the reconstruction of the D-meson's decay vertex and it quotes the mean number of linked CST hits found in the data samples of the different decays channels.*

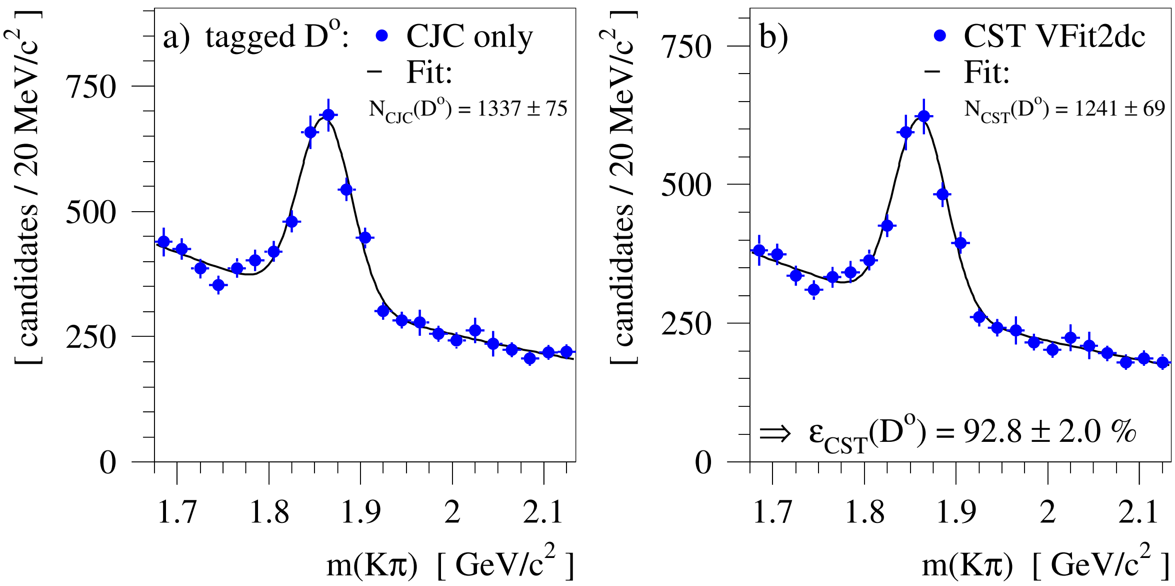

Figure 5.21: *(a) The mass spectrum of tagged D^0 candidates within the acceptance of both CST layers is reconstructed by the means of the CJC alone. (b) Only the candidates with at least three linked CST hits and a convergent* `VFit2dc` *vertex fit ($\chi^2 < 100$) are shown. The CST D^0 efficiency is determined from the fit results (solid lines) with $\varepsilon_{CST}(D^0) = 92.8 \pm 2.0\%$.*

Also the total D-meson efficiency is enhanced significantly: To estimate the signal gain the dependence of the D-meson efficiency on the CST hit efficiency ε_{hit} can be written as

$$\varepsilon_{CST}(D) \;\propto\; \varepsilon_{hit}^{N} + N \cdot \varepsilon_{hit}^{N-1} \cdot (1 - \varepsilon_{hit}), \tag{5.13}$$

where the first term gives the fraction of decays with all N possible CST hits detected and the second term denotes the probability to miss one of them. From the measured D^0 efficiency an enhancement by a factor of 1.5 in two body decays and even by a factor of 1.8 in three body decays is expected.

The mean numbers of linked CST hits found in the data sample of the different decay channels are listed in table 5.8. As a trade off for the signal gain the missing CST information in 40-60% of the candidates results in a decay length resolution which is by 20-30% worse than for candidates with at least two linked CST hits per track.

The CST D^0 efficiency is measured with the signal shown in figure 5.21a. The sample is reconstructed with the CJC alone. The D^0 decay particles are ensured to be inside the acceptance of both CST layers by requiring the CJC track crossings to be within the active CST length by three units of the extrapolation error. The spectrum in figure 5.21b contains only candidates with at least three CST hits associated to the kaon and pion tracks and for which the vertex fit `VFit2dc` converged with $\chi^2 < 100$. The CST efficiency is determined from the extracted signal numbers to be $\varepsilon_{CST}(D^0) = 92.8 \pm 2.0\%$.

To reproduce $\varepsilon_{CST}(D^0)$ in the simulation, 3.7% of the all reconstructed CST p-side hits are discarded at random, where the method does not differentiates between signal and

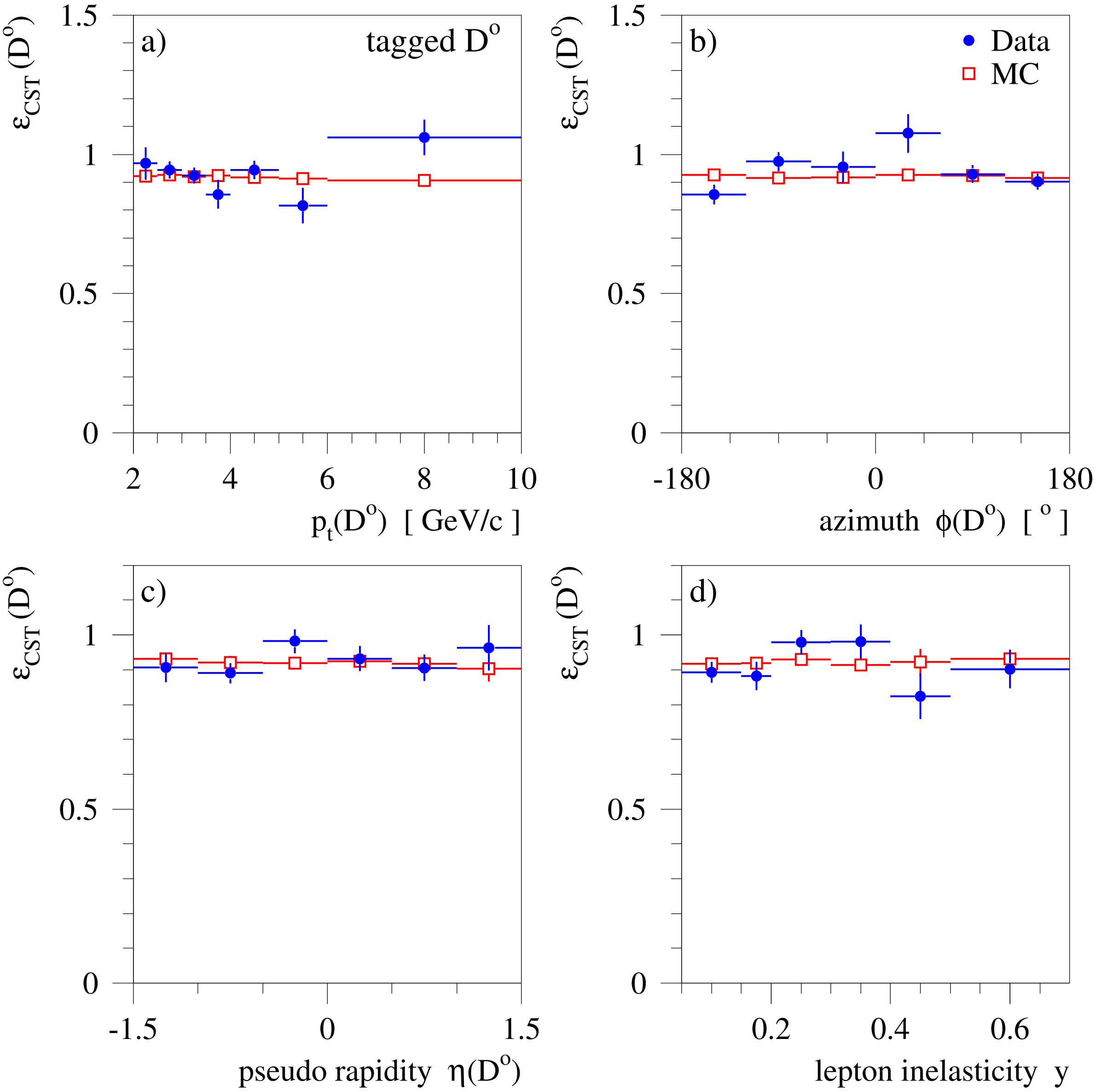

Figure 5.22: *The dependences of the CST D^0-meson efficiency are measured by dividing the samples shown in figure 5.21 into bins of (a) the transverse momentum $p_t(D^0)$, (b) the azimuthal angle $\phi(D^0)$ and (c) the pseudo rapidity $\eta(D^0)$ of the D^0-meson. In addition its dependence on the event kinematics is shown on the example of the lepton inelasticity y (d). Signal efficiencies larger than one are possible, because they are determined with independent fits to the mass spectra with and without CST hit requirements (see also app. E).*

Efficiency/purity [%]	D^+	D^0	D_s^+	D^{*+}
ε_{CJC}	68.0	76.3	66.0	66.6
ε_{SPC}	93.9	93.8	94.1	93.7
ε_{CST}	91.1	94.7	88.7	94.8
ε_{link}	90.5	95.9	91.3	96.0
ε_{det}	52.7	65.0	50.3	56.7
p_{CJC}	97.9	97.3	98.0	98.3
p_{SPC}	96.0	96.1	96.0	95.7
p_{link}	99.0	99.2	98.8	99.2
p_{det}	93.0	92.7	92.9	93.2
ε_{ST}	92.7	91.5	93.7	91.7
ε_m	96.8	95.4	96.1	93.4
$(\varepsilon/p)_{tot}$	50.8	61.2	48.8	52.1

Table 5.9: *The detector efficiencies and purities found with simulated D-meson decays are summarized for the different channels.*

noise hits. About half of these inefficiencies are explained by dead read-out channels which have not been simulated, losses in the read-out and reconstruction chain account for the rest. Simultaneously additional noise hits are invented to leave the CST occupancy unchanged. The rejection and invention of hits is done independently of each other to avoid unwanted correlation effects.

In addition to the inclusive measurement of $\varepsilon_{CST}(D^0)$ its dependences on the most important variables describing the D-meson and event kinematics are measured and compared to the results found in simulated decays. As can be seen from the examples given in figure 5.22 $\varepsilon_{CST}(D^0)$ is fairly constant in the studied observables and within the statistical uncertainties of the measurements well reproduced by the simulation.

The CST D-meson efficiency used for the cross section measurement is determined with simulated decays. Thereto it is further divided into the simulated CST hit efficiency ε_{CST} and into the efficiency ε_{link} and purity p_{link} of the CST hit linking:

$$\varepsilon_{CST}(D) = N_r/N_a = N_s/N_a \cdot \frac{N_{s+r}/N_s}{N_{s+r}/N_r} = \varepsilon_{CST} \cdot \frac{\varepsilon_{link}}{p_{link}} , \tag{5.14}$$

where N_a denotes the number of simulated decays inside the CST acceptance, N_s the number for which the required number of CST signal hits have been simulated and N_r the number for which the linking associated the required number of reconstructed CST hits. N_{s+r} stands for the number of decays which meet the hit condition on the simulation and reconstruction level.

The results for the different channels are summarized in table 5.9. Because the D^{*+} channel is used to calibrate the simulation, the D^{*+} cross section measured by means of the CST is not completely independent of the measurement based on the CJC alone.

A systematic error of 1% per CST hit is estimated from the uncertainty in the measured D^0 efficiency[8]. In the experimental error of the cross section measurements it is multiplied with the mean number of linked CST hits per D-meson candidate (cf. tab. 5.8).

[8]The calculation of the error on the signal efficiency is discussed in appendix E.

Chapter 6

Lifetime Tagging

The developed lifetime tagging method is crucial for the measurement of the D-meson production cross sections, because it enhances the signal qualities substantially. After having discussed the reconstruction algorithms in the previous chapter, the focus lies in the following on the properties of the lifetime tag itself.

At first a simplified model of $D^0 \to K^-\pi^+$ decays is presented which considers besides the measured impact parameter resolution also the topology of the D-meson decay to determine the decay length resolution. Its results allow insights into general properties of lifetime tagging in exclusive heavy flavor decays, especially concerning the dependence of the tag on the D-meson's momentum.

Thereafter the variables used in the lifetime tag are discussed and the selection criteria applied in the different D-meson channels are given which allow a clear signal identification and a reliable signal extraction also in channels previously not accessible at HERA.

The efficiency of these selection criteria are determined with simulated D-meson decays. This method is reliable only, if the simulation describes the decay length resolution function accurately. Two methods by which the high quality of the simulation is proven are discussed in section 6.3. The excellent level of agreement between data and simulation is one of the major achievements of this thesis.

After having proven the simulation's quality the lifetime tagging efficiencies found by the simulation are discussed. A focus lies on D-mesons produced in cascade decays of beauty quarks which have distinctively different properties concerning the lifetime tag, because their decay length is enhanced due to the long lifetimes of the B-mesons.

At the end of the chapter a method to estimate the systematic error is discussed.

6.1 $D^0 \to K^-\pi^+$ decay model

In section 5.1.2 the measurement of the p_t dependence of the impact parameter resolution has been discussed. This measurement is used in the following to study the influence of the decay topology and of multiple scattering (MS) on the decay length resolution with a simplified model of $D^0 \to K^-\pi^+$ decays.

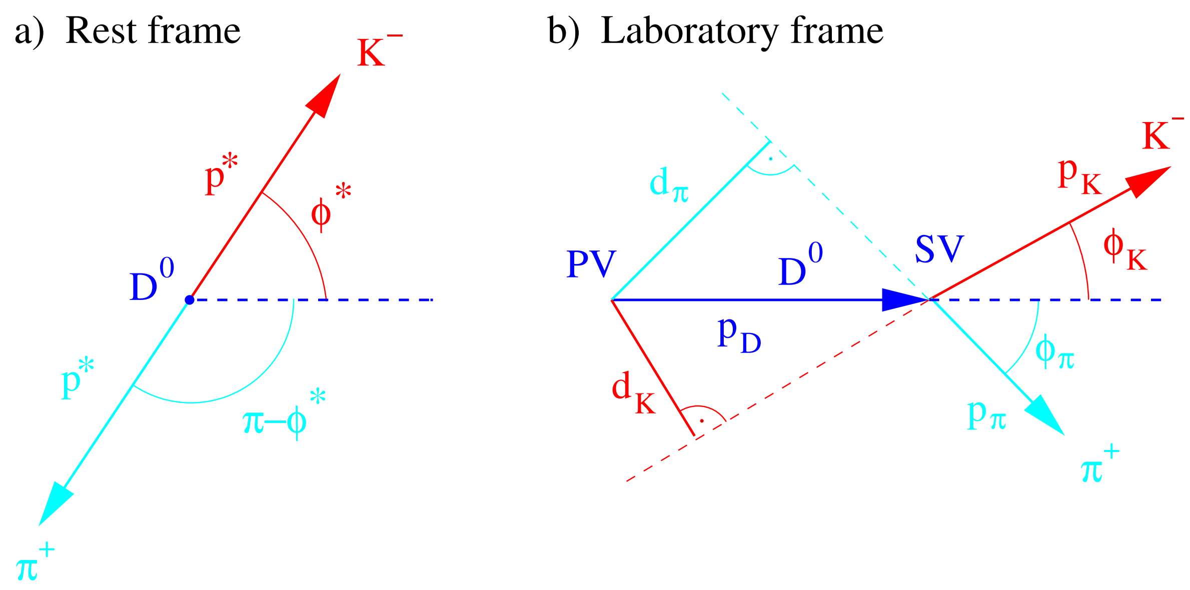

Figure 6.1: *The momenta and angles in $D^0 \to K^-\pi^+$ are schematically drawn (a) in the D^0 rest frame and (b) in the laboratory frame (see text). The D-meson's production (PV) and decay points (SV) are indicated to define the decay particles' impact parameters d_K and d_π.*

6.1.1 Model description

The aim of the model is to estimate the mean decay length error $\langle\sigma_l\rangle$ and the mean decay length significance $\langle S_l\rangle$ as a function of the D^0 momentum p_D. The idea is to simulate a large number of different decay topologies at a fixed p_D and average the values of the decay length error calculated for the specific topology with the measured impact parameter resolution. The functional dependence is then obtained by varying the p_D value.

A representative sample of decay topologies is most easily simulated in the rest frame of the D^0, because in this system the decay is isotropic and the decay particles are back-to-back with a total momentum p^* depending on the involved masses alone [17]:

$$p^* = \frac{\sqrt{(m_D^2 - (m_K + m_\pi)^2) \cdot (m_D^2 - (m_K - m_\pi)^2)} \cdot c}{2 \cdot m_D} = 861 \text{ MeV/c}, \tag{6.1}$$

where m_D, m_K and m_π denote the masses of the D^0, the kaon and the pion.

Only two dimensional decays are simulated and their topology is therefore defined by a single parameter. The angle ϕ^* between the kaon and D^0 flight directions in the D^0 rest frame is chosen (see fig. 6.1a), because for the isotropic decay ϕ^* is uniformly distributed. $N = \mathcal{O}(10^6)$ topologies with equidistant values of ϕ^* are considered for each p_D value. The decay particles' momenta fixed by p^* and ϕ^* are then boosted into the laboratory frame in which the D-meson has a total momentum p_D.

The mean separation distance $\langle l \rangle$ between the D^0 production and decay points in the laboratory frame is given by

$$\langle l \rangle = \frac{p_D}{m_D} \cdot c\tau = \beta \cdot \gamma \cdot c\tau, \tag{6.2}$$

where $c\tau$ denotes the mean lifetime of the D^0 meson and $\beta = p_D \cdot c / E_D$ and $\gamma = E_D / m_D \cdot c^2$ with $E_D^2 = m_D^2 \cdot c^4 + p_D^2 \cdot c^2$ have been introduced.

The error on the decay length depends on the resolution of the production and decay points. In the reconstruction the former is given by the event's primary vertex. Its accuracy does not depend on p_D and therefore is neglected in the calculation of the decay length error[1].

The decay point in two dimensions is defined as the intersection point of the kaon and pion flight trajectories which are approximated in the error calculation with straight lines. The uncertainty perpendicular to the particle's momentum equals the impact parameter resolution which has been measured in data as a function of the particle's transverse momentum p_t (cf. sec. 5.1.2) to be

$$\sigma_d^2 = \sigma_{int}^2 + \left(\frac{A_{MS}}{p_t}\right)^2 = (57\ \mu\text{m})^2 + \left(\frac{80\ \mu\text{m}}{p_t[\text{GeV/c}]}\right)^2, \tag{6.3}$$

where the first term denotes the intrinsic detector resolution and the second models the p_t depending multiple scattering contribution. In the simulated radial decays p_t is set to the total momentum p_K of the kaon, respectively p_π of the pion in the laboratory frame (see fig. 6.1b). Their mean values are shown in figure 6.2a as a function of p_D. The uncertainty in the decay particles' flight directions is neglected in the error calculation.

Due to the linearization of the flight trajectories the calculation of the intersection point fails for (anti)parallel kaon and pion momenta[2] and therefore the error calculation diverges for these topologies. Thus ϕ^* is simulated in the restricted range $[\Delta, \pi - \Delta]$[3] only, where the cutoff is set to $\Delta = 0.5$ mrad.

This behavior represents the major drawback of the model: because the estimated error is divergent in ϕ^*, the average $\langle \sigma_l \rangle$ depends on the chosen cutoff Δ. Thus the absolute normalization of the p_D dependent resolution is not described by the model and therefore it is normalized at high p_D to the following estimation.

The angles ϕ_K and ϕ_π between the decay particles and D^0 momenta in the laboratory frame (see fig. 6.1b) given by the Lorentz transformation of $\sin \phi^*$:

$$\sin \phi_\mu = \frac{\sin \phi^*}{\sqrt{\gamma^2 \cdot (\pm \cos \phi^* + \beta / \beta_\mu^*)^2 + \sin^2 \phi^*}}, \qquad \mu = K, \pi, \tag{6.4}$$

where according to the ϕ^* definition the positive sign applies for the kaon, and the velocities $\beta_\mu^* = p^* \cdot c / E_\mu^* = p^* / \sqrt{m_\mu^2 \cdot c^2 + p^{*\,2}}$ have been introduced for the decay particles.

[1] Partially it is already included in the utilized impact parameter resolution, cf. sec. 5.1.2

[2] A most probable point of common origin can always be found for circular trajectories.

[3] Negative ϕ^* values are omitted due to the invariance under reflections on the D^0 flight direction.

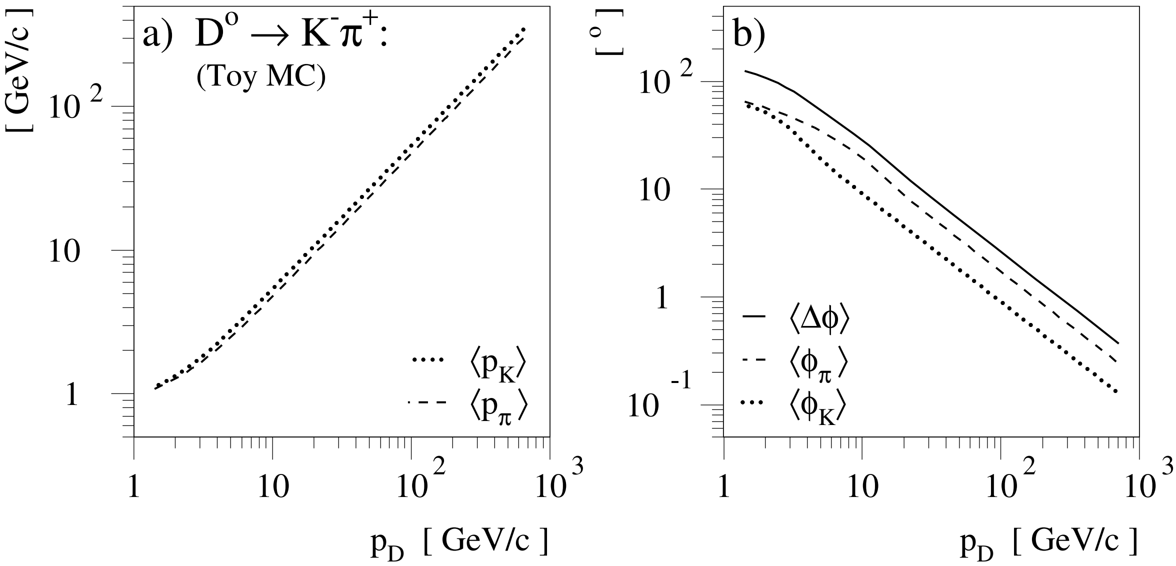

Figure 6.2: **(a)** *The mean total momentum $\langle p_K \rangle$ of the kaon (dotted) and $\langle p_\pi \rangle$ of the pion (dashed) in the laboratory frame are shown as a function of the total D^0 momentum p_D.* **(b)** *Similar to (a) but the dependences of the mean angles $\langle \phi_K \rangle$ (dotted) and $\langle \phi_\pi \rangle$ (dashed) and of the mean opening angle $\langle \Delta\phi \rangle = \langle \phi_K + \phi_\pi \rangle$ between the decay particles (solid) are shown.*

Their mean values and the mean opening angle $\langle \Delta\phi \rangle = \langle \phi_K + \phi_\pi \rangle$ between them are shown in figure 6.2b as a function of p_D.

With these angles the decay length l can be written as an average over the impact parameters d_K and d_π of the two particles (cf. fig. 6.1b) projected onto the D^0 flight direction:

$$l = \frac{1}{2}\left(\frac{d_K}{\sin\phi_K} + \frac{d_\pi}{\sin\phi_\pi}\right). \tag{6.5}$$

In the high p_D limes, i.e. $\gamma \gg 1$, the decay particles' momenta become large and therefore the errors on their impact parameters approach the asymptotic value σ_{int} (cf. eq. 6.3). The decay length error can therefore be estimated with

$$\sigma_l^2 \approx \left(\frac{\sigma_{int}}{2\cdot\sin\phi_K}\right)^2 + \left(\frac{\sigma_{int}}{2\cdot\sin\phi_\pi}\right)^2 \approx 2\left(\frac{\gamma\cdot\sigma_{int}}{2}\right)^2, \qquad \gamma \gg 1, \tag{6.6}$$

where for the last approximation $\sin\phi_\mu \approx 1/\gamma$ is used (see eq. 6.4).

6.1.2 Results

In the following the results obtained from the presented $D^0 \to K^-\pi^+$ decay model are discussed. First the description of the high p_D regime ($\gamma \gg 1$) is compared to the expected behavior estimated above. The low p_D regime discussed thereafter has more

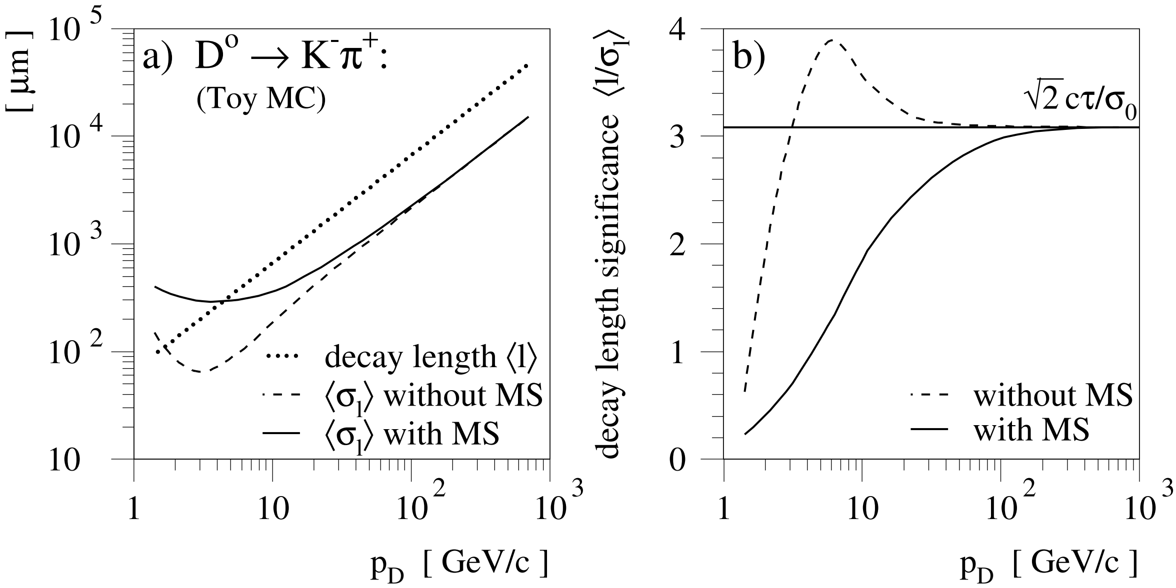

Figure 6.3: **(a)** *The p_D dependence of the mean decay length $\langle l \rangle$ (dotted) and its error $\langle \sigma_l \rangle$ are shown considering the intrinsic detector resolution only (dashed) and including multiple scattering effects (MS, solid).* **(b)** *The resulting mean decay length significance $\langle S_l \rangle$ as predicted by the model is plotted (see text).*

relevance herein: due to the threshold production of heavy flavors in ep scattering, the majority of the analyzed D-mesons have $p_t(D) < 10$ GeV/c.

$\langle l \rangle$ is proportional to its momentum p_D (cf. eq. 6.2) and thus depends linearly on γ. But also the mean resolution of the decay lengths $\langle \sigma_l \rangle$ deteriorates proportional to γ (cf. eq. 6.6), because the mean opening angles of the decay particles decrease proportional to $1/\gamma$ in this regime (cf. fig. 6.2b). Due to these small opening angles the position of the intersection point along the D^0 momentum direction is not well defined and therefore $\langle \sigma_l \rangle$ increases.

In figure 6.3a the p_D dependences of the mean decay length $\langle l \rangle$ and its error $\langle \sigma_l \rangle$ are shown. The model describes the expected linear increase of $\langle \sigma_l \rangle$ with rising $p_D \propto \gamma$ in the high p_D regime.

Thus a large decay length on its own is not a clear evidence for D-meson decays, but in addition its error must be considered. Therefore the lifetime tag is based on the significance of the decay length $S_l = l/\sigma_l$. Due to the γ dependences of $\langle l \rangle$ and $\langle \sigma_l \rangle$ its mean value converges to an asymptotic value which can be estimated from equations 6.2 and 6.6 with

$$\langle S_l \rangle = \langle l/\sigma_l \rangle \approx \frac{\beta \cdot \gamma \cdot c\tau}{\gamma \cdot \sigma_{int}/\sqrt{2}} \approx \sqrt{2} \cdot c\tau/\sigma_{int}, \qquad \gamma \gg 1, \tag{6.7}$$

where $\beta \approx 1$ has been used. Thus for $\gamma \gg 1$ $\langle S_l \rangle$ depends on the mean lifetime $c\tau$ of the D-meson and the intrinsic impact parameter resolution σ_{int} only, where σ_{int} is given by the intrinsic hit resolution and the geometric layout of the vertex detector alone.

In the low p_D regime the influence of the decay topology and of multiple scattering (MS) are studied separately. Thereto the p_D dependences of $\langle\sigma_l\rangle$ and $\langle S_l\rangle$ are determined with and without considering the MS contribution to the impact parameter resolution (cf. eq. 6.3). The influence of the decay topology is studied with the results obtained for the pure intrinsic detector resolution, i.e. $\sigma_d = \sigma_{int}$, and the impact of MS becomes clear if comparing the two results.

Neglecting MS effects $\langle\sigma_l\rangle$ has a well pronounced minimum at $p_D \approx 3$ GeV/c and approaches quickly the expected linear behavior as can be seen from figure 6.3a. Consequently $\langle S_l\rangle$ has a maximum in the low p_D regime before approaching its asymptotic value.

The origin of the extrema can be understood from the decay topology: the best resolution of the intersection point is achieved for perpendicular trajectories. In average the kaon and pion momenta are perpendicular for $p_D \approx 2.7$ GeV/c ($\langle\Delta\phi\rangle = 90^o$ in fig. 6.2b). The shift of the minimum towards a little higher p_D value origins from the slightly asymmetric topology in the laboratory frame arising from the different masses of the decay particles. Therefore the best resolution $\langle\sigma_l\rangle$ is achieved for $\langle\Delta\phi\rangle \approx 75^o$.

Including the multiple scattering term in the impact parameter resolution changes the picture drastically: The decay length resolution $\langle\sigma_l\rangle$ becomes worse by a factor 2-5 in the low p_D regime. Instead of an optimal separation power in this regime, $\langle S_l\rangle$ approaches its asymptotic value only slowly without any intermediate maximum.

6.1.3 Lessons to learn

The following conclusions can be drawn from the results of the discussed $D^0 \to K^-\pi^+$ decay model:

- Not the intrinsic detector resolution, but multiple scattering effects dominate the decay length resolution in the low p_D regime, where the majority of the D-mesons are produced in ep scattering. This is a major difference to recent LEP experiments, where the produced charm quarks have a total momentum of approximately half of the center of mass energy, i.e. $p_c \approx 45$ GeV/c on the Z^0-resonance, and where the intrinsic resolution has therefore a more crucial role.

- The material in the flight path of the decay particles has therefore to be reduced to a bare minimum. This is achieved in the H1 experiment with a carbon fiber beam pipe with aluminum liner ($d/X_0 = 0.6\%$) and a design of the CST with the read-out electronics at the ends and a central region consisting essentially only of active sensor material (in total $d/X_0 = 1\%$ between the interaction region and the second silicon layer[4]).

- An accurate description of MS effects as achieved by `CSTCOR` is essential.

[4]MS in the second silicon layer or thereafter does not affect the CST direction measurement.

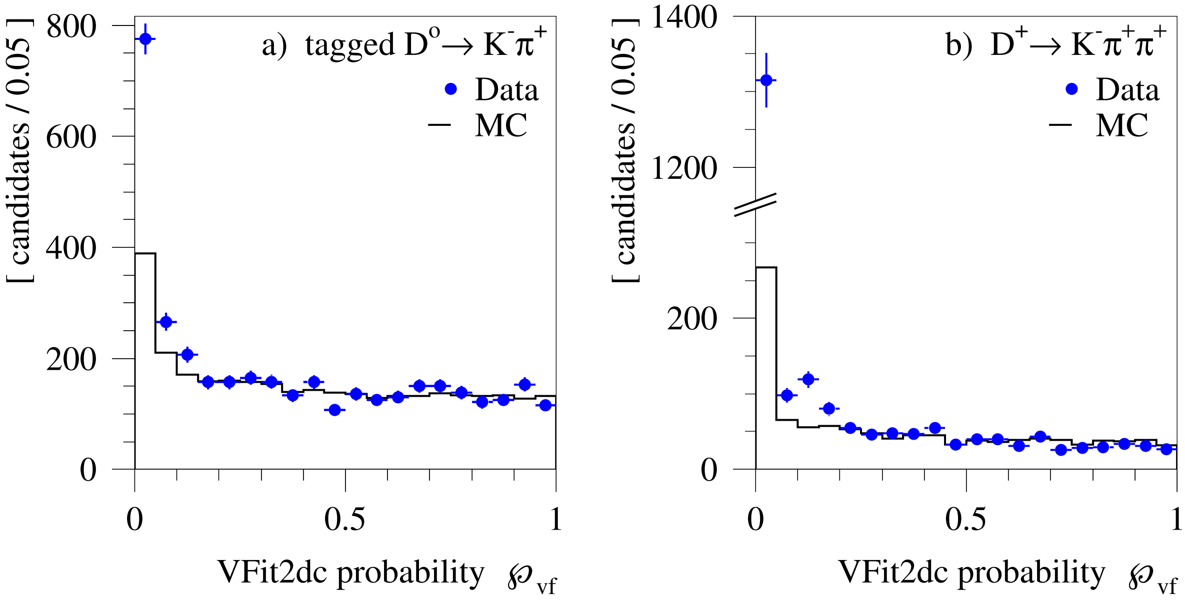

Figure 6.4: *The* `VFit2dc` *probability distributions in the signal regions of (a) tagged $D^0 \to K^-\pi^+$ and (b) selected $D^+ \to K^-\pi^+\pi^+$ decays are shown for data (dots) and simulated events (histograms). The latter are normalized to the data above $\mathcal{P}_{\mathrm{vf}} > 0.2$.*

- The lifetime tag is based on the decay length significance $S_l = l/\sigma_l$ rather than on the decay length itself, because the impacts of the specific decay topology and of multiple scattering on the decay length resolution is reflected in the calculated error.
- The small mean decay length significance in the low momentum regime explains the rather low efficiency of the lifetime tag.

6.2 Lifetime tag

In the following the variables used for the lifetime tag which have already been introduced in chapter 5 are discussed in more detail. The selection criteria applied in the different decay channels are summarized in table 6.1. While quality cut values are set consistent in all channels, the cuts in the lifetime sensitive S_l and $(2 \times S_d)$ variables are chosen to obtain signal-to-noise ratios of approximately one in the mass spectra.

6.2.1 Vertex fit probability $\mathcal{P}_{\mathrm{vf}}$

The upper tail probability $\mathcal{P}_{\mathrm{vf}}$ of the track-vertex fitter `VFit2dc` is a measure of the compatibility of a candidate with the hypothesis of a common origin of the decay particles' tracks and with the directional constraint. A flat distribution is expected for candidates consistent with this picture, if the calculated covariance matrices of the input parameter correctly describe their resolutions (cf. sec. 5.1.2). Candidates not in agreement with the fit model cumulate at small probabilities.

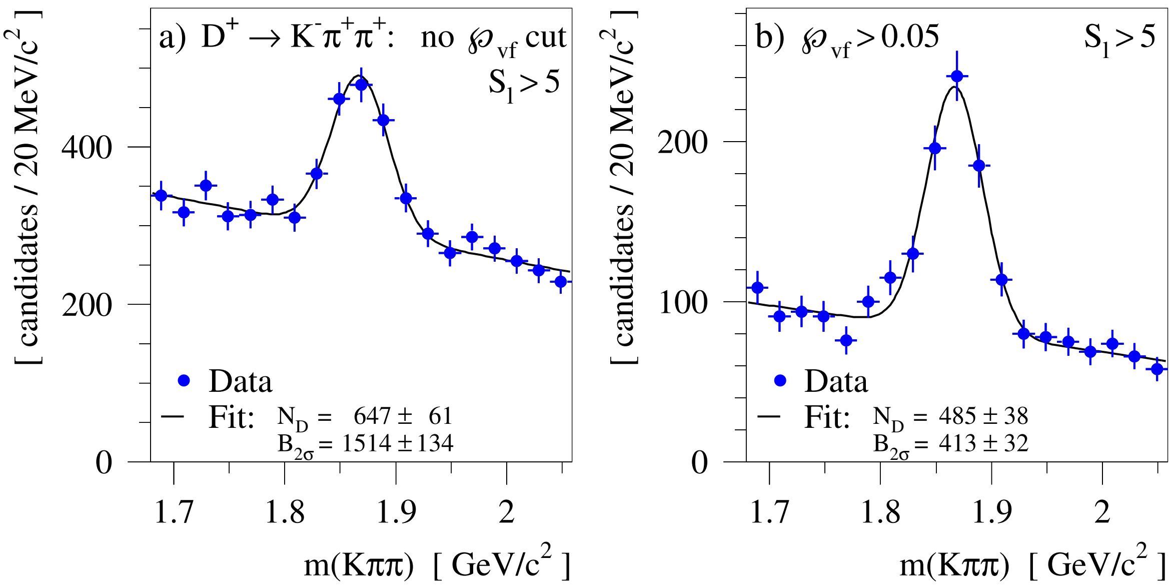

Figure 6.5: *The $m(K\pi\pi)$ spectra of D^+ candidates are shown (a) without a cut and (b) with a $\mathcal{P}_{vf} \geq 0.05$ cut on the* `VFit2dc` *fit probability. The candidates are required to have a significant primary and secondary vertex separation (cf. tab. 6.1).*

The `VFit2dc` probability distributions obtained for fits of two body decays $D^0 \to K^-\pi^+$ and three body decays $D^+ \to K^-\pi^+\pi^+$ are shown in figure 6.4. For $\mathcal{P}_{\rm vf} > 0.2$ the distributions are fairly flat as expected and the data are well described by the simulation. At lower $\mathcal{P}_{\rm vf}$ values a clear excess can be seen which arises from the combinatorial background. Due to this background the excess is more prominent in data than in the distributions found with simulated signal decays. The excess in the D^+ channel is higher than in tagged D^0 decays, because the phase space available for the combinatorial background is larger for the former.

The candidates which are in disagreement with the fit model are rejected by a minimal requirement on the vertex fit probability $\mathcal{P}_{\rm vf} \geq 0.05$ in all decay channels. This cut value corresponds to an $\chi^2 < 3.8$ cut in two body decays with one available degree of freedom (ndf) and $\chi^2 < 6.0$ in three body decays with ndf $= 2$.

The $\mathcal{P}_{\rm vf}$ cut improves the signal-to-noise ratio by a factor of 1.6 in the untagged D^0 channel and even by 2.7 in the D^+ channel which can be seen from the $m(K\pi\pi)$ spectra before and after the $\mathcal{P}_{\rm vf}$ cut shown in figure 6.5. The signals used for these measurements meet all lifetime requirements quoted in table 6.1, i.e. they have a significant primary and secondary vertex separation. Due to this separation the lever arm of the directional constraint is sufficiently large to reject a substantial number of background events.

The signal efficiencies as a function of the $\mathcal{P}_{\rm vf}$ cut are shown in figure 6.6 for the untagged D^0 and the D^+ signals. The method to obtained these efficiencies will be discussed in the next section. Especially at low probabilities the efficiency curves differ from the linear behavior expected for a flat probability distribution. The reason for the enhancement are impurities in the reconstruction chain, especially wrong CST hit assignments

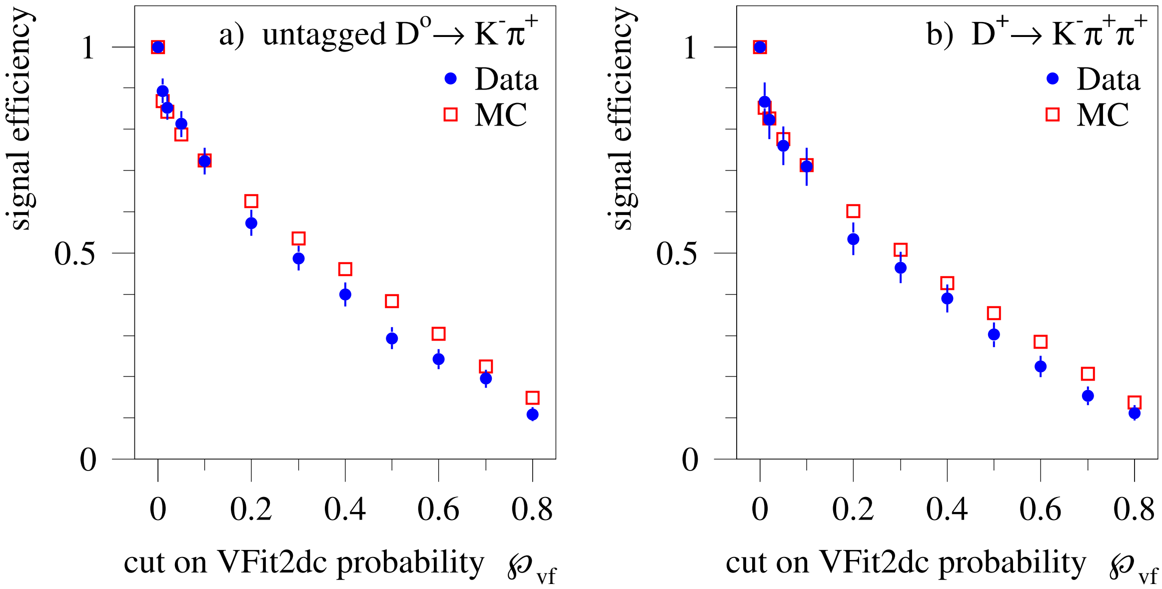

Figure 6.6: *The signal efficiencies are shown as a function of the* `VFit2dc` *probability $\mathcal{P}_{vf}$ cut in (a) the untagged D^0 and (b) the D^+ channels for data (dots) and simulated decays (open boxes).*

(cf. sec. 5.1.2) which are also visible in the probability distribution of simulated signal decays shown in figure 6.4.

Herein these impurities only deteriorate the signal-to-background ratio as long as the simulation accurately reproduces them: the $\mathcal{P}_{\text{vf}} \geq 0.05$ cut reduces the untagged D^0 signal by $19 \pm 3\%$ in data instead of the expected 5%, but the value is in good agreement with a reduction of 21% in simulated decays. In the D^+ channel $24 \pm 5\%$ of the signal is discarded (cf. fig. 6.5) well comparable with 22% obtained by the simulation.

6.2.2 Radial decay length l

D-meson decays follow an exponential decay law, i.e. the probability $\mathcal{P}$ that a D-meson has not decayed after a time t^* is given by

$$\mathcal{P}(t^*) = e^{-t^*/\tau}, \qquad t^* \geq 0, \tag{6.8}$$

where the decay time t^* is measured in the rest frame of the D-meson and τ denotes its mean lifetime in this system. The world average values of $c\tau$ which are of the order of some 100 μm have been given in table 1.2. The radial decay length l in the laboratory frame can then be calculated from the decay time t^* of the decay by

$$l = \frac{p_t(D)}{m_D} \cdot c \cdot t^*, \tag{6.9}$$

where $p_t(D)$ is the transverse momentum of the D-meson, m_D its nominal mass and c denotes the speed of light. Thus most signal events have a small l due to the exponential decay spectrum and the steep $p_t(D)$ spectrum.

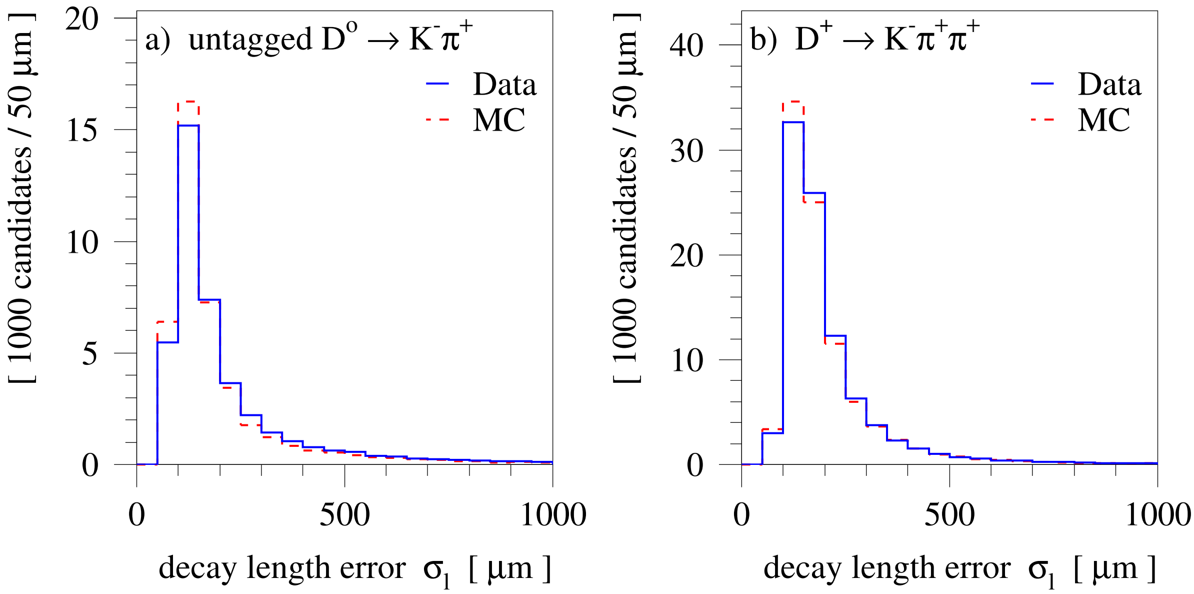

Figure 6.7: *The calculated decay length error distributions of events in the signal region are shown in (a) the untagged $D^0 \to K^-\pi^+$ and (b) in the $D^+ \to K^-\pi^+\pi^+$ decay channels for data (solid) and simulated events (dashed).*

The decay length l is reconstructed as the radial distance between the measured primary and secondary vertex positions as discussed in chapter 5. The sign of the decay length is positive for candidates with parallel and negative for anti-parallel and therefore inconsistent decay and flight directions.

The simplified $D^0 \to K^-\pi^+$ decay model presented in section 6.1 has shown that the decay length on its own is not an appropriate mean to distinguish signal and background events. Therefore only an upper limitation of $|l| \leq 5$ mm is made to reject backgrounds from long living particles, e.g. K^0 and Λ^0 decays or photon conversions in the detector material.

6.2.3 Decay length error σ_l

The decay length error σ_l is given by the accuracy achieved in the primary and secondary vertex reconstruction. Due to the directional constraint these positions are correlated with each other and with the measured decay particles' momenta. The error calculation takes these correlations fully into account.

The decay topology has a strong influence on σ_l as already discussed in the last section. The observed error distributions therefore depend not only on the decay channel and the number of tracks available for the secondary vertex fit, but also on the composition of the sample depending on the kinematical selection criteria.

Figure 6.7 shows two examples of σ_l distributions for events in the signal region of the D-meson mass spectra. In untagged $D^0 \to K^-\pi^+$ decays higher kaon and pion transverse momenta are selected than in the D^+ channel. On the other hand the position of the secondary vertex is more accurately defined in the three body decay $D^+ \to K^-\pi^+\pi^+$.

In the end the σ_l distributions in the different channels are very similar: a mean decay length error of about 200 μm with a most probable value of $100 - 150$ μm and a long tail towards larger errors is observed. Because the events in these tails have no well defined decay length, they are rejected by requiring $\sigma_l \leq 300$ μm.

6.2.4 Decay length significance S_l

The signed decay length significance $S_l = l/\sigma_l$ is the major variable used for the lifetime tag. The calculation of the error σ_l considers all effects relevant for the decay length resolution of each individual D-meson candidate. Thus S_l allows to classify each candidate according to the significance of its vertex separation and therefore it represents a powerful mean to identify events with lifetime information.

The cross section measurement relies crucially on an accurate description of the data by the detector simulation. All aspects of the decay length reconstruction discussed up to know culminate in the measured S_l spectrum and it will therefore be used as a comprehensive test of the simulation's quality which will be presented in the next section.

The lifetime tag based essentially on S_l alone facilitates in addition the verification of the simulation's quality: instead of having to consider a multidimensional parameter space, it is usually sufficient to regard merely the S_l distribution. The degree of agreement between data and simulation achieved in S_l is thus also a measure for the systematic error introduced by the lifetime tag which will also be discussed in a separate section later on.

6.2.5 Impact parameter significance S_d

The impact parameter d denotes the minimal distance of the non-vertex fitted track to the event's primary vertex. Its sign is determined by intersecting the track with an axis defined by the D-meson's momentum direction and the primary vertex position: the sign of the impact parameter is chosen positive, if the intersection point lies in "front" of the primary vertex position with respect to the D-meson flight direction, and negative if it is "behind" the primary vertex[5].

The significance of the impact parameter $S_d = d/\sigma_d$ is a measure for the lifetime information of a single track. Because the secondary vertex position is determined with the decay particles' tracks, S_l and S_d are highly correlated and therefore only minor improvements are gained by a additional requirement in S_d.

[5] Defining track parameters d'_{ca} and ϕ' equivalent to d_{ca} and ϕ, but with respect to the primary vertex position instead of the origin, the sign of the impact parameter is given by the sign of the product $d'_{ca} \cdot (\phi' - \phi_D)$, where ϕ_D denotes the D-meson flight direction and $(\phi' - \phi_D) \in [-\pi, \pi]$.

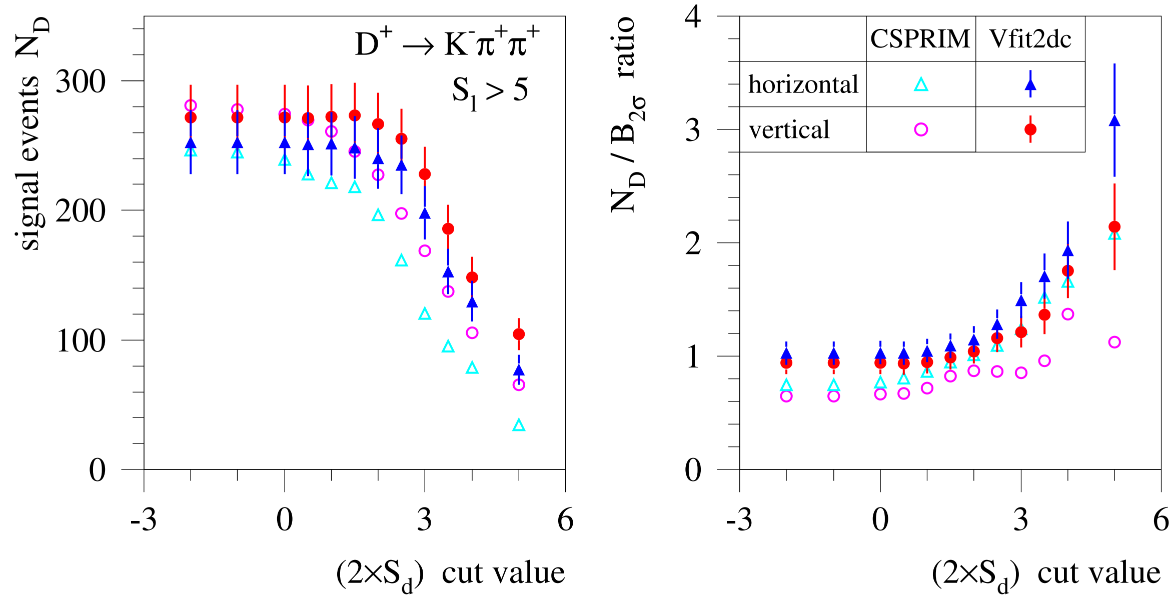

Figure 6.8: *(a) The number of D^+ signal events N_D and (b) the signal-to-background ratio $N_D/B_{2\sigma}$ extracted from the $m(K\pi\pi)$ mass spectra are shown as a function of the $(2 \times S_d)$ cut value for vertical (triangles) and horizontal (dots) decays separately. The mass spectra without $(2 \times S_d)$ cut are shown in figure 5.14. The impact parameters are calculated with respect to the primary vertex position determined with* `CSPRIM` *(open symbols) and to its* `VFit2dc` *improved position (solid symbols). The error bars on the latter measurements are of statistical nature.*

Still such a requirement in S_d is formulated. It rejects candidates with only one track with a significant impact parameter. Such events suffer from backgrounds caused by impurities of the track reconstruction, especially of the CST space point linking. The $(2 \times S_d)$ cut requires a minimal S_d of at least two decay tracks, because two improperly reconstructed tracks in one candidates are much less likely than a single one.

For the lifetime tag the impact parameter is calculated with respect to the primary vertex position $\vec{r}_{2dc}$ fitted by `VFit2dc`. This is strictly speaking not correct, because this fitted position is due to directional constraint correlated with the tracks of the decay particles. In addition this correlation is not considered in the calculation of σ_d. An unbiased impact parameter calculation is possible with respect to the position $\vec{r}_{prim}$ determined by `CSPRIM` alone.

The directional constraint improves the primary vertex resolution mostly perpendicular to the D-meson flight direction. Thus it hardly improves the decay length resolution for which the projection of the primary vertex error onto the flight direction is relevant (see sec. 5.2.2). But for the impact parameter the primary vertex resolution perpendicular to the flight direction is relevant which is exactly the projection improved by `VFit2dc`. Therefore the resolution of d becomes better if calculated with respect to $\vec{r}_{2dc}$ instead of $\vec{r}_{prim}$.

Most improvement is expected for vertical decays, because the error on the x-position of the primary vertex $\sigma(x_{pv})$ is significantly reduced by `VFit2dc` (cf. sec. 5.2.2). Because the primary vertex's y-position is already well confined by the small size of the interaction

Lifetime tagging cuts	D^+	D^0	D_s^+	D^{*+}
$\mathcal{P}_{\mathrm{vf}} >$	0.05			
$\|l\| <$	5 mm			
$\sigma_l <$	300 μm			
$S_l >$	5.0	3.0	2.0	1.0
$(2 \times S_d) >$	2.5	2.0	1.0	-1.0

Table 6.1: *The cuts of the lifetime tag are summarized for the different decay channels. The variables and the cut values are discussed in the text.*

region, $\sigma(y_{pv})$ is hardly improved by the directional constraint and therefore only a minor gain is anticipated for horizontal decays.

To quantify these improvements the `VFit2dc` results are compared with results obtained from an uncorrelated primary and secondary vertex reconstruction with `CSPRIM` and `VFit2du`[6], where the impact parameters are calculated with respect to $\vec{r}_{prim}$.

The two methods are first compared in terms of extracted signal numbers which are shown in figure 6.8a for the D^+ decay channel as a function of the $(2 \times S_d)$ cut value. Without an effective $(2 \times S_d)$ cut the same number of signal events are obtained with the two methods. The D^+ candidates are selected with a $S_l > 5$ cut and thus more vertical decays, defined by $|\cos\phi_D| < 1/\sqrt{2}$, are found due to the better σ_l resolution in this direction. As can be seen from the figure the number of signal events decreases with rising $(2 \times S_d)$ cut values slower, if d is calculated with respect to $\vec{r}_{2dc}$.

In figure 6.8b the signal-to-background ratio $N_D/B_{2\sigma}$ in the $m(K\pi\pi)$ spectra are shown as a function of the $(2 \times S_d)$ cut value. The ratio in the spectra without cut is already improved by the directional constraint (cf. sec. 5.2.2). For horizontal decays $N_D/B_{2\sigma}$ improves with rising $(2 \times S_d)$ cut values in the same way for both reconstruction methods. For vertical decays $N_D/B_{2\sigma}$ is hardly improved by the $(2 \times S_d)$ cut, if d is calculated with respect to $\vec{r}_{prim}$. But if S_d is determined with $\vec{r}_{2dc}$, $N_D/B_{2\sigma}$ in vertical decays increases nearly as fast as for horizontal decays.

The higher signal efficiency and the better signal-to-background ratio achieved with the $(2 \times S_d)$ cut, if S_d is determined with $\vec{r}_{2dc}$ justifies the not strictly correct calculation of d and σ_d.

6.3 Verification of the simulation

The efficiency of the lifetime tag is determined with simulated D-meson decays. Two methods are discussed to ensure the reliability of the simulation to describe this efficiency.

[6]A similar comparison of the two reconstruction methods has already been discussed in section 5.2.2.

The decomposition method determines the signal and background composition by fitting two independently determined shapes to the variable distributions. The result can then be compared to the signal extraction with the reconstructed mass spectrum.

The more direct method to compare the signal efficiencies measured in data and simulated samples is only applicable in the tagged D^0 channel due to the high background rates in the isoscalar D-meson channels. Therefore in these channels the signal efficiencies can only be measured in reference to samples in which the signal significance necessary for a reliable signal extraction is enhanced with a partial lifetime tag.

6.3.1 Decomposition

The variables of the lifetime tag are chosen according to their power to distinguish signal and background events. This capability arises from the lifetime information present in the signal contrary to the background which originates predominantly at the interaction point itself. Thus the reconstructed variable distributions contain information on the composition of the sample and this information is used herein to verify the reliability of the detector simulation.

Fitting method

Thereto the variable distributions dN/dx of events in the signal region of the reconstructed mass spectrum are decomposed into signal (S) and background (B) contributions. The signal region R_S is defined in the mass spectrum by a 2-σ window around the nominal D-meson mass, where σ denotes the width of the fitted signal Gaussian. In decays with intermediate resonances the candidates in R_S are in addition requested to be within 2-σ of the nominal mass of the resonance.

The decomposition fits two histograms describing the shapes of S and B to the histogram with the variable distribution of events in R_S: $dN/dx = N_S \cdot S + N_B \cdot B$. In the fit the only free parameters are the normalizations N_S of the signal and N_B of the background. The shapes S and B are determined independently as follows:

- The reconstructed dN/dx distribution of simulated D-meson decays defines S which describes the shape expected for the signal. In the simulation the two main sources of D-mesons, charm and beauty production, are considered according to their expected production rates.
- The dN/dx distribution of data events in the side bands of the reconstructed mass spectrum is used to determine the shape of B. The side bands are defined as the regions of the mass spectrum to the left and right of the signal window, but still within 250 MeV/c^2 of the nominal mass.

Because the histograms describing S and B are determined with samples five to ten times larger than the fitted sample, their statistical errors are neglected in the χ^2 function minimized by the binned fit.

The fitted normalizations N_S and N_B can be compared to N_D and $B_{2\sigma}$ determined with the fit to the reconstructed mass spectrum, where N_D denotes the fitted number of D-mesons and $B_{2\sigma}$ the number of background events within a 2-σ window below the signal. The decomposition of dN/dx thus represents an independent signal determination equivalent to the fit to the mass spectrum.

Decomposed l and S_l spectra in tagged D^0 decays

In figure 6.9 the decompositions of the decay length and the decay length significance spectra are shown for tagged D^0 mesons. The results describe the two data distributions very well, in the case of S_l a good agreement over three orders of magnitudes is achieved. This agreement is also expressed by the fits' excellent χ^2/ndf values of 35/38 (l) and 34/32 (S_l). The decompositions determine the signal with $N_S = 1733 \pm 108$ (l) and $N_S = 1760 \pm 100$ (S_l) which is fully consistent with $N_D = 1638 \pm 78$ extracted with the fit to the reconstructed $m(K\pi)$ spectrum shown in figure 6.9a.

This implies that the fit results accurately describes the compositions of the l and S_l distributions. As expected the D-meson signals are clearly enhanced towards positive decay lengths and significances, while the negative sides of the distributions are dominated by background.

Mathematically the signal shape of l can be obtained by folding the exponential decay spectrum in the D-meson's rest frame with the momentum spectrum of the reconstructed D-mesons and the decay length resolution function of the detector. In the S_l signal shape the expected resolution function is unfolded from the l spectrum.

Thus the decomposition simultaneously tests several assumptions:

- due to the strong dependence of l and σ_l on the decay kinematics the data has to be accurately reproduced by the simulated sample used to describe the signal shape with respect to the kinematical composition,
- the events in the side bands are an adequate representation of the background in the signal region,
- the mean lifetime $c\tau$ used in the simulation is correct and
- the detector simulation accurately describes the decay length resolution function which depends on the detector properties as well as on the performance of the reconstruction algorithms.

The first point is tested by the cross section measurements presented in the next section[7]. Because the background is mostly of combinatorial nature, the second assumption is seen as uncritical. The world average values of the mean lifetimes of D-mesons used in the simulation have been measured by several experiments with high precision and should therefore be reliable.

[7] The strong dependences of σ_l and S_l on the D-meson kinematics are also the reason, why the results of the decompositions are not used for the cross section measurements.

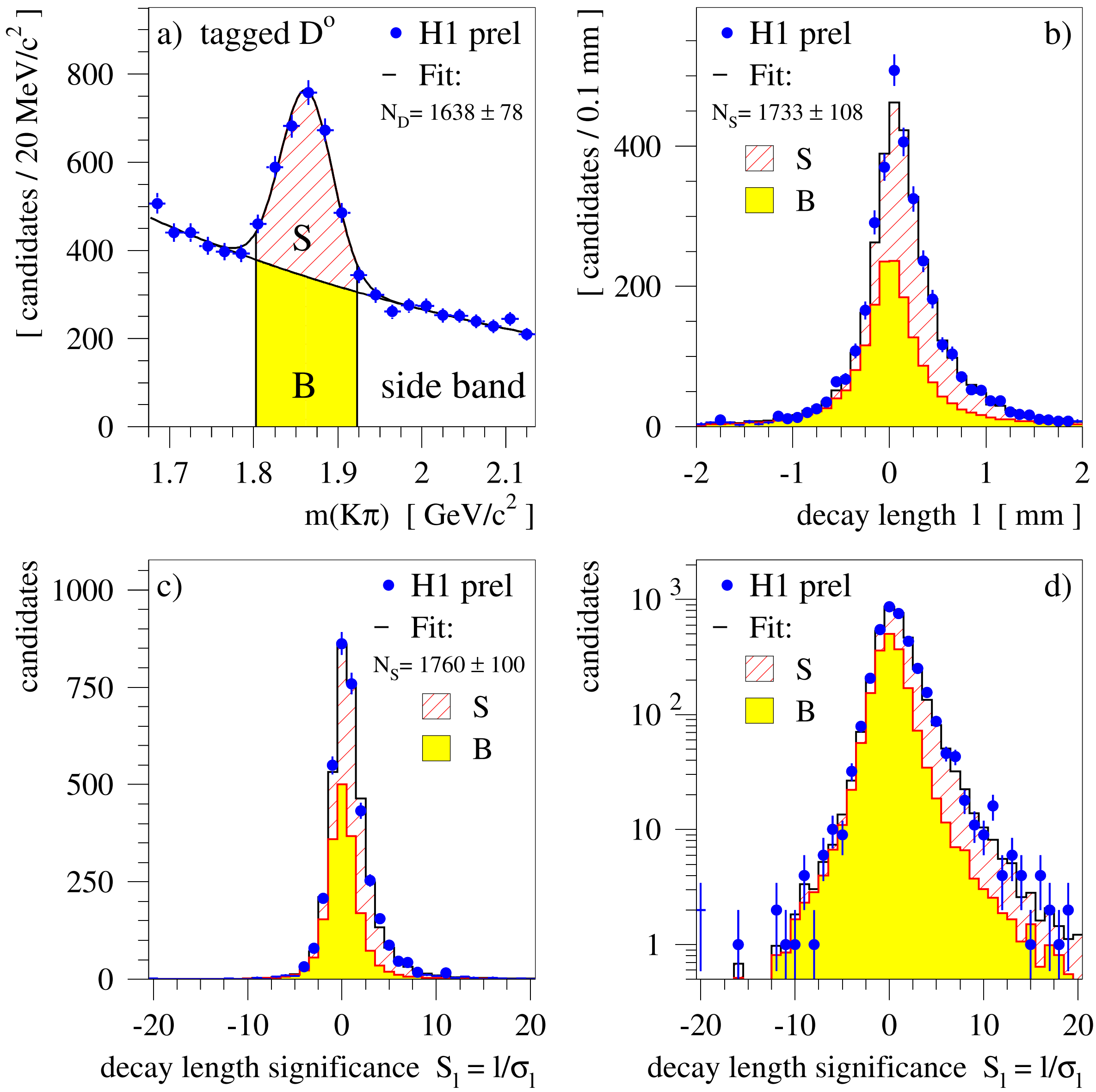

Figure 6.9: **(a)** *The $m(K\pi)$ mass spectrum of tagged D^0 candidates with a convergent* `VFit2dc` *fit ($\chi^2 < 100$) is shown. The data (dots) have the H1 preliminary stamp. The signal region and its composition into signal (S, hashed) and background (B, shaded) as found by the fit are indicated.* **(b)** *The composition of the decay length spectrum of events in the signal region is fitted as explained in the text.* **(c/d)** *The decay length significance spectrum and the result of the decomposition are shown with linear and logarithmic scales. The results are further discussed in the text.*

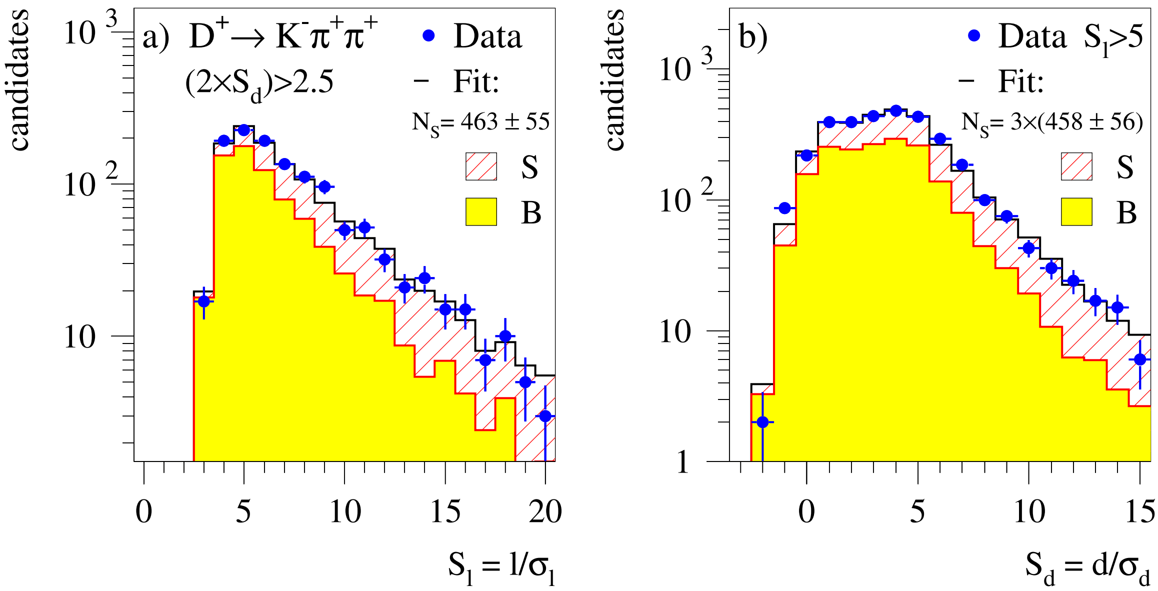

Figure 6.10: *(a) The S_l distribution of D^+ candidates in the signal region of the $m(K\pi\pi)$ spectrum and (b) the S_d distribution of their decay particles are shown. The candidates meet all conditions of the lifetime tag but the one in the plotted variable itself. The data (dots) are well described by the fitted decompositions into signal (S, hashed) and background contributions (B, shaded).*

Thus the decompositions of the l and S_l distributions are a major test, whether the detector simulation accurately reproduces the decay length resolution function. In addition the excellent description in both, l and S_l, indirectly proves the accuracy of the σ_l calculation.

The actual resolution function can be measured with the reconstructed l spectrum of events originating at the primary vertex, e.g. with the combinatorial background. But the shape determined with events of the side bands is slightly asymmetric with an enhancement towards the positive side (to be seen best in figure 6.9d): about 10% more events with positive significances are counted. This asymmetry arises from only partially reconstructed heavy flavor decays with lifetime information. The detector's decay length resolution function is therefore described by the negative side of l shape only.

Decompositions in the isoscalar decay channels

The signal-to-background ratio S/B in the tagged D^0 decays is fairly good without applying any lifetime requirements due to the Δm-tagging technique. Such a reasonable S/B ratio is a necessary precondition for a reliable decomposition of the variable distributions. Due to large combinatorial backgrounds this condition is not met in the decay channels of the isoscalar D-mesons. Thus the method presented for the tagged D^0 channel can not be directly applied to them.

In figure 6.10 the fitted compositions of the S_l and S_d distributions of events in the D^+ signal region of the $m(K\pi\pi)$ spectrum are shown. They are both biased towards a significant vertex separation by requiring all cuts of the lifetime tag but the condition in the variable itself. Therefore the S/B ratio in the S_l distribution is mainly enhanced by the $(2 \times S_d) > 2.5$ condition, while $S_l > 5$ improves the ratio in the S_d spectrum.

Because S_l and S_d are highly correlated the decomposition tests the distributions stronger for events with significant lifetime information. Therefore the method bears less significance than in the untagged D^0 channels. Still the distributions of the lifetime tag are tested in the region of the parameter space relevant for the measurement.

The results of the decompositions shown in figure 6.10 describe the data distributions very well which is confirmed by the good χ^2/ndf values 14/16 and 19/16 achieved in the fits to the S_l (fig. 6.10a) and S_d spectra (fig. 6.10b). Also the fitted numbers of signal events agree well with the numbers extracted from the corresponding $m(K\pi\pi)$ mass spectra: $N_S = 463 \pm 55$ obtained from the decomposition of S_l is consistent with $N_D = 537 \pm 45$ and $N_S = 3 \times (458 \pm 56)$ found with the S_d distribution of the three decay particles compare well with $N_D = 525 \pm 42$.

In the untagged D^0 decay channel the wrong charge combinations contain the equivalent lifetime information as the correctly assigned signal events. Therefore the method can not be applied, because the events of the side bands are not an accurate representation of the background below the signal. In the D_s^+ channel the small size of the signal and the low S/B ratio diminish the significance of the decompositions. A method to test the descriptive power of the simulation which is applicable in all channels is discussed in the following.

6.3.2 Signal efficiency measurements

The most direct way to verify the accuracy by which the simulation describes the efficiency of the lifetime tag is to measure it in data and simulated samples and compare the results. Due to the different background contaminations in data and simulated samples, the efficiency has to be measured for signal events only.

The method of the measurement in the tagged D^0 channel is explained in figure 6.11 on the example of the decay length significance S_l. The reference sample are tagged D^0 candidates which meet the kinematical selection criteria (see table 5.3) and for which the `VFit2dc` fit converged with $\chi^2 < 100$ (cf. fig. 6.9a). The number N_r of signal events in this reference sample is determined with a fit to the $m(K\pi)$ spectrum.

Then the number of signal events N_c which meet successive S_l cuts are determined with the corresponding mass spectra shown in figure 6.11a. With the results of these signal extractions the D^0 signal efficiency $\varepsilon_D = N_c/N_r$ can be measured as a function of the S_l cut value. In the figure the successive signal reduction is seen best by comparing the mass spectra within a row, while the spectra within a column give an impression on the improving signal-to-background ratio.

In figure 6.11b the signal efficiencies measured with data and simulated D^{*+} decays are compared. The measurement points are correlated, because each sample is a subset of all samples at lower cut values. Thus in the efficiency difference between data and simulation

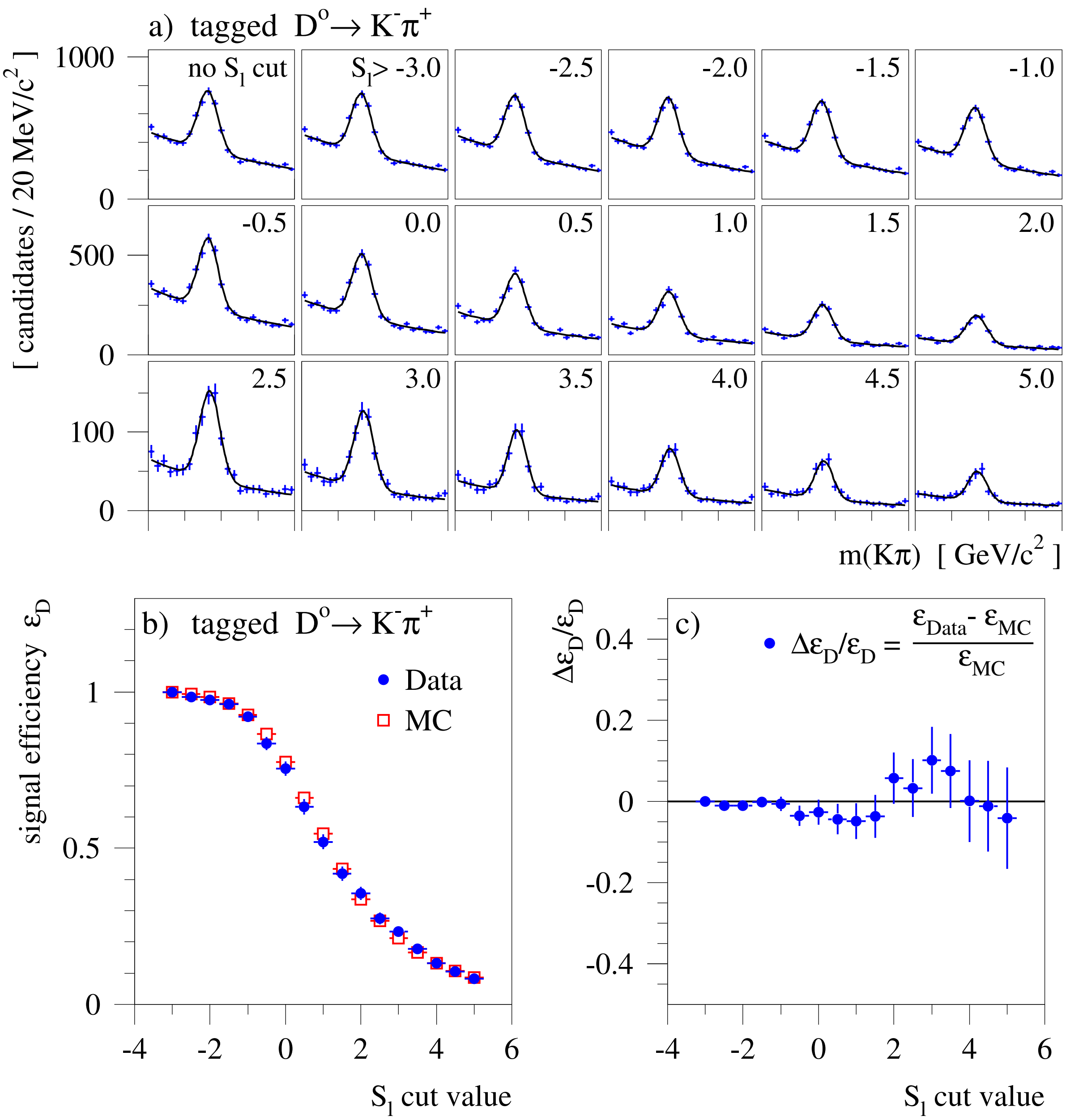

Figure 6.11:
(a) *The* $m(K\pi)$ *mass spectra of tagged* D^0 *candidates in the range* $(1.675, 2.135)$ GeV/c^2 *and the fitted curves of the signal extraction are shown for successive cuts on the decay length significance* S_l *as indicated in the right upper corners.*
(b) *The number of signal events extracted by the fits to the mass spectra are used to measure the signal efficiency* ε_D *in data (dots) and simulated events (open boxes) as a function of the* S_l *cut value with reference to the signal extracted from the spectrum without* S_l *cut.*
(c) *The relative difference* $\Delta\varepsilon_D/\varepsilon_D$ *between* ε_D *measured in data and simulation is shown as a function of the* S_l *cut value. The results are further discussed in the text.*

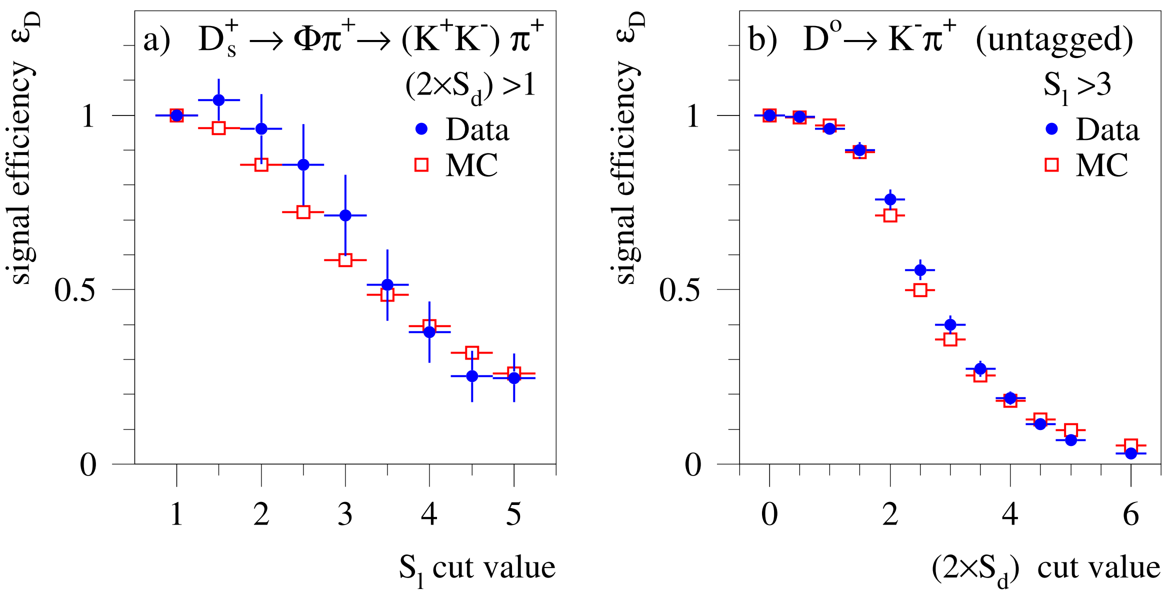

Figure 6.12: *The measured signal efficiencies ε_D are shown as a function of (a) the S_l cut value in the D_s^+ and (b) of the $(2\times S_d)$ cut value in the untagged D^0 decay channel. The selected candidates meet all residual conditions of the lifetime tag. The efficiencies found with simulated decays (open boxes) describe the data (dots) within the indicated statistical errors fairly well.*

at a certain cut value shown in figure 6.11c all differences in the measurements to the right are cumulated. The bars indicate the statistical error of the single measurements[8].

The simulation describes ε_D in a wide range of S_l cut values fairly well. The relative differences between data and simulation are below 10% in all measurement points (cf. fig. 6.11c). They are well covered by the systematical error assigned to the lifetime tag (see sec. 6.5).

Assumptions similar to the ones necessary for a reliable decomposition of the S_l distribution have to be met to obtain such a good agreement: the kinematical compositions of the data and simulated sample have to be similar, the mean D^0 lifetime used in the simulation must be correct and the decay length resolution function must be accurately described by the detector simulation. The same argumentation as given above for the decomposition hold for the first two assumptions and therefore the comparison of the data and simulated efficiencies is a major test of the simulated detector resolution.

The only difference between the decompositions and the signal efficiency measurements is the background subtraction method: while the combinatorial background in the reconstructed mass spectrum can be easily modeled for the signal extraction, the rather complicated shape of its dN/dx distribution needed for the decomposition has to be determined with the help of data events in the side bands of the mass spectrum.

The large background rates in the isoscalar D-meson channels do not allow a direct measurement of the signal efficiencies. To test the simulation also in these channels the

[8]The correlation between N_r and N_c is estimated for the error calculation with the ratio $\sigma(N_c)/\sigma(N_r)$ of the errors evaluated by the fits. A motivation for this estimation can be found in appendix E.

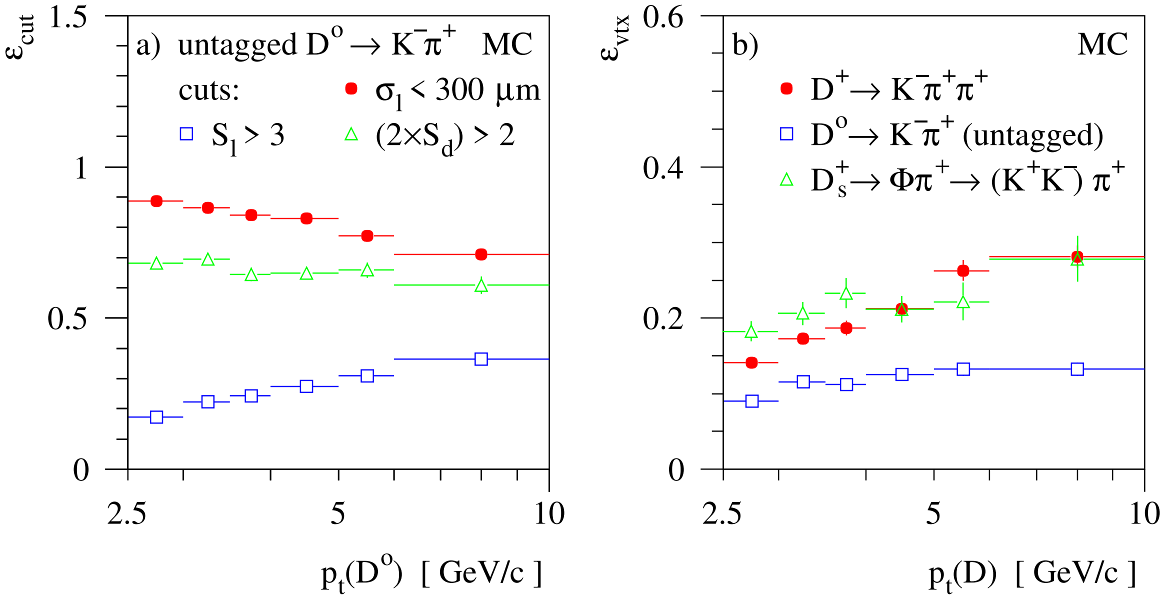

Figure 6.13: (a) *The efficiencies of the consecutively applied lifetime tagging cuts σ_l- (dots), S_l- (open squares) and last the $(2\times S_d)$-cut (open triangles) are determined in the $p_t(D)$ bins of the differential D^0 production cross section measurement with simulated charm decays.* **(b)** *The total efficiencies ε_{vtx} of the lifetime tag in the decay channels of the isoscalar D-mesons are shown as a function of $p_t(D)$.*

method already used for the decomposition is applied: for a reliable signal extraction the signal-to-background ratio in the reconstructed mass spectra is enhanced by requiring all conditions of the lifetime tag and only the cut in the variable under study is varied. The signal efficiency is then determined with respect to the signal extracted from the mass spectrum without a cut in the specific variable.

In figure 6.12 two examples of such measurements are given: the measured S_l-dependence of the D_s^+ signal efficiency ε_D (fig. 6.12a) and ε_D for untagged D^0 as a function of the $(2 \times S_d)$ cut value (fig. 6.12b) are shown. The relative difference between ε_D measured in data and with simulated decays is of the order of 10-20% which is mostly covered by the statistical error of the measurements.

6.4 Lifetime tagging efficiency

The efficiencies of the lifetime tag ε_{vtx} in the different channels, determined with simulated D-meson decays, are summarized in table 6.2, where also the efficiencies of the separate consecutive cuts (cf. tab. 6.1) are given.

It is interesting to see, whether the insights gained with the simplified D^0 decay model previously discussed are confirmed in decays processed by the full detector simulation and reconstruction chain. In figure 6.13a the efficiencies of the major lifetime tagging cuts in the untagged D^0 channel are shown as a function of the D-meson's transverse momentum $p_t(D)$.

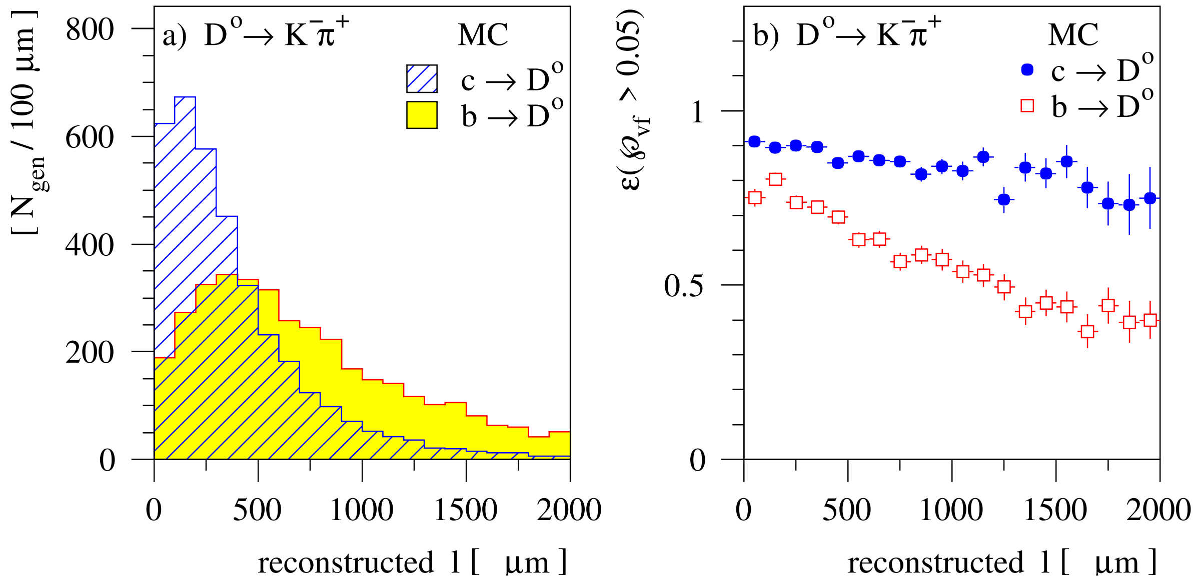

Figure 6.14: (a) *The reconstructed decay length spectra of simulated charm (hashed) and beauty decays (shaded) in the untagged D^0 channel are shown. The charm distribution is normalized to the integrated luminosity $\mathcal{L}$ of the data sample, while the beauty sample represents $20 \times \mathcal{L}$.* **(b)** *The efficiency of the $\mathcal{P}_{vf}$ cut decreases as a function of l faster for beauty (open boxes) than for charm decays (dots), because the directional constraint of* `VFit2dc` *is not necessarily met in the cascade decays of beauty quarks.*

As expected the requirement on σ_l rejects a larger fraction of events at higher momenta, because the decay length resolution deteriorates. On the other hand the efficiency of the S_l-cut rises nearly linearly with $p_t(D)$ which has also been predicted by the D^0 decay model. The $(2 \times S_d)$ efficiency has only a slight $p_t(D)$ dependence.

In figure 6.13b the total lifetime tagging efficiencies in the isoscalar D-meson channels are shown as a function of $p_t(D)$. The efficiency improves with rising $p_t(D)$ faster in the three body D^+ and D_s^+ decays, a factor two in the accessible kinematical range, than in the D^0 channel with only two decay particles, where only a slight increase can be seen. Rather small dependences of ε_{vtx} on $\eta(D)$ and the event kinematics are observed in all channels.

The mean lifetime of B-mesons is with $c\tau \approx 470\ \mu$m [17] even larger than for D-mesons. Because the decay length is reconstructed herein as the separation of the primary and secondary vertices, D-meson's produced in cascade decays of b quarks are enhanced at large l's as can be seen in figure 6.14a on the reconstructed l spectra of simulated charm and beauty decays in the untagged D^0 channel. The efficiencies of the S_l and $(2 \times S_d)$ cuts is therefore significantly higher for beauty events (cf. tab. 6.2).

But D-mesons produced in beauty decays are not necessarily in agreement with the directional constraint in `VFit2dc` which assumes the D-meson momentum direction to point back to the primary vertex. The probability of the `VFit2dc` fit is therefore low for beauty decays in which the D-meson and the initial b have significantly different momentum directions.

Lifetime tag efficiency [%]	D^+		D^0		D_s^+		D^{*+}	
	ε_c	ε_b	ε_c	ε_b	ε_c	ε_b	ε_c	ε_b
$\varepsilon_{\mathcal{P}_{\text{vf}}}$	81.9	60.6	86.2	58.9	80.3	57.3	85.8	62.4
$\varepsilon_{max(l)}$	99.6	99.5	99.4	99.0	99.7	99.7	99.3	99.1
ε_{σ_l}	88.3	86.8	83.9	83.2	75.7	76.0	81.3	80.9
ε_{S_l}	29.9	50.3	23.7	58.1	37.8	66.7	56.9	82.1
$\varepsilon_{(2\times S_d)}$	90.5	92.1	66.1	78.0	91.7	94.7	99.9	99.9
$\Pi\ \varepsilon$	19.5	24.1	11.3	21.9	21.0	27.5	39.4	41.1
$f_{\text{acp}}^{b/c} = N_{\text{acp}}^b / N_{\text{acp}}^c$	0.102		0.116		0.203		0.076	
$f_{\text{rec}}^{b/c} = N_{\text{rec}}^b / N_{\text{rec}}^c$	0.120		0.225		0.265		0.077	
ε_{vtx}	19.9		12.4		22.2		39.4	

Table 6.2: *The efficiencies of the consecutive lifetime tagging cuts (cf. tab. 6.1) are determined with simulated charm (ε_c) and beauty decays (ε_b) in the different decay channels. The beauty contents in the D-meson samples before ($f_{acp}^{b/c}$) and after the lifetime tag ($f_{rec}^{b/c}$) are determined with the* `AROMA` *program (cf. chap. 1) and are used in the calculation of the total efficiencies ε_{vtx} (see text).*

The efficiency of the $\mathcal{P}_{\text{vf}}$ cut in charm and beauty decays is shown in figure 6.14b as a function of the reconstructed decay length: it decreases for beauty decays with rising vertex separation, because the reconstructed decay direction becomes more accurate with an increasing length of the lever arm and therefore the directional constraint is more restrictive at large l's. The total efficiencies of the $\mathcal{P}_{\text{vf}}$ cut for charm and beauty are listed in table 6.2.

In total the beauty content $f_{\text{acp}}^{b/c} = N_{\text{acp}}^b / N_{\text{acp}}^c$ in D-meson decays inside the kinematical and geometrical acceptance is enhanced by the lifetime tag in the reconstructed D-meson samples in which the fraction of beauty to charm decays is denoted by $f_{\text{rec}}^{b/c} = N_{\text{rec}}^b / N_{\text{rec}}^c$. In table 6.2 the beauty contents in the different channels before and after the lifetime tag are listed. They have been determined with simulated charm and beauty decays, where the contributions of the latter have been scaled up by a factor of 4.3 as discussed in section 1.5.

In the D^{*+} sample the beauty content is inherently low due to the small $f(b \to D^{*+})$ fraction, while it is for the same reason rather high in the D_s^+ channel (cf. tab. 1.2). In both it is only moderately enhanced, because rather weak lifetime requirements are applied. In the D^+ and the untagged D^0 channel tight lifetime tagging cuts are necessary, but while the increase in $f_{\text{rec}}^{b/c}$ is just 20% for the long lived D^+ mesons, $c\tau(D^+) \approx 2/3 \cdot c\tau(B)$, the beauty content is enlarged in the reconstructed D^0 sample by a factor two due to the rather short lifetime of the meson: $c\tau(D^o) \approx 1/4 \cdot c\tau(B)$ (cf. tab. 1.2).

Because the measured cross sections include D-meson of both sources, charm and beauty

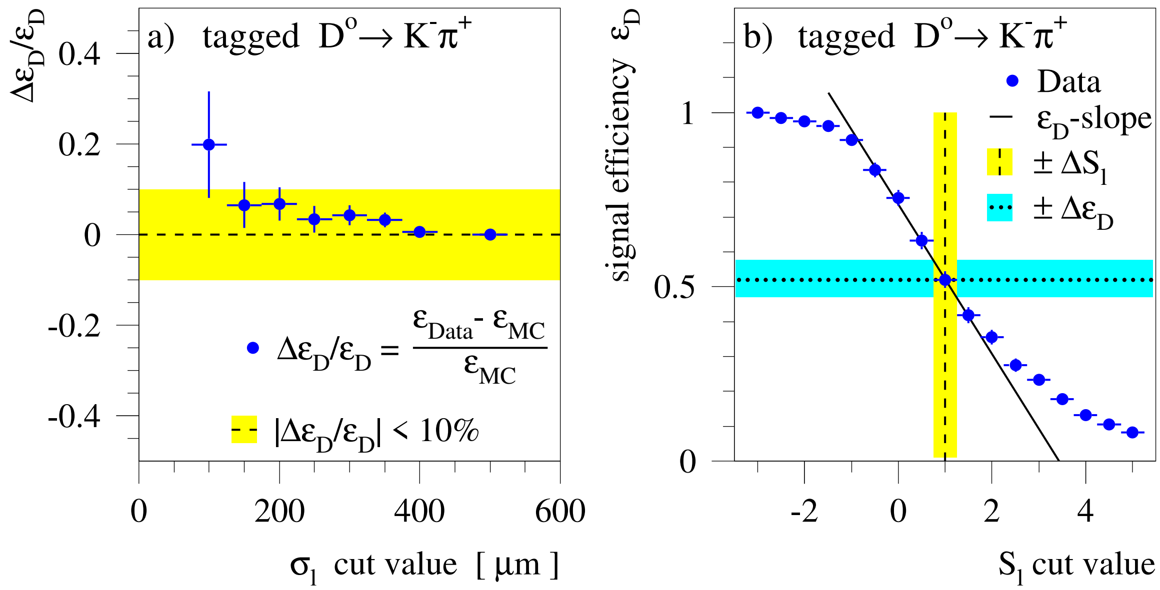

Figure 6.15: **(a)** *The relative difference in ε_D measured in data and simulated D^{*+} samples is shown as a function of the σ_l cut value. The shaded band indicates a systematic error of $\pm 10\%$.* **(b)** *The systematic error of the lifetime tag (dark shaded horizontal band) is estimated by propagating the error in σ_l (light shaded vertical band) into the signal efficiency ε_D of the S_l cut which depends on the measured slope of the ε_D curve indicated by the solid line.*

production, the efficiency of the lifetime tag is averaged according to the expected $f_{\rm rec}^{b/c}$ ratios in the reconstructed samples:

$$\varepsilon_{vtx} = \frac{N_{\rm rec}^c + N_{\rm rec}^b}{N_{\rm acp}^c + N_{\rm acp}^b} = \varepsilon_c \cdot \frac{1 + f_{\rm rec}^{b/c}}{1 + f_{\rm rec}^{b/c} \cdot \varepsilon_b/\varepsilon_c}, \tag{6.10}$$

where $\varepsilon_c = N_{\rm rec}^c/N_{\rm acp}^c$ and $\varepsilon_b = N_{\rm rec}^b/N_{\rm acp}^b$ denote the lifetime tagging efficiencies determined with charm, respectively beauty decays. The correction to ε_c is largest ($\sim 10\%$) in the untagged D^0 channel (cf. tab. 6.2).

6.5 Systematic errors

A straight forward way to estimate the systematic error of the lifetime tag would be to take the relative differences $\Delta\varepsilon_D/\varepsilon_D$ between the S_l cut efficiencies measured in data and simulated samples (cf. fig. 6.11c). But as discussed in section 6.3 this measurement depends strongly on the correct description of the kinematical sample composition in data and any discrepancy leads to an overestimation of the systematic error. Therefore a different approach is taken.

All major variables of the lifetime tag rely on an accurate error calculation: $S_l = l/\sigma_l$, $S_d = d/\sigma_d$ and also $\mathcal{P}_{\rm vf}$ depends indirectly on σ_d because the minimized χ^2 function is

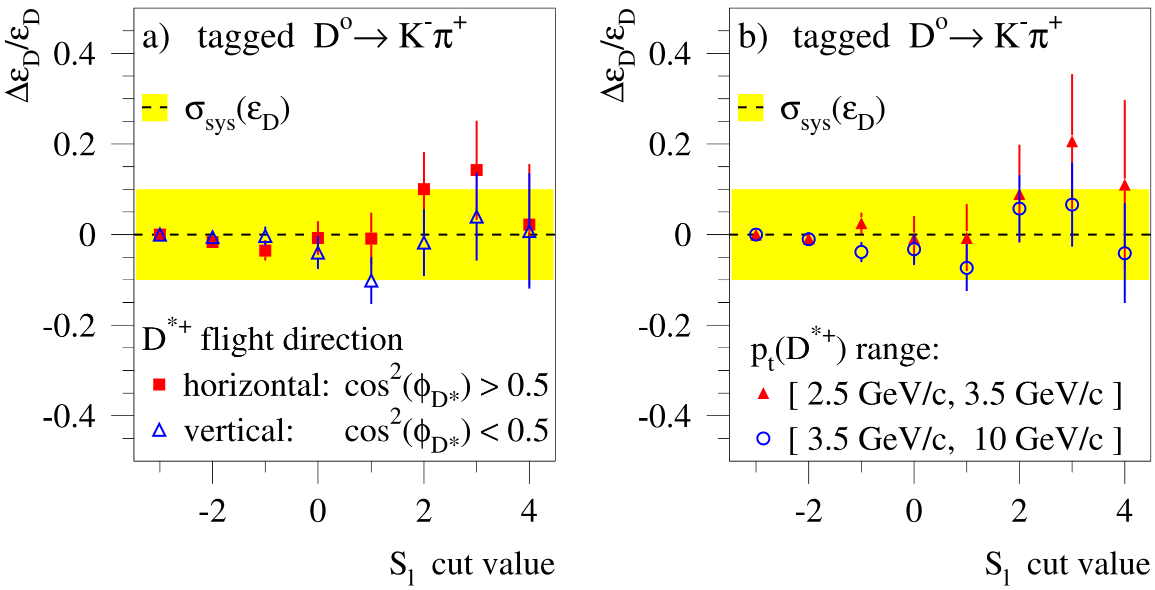

Figure 6.16: *To investigate any dependences of the systematic error $\sigma_{sys}(\varepsilon_D)$ (shaded bands) on the decay kinematics $\Delta\varepsilon_D/\varepsilon_D$ is measured as a function of S_l separately* **(a)** *for horizontal (solid boxes) and vertical D^{*+} decays (open triangles) and* **(b)** *in two different bins of the D^{*+} transverse momentum (low $p_t(D^{*+})$ solid triangles and high $p_t(D^{*+})$ open dots).*

inversely proportional to the covariance matrices of the input parameters. In addition σ_l has a weaker dependence on $p_t(D)$ in the accessible kinematical range than S_l (cf. sec. 6.4). Therefore the accuracy by which the simulation describes the σ_l distribution is a better measure for the lifetime tag's systematic error.

Thereto the σ_l distribution of signal events is scanned in the similar way as the S_l spectrum by determining the signal efficiency ε_D as a function of the maximal σ_l cut value. In figure 6.15a the relative signal efficiency difference $\Delta\varepsilon_D/\varepsilon_D$ between the measurements in data and simulated samples is shown as a function of the σ_l cut value for tagged D^0 mesons. The differences are well covered by the indicated error band and the maximal systematic error on σ_l can therefore be estimated by 10%.

The systematic error of the lifetime tag can then be found by propagating this error in σ_l into the signal efficiency of the major tagging variable $S_l = l/\sigma_l$. The size of the systematic error $\Delta\varepsilon_D$ in ε_D depends therefore on the slope of the efficiency curve at the S_l cut value as indicated in figure 6.15b: a systematically wrong calculation of S_l by $\pm\Delta S$ is equivalent to a $\pm\Delta S$ shift of the applied cut value (shaded vertical band). $\Delta\varepsilon_D$ is then given by the difference of the measured ε_D for the nominal and the shifted cut values (shaded horizontal band).

The similar method is also applied in the other decay channels and the relative systematic errors on the signal efficiency, which directly propagates into the systematic error on the measured cross sections, are found to be well covered by $\pm10\%$.

The dependences of the systematic error on the decay kinematics are of interest especially with respect to the differential cross section measurements. Thereto $\Delta\varepsilon_D/\varepsilon_D$ measured in subsets of the data and simulated D-mesons samples are compared. Two examples are shown in figure 6.16: the dependence of $\Delta\varepsilon_D/\varepsilon_D$ on the S_l cut value is measured separately for horizontal and vertical decays (fig. 6.16a) and in two different bins of $p_t(D)$ (fig. 6.16b) for tagged D^0 mesons. Due to the asymmetric beam spot the former tests the accuracy by which the simulation describes the `CSPRIM` primary vertex determination which plays a crucial role in the lifetime tag and which depends on a correct simulation of the full hadronic final state. Similar to the shown examples no indications for any dependence of $\Delta\varepsilon_D/\varepsilon_D$ on the decay or the event kinematics are found.

Chapter 7

Measurement Results

The basic quantities measured herein are the D-meson production cross sections in deep inelastic ep-scattering within the visible kinematical range the definition of which is motivated by the acceptance of the H1 detector. Exploiting the finite lifetimes of the D-mesons a consistent measuring method can be applied to all D-meson states. The production rates measured inclusively and as a function of variables describing the D-meson and event kinematics are discussed in the first part of the chapter.

The consistent measuring method in all channels invites the measurement of fragmentation ratios (FR) in which most of the systematic uncertainties cancel: the FR put the rates by which the different D-meson states are produced into relation. Because they have already been measured at e^+e^- annihilation experiments with high precision, they allow a comparison of the fragmentation process in e^+e^-- and ep-scattering and therefore the assumed universality of the fragmentation process can be tested.

7.1 D-meson production cross sections

In the following the measured D-meson production cross sections $\sigma_{vis}(ep \to eDX)$ in the visible range, defined by $p_t(D) \geq 2.5$ GeV/c, $|\eta(D)| \leq 1.5$, 2 GeV$^2 \leq Q^2 \leq 100$ GeV^2 and $0.05 \leq y \leq 0.7$, are discussed. In table 7.2 the results of the signal extractions from the mass spectra are given which are used for the inclusive cross section measurements summarized in table 7.3. The systematical errors of these measurements are listed in table 7.4. The details of the differential results shown in the following can be found in appendix A.

The well established D^{*+} production cross section serves herein as a reference measurement and as a comprehensive test for the complete analysis chain including the lifetime tag. After having proven the reliability of the measuring method the results in the previously unaccessible decay channels are discussed: beginning with the D_s^+ channel with rather limited statistics and only a moderate signal quality, the untagged D^0 and, for the first time at HERA, also the D^+ production cross sections are presented in which sound signals of good quality are available due to the lifetime tagging method.

$\sigma_{\mathbf{vis}}(\mathbf{ep} \to \mathbf{e'D^{*+}X})$ **by means of the CJC**	$p_t(D^{*+})$ cut [GeV/c]	Q^2 range [GeV^2]	σ_{vis}	± stat. [nb]	± syst.
this measurement			6.30	±0.42	
published value [14]	≥ 1.5	[1, 100]	8.50	±0.42	$^{+1.20}_{-1.00}$
AROMA LO + PS prediction			6.12	±0.74	
this measurement			5.28	±0.42	
published value [12]	≥ 1.5	[2, 100]	5.75	±0.35	±0.79
AROMA LO + PS prediction			5.53	±0.66	
this measurement			3.97	±0.25	
published value [15]	≥ 2.0	[2, 100]	4.20	±0.90	
AROMA LO + PS prediction			3.86	±0.46	
by means of the CJC			2.90	±0.19	$^{+0.56}_{-0.37}$
by means of the CST	≥ 2.5	[2, 100]	2.90	±0.20	$^{+0.58}_{-0.44}$
AROMA LO + PS prediction			2.61	±0.31	

Table 7.1: *The D^{*+} production cross sections measured by means of the CJC alone are compared to previously published H1 measurements and the value measured by means of the CST. The visible range of the measurements is defined by $0.05 \leq y \leq 0.7$, $|\eta(D^{*+})| \leq 1.5$ and the different minimal $p_t(D^{*+})$ cuts and Q^2 ranges quoted.*

7.1.1 D^{*+} production

The D^{*+} cross section has already been measured previously in similar kinematical ranges. These measurements are redone by means of the CJC alone and compared to the published values to put the present measurement on solid grounds. Once the CJC analysis chain has been established, the D^{*+} cross section measurement is repeated with a lifetime tagged D^{*+} sample as a comprehensive test for the lifetime tagging method.

Comparisons with published measurements

The kinematical ranges of the published H1 D^{*+} production cross section measurements in [12, 14, 15] differ from the visible range definition with respect to the minimal $p_t(D^{*+})$ cut and the Q^2 range. The exact range definitions are quoted in table 7.1. The measurements of σ_{vis} in these very ranges is repeated and therefore the comparison is independent from any extrapolations based on calculated QCD predictions.

The published and the presented D^{*+} measurements differ in two respects: the HERA center of mass energy was augmented in 1998 from $\sqrt{s} = 300$ GeV to $\sqrt{s} = 318$ GeV which leads to an expected rise of 6% in σ_{vis} and the kaon and pion from the D^0 decay

Fit results	χ^2/ndf	N_D	$m(D)$ [MeV/c^2]	$\sigma(D)$ [MeV/c^2]	$B_{2\sigma}$	$N_D/B_{2\sigma}$
D^+	12.5/14	350 ± 31	1869.0 ± 2.2	23.9 ± 2.2	284 ± 25	1.23 ± 0.15
D^0	15.5/18	408 ± 31	1863.9 ± 3.5	33.6 ± 3.0	414 ± 36	0.99 ± 0.11
D_s^+	14.6/19	78 ± 19	1968.6 ± 6.7	26.2 ± 6.3	133 ± 31	0.59 ± 0.20
D^{*+} (CJC)	13.6/18	1101 ± 70	1861.9 ± 1.9	31.8 ± 2.2	1502 ± 94	0.73 ± 0.07
D^{*+} (CST)	26.9/18	468 ± 32	1865.9 ± 2.1	30.0 ± 2.1	205 ± 15	2.28 ± 0.23

Table 7.2: *The fit results of the signal extractions with the reconstructed mass spectra are listed for the different decay channels: the fitted χ^2/ndf values, the numbers of signal events N_D, the means $m(D)$ and widths $\sigma(D)$ of the signal Gaussians, the numbers of background events $B_{2\sigma}$ within a 2-σ window below the signal and the signal-to-background ratio $N_D/B_{2\sigma}$ are quoted.*

are requested herein to be within the acceptance of both CST layers to be comparable with the CST measurements, while in the published results all candidates within the CJC acceptance have been considered.

The results of the measurements are listed in table 7.1 and good agreement with the published values and also with the quoted `AROMA` leading order QCD (LO) predictions, which include also a Parton Shower (PS) evolution, is found. The present measurement tends to be slightly lower, especially with respect to the most recent publication [14]. But regarding the rather large systematic errors which have been determined only for the visible range used herein and which are expected to be even larger for $Q^2 < 2$ GeV^2 due to the limited SpaCal acceptance, the values agree within about one standard deviation.

Comparison between CJC and CST measurements

The $m(K\pi)$ and Δm spectra of the D^{*+} sample reconstructed in the visible range by means of the CJC and by means of the CST lifetime tag are shown in figure 7.1. The signal loss, but also the obvious improvement of the signal quality seen in the spectra can be quantified by comparing the results of the signal extraction quoted in table 7.2: the signal is reduced in the lifetime tagged sample by a factor 2.4, while at the same time the signal-to-background ratio $N_D/B_{2\sigma}$ is enhanced from 0.73 to 2.28 by a factor 3.1.

The cross sections measured with these two sample, which allow a comprehensive test of the CST detector simulation with respect to the detector efficiency and the lifetime tag, are quoted in table 7.1. The results are identical by chance and compare well with the quoted prediction of the LO `AROMA` calculation.

The good agreement between the CJC and CST measurements is on the other hand not too surprising, because the CJC D^{*+} sample has been used to calibrate the simulated CST efficiency and the measured signal efficiencies of the lifetime tag have already been compared to the simulation in the previous chapter and a good agreement was found. Interesting to note is that the relative statistical errors of the two measurements are

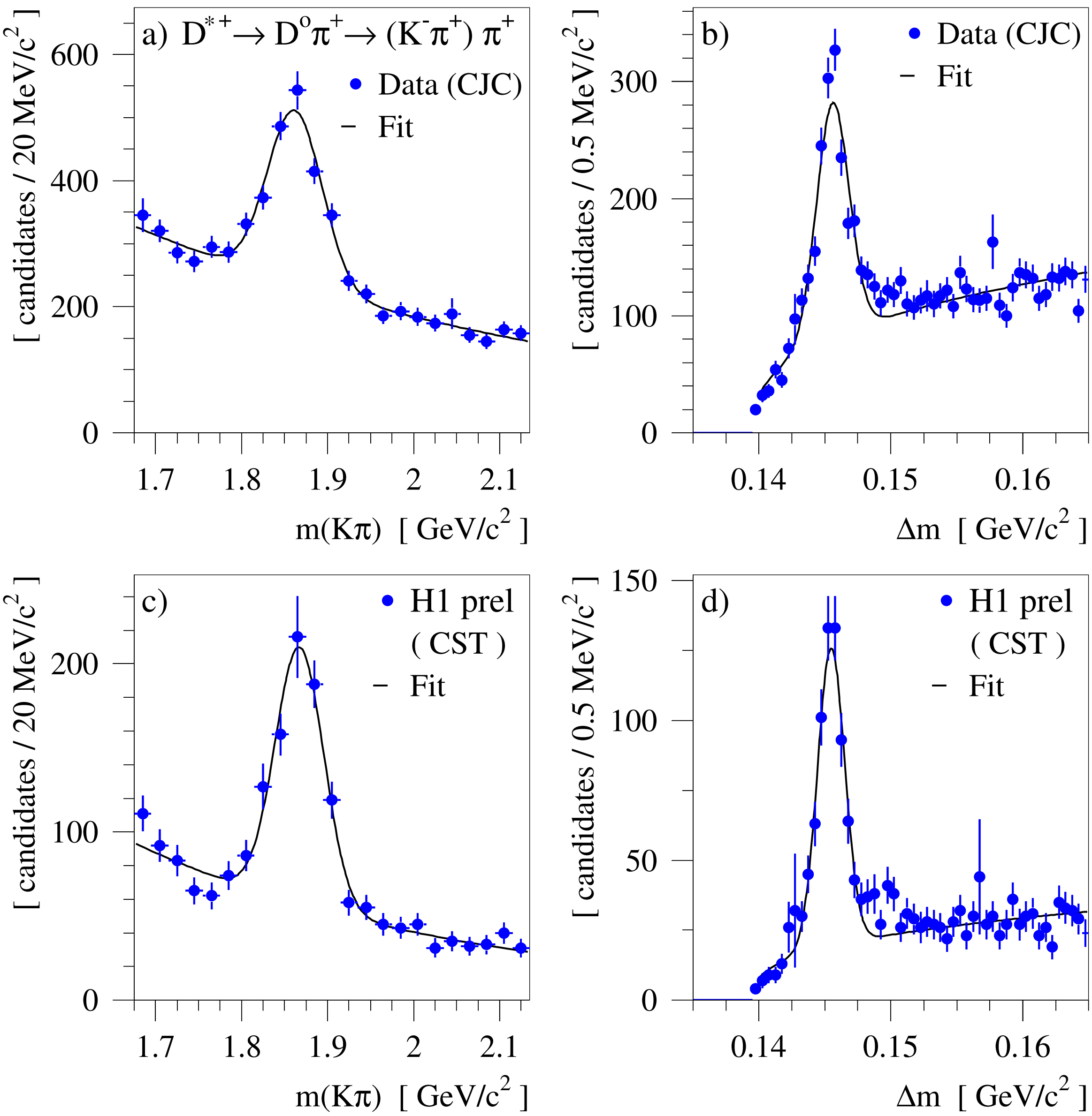

Figure 7.1: *(a,c) The $m(K\pi)$ spectra within a ± 3.6 MeV/c^2 window around the nominal Δm mass difference and (b,d) the Δm distributions after a 2-σ cut in $m(K\pi)$ are shown for D^{*+} candidates reconstructed by means of the CJC alone (a,b) and by means of the CST lifetime tag (c,d).*

equivalent, i.e. the larger error expected due to the signal loss is just compensated by the reduced uncertainty in the subtraction of the diminished background in the CST sample.

Though in the CST measurement additional sources of systematic errors which are summarized in table 7.4 have to be considered: besides the rather large errors introduced by the CJC efficiency and SpaCal energy calibration which enter both measurements, the systematics of the lifetime tag and the CST efficiency are the dominant error sources in the CST cross section measurements, while the simulated detector resolution and the error due to the signal extraction are of minor importance in the D^{*+} channel. The CJC

Cross sections [nb]	D^+	D^0	D_s^+	D^{*+}
$\sigma_{vis}(ep \to eDX)$	2.16	6.53	1.67	2.90
stat. error on σ_{vis}	±0.19	±0.49	±0.41	±0.20
syst. error on σ_{vis}	$^{+0.46}_{-0.35}$	$^{+1.06}_{-1.30}$	±0.54	$^{+0.58}_{-0.44}$
AROMA LO prediction σ_{vis}	2.45	5.54	1.15	2.61
uncertainty of the prediction	±0.30	±0.69	±0.30	±0.31
estimated beauty content	$10 \pm 3\%$	$9 \pm 3\%$	$17 \pm 7\%$	$7 \pm 2\%$

Table 7.3: *The D-meson production cross sections measured by means of the CST in the visible kinematical range, defined by* $p_t(D) \geq 2.5$ GeV/c, $|\eta(D)| \leq 1.5$, $2\ \mathrm{GeV}^2 \leq Q^2 \leq 100\ \mathrm{GeV}^2$ *and* $0.05 \leq y \leq 0.7$, *are quoted for the different D-meson states. The statistical and systematical errors of the measurements are quoted, where the latter are listed according to their sources in table 7.4 below. The uncertainties on the predictions of the cross sections and beauty contents, estimated by LO calculations, contain the model dependences and the uncertainties of the beauty normalization and the fragmentation fractions (see text and sec. 1.5).*

Source of Uncertainty [%]	D^+	D^0	D_s^+	D^{*+}
acceptance	$< \pm2.0$			
CJC efficiency	$^{+15.0}_{-3.0}$	$^{+10.0}_{-2.0}$	$^{+15.0}_{-3.0}$	$^{+15.0}_{-3.0}$
CJC resolution ($\pm10\%$)	$^{+3.0}_{-1.5}$	$^{+0.6}_{-0.7}$	$^{+1.8}_{-3.7}$	$^{+2.4}_{-0.5}$
CST efficiency	±5.6	±3.6	±5.4	±3.6
CST resolution ($\pm20\%$)	$^{+2.0}_{-1.0}$	$^{+0.4}_{-0.1}$	$^{+0.1}_{-3.6}$	$^{+1.5}_{-0.2}$
lifetime tag	±10.0			
SpaCal calibration ($\pm4\%$)	$^{+3.6}_{-7.3}$	$^{+3.4}_{-8.1}$	$^{+4.5}_{-7.8}$	$^{+4.5}_{-9.0}$
signal extraction	$^{+1.7}_{-0.4}$	$^{+4.9}_{-13.4}$	$^{+1.4}_{-12.1}$	$^{+3.7}_{-3.2}$
branching ratio	±6.7	±2.3	±24.7	±2.3
ISR correction	±2.6			
ST efficiency	±1.0			
total systematic error	$^{+21.2}_{-16.0}$	$^{+16.5}_{-19.9}$	$^{+32.0}_{-31.8}$	$^{+20.0}_{-15.2}$

Table 7.4: *The relative systematic errors on the production cross section measurements are listed in percent according to their sources for the different decay channels.*

measurement suffers on the other hand from an unclear signal extraction reflected by a relative systematic error of +10% (cf. sec. 5.3).

These results implicate that the inclusive CJC D^{*+} cross section measurement is not improved by the CST due to the lower signal efficiency and the additional errors introduced by the lifetime tag, even though the signal quality can be enhanced significantly.

Differential cross section measurements

In addition to the comparison of the inclusive D^{*+} cross sections, the dependences of σ_{vis} on variables describing the D-meson and the event kinematics are measured by means of the CJC alone and compared to the results obtained with the lifetime tagged sample. This comparison tests the reliability of the simulation to describe the respective dependences of the CST efficiencies accurately.

The results are shown in figure 7.2: the CJC measurements are indicated as solid lines with shaded error bands representing the statistical errors. The differential cross sections measured with the CST lifetime tagged D^{*+} sample are plotted as solid dots, where the inner error bars represent the statistical and the outer the quadratically summed statistical and systematical errors. The almost identical systematical uncertainties of the CJC measurement are not shown.

The dependences measured with and without CST information are in very good agreement for all tested variables: the transverse momentum $p_t(D^{*+})$ and pseudo rapidity $\eta(D^{*+})$ spectra which describe the D^{*+} kinematics (fig. 7.2a,b), the distribution of the azimuthal angle $\phi(D^{*+})$ expected to be flat for an reliable simulation (fig. 7.2c) and the variables Q^2, y and x_{Bj} describing the kinematics of the ep scattering process (fig. 7.2d-f).

From these comparison can be concluded that the simulation describes all crucial dependences of the CST detector and lifetime tagging efficiencies accurately, because they all enter into these differential CST cross section measurements.

In figure 7.3 the measured differential cross sections are compared to QCD predictions. The LO calculation with the `AROMA` program, described in detail in section 1.5, uses the GRV-98-LO proton structure functions and a charm mass of 1.5 GeV/c^2. The fragmentation process is described by the Parton Shower model in the perturbative regime and by the Lund String model including the Peterson fragmentation function for the confinement ruled hadronization process. Subsequent decays of particles produced in the fragmentation process, e.g. $B \to D$ or $D^{*+} \to D^0\pi^+$, are fully simulated.

The calculated central values are indicated in figure 7.3 by solid lines and the dark shaded error bands represent the model dependences of the prediction, mainly the uncertainties of the fragmentation process and the charm mass. The included contribution of D-mesons produced in cascade decays of b quarks, shown separately as dashed lines with bright shaded bands indicating the model dependences, has been scaled by a factor of 4.3 as recently published by H1 [40] and the measurement's relative error of 30% is added to the uncertainties of the prediction (cf. sec. 1.5).

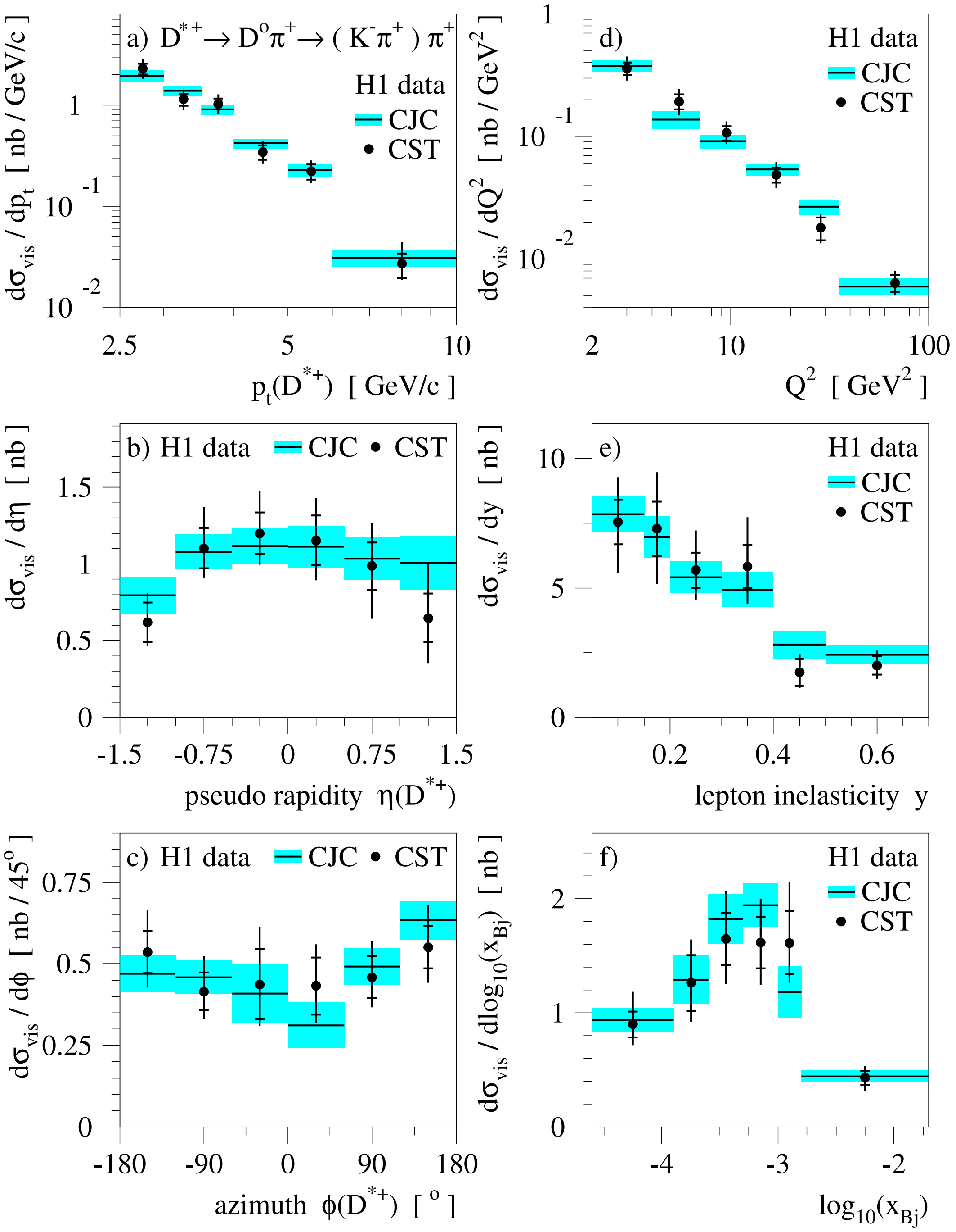

Figure 7.2: *The D^{*+} production cross section measured by means of the CST (dots) is compared to the measurements by means of the CJC alone (solid lines) in bins of kinematical D^{*+} variables* **(a-c)** *and of variables describing the event kinematics* **(d-f)**. *The error bars of the CST measurements are of statistical and systematical nature, while for the CJC measurements the shaded bands represent the statistical errors only.*

The HVQDIS program, also described in more detail in section 1.5, is based on next-to-leading order QCD calculations (NLO), supplemented by a Peterson fragmentation with $\varepsilon_c = 0.036$. The proton structure functions (GRV-98-HO) and charm mass are used consistent with the AROMA calculations. But HVQDIS includes neither a perturbative evolution of the fragmentation functions nor the cascade decays of particles produced in the fragmentation process.

Therefore HVQDIS can predict only the contribution of D^{*+}-mesons produced directly in the fragmentation process and for the beauty contribution the LO calculation is used. In figure 7.3 only the central values of the calculations are indicated as dotted lines because the model dependences are expected to be similar to the ones of the LO calculations.

The LO and NLO calculations agree very well in their inclusive[1] and in their differential cross section predictions as can be seen from figure 7.3. This can be attributed to the consistent sets of proton structure functions used for the calculations, because the evolution of the structure function at a fixed order compensates partially for higher order corrections and therefore the difference between LO and NLO is expected to be small.

The residual differences between the LO and NLO prediction, e.g. the different slopes of the $p_t(D^{*+})$ spectrum, may origin in the different treatment of the fragmentation process: in the LO calculation the parton shower accounts for the perturbative evolution of the fragmentation function which leads via gluon emissions of the heavy quark to a softer $p_t(D^{*+})$ spectrum.

No such evolution is made in the NLO calculation. Because the quoted Peterson parameter has been determined with recent LEP data under consideration of such an evolution [31], the HVQDIS calculations are valid only under the assumption that the corrections from the evolution are negligible which holds only at small $p_t(D^{*+})$ and could lead to the disagreements seen at higher momenta.

A large amount of isoscalar D-meson are produced in cascade decays of excited spin states and no comparisons between data and NLO are made in these channels, because HVQDIS does not include such subsequent decays which lead to different spectra of the cross sections. But the good agreement between the LO and NLO prediction seen in the D^{*+} channel indicate that a comparison with LO calculations is sufficient.

As can be seen from figure 7.3 the data is very well described by the QCD predictions in all variables characterizing the D-meson and event kinematics. Even the $p_t(D^{*+})$ and $\eta(D^{*+})$ spectra, in which previously slight disagreements between data and QCD predictions have been seen [14], agree within the errors of the measurements and the uncertainties of the prediction. The good agreement can be attributed to the more recent sets of proton structure functions used for the calculations which include the latest HERA measurements.

Only in the distribution of the inelasticity $z_e(D^{*+})$ shown in figure 7.3c, which is a measure of the momentum fraction transfer from the photon to the D-meson and which is sensitive to the hardness of the fragmentation process (cf. sec. 1.4), a slightly softer spectrum as expected is seen.

[1] The charm contribution to the D^{*+} production cross section in the visible range is predicted with 2.43 nb (LO) and 2.55 nb (NLO).

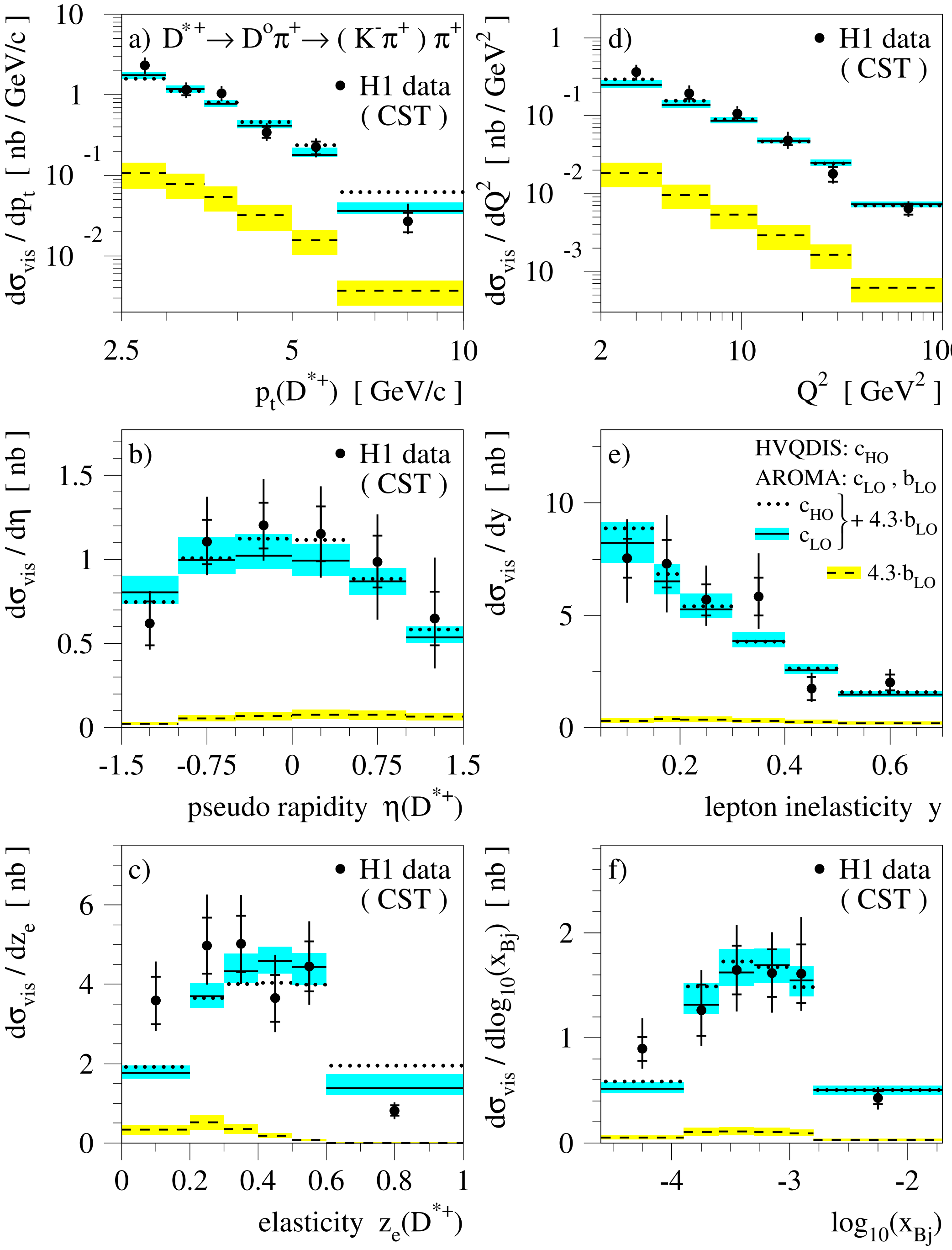

Figure 7.3: *The D^{*+} production cross section measured by means of the CST is shown in bins of kinematical D^{*+} variables* **(a-c)** *and of variables describing the event kinematics* **(d-f)**. *The data (dots) are compared to LO (dark shaded, central values as solid lines) and NLO QCD calculations (only central values as dotted lines). The contribution of D^{*+} mesons produced in b quark cascade decays (light shaded, central values as dashed lines) is calculated in LO only and its normalization is scaled by a factor 4.3 (see text).*

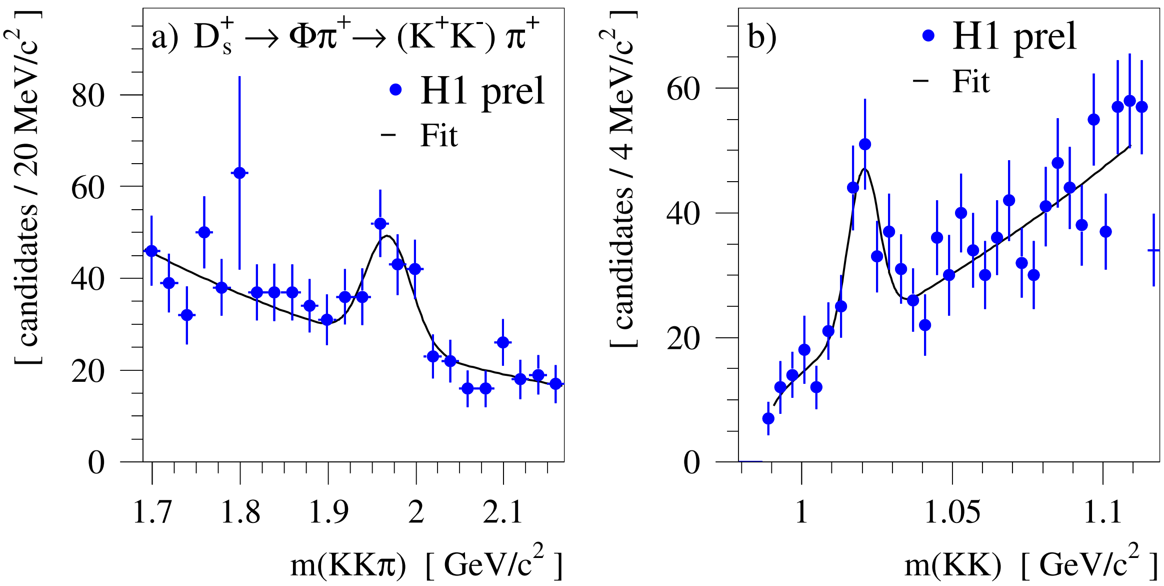

Figure 7.4: (a) *The $m(KK\pi)$ mass distributions of D_s^+ candidates and* **(b)** *the $m(KK)$ spectrum of the intermediate Φ-resonance candidates are shown for H1 preliminary data (dots). The functions indicate the fit results of the signal extraction.*

7.1.2 D_s^+ production

The D_s^+ signal used for the cross section measurement is shown in figure 7.4. The results of the signal extraction from the $m(KK\pi)$ spectrum is given in table 7.2. The size of the signal is smaller compared to the other channels and also the signal-to-background ratio is rather poor out of several reasons:

- The production of strangeness in the fragmentation process is suppressed due to the higher s quark mass compared to the up and down quarks.
- Even if the analyzed D_s^+ decay channel is the most frequent into charged particles only, its branching ratio $BR(D_s^+ \to (\Phi \to K^+K^-)\pi^+)$ is rather small (cf. tab. 1.2).
- Due to the small opening angles of the kaons produced in the Φ decay the D_s^+ mass resolution is very sensitive to the momentum calibration [64]. Therefore the decay channel suffers most under the incomplete detector calibration. Thus tight selection criteria on the decay particles' momenta leading to a small kinematical acceptance are necessary for a reasonable signal quality.
- Being a three body decay the detector efficiency is lower than for the decays into two particles only.
- The mean D_s^+ lifetime is only half as large as $c\tau(D^+)$ (cf. tab. 1.2) and only weak lifetime tagging requirements are possible due to the limited statistics to enhance the signal quality.

The resulting D_s^+ production cross section is given in table 7.3. The measured value is higher than the LO expectation, but considering the large statistical and systematical

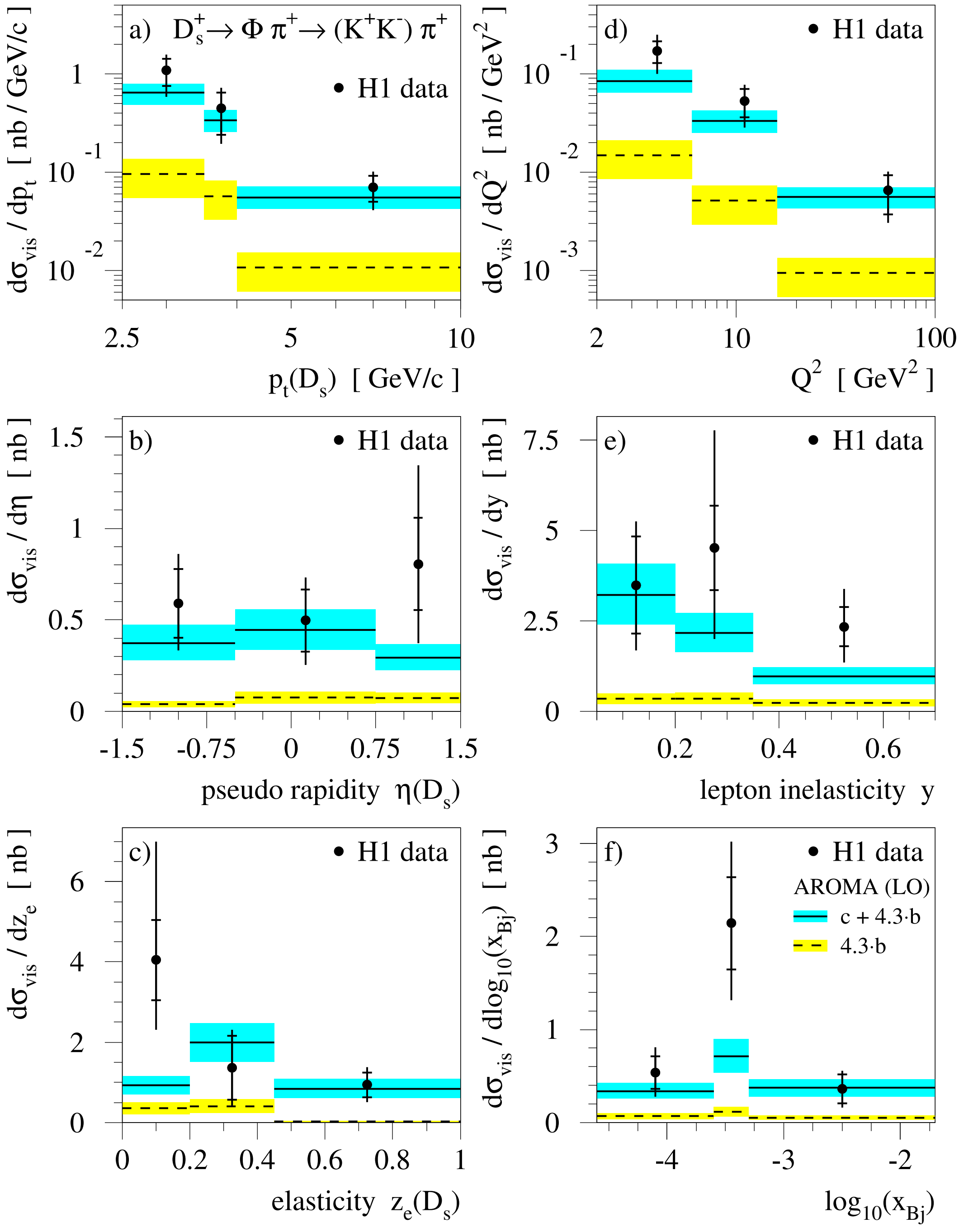

Figure 7.5: *The D_s^+ production cross section measured by means of the CST is shown in bins of kinematical D_s^+ variables* **(a-c)** *and of variables describing the event kinematics* **(d-f)**. *The data (dots) are compared to leading order calculations (dark shaded), where the calculated contribution of D_s^+ mesons produced in cascade decays of b quarks (light shaded) is scaled by a factor 4.3 (cf. sec. 1.5).*

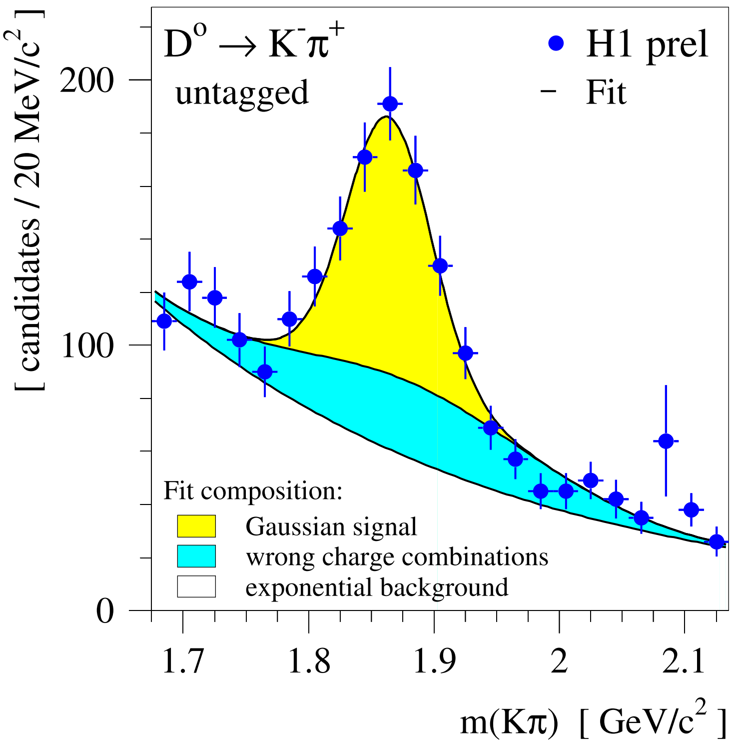

Figure 7.6: *The $m(K\pi)$ spectrum is shown for untagged D^0 meson candidates. The decomposition of the data (dots) into correctly assigned signal events (bright shading), the wrong charge combinations (dark shading) and the exponential background is separately indicated.*

errors well compatible with it. The large systematic error arises mainly from the relative uncertainty of 25% in the branching ratio of the decay [17].

Also the uncertainty of the LO prediction is larger than in the other channels, because of the large error in the fragmentation factor (cf. tab. 1.2). In addition the expected beauty contribution to σ_{vis} is with $17 \pm 7\%$ about twice as large than in the other channels (cf. tab. 7.3) and is afflicted with a considerable error.

The differential cross section measurements shown in figure 7.5 have due to the large statistical errors only limited significance. Still a good agreement can be seen. Similar to the D^{*+} channel an enhancement towards small elasticities $z_e(D_s^+)$ is visible (see fig. 7.5c).

7.1.3 D^0 production

The $m(K\pi)$ spectrum of the untagged D^0 meson candidates used for the cross section measurement is shown in figure 7.6. The fit model of the signal extraction has been discussed in detail in section 5.3.

The result of the signal extraction is given in table 7.2. The signal contains 408 ± 31 D^0 events over a combinatorial background of a similar size. The fitted mean is in very good agreement with the world average value of the D^0 meson mass, while the fitted width

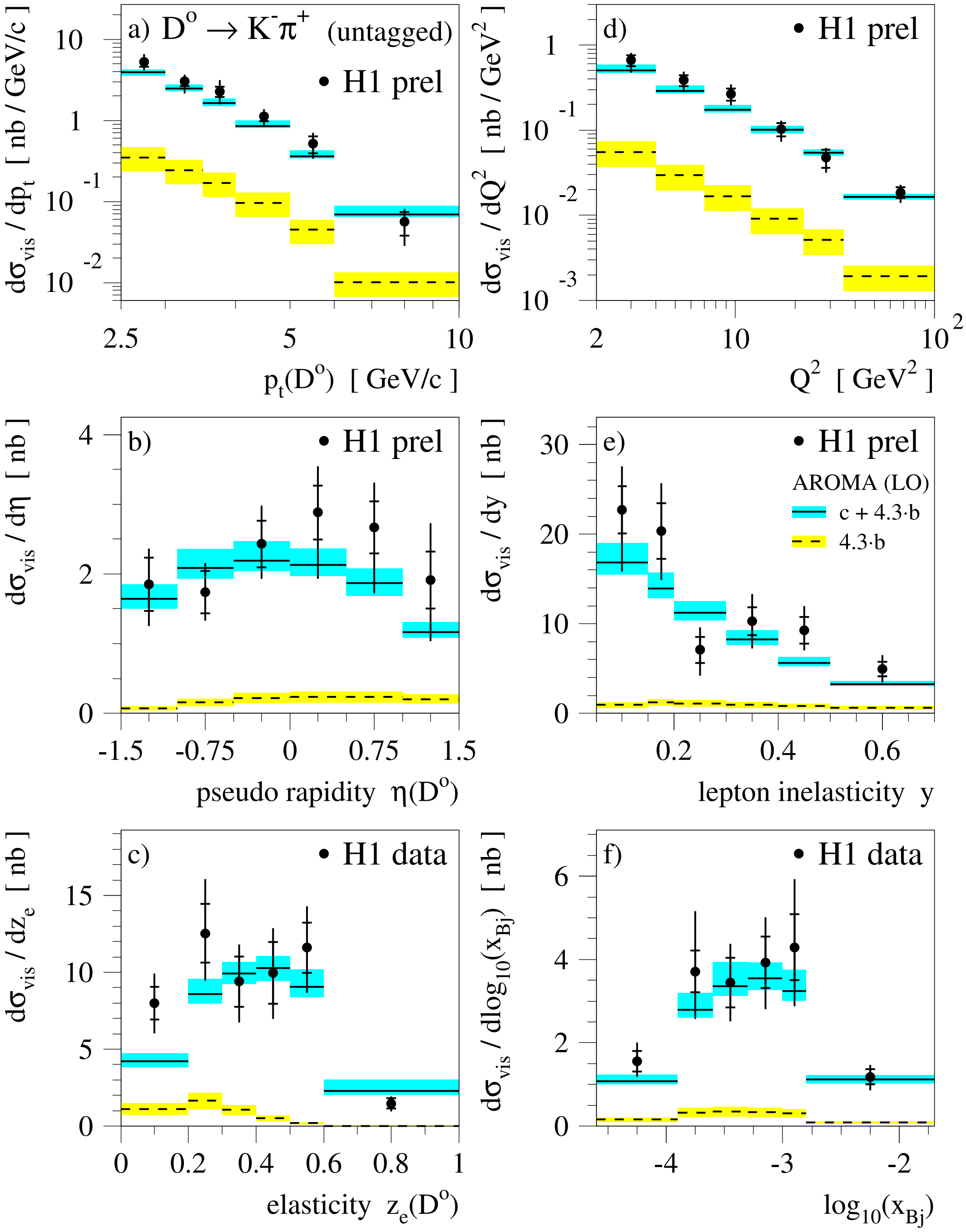

Figure 7.7: *The D^0 production cross section measured by means of the CST is shown in bins of kinematical D^0 variables* **(a-c)** *and of variables describing the event kinematics* **(d-f)**. *The data (dots) are compared to leading order calculations (dark shaded), where the calculated contribution of D^0 mesons produced in cascade decays of b quarks (light shaded) is scaled by a factor 4.3 (cf. sec. 1.5).*

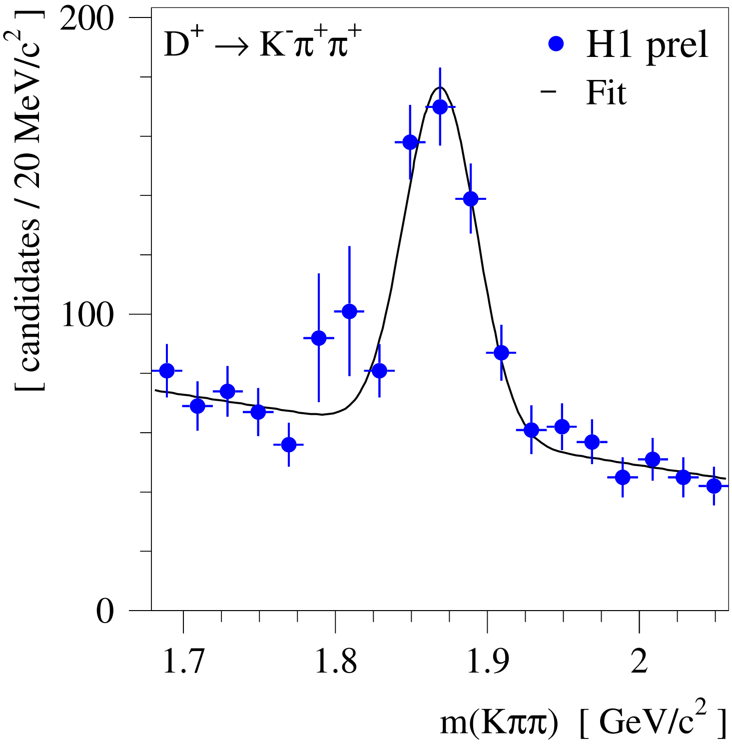

Figure 7.8: *The $m(K\pi\pi)$ mass spectrum of D^+ candidates (dots) and the fit result of the signal extraction are shown. The two high bins with large errors to the left of the signal peak contain both one D^+ candidate with event weight 20 (see text).*

of 33.6 ± 3.0 MeV/c^2 is larger than the expectation of 26 MeV/c^2 seen with simulated decays. This discrepancy in the mass resolution is attributed to the incomplete detector calibration.

The result of the D^0 production cross section measurement can be found in table 7.3. The dominant error of the measurement is of systematical nature, where the main sources are (cf. tab. 7.4): the CJC track efficiency, the SpaCal energy calibration, the lifetime tag systematics and also the signal extraction due to the complicated background situation: if a linear function is used instead of the exponential function to model the combinatorial background, a 13.2% smaller signal is extracted with a worse, but still acceptable χ^2/ndf value of 26/18.

The inclusive D^0 cross section measurement is slightly higher than the LO prediction (cf. tab. 7.3), but they agree still within less than one σ. Also the differential cross section measurements shown in figure 7.7 are in good agreement in all major variables describing the D^0 and event kinematics. Again the only minor discrepancy is seen at small elasticities $z_e(D^0)$, where the calculations underestimate the data.

7.1.4 D^+ production

In figure 7.8 the $m(K\pi\pi)$ spectrum of D^+ candidates is shown which is used for the first D^+ production cross section measurement at HERA. The result of the signal extraction

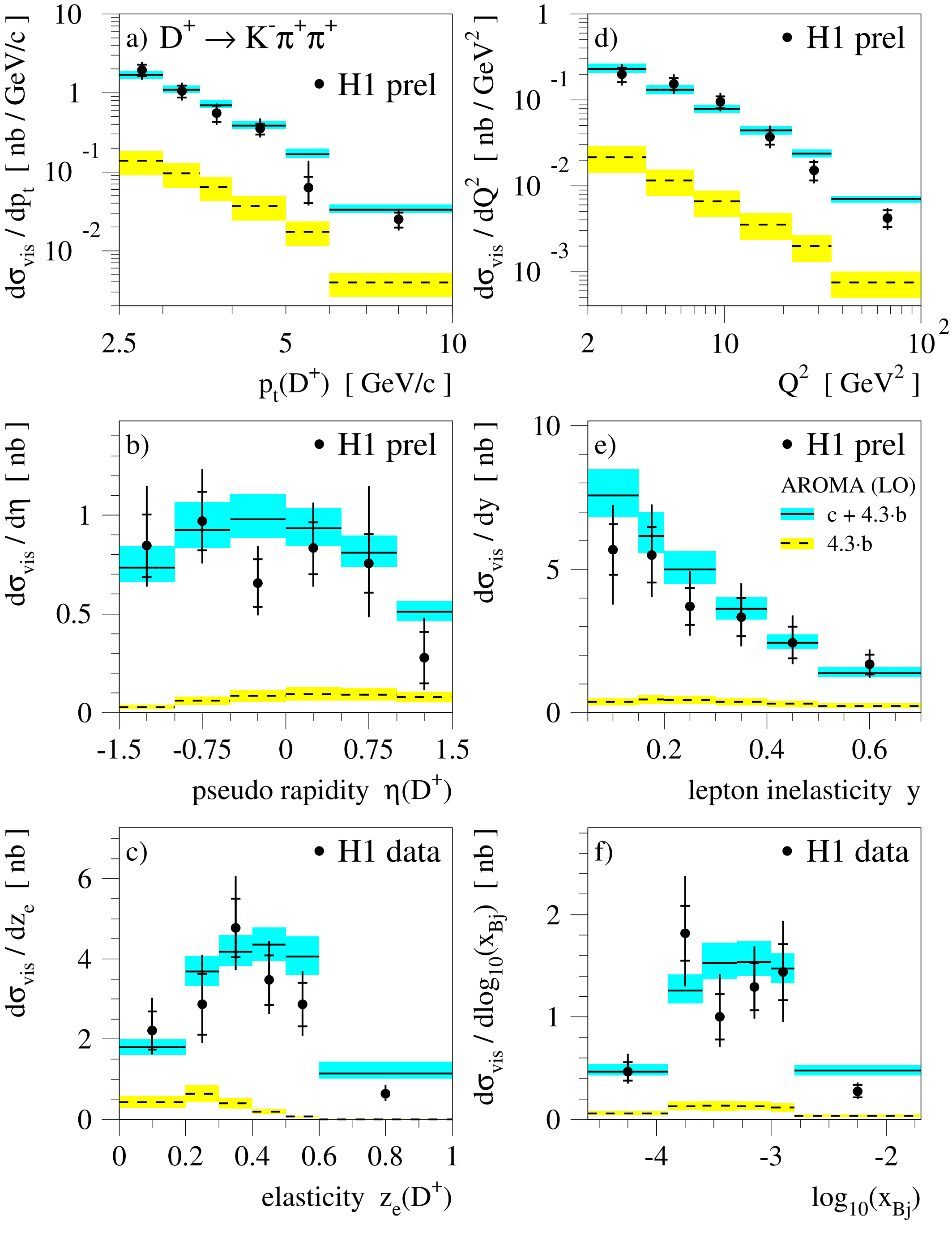

Figure 7.9: *The D^+ production cross section measured by means of the CST is shown in bins of kinematical D^+ variables* **(a-c)** *and of variables describing the event kinematics* **(d-f)***. The data (dots) are compared to leading order calculations (dark shaded), where the calculated contribution of D^+ mesons produced in cascade decays of b quarks (light shaded) is scaled by a factor 4.3 (cf. sec. 1.5).*

with a good χ^2/ndf value of 12.5/14 is given in table 7.2: the well pronounced D^+ signal contains 350 ± 31 signal events with an excellent signal-to-background ratio of about 1.23. The fitted D^+ mass is in very good agreement with the world average value of $m(D^+) = 1869.3 \pm 0.5$ MeV/c^2 [17]. The fitted width is only slightly higher than the mass resolution of 21 MeV/c^2 found with simulated decays.

The two high bins with large errors to the left of the signal peak at $m(K\pi\pi) \approx 1.8$ GeV/c^2 contain both one D^+ candidate with an event weight of 20. As discussed in section 4.2 the event weights origin from the prescaling procedure on Level 4: Only one out of 20 events is kept for Q^2 values below 5 GeV^2 as long as the event is not saved by one of the final state finders. D-meson candidates are mostly rescued by the open charm finder `HQSEL`.

Due to the prescaling all candidates must enter into the mass spectrum according to their event weight and the statistical error in the respective histogram bin is augmented by the same amount. The χ^2 fit of the signal extraction considers these errors and therefore the significance of the two high bins is low.

The result of the D^+ production cross section measurement can be found in table 7.3. Again the major error of the measurement is of systematical nature and the contributions of the different sources are listed in table 7.4: dominant are once again the uncertainties in the detector and lifetime efficiencies and in the energy calibration of the SpaCal calorimeter, but also the relative error in the branching ratio is significant.

The measured D^+ cross sections compares well with the LO prediction (cf. tab. 7.3): as the only measurement it is smaller than the expectation, but the difference between the data and the QCD prediction is well below one σ.

The measured differential cross sections are compared in figure 7.9 with the LO prediction and an excellent agreement is found in all distributions: the transverse momentum $p_t(D^+)$ and pseudo rapidity $\eta(D^+)$ spectra which describe the D^+ kinematics (fig. 7.9a,b) and also the fragmentation and kinematics sensitive $z_e(D^+)$ distribution is accurately reproduced (fig. 7.9c). In addition the dependences on the Q^2, y and x_{Bj} variables which describe the kinematics of the ep scattering process show a very good agreement (fig. 7.9d-f).

7.2 Fragmentation ratios

The fragmentation ratios can not be derived directly from the measured cross sections, because the definition of the visible range via the D-meson properties $p_t(D)$ and $\eta(D)$ has a slight channel dependence (cf. sec. 3.2). In addition the expected contribution of D-mesons from b decays differs between the channels (cf. tab. 7.3). Therefore the fragmentation factors $f(c \to D)$, in which both effects are corrected for, are deduced as an intermediate step.

7.2.1 Fragmentation factors

The fragmentation factors $f(c \to D)$ denote the probability of an initial charm to produce a D-meson of a certain type (cf. sec. 1.4). They are deduced from the measured and predicted LO D-meson production cross sections via the equation

$$f(c \to D) = \frac{\sigma_{vis}^{meas}(ep \to e'DX) - \sigma_{vis}^{calc}(ep \to b\bar{b} \to e'DX)}{\frac{\sigma_{vis}^{calc}(ep \to c\bar{c} \to e'DX)}{f_{w.a.}(c \to D)}}, \tag{7.1}$$

where the predicted beauty contribution $\sigma_{vis}^{calc}(ep \to b\bar{b} \to e'DX)$ is subtracted from the measured cross section $\sigma_{vis}^{meas}(ep \to e'DX)$. In the denominator the world average value $f_{w.a.}(c \to D)$ used for the prediction of the charm contribution $\sigma_{vis}^{calc}(ep \to c\bar{c} \to e'DX)$ is removed.

In table 7.5 the deduced $f(c \to D)$ factors are listed for the different channels. The quoted systematical errors contain the experimental uncertainties, while the theoretical errors sum the model dependences of the predictions and the uncertainties in the branching ratios and the beauty contents.

The $f(c \to D)$ factors have in addition the advantage to be directly compared to results from e^+e^- experiments. The world average values quoted in table 7.5 are a compilation of CLEO, ARGUS and LEP results [34]. The deduced $f(c \to D)$'s compare well with these world average values. As the only measurement the central value of $f(c \to D^+)$ is below the values measured at the e^+e^- experiments, all others are slightly higher.

7.2.2 Fragmentation ratio measurements

The fragmentation ratios (FR) are quotients in the $f(c \to D)$ factors (cf. tab. 7.6) and therefore systematical and theoretical errors common in all channels cancel. In figure 7.10 the measured differential D^+, D^0 and D^{*+} cross sections are divided by their LO predictions and compared to each other to identify differences not common in all channels.

Fragmentation factors	D^+	D^0	D_s^+	D^{*+}
$f(c \to D)$	0.202	0.658	0.156	0.263
stat. error	± 0.020	± 0.054	± 0.043	± 0.019
syst. error	$^{+0.045}_{-0.033}$	$^{+0.117}_{-0.142}$	$^{+0.036}_{-0.035}$	$^{+0.056}_{-0.042}$
theo. error	$^{+0.029}_{-0.021}$	$^{+0.086}_{-0.048}$	$^{+0.050}_{-0.046}$	$^{+0.031}_{-0.022}$
$f_{w.a.}$ = world average [34]	0.232 ± 0.018	0.549 ± 0.026	0.101 ± 0.027	0.235 ± 0.010

Table 7.5: *The fragmentation factors are deduced from the measured and predicted D-meson production cross sections. The small b contributions are subtracted. The deduced values compare well with present world average numbers.*

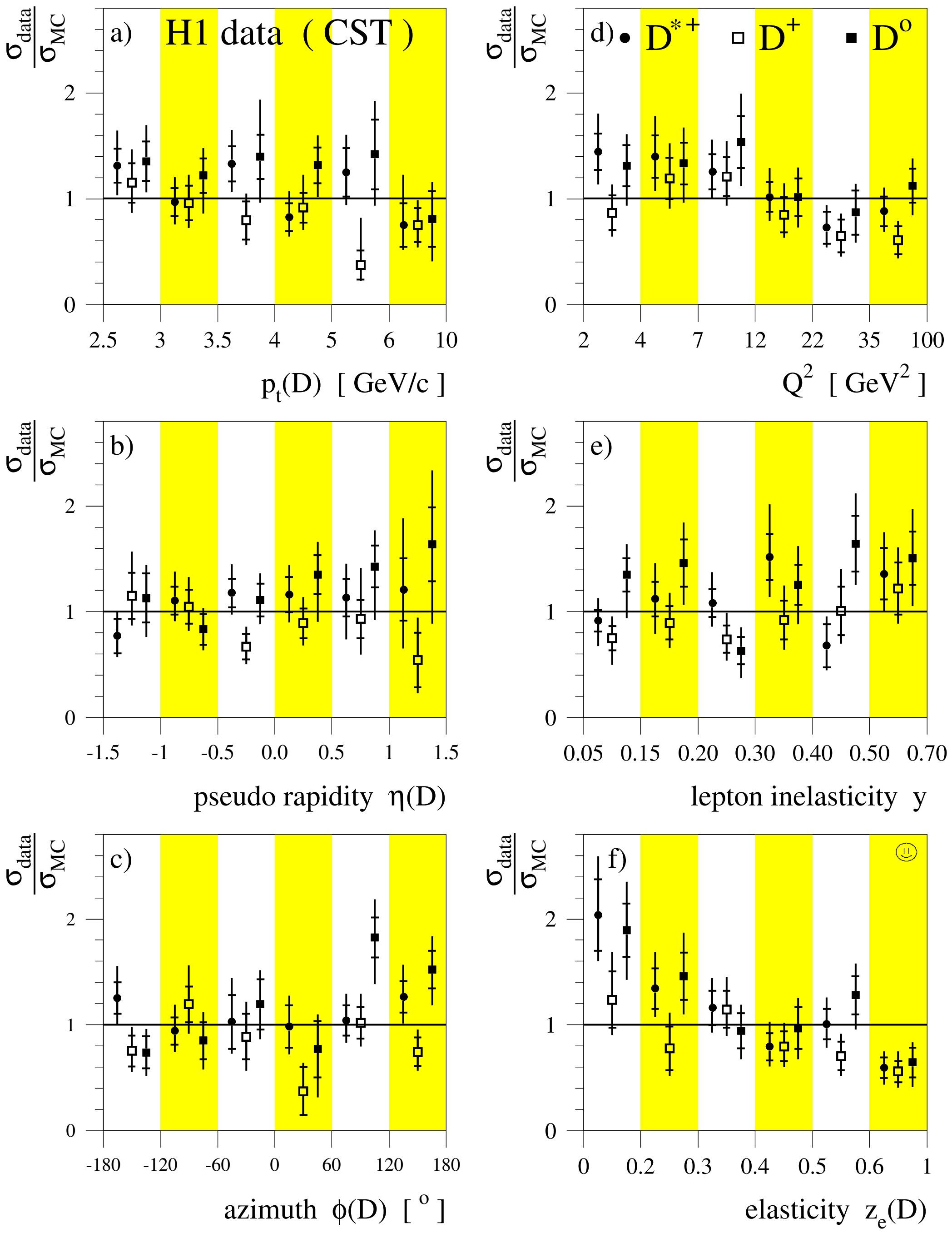

Figure 7.10: *The ratios of the D^{*+}, D^{+} and D^{0} production cross sections measured by means of the CST to the leading order* `AROMA` *predictions are shown in bins of kinematical D-meson variables* **(a-c,f)** *and of variables describing the event kinematics* **(d,e)**. *The error bars include the statistical and the quadratically summed statistical, systematical and theoretical errors.*

In general these ratios confirm the very good agreement between the data and the LO QCD predictions. The ratios in $p_t(D)$ and $\eta(D)$ describing the D-meson kinematics (fig. 7.10a,b) are fairly flat in all decay channels. The almost constant ratios in the $\phi(D)$ bins (fig. 7.10c) prove the accurate implementation of the azimuth dependent detector efficiencies in the simulation.

In figure 7.10d a minor common trend might hint at a slightly steeper Q^2 spectrum in data than predicted by the calculations, but considering the errors of the data the significance is only limited. Even if such a trend is present, it would cancel in the FR's, because it is common to all D-mesons. In the y bins (fig. 7.10e) the ratios of the different D-meson types fluctuate randomly and no common systematics can be seen.

In figure 7.10f a rather clear enhancement towards small $z_e(D)$ values can be seen, at least in the D^{*+} and D^0 channel. The trend is not as pronounced for the D^+ meson. Also in the D_s^+ channel, which is not included in the comparison due to its limited statistical significance and the different binning, a similar trend could be seen (cf. fig. 7.5c).

Thus from these comparisons can be concluded that there is no indication for any different systematics in the analyzed D-meson channels and therefore the determination of the FR's from the deduced $f(c \to D)$ factors is justified.

The results of the FR measurements listed in table 7.6 are discussed hereafter using the following abbreviations:

$$\begin{aligned}
&f^+ = f(c \to D^+), \quad f^0 = f(c \to D^0), \quad f_s = f(c \to D_s^+),\\
&f^{*+} = f(c \to D^{*+}), \quad f^{*0} = f(c \to D^{*0}), \quad f_s^* = f(c \to D_s^{*+})\\
&\text{and } BR = BR(D^{*+} \to D^0\pi^+) = 0.677 \pm 0.005 \quad [17].
\end{aligned}$$

The errors quoted in table 7.6 are of statistical and systematical nature. The systematical errors of the ratios measured herein are obtained by rising, respectively lowering all central values of $f(c \to D)$ at the same time by one sigma which is motivated by the equivalent error sources present in all channels. They contain beside of the experimental systematics also the theoretical uncertainties and the errors in the branching ratios which are all added quadratically.

Isospin invariance

The fragmentation process is believed to be invariant of the light quark's isospin (up or down flavor) which forms together with the initial charm quark the bound D-meson state. This isospin invariance is tested by the R ratio. There are several definitions found in the literature, where the most common is defined by the fragmentation factors of the D^0, D^+ and D^{*+} mesons:

$$R = \frac{f^0 - f^+}{2 \cdot f^{*+} \cdot BR} = 1 + \frac{(f^0_{dir} + f^{*0}) - (f^+_{dir} + f^{*+})}{2 \cdot f^{*+} \cdot BR}, \tag{7.2}$$

where f^0_{dir} and f^+_{dir} denote the probabilities to produce the isoscalar mesons directly in the fragmentation process which allows a decomposition of $f(c \to D)$ into the different branches of the fragmentation tree (cf. sec. 1.4):

$$f^0 = f^0_{dir} + f^{*0} + f^{*+} \cdot BR \quad \text{and} \quad f^+ = f^+_{dir} + f^{*+} \cdot (1 - BR). \tag{7.3}$$

The R ratio is expected to be equal one, if $(c\bar{u})$ states are produced in the fragmentation process at the same rate as $(c\bar{d})$ states: $(f^0_{dir} + f^{*0}) = (f^+_{dir} + f^{*+})$.

In table 7.6 the R values measured at the ALEPH and DELPHI e^+e^- experiments are compared to the ratio measure herein: while the e^+e^- results confirm the expected isospin invariance very well, the measured $R = 1.28 \pm 0.19 \pm 0.12$ is by $1.2 \cdot \sigma$ larger than one.

The table also quotes results from the OPAL collaboration which measured in addition $f(c \to D^{*0})$. The denominator of the R' ratio contains an additional $(f^{*0} - f^{*+})$ term and the relative large error in R' origins from the uncertainties in f^{*0}. The collaboration has also published the ratio R^* in the vector meson states only. The results for R' and R^* also confirm the isospin invariance.

Vector meson production

The $P_V = \frac{VM}{PS+VM}$ ratio denote the fraction of D-mesons produced in a spin excited state. It is expected to be similar for the different bound states $(c\bar{u})$, $(c\bar{d})$ and $(c\bar{s})$ and is therefore measured either in one of the these systems separately, e.g. P^d_V or P^s_V, or in a combination of them, e.g. P^{u+d}_V. The ratios P'_V and $P^\dagger_V$ require implicitly $f^{*0} = f^{*+}$, i.e. they assume isospin invariance.

The P^d_V ratio determines the vector meson fraction with only the $(c\bar{d})$ states. The denominator is corrected for the D^{*+} mesons which decay into the D^0 channel (cf. eq. 7.3). The measured value $P^d_V = 0.693 \pm 0.045 \pm 0.010$ quoted table 7.6 is higher than the ALEPH result by $1.4 \cdot \sigma$. The ALEPH value is also confirmed by the results of the OPAL P^{u+d}_V ratio and the P^s_V ratio measured with $(c\bar{s})$ states by the ALEPH collaboration.

In the P'_V and $P^\dagger_V$ ratios a very good agreement with the DELPHI and ZEUS results is achieved, because the higher vector meson rate seen in the $(c\bar{d})$ system is compensated by the rather large R value due to the assumed isospin invariance. These ratios are therefore less sensitive to the actual fraction of D-mesons produced in an excited spin state.

Strangeness suppression

The fragmentation into a $(c\bar{s})$ state is suppressed due to the higher mass of the s quark compared to u and d which is expressed by the γ_s ratio. In table 7.6 the measured $\gamma_s = 0.36 \pm 0.10 \pm 0.08$ is compared to the LEP results compiled up to the year 1995[2] and a good agreement is found. But not only the statistical error in the measured γ_s is large,

[2]Using the updated $f(c \to D)$ values in [34] a slightly lower value of $\gamma_s = 0.26 \pm 0.03 \pm 0.07$ is obtained.

Fragmentation ratios	value	±	stat.	±	syst.	Exp.	reference
$R = \frac{f^0 - f^+}{2 \cdot f^{*+} \cdot BR}$	1.02	±	0.12			A	[65]
	0.96	±	0.05	±	0.07	D	[66]
	1.28	±	**0.19**	±	**0.12**	**H1**	
$R' = \frac{f^0 - f^+}{f^{*0} - f^{*+} + 2 \cdot f^{*+} \cdot BR}$	1.19	±	0.36			O	[67]
$R^* = \frac{f^{*0}}{f^{*+}}$	0.94	±	0.31			O	[67]
$P_V^d = \frac{f^{*+}}{f^+ + f^{*+} \cdot BR}$	0.595	±	0.045			A	[65]
	0.693	±	**0.045**	±	**0.010**	**H1**	
$P_V^{u+d} = \frac{f^{*0} + f^{*+}}{f^0 + f^+}$	0.57	±	0.05			O	[67]
$P_V^s = \frac{f_s^*}{f_s}$	0.60	±	0.19			A	[65]
$P'_V = \frac{2 \cdot f^{*+}}{f^0 + f^+}$	0.620	±	0.014	±	0.029	D	[66]
	0.613	±	**0.061**	±	**0.034**	**H1**	
$P_V^\dagger = \frac{f^{*+}}{f^0 - f^{*+} \cdot BR}$	0.546	±	0.045	±	0.028	ZEUS	[68]
	0.549	±	**0.083**	±	**0.056**	**H1**	
$\gamma_s = \frac{2 \cdot f_s}{f^0 + f^+}$	0.31	±	0.07			ADO	[69]
	0.36	±	**0.10**	±	**0.08**	**H1**	
$\gamma_s^\dagger$	0.27	±	0.04	±	0.07	ZEUS	[70]

Table 7.6: *The measured fragmentation ratios (bold, marked as H1 results) and the comparisons with ZEUS and LEP results (LEP experiments: A=ALEPH, D=DELPHI, O=OPAL) are discussed in the text. In the definitions of the ratios the following abbreviations have been used:* $f^+ = f(c \to D^+)$, $f^0 = f(c \to D^0)$, $f_s = f(c \to D_s^+)$, $f^{*+} = f(c \to D^{*+})$, $f^{*0} = f(c \to D^{*0})$, $f_s^* = f(c \to D_s^{*+})$ *and* $BR = BR(D^{*+} \to D^0 \pi^+)$.

but also the uncertainty in the $BR(D_s^+ \to (\Phi \to K^+K^-)\pi^+)$ branching ratio leads to a significant systematic error.

The quoted $\gamma_s^\dagger$ value of the ZEUS collaboration is deduced from measured D_s^+ and D^{*+} production cross sections in photoproduction by adjusting the respective parameter in the `LUND` string model until the ratio of the cross sections is reproduced by the `PYTHIA` Monte Carlo generator. No corrections for the (different) beauty contributions are made. By comparing the $(c\bar{s})$ system to D^{*+} vector meson state only, isospin invariance is assumed and the P_V ratio has to be fixed to the value measured by e^+e^- experiments.

Interpretation of the results

There are at least two ways to interpret the results of the fragmentation ratio measurements. Either the P_V ratio is larger in ep than in e^+e^- scattering. In addition the isospin invariance is broken in the fragmentation process of ep scattering and the formation of a $(c\bar{u})$ state is more probable than a $(c\bar{d})$ state. The relative enhancement is expressed by the measured ratio $(f^0 - f^{*+} \cdot BR)/(f^+ + f^{*+} \cdot BR) = 1.26 \pm 0.20$ *(stat.)* ± 0.11 *(syst.)* which has only a limited significance of $1.1 \cdot \sigma$ though.

A possible explanation for a broken isospin invariance could be a so called "beam drag effect" in the remnant of the proton the valence quark content $(uu\bar{d})$ of which might enhance the $\bar{D}^0$ production over a D^+ formation. The signature of such an effect would be an enlarged D^0 production in the forward direction $\eta(D) \gg 0$, i.e. close to the beam remnant. Indeed such an enhancement might be hinted in figure 7.7b, but in the same bins also the D^{*+} data, a $(c\bar{d})$ state, lies above the prediction (cf. fig. 7.10b).

But the slightly higher values in all ratios could also be explained, if the measured value of the D^+ production is too low by 10-20% either due to a statistical fluctuation, the relative statistical error in the cross section is about 9%, or due to an inefficiency not covered by the simulation. Possible candidates for the latter are the Level 4 trigger, which would be surprising as the other channels do not seem to be affected, or a not accurately described CST linking inefficiency at large l values which would affect the long living D^+ meson at most, but no evidence for a discrepancy between data and simulation could be found (cf. sec. 5.1.2).

Chapter 8

Conclusions and Outlook

Production cross sections are measured in deep inelastic ep scattering for the vector D^{*+} and for the pseudoscalar charmed mesons D^0, D_s^+ and, for the first time at HERA, also D^+ mesons through their decay $D^+ \rightarrow K^-\pi^+\pi^+$. The consistent measuring method applied in all channels takes advantage of the finite lifetimes of 0.4 to 1 ps for the pseudoscalar mesons which leads to a separation of their production and decay vertices. A newly developed lifetime tagging technique, based on the high-precision tracking capabilities of the H1 silicon vertex detector CST, exploits this separation distance l to distinguish signal and background processes and thus the signal qualities are improved substantially.

At the heart of the lifetime tag are the two dimensional track-vertex fitter `VFit2dc` which allows a precise reconstruction of l with a high purity and the track extrapolation routine `CSTCOR` necessary for an accurate calculation of the error σ_l made in the l reconstruction. The combination of both in $S_l = l/\sigma_l$ allows to classify each D-meson candidate according to the significance of its vertex separation and therefore represents a powerful variable to identify events with lifetime information.

The signal efficiencies necessary for the cross section measurements are determined herein with simulated D-meson decays. This procedure relies crucially on an accurate description of the data by the detailed detector simulation which is tuned with measurements of basic detector properties. Rigorous comparisons between data and simulation prove the high quality of the latter.

The measurement of the D^{*+} production cross section with the well known Δm-tagging technique not only allows to establish ties to previously published results, but it is also used as a final comprehensive test for the lifetime tagging method.

The measured inclusive and single differential D-meson production cross sections in variables describing the D-meson and event kinematics are compared to leading and, in case of the D^{*+} meson, also next-to-leading order QCD calculations and a good agreement within the errors of the measurements, dominated by the experimental systematics, is found.

The consistent method used to measure the production cross sections invites the measurement of the fragmentation ratios R, P_V and γ_s in which most of the systematic uncertainties cancel. They put the rates by which the different D-mesons are produced in the fragmentation process into relation. Because these ratios have already been measured by e^+e^- annihilation experiments, they allow for the first time a comprehensive comparison of the fragmentation process in e^+e^- and ep scattering and therefore the assumed universality of the fragmentation process can be tested.

All measured ratios are slightly higher than the LEP values, but are within their errors compatible with them: in R, which tests the isospin invariance of the fragmentation process, the disagreement accounts for 1.2 standard deviations and in P_V^d, which denotes the D^{*+} vector mesons fraction with respect to all bound $(c\bar{d})$ states produced in the charm fragmentation process, the measurement is higher than the ALEPH value by $1.4 \cdot \sigma$. The measured strangeness suppression factor γ_s is within its errors in agreement with the combined LEP and with ZEUS results.

Thus the description of the fragmentation process determined with e^+e^- data describes the D-meson formation in ep collisions indeed very well, wherefore several assumptions necessary for the universality of the fragmentation process have to be met (cf. sec. 1.3.4). Only the D^+ cross section may indicate a difference to e^+e^- results, because its measured value is a little bit lower with respect to the other D-meson cross sections and therefore responsible for the slightly higher fragmentation ratios. The D^+ is the D-meson most sensitive to the direct production of pseudo scalar mesons in the fragmentation process.

Outlook

To improve the accuracy of the cross section measurements, the dominant systematic error has to be reduced. This can be achieved by a proper calibration of the SpaCal energy measurement needed for the reconstruction of the event kinematics. The large uncertainty in the CJC track efficiency could be reduced by measuring it in the analyzed data set and tune the CJC simulation accordingly. In addition an advanced CJC simulation software is currently being developed which will yield a more accurate description of the drift chamber responses.

The statistical error, the dominant error in the measured fragmentation ratios, can be reduced by improving the signal quality in the reconstructed mass spectra. The final calibration of the central tracking systems used in the reprocessing of the data will enhance the mass resolution and therefore the signal-to-background ratio in the mass spectra will increase. Especially in the D_s^+ channel major improvements are expected which may also allow to relax the kinematical requirements posed on the decay particles and therefore enlarge the poor statistics in this channel.

The decay length dependence of the CST space point linking used herein (cf. sec. 5.1.2) might be a weak point of the presented analysis: if the simulation underestimates the effect, for which no evidence was found, the measured production rate of long living D^+ meson would be systematical too low, while the impact in the other channels with shorter D-meson lifetimes would be smaller. This could explain the higher fragmentation ratios measured herein. The improved calibration of the CJC may allow a CST hit linking with high purity on the basis of non-vertex fitted CJC tracks which would avoid the undesirable decay length dependence of the CST space point linking.

In section 6.4 the distinctively different properties of D^0 mesons produced in charm and in beauty decays have been discussed: the differences arise on the one hand from the compared to the D^0 meson substantially longer B-meson lifetime and on the other hand from the flight direction of the D^0 meson which points in charm decays back to the interaction point which is not necessarily the case in beauty cascade decays.

Simply changing the requirement on the `VFit2dc` fit probability from $\mathcal{P}_{\rm vf} > 0.05$ to $\mathcal{P}_{\rm vf} < 0.05$ leads to an expected D^0 meson signal of about 110 events with, according to QCD calculations, a beauty content of more than 50%. Of course also the signal quality deteriorates drastically, because of the at small $\mathcal{P}_{\rm vf}$ values dominant combinatorial background (cf. sec. 6.2). But the finding may inspire a more refined analysis of the decay length spectrum and the decay topology of D^0 decays which could yield a beauty measurement based on the solid fundament of charm production.

The decay length resolution can be improved by exploiting the CST z measurement in a three dimensional vertex reconstruction, even if only the $r\phi$-projection of the vertex separation is considered. In addition the mass resolution can be enhanced due to a polar angle measurement improved by the precise CST z measurements. But such a three dimensional approach must consider the more difficult CST linking in this projection, a high purity of which is crucial for a reliable reconstruction of both, invariant masses and decay lengths.

After the muon impact parameter analysis in beauty decays [40, 41] and the presented lifetime tagging method for exclusive decays of D-mesons the logical next step of vertexing at H1 is the development of a more inclusive heavy flavor lifetime tag, e.g. tagging of charm and beauty jets, by which the statistics, in exclusive decay channels limited by the small branching ratios, could be enlarged.

In the presented study of exclusive decays backgrounds arising from residual impurities of the reconstruction chain are of minor importance, because they can be easily modeled for the signal extraction from the mass spectra. They will need more considerations, if the background subtraction necessary for a signal determination is based on lifetime sensitive spectra. The decomposition of the S_l distribution discussed in section 6.3 is an example of such a signal extraction, where the complicated shape of the background has been determined with the help of events in the side bands of the mass spectrum, a method which therefore also relies on the full reconstruction of the D-meson decay.

List of Figures

List of Tables

Bibliography

[1] D. Pitzl *et al.*, Nucl. Instr. Meth. **A454** (2000) 334, `hep-ex/0002044`.

[2] M. Glück *et al.*, Phys. Rev. **D54** (1996) 5515, `hep-ph/9605297`.

[3] F. Halzen and A.D Martin, *Quarks and Leptons*, John Wiley & Sons Inc. (1984); R.K. Ellis, W.J Stirling and B.R. Webber, *QCD and Collider Physics*, University Press (1996).

[4] J.D. Bjorken and E.A. Paschos, Phys. Rev. **185** (1969) 1975; R. Feynman, Phys. Rev. Lett. **23** (1969) 1415.

[5] J.D. Bjorken, Phys. Rev. **163** (1967) 1767.

[6] M. Gell-Mann, Phys. Lett. **8** (1964) 214; G. Zweig, CERN Reports CERN-TH-401 and CERN-TH-412 (1964).

[7] G. 't Hooft and M.J.G. Veltman, Nucl. Phys. **B44** (1972) 189; see also: G. 't Hooft, Nucl. Phys. Proc. Suppl. **74** (1999) 413, `hep-th/9808154`.

[8] C. Adloff *et al.* (H1 Collaboration), Eur. Phys. J. **C21** (2001) 33, `hep-ex/0012053`.

[9] S. Bethke, J. Phys. **G26** (2000) R27, `hep-ex/0004021`.

[10] V.N. Gribov and L.N. Lipatov, Sov. J. Nucl. Phys. **15** (1972) 438; G. Altarelli and G. Parisi, Nucl. Phys. **B126** (1977) 29.

[11] D.E. Sober, *Basic of QCD Pertubation Theory*, SLAC report SLAC-R-508 (1996), `hep-ph/9702203`.

[12] C. Adloff *et al.* (H1 Collaboration), Nucl. Phys. **B545** (1999) 21, `hep-ex/9812023`.

[13] J. Breitweg *et al.* (ZEUS Collaboration), Eur. Phys. J. **C12** (2000) 35, `hep-ex/9908012`.

[14] C. Adloff *et al.* (H1 Collaboration), Phys. Lett. **B528** (2002) 199, `hep-ex/0108039`.

[15] S. Aid *et al.* (H1 Collaboration), Phys. Lett. **B520** (2001) 191, `hep-ex/0108047`.

[16] R.A. Eichler and Z. Kunszt, Nucl. Phys. **B308** (1988), 791.

[17] Particle Data Group, Eur. Phys. J. **C15** (2000) 1.

[18] C. Adloff *et al.* (H1 Collaboration), Z. Phys. **C72** (1996) 593, `hep-ex/9607012`.

[19] G. Levman, *Muon Pair Production by Two Photon Collisions at HERA*, in: "Physics at HERA", eds. W. Buchmüller, G. Ingelman, DESY **1** (1992) 623.

[20] P. Nason, *Heavy Quark Production*, in 'Heavy Flavors', eds. A.J. Buras, M. Lindner, World Scientific, Singapore **10** (1992) 556;
S. Frixione *et al.*, Adv. Ser. Direct. High Energy Phys. **15** (1998) 609, `hep-ph/9702287`.

[21] M. Bengtsson and T. Sjostrand, Nucl. Phys. **B289** (1987) 810.

[22] G. Marchesini *et al.*, Comp. Phys. Commun. **67** (1992) 465.

[23] B. Andersson *et al.*, Phys. Rept. **97** (1983) 31;
T. Sjöstrand, Int. J. Mod. Phys. **A3** (1988) 751.

[24] T. Sjöstrand, Comp. Phys. Commun. **82** (1994) 74;
T. Sjöstrand, CERN Report CERN-TH-7112-93-REV (1995), `hep-ph/9508391`.

[25] F. Becattini, Z. Phys. **C69** (1996), 485.

[26] Y. Pei, Z. Phys. **C72** (1996), 39.

[27] W. Bartel *et al.* (JADE Collaboration), Phys. Lett. **B134** (1984) 275.

[28] C. Peterson *et al.*, Phys. Rev. **D27** (1983) 105.

[29] D. Besson, Eur. Phys. J. **C15** (1998) 218.

[30] R.A. Briere *et al.* (CLEO Collaboration), Phys. Rev. **D62** (2000) 072003, `hep-ex/0004028`.

[31] P. Nason and C. Oleari, Nucl. Phys. **B565** (2000) 245, `hep-ph/9903541`.

[32] S. Frixione *et al.*, J. Phys. **G27** (2001), 1111.

[33] M. Cacciari and P. Nason, *Is There a Significant Excess in Bottom Hadroproduction at the TEVATRON?*, submitted to Phys. Rev. Lett., `hep-ph/0204025`.

[34] L. Gladilin, *Charm Hadron Production Fractions*, unpublished, `hep-ex/9912064`.

[35] S. Stone, *Charmed Meson Decays*, in 'Heavy Flavors', eds. A.J. Buras, M. Lindner, World Scientific, Singapore **10** (1992) 334.

[36] G. Ingelman *et al.*, Comput. Phys. Commun. **101** (1997) 135, `hep-ph/9605285`.

[37] B.W. Harris and J. Smith, Phys. Rev. **D57** (1998) 2806, `hep-ph/9706334`;
B.W. Harris *et al.*, *Heavy Quark Production in Deep Inelastic Scattering at HERA*, to be published in "Hamburg 1998/1999, Monte Carlo generators for HERA physics", `hep-ph/9905365`.

[38] M. Gluck *et al.*, Eur. Phys. J. **C5** (1998) 461, `hep-ph/9806404`.

[39] H.L. Lai *et al.*, Eur. Phys. J. **C12** (2000) 375, `hep-ph/9903282`.

[40] H1 and ZEUS Collaboration, *Heavy Quark Production in Deep Inelastic Scattering*, contributed paper to EPS2001, Budapest, Hungary, `hep-ex/0110036`.

[41] H1 and ZEUS Collaboration, *Open Charm and Beauty Production at HERA*, in "Osaka 2000, High Energy Physics", eds. C.S. Lim, T. Yamanaka, World Scientific, Singapore, **2** (2001) 808, `hep-ex/0011034`.

[42] S. Lüders, *A Measurement of the Beauty Cross Section via $B \to J/\psi X$ at HERA*, Ph.D. Thesis, ETH Zurich (2001).

[43] M. Bieler *et al.*, *Recent and Past Experiences with Beam–Beam Effects at HERA*, in "Beam–Beam Effects in Large Hadron Colliders (LHC99)", proc. eds. J. Poole, F. Zimmermann, CERN SL-99-039-AP (1999).

[44] I. Abt *et al.* (H1 Collaboration), Nucl. Instr. Meth. **A386** (1997) 310.

[45] J. Bürger *et al.*, Nucl. Instr. Meth. **A279** (1989) 217.

[46] K. Müller *et al.*, Nucl. Instr. Meth. **A312** (1992) 457.

[47] B. Andrieu *et al.* (H1 Calorimeter Group), Nucl. Instr. Meth. **A336** (1993) 460.

[48] R.D. Appuhn *et al.* (H1 SpaCal group), Nucl. Instrum. Meth. **A386** (1997) 397.

[49] H1 Collaboration, *Technical proposal for the upgrade of the backward region of the H1 detector*, DESY internal report PRC-93/02.

[50] E. Elsen, *The H1 Trigger and Data Acquisition System*, H1 Internal Note H1-01/93-262 (1993).

[51] *GEANT — Detector Description and Simulation Tool*, CERN Program Library Long Writeup W5013.

[52] G.J. Feldman *et al.*, Phys. Rev. Lett. **38** (1977) 1313.

[53] H.C. Schultz-Coulon *et al.*, IEEE Trans. Nucl. Sci. **46** (1999) 915.

[54] T. Ahmed *et al.* (H1 Collaboration), Z. Phys. **C66** (1995) 529.

[55] A. Arbuzov *et al.*, Comput. Phys. Commun. **94** (1996) 128, `hep-ph/9511434`.

[56] D. Müller, *A Measurement of the Gluon Density in the Proton Based on Charm Production at HERA*, Ph.D. Thesis, University of Zurich (1998).

[57] H. Jung, Comput. Phys. Commun. **86** (1993) 147.

[58] A. Meyer, *Measurement of the Structure Function $F_2(x, Q^2)$ of the Proton at Low Q^2 with the H1 Detector at HERA Using the New Detector Components Spacal and BDC*, Ph.D. Thesis, University of Hamburg (1997).

[59] R. L. Gluckstern, Nucl. Instr. Meth. **24** (1963) 381.

[60] S. Hengstmann, *A Measurement of Diffractive Charm Production at HERA*, Ph.D. Thesis, University of Zurich (2000).

[61] A. Schwank, *Effizienzbestimmung von Detektorkomponenten des H1-Experiments mit Hilfe kosmischer Strahlung*, Diploma thesis, University of Hamburg (1998).

[62] S. Mohrdieck, *Inelastische J/Psi-Erzeugung in Elektroproduktion am H1-Experiment bei HERA*, Ph.D. Thesis, University of Hamburg (2000).

[63] W. Erdmann, *Untersuchung der Photoproduktion von D^*-Mesonen am ep-Speicherring HERA*, Ph.D. Thesis, ETH Zurich (1996).

[64] E. Elsen, *Investigation of the Mass Resolution of the Jade Detector*, DESY report F22-78-02.

[65] R. Barate *et al.* (ALEPH Collaboration), Eur. Phys. J. **C16** (2000), 597, `hep-ex/9909032`

[66] P. Abreu *et al.* (DELPHI Collaboration), Eur. Phys. J. **C12** (2000), 225.

[67] K. Ackerstaff *et al.* (OPAL Collaboration), Eur. Phys. J. **C5** (1998), 1, `hep-ex/9802008`.

[68] J. Breitweg *et al.* (ZEUS Collaboration), *Study of inclusive D^0 photoproduction at HERA*, to be published in the proceedings of International Europhysics Conference on High-Energy Physics (HEP 2001), Budapest, Hungary, 12-18 Jul 2001.

[69] G. Altarelli *et al.*, *Workshop on Physics at LEP2*, CERN Report CERN-96-01-V-2 (1996) p.112.

[70] J. Breitweg *et al.* (ZEUS Collaboration), Phys. Lett. **B481** (2000) 213, `hep-ex/0003018`.

[71] W.H. Barkas *et al.*, *Tables of Energy Losses and Ranges of Heavy Charged Particles*, NASA report NASA-SP-3013 (1964).

[72] *GEANT — Detector Description and Simulation Tool*, CERN Program Library Long Writeup W5013, PHYS332-4, p. 252f;
R. Fernow, *Introduction to experimental particle physics*, Cambridge University Press (1986), p. 42ff.

[73] P. Avery, *Applied Fitting Theory I*, CLEO note CBX 91-72 (1991) , `http://www.phys.ufl.edu/~avery/fitting.html`.

[74] P. Billoir *et al.*, Nucl. Instr. Meth. **A241** (1985) 115.

[75] G. Lutz, Nucl. Instr. Meth. **A337** (1993) 66.

Appendix A

Bin wise Signals and Cross Sections

In the following the bin wise invariant mass spectra are shown which are used for the differential cross section measurements, the results of the signal extraction obtained from fits to these spectra are listed and the numerical values of the single differential D-meson production cross section measurements are given.

The results are sorted according to the investigated D-meson channels in the following order:

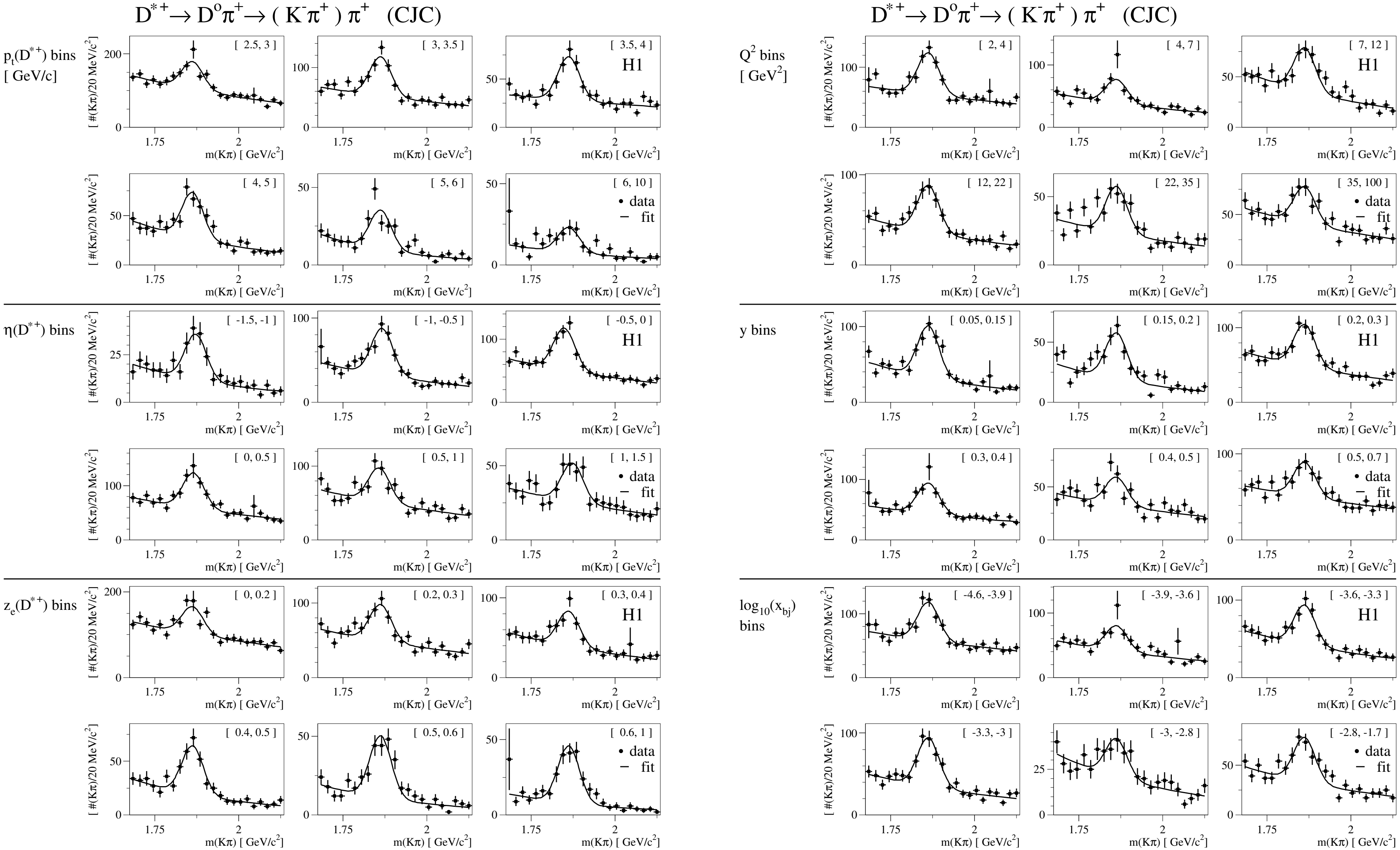

Figure A.1: *The bin wise $m(K\pi)$ mass spectra of D^{*+} tagged D^0 candidates are shown. The D^{*+} tag requires a reconstructed Δm mass difference within a 3-σ window around the nominal value. The selection is done without using any CST information, but the decay tracks of the D^0 candidates are required to be within the geometrical acceptance of both CST silicon layers. The bin ranges are given in the upper right corner of the histograms. The fitted curves are the results of the signal extraction which are used to determine the central values of the differential cross section measurements. The numerical fit results are listed in table A.1.*

Bin wise fit results in the D^{*+} channel (CJC)

$p_t(D^{*+})$ [GeV/c]	χ^2 / ndf	$N(D^0)$	$B_{2\sigma}$	$N_D/B_{2\sigma}$
[2.5, 3.0]	14.8 / 18	301 ± 38	662 ± 17	0.46 ± 0.06
[3.0, 3.5]	18.6 / 18	262 ± 27	332 ± 12	0.79 ± 0.09
[3.5, 4.0]	18.2 / 18	182 ± 21	178 ± 9	1.02 ± 0.13
[4.0, 5.0]	15.4 / 18	186 ± 21	172 ± 9	1.08 ± 0.13
[5.0, 6.0]	26.2 / 18	101 ± 14	64 ± 5	1.58 ± 0.25
[6.0, 10.0]	24.0 / 18	62 ± 11	49 ± 5	1.26 ± 0.26

Q^2 [GeV^2]	χ^2 / ndf	$N(D^0)$	$B_{2\sigma}$	$N_D/B_{2\sigma}$
[2, 4]	18.7 / 18	279 ± 28	347 ± 13	0.80 ± 0.09
[4, 7]	17.8 / 18	153 ± 25	247 ± 10	0.62 ± 0.11
[7, 12]	19.0 / 18	172 ± 22	228 ± 10	0.75 ± 0.10
[12, 22]	10.5 / 18	210 ± 23	231 ± 10	0.91 ± 0.11
[22, 35]	28.7 / 18	137 ± 18	149 ± 8	0.92 ± 0.13
[35, 100]	17.0 / 18	147 ± 22	262 ± 10	0.56 ± 0.09

$\eta(D^{*+})$	χ^2 / ndf	$N(D^0)$	$B_{2\sigma}$	$N_D/B_{2\sigma}$
[-1.50, -1.00]	11.4 / 18	96 ± 15	76 ± 6	1.26 ± 0.21
[-1.00, -0.50]	15.3 / 18	221 ± 23	207 ± 10	1.07 ± 0.12
[-0.50, 0.00]	9.5 / 18	266 ± 27	326 ± 12	0.82 ± 0.09
[0.00, 0.50]	11.2 / 18	261 ± 32	371 ± 13	0.70 ± 0.09
[0.50, 1.00]	26.0 / 18	186 ± 25	326 ± 12	0.57 ± 0.08
[1.00, 1.50]	13.6 / 18	105 ± 18	162 ± 8	0.65 ± 0.12

y	χ^2 / ndf	$N(D^0)$	$B_{2\sigma}$	$N_D/B_{2\sigma}$
[0.05, 0.15]	21.2 / 18	272 ± 24	210 ± 10	1.29 ± 0.13
[0.15, 0.20]	40.6 / 18	154 ± 18	123 ± 7	1.25 ± 0.16
[0.20, 0.30]	15.5 / 18	225 ± 25	309 ± 11	0.73 ± 0.09
[0.30, 0.40]	10.9 / 18	202 ± 28	278 ± 11	0.73 ± 0.10
[0.40, 0.50]	25.0 / 18	104 ± 20	211 ± 9	0.50 ± 0.10
[0.50, 0.70]	11.7 / 18	160 ± 24	321 ± 11	0.50 ± 0.08

$z_e(D^{*+})$	χ^2 / ndf	$N(D^0)$	$B_{2\sigma}$	$N_D/B_{2\sigma}$
[0.00, 0.20]	23.7 / 18	254 ± 38	651 ± 16	0.39 ± 0.06
[0.20, 0.30]	21.5 / 18	196 ± 25	311 ± 11	0.63 ± 0.08
[0.30, 0.40]	10.8 / 18	177 ± 23	249 ± 10	0.71 ± 0.10
[0.40, 0.50]	11.4 / 18	181 ± 19	123 ± 7	1.47 ± 0.18
[0.50, 0.60]	26.1 / 18	157 ± 16	70 ± 5	2.23 ± 0.29
[0.60, 1.00]	14.2 / 18	151 ± 15	51 ± 5	2.99 ± 0.42

$\log_{10}(x_{Bj})$	χ^2 / ndf	$N(D^0)$	$B_{2\sigma}$	$N_D/B_{2\sigma}$
[-4.6, -3.9]	13.9 / 18	242 ± 28	368 ± 13	0.66 ± 0.08
[-3.9, -3.6]	19.9 / 18	155 ± 26	263 ± 11	0.59 ± 0.10
[-3.6, -3.3]	10.8 / 18	206 ± 24	269 ± 11	0.77 ± 0.10
[-3.3, -3.0]	17.5 / 18	240 ± 24	220 ± 10	1.09 ± 0.12
[-3.0, -2.8]	18.9 / 18	84 ± 16	133 ± 7	0.63 ± 0.12
[-2.8, -1.7]	21.2 / 18	179 ± 21	211 ± 9	0.85 ± 0.11

Table A.1: *The results of the bin wise signal extraction of D^{*+} tagged D^0-mesons are given which are obtained from the fits to the mass spectra shown in figure A.1. The mean and the width used in the fit are fixed to the values determined with the inclusive signal:* $m(D^0) = 1861.9 \pm 1.9$ GeV/c^2 *and* $\sigma_m = 31.8 \pm 2.2$ GeV/c^2 *(cf. tab. 7.2).*

$\sigma_{vis}(ep \to eD^{*+}X)$: single differential CJC results

$p_t(D^{*+})$ [GeV/c]	$d\sigma/dp_t$ [nb/GeV/c]	errors [nb/GeV/c] statistical	experimental		theoretical	
[2.5, 3.0]	1.958	±0.249	+0.405	−0.313	+0.058	−0.052
[3.0, 3.5]	1.385	±0.143	+0.267	−0.204	+0.038	−0.052
[3.5, 4.0]	0.916	±0.106	+0.187	−0.113	+0.028	−0.027
[4.0, 5.0]	0.421	±0.046	+0.094	−0.058	+0.014	−0.012
[5.0, 6.0]	0.228	±0.031	+0.044	−0.029	+0.006	−0.008
[6.0, 10.0]	0.031	±0.006	+0.012	−0.004	+0.001	−0.001

Q^2 [GeV^2]	$d\sigma/dQ^2$ [nb/GeV^2]	errors [nb/GeV^2] statistical	experimental		theoretical	
[2, 4]	0.3757	±0.0379	+0.0785	−0.0582	+0.0174	−0.0099
[4, 7]	0.1376	±0.0228	+0.0271	−0.0204	+0.0042	−0.0038
[7, 12]	0.0910	±0.0116	+0.0227	−0.0147	+0.0024	−0.0037
[12, 22]	0.0536	±0.0059	+0.0108	−0.0068	+0.0014	−0.0015
[22, 35]	0.0266	±0.0036	+0.0076	−0.0033	+0.0009	−0.0008
[35, 100]	0.0060	±0.0009	+0.0012	−0.0006	+0.0002	−0.0002

$\eta(D^{*+})$	$d\sigma/d\eta$ [nb]	errors [nb] statistical	experimental		theoretical	
[-1.50, -1.00]	0.80	±0.12	+0.15	−0.08	+0.02	−0.04
[-1.00, -0.50]	1.08	±0.11	+0.21	−0.08	+0.03	−0.03
[-0.50, 0.00]	1.12	±0.11	+0.21	−0.08	+0.04	−0.03
[0.00, 0.50]	1.11	±0.14	+0.21	−0.16	+0.03	−0.04
[0.50, 1.00]	1.03	±0.14	+0.25	−0.33	+0.04	−0.03
[1.00, 1.50]	1.01	±0.17	+0.45	−0.43	+0.05	−0.03

y	$d\sigma/dy$ [nb]	errors [nb] statistical	experimental		theoretical	
[0.05, 0.15]	7.85	±0.69	+1.45	−1.71	+0.20	−0.25
[0.15, 0.20]	6.96	±0.81	+1.71	−1.45	+0.21	−0.23
[0.20, 0.30]	5.42	±0.61	+1.41	−0.74	+0.19	−0.14
[0.30, 0.40]	4.93	±0.68	+1.18	−0.83	+0.18	−0.13
[0.40, 0.50]	2.80	±0.53	+0.73	−0.42	+0.12	−0.10
[0.50, 0.70]	2.42	±0.37	+0.65	−0.37	+0.08	−0.15

$z_e(D^{*+})$	$d\sigma/dz_e$ [nb]	errors [nb] statistical	experimental		theoretical	
[0.00, 0.20]	3.78	±0.56	+0.72	−0.34	+0.14	−0.11
[0.20, 0.30]	4.96	±0.63	+0.96	−0.40	+0.14	−0.22
[0.30, 0.40]	4.76	±0.61	+0.90	−0.56	+0.18	−0.13
[0.40, 0.50]	4.82	±0.51	+0.91	−0.64	+0.16	−0.13
[0.50, 0.60]	4.25	±0.44	+1.06	−0.66	+0.13	−0.13
[0.60, 1.00]	0.98	±0.10	+0.23	−0.20	+0.02	−0.03

$\log_{10}(x_{Bj})$	$d\sigma/dx_{Bj}$ [nb]	errors [nb] statistical	experimental		theoretical	
[-4.6, -3.9]	0.94	±0.11	+0.24	−0.12	+0.06	−0.03
[-3.9, -3.6]	1.29	±0.21	+0.30	−0.23	+0.03	−0.05
[-3.6, -3.3]	1.82	±0.22	+0.39	−0.31	+0.06	−0.06
[-3.3, -3.0]	1.94	±0.19	+0.37	−0.25	+0.06	−0.06
[-3.0, -2.8]	1.18	±0.22	+0.43	−0.20	+0.03	−0.03
[-2.8, -1.7]	0.44	±0.05	+0.11	−0.09	+0.01	−0.01

Table A.2: *The results of the single differential D^{*+} production cross section measurements are given. The measurements are done without using any CST information, but the decay tracks of the selected D^0-mesons are required to be within the geometrical acceptance of both CST silicon layers. Beside of the statistical errors from the signal extraction, the systematical errors arising from the experimental method and the theoretical errors are quoted, where the latter includes the uncertainties of the decay's branching ratio and the model dependencies of the acceptance determination.*

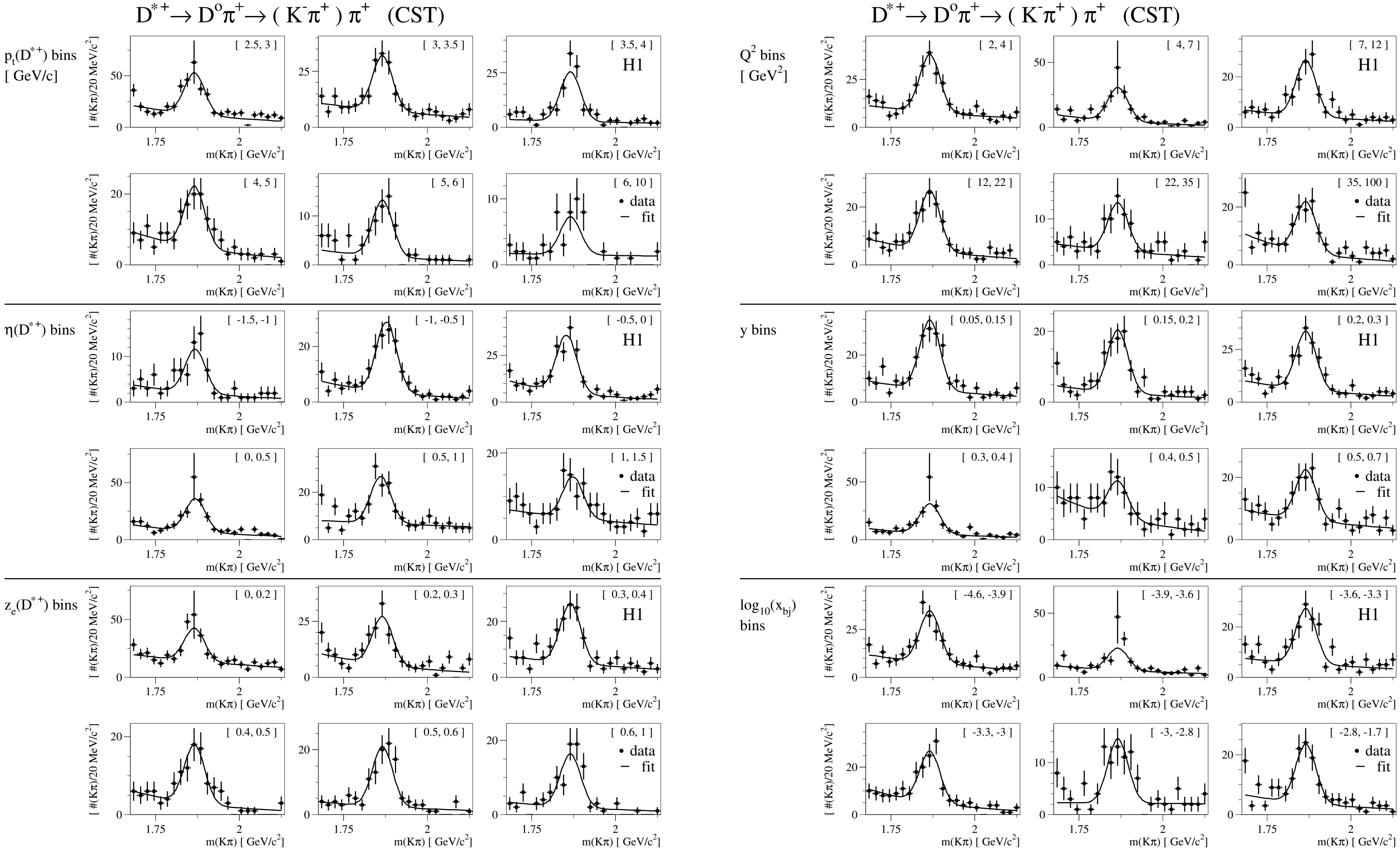

Figure A.2: *The bin wise $m(K\pi)$ mass spectra of D^{*+} tagged D^0 candidates are shown. The D^{*+} tag requires a reconstructed Δm mass difference within a 3-σ window around the nominal value. The D^0 candidates are reconstructed with the CST and fulfill life time tagging requirements. The bin ranges are given in the upper right corner of the histograms. The fitted curves are the results of the signal extraction which are used to determine the central values of the differential cross section measurements. The numerical fit results are listed in table A.3.*

Bin wise fit results in the D^{*+} channel (CST)

$p_t(D^{*+})$ [GeV/c]	χ^2 / ndf	$N(D^0)$	$B_{2\sigma}$	$N_D/B_{2\sigma}$
[2.5, 3.0]	42.9 / 18	152 ± 19	75 ± 5	2.03 ± 0.29
[3.0, 3.5]	9.7 / 18	92 ± 13	45 ± 4	2.05 ± 0.34
[3.5, 4.0]	23.3 / 17	86 ± 11	16 ± 3	5.23 ± 1.07
[4.0, 5.0]	8.2 / 17	65 ± 10	30 ± 3	2.18 ± 0.43
[5.0, 6.0]	11.2 / 14	43 ± 8	10 ± 2	4.25 ± 1.23
[6.0, 10.0]	9.8 / 11	22 ± 6	9 ± 2	2.37 ± 0.88

Q^2 [GeV^2]	χ^2 / ndf	$N(D^0)$	$B_{2\sigma}$	$N_D/B_{2\sigma}$
[2, 4]	12.7 / 18	113 ± 14	48 ± 4	2.38 ± 0.35
[4, 7]	17.3 / 18	98 ± 14	28 ± 3	3.47 ± 0.65
[7, 12]	15.0 / 18	84 ± 11	27 ± 3	3.13 ± 0.56
[12, 22]	10.4 / 18	78 ± 11	30 ± 3	2.62 ± 0.47
[22, 35]	10.4 / 17	40 ± 8	18 ± 3	2.17 ± 0.56
[35, 100]	28.8 / 18	66 ± 11	27 ± 3	2.42 ± 0.50

$\eta(D^{*+})$	χ^2 / ndf	$N(D^0)$	$B_{2\sigma}$	$N_D/B_{2\sigma}$
[-1.50, -1.00]	11.9 / 17	36 ± 8	12 ± 2	2.97 ± 0.84
[-1.00, -0.50]	9.6 / 18	95 ± 11	22 ± 3	4.33 ± 0.77
[-0.50, 0.00]	21.7 / 18	116 ± 13	33 ± 4	3.55 ± 0.57
[0.00, 0.50]	19.0 / 17	109 ± 15	43 ± 4	2.54 ± 0.44
[0.50, 1.00]	20.3 / 18	75 ± 12	41 ± 4	1.81 ± 0.33
[1.00, 1.50]	14.0 / 18	36 ± 9	30 ± 3	1.18 ± 0.31

y	χ^2 / ndf	$N(D^0)$	$B_{2\sigma}$	$N_D/B_{2\sigma}$
[0.05, 0.15]	16.6 / 18	111 ± 13	32 ± 4	3.45 ± 0.54
[0.15, 0.20]	16.2 / 18	67 ± 10	16 ± 3	4.04 ± 0.86
[0.20, 0.30]	18.0 / 18	104 ± 13	36 ± 4	2.85 ± 0.45
[0.30, 0.40]	18.3 / 18	97 ± 14	31 ± 4	3.11 ± 0.57
[0.40, 0.50]	10.2 / 18	26 ± 8	26 ± 3	1.01 ± 0.33
[0.50, 0.70]	13.2 / 18	60 ± 11	39 ± 4	1.55 ± 0.32

$z_e(D^{*+})$	χ^2 / ndf	$N(D^0)$	$B_{2\sigma}$	$N_D/B_{2\sigma}$
[0.00, 0.20]	15.6 / 18	108 ± 18	84 ± 6	1.29 ± 0.23
[0.20, 0.30]	27.2 / 17	81 ± 12	34 ± 4	2.42 ± 0.44
[0.30, 0.40]	17.6 / 18	81 ± 11	30 ± 3	2.66 ± 0.48
[0.40, 0.50]	7.5 / 14	57 ± 9	18 ± 3	3.19 ± 0.75
[0.50, 0.60]	11.2 / 15	70 ± 10	15 ± 3	4.61 ± 1.04
[0.60, 1.00]	12.1 / 12	54 ± 9	12 ± 3	4.43 ± 1.24

$\log_{10}(x_{Bj})$	χ^2 / ndf	$N(D^0)$	$B_{2\sigma}$	$N_D/B_{2\sigma}$
[-4.6, -3.9]	16.9 / 18	102 ± 13	45 ± 4	2.27 ± 0.35
[-3.9, -3.6]	19.9 / 18	65 ± 13	33 ± 4	1.94 ± 0.43
[-3.6, -3.3]	25.6 / 18	82 ± 12	32 ± 4	2.56 ± 0.46
[-3.3, -3.0]	9.7 / 17	82 ± 11	31 ± 4	2.62 ± 0.48
[-3.0, -2.8]	20.2 / 17	47 ± 8	13 ± 2	3.51 ± 0.84
[-2.8, -1.7]	22.4 / 18	74 ± 11	24 ± 3	3.14 ± 0.60

Table A.3: *The results of the bin wise signal extraction of D^{*+} tagged D^0-mesons are given which are obtained from the fits to the mass spectra shown in figure A.2. The mean and the width used in the fit are fixed to the values determined with the inclusive signal: $m(D^0) = 1865.9 \pm 2.1$ GeV/c^2 and $\sigma_m = 30.0 \pm 2.1$ GeV/c^2 (cf. fig. 7.2).*

$\sigma_{vis}(ep \to eD^{*+}X)$: single differential CST results

$p_t(D^{*+})$ [GeV/c]	$d\sigma/dp_t$ [nb/GeV/c]	errors [nb/GeV/c] statistical	experimental		theoretical	
[2.5, 3.0]	2.307	±0.283	+0.500	−0.396	+0.069	−0.057
[3.0, 3.5]	1.147	±0.157	+0.227	−0.190	+0.029	−0.035
[3.5, 4.0]	1.034	±0.129	+0.210	−0.155	+0.027	−0.033
[4.0, 5.0]	0.344	±0.055	+0.085	−0.055	+0.011	−0.009
[5.0, 6.0]	0.224	±0.041	+0.048	−0.037	+0.006	−0.009
[6.0, 10.0]	0.027	±0.007	+0.015	−0.004	+0.001	−0.001

Q^2 [GeV^2]	$d\sigma/dQ^2$ [nb/GeV^2]	errors [nb/GeV^2] statistical	experimental		theoretical	
[2, 4]	0.3592	±0.0428	+0.0785	−0.0616	+0.0135	−0.0092
[4, 7]	0.1928	±0.0274	+0.0445	−0.0357	+0.0049	−0.0056
[7, 12]	0.1071	±0.0143	+0.0213	−0.0148	+0.0031	−0.0035
[12, 22]	0.0486	±0.0068	+0.0109	−0.0084	+0.0014	−0.0013
[22, 35]	0.0180	±0.0038	+0.0036	−0.0026	+0.0005	−0.0007
[35, 100]	0.0064	±0.0010	+0.0013	−0.0009	+0.0002	−0.0002

$\eta(D^{*+})$	$d\sigma/d\eta$ [nb]	errors [nb] statistical	experimental		theoretical	
[-1.50, -1.00]	0.62	±0.13	+0.14	−0.09	+0.02	−0.02
[-1.00, -0.50]	1.10	±0.13	+0.23	−0.14	+0.03	−0.03
[-0.50, 0.00]	1.20	±0.14	+0.24	−0.15	+0.03	−0.03
[0.00, 0.50]	1.15	±0.16	+0.22	−0.20	+0.03	−0.04
[0.50, 1.00]	0.99	±0.15	+0.23	−0.31	+0.03	−0.02
[1.00, 1.50]	0.65	±0.16	+0.32	−0.25	+0.03	−0.02

y	$d\sigma/dy$ [nb]	errors [nb] statistical	experimental		theoretical	
[0.05, 0.15]	7.54	±0.86	+1.50	−1.77	+0.19	−0.21
[0.15, 0.20]	7.29	±1.06	+1.90	−1.86	+0.22	−0.20
[0.20, 0.30]	5.69	±0.69	+1.37	−0.91	+0.19	−0.15
[0.30, 0.40]	5.83	±0.84	+1.72	−1.15	+0.16	−0.15
[0.40, 0.50]	1.74	±0.52	+0.48	−0.28	+0.07	−0.09
[0.50, 0.70]	2.01	±0.36	+0.45	−0.37	+0.05	−0.11

$z_e(D^{*+})$	$d\sigma/dz_e$ [nb]	errors [nb] statistical	experimental		theoretical	
[0.00, 0.20]	3.59	±0.60	+0.76	−0.47	+0.12	−0.10
[0.20, 0.30]	4.98	±0.70	+1.05	−0.67	+0.13	−0.19
[0.30, 0.40]	5.02	±0.70	+0.99	−0.71	+0.18	−0.13
[0.40, 0.50]	3.65	±0.59	+0.91	−0.61	+0.11	−0.10
[0.50, 0.60]	4.46	±0.63	+0.92	−0.74	+0.11	−0.13
[0.60, 1.00]	0.82	±0.13	+0.17	−0.17	+0.02	−0.02

$\log_{10}(x_{Bj})$	$d\sigma/dx_{Bj}$ [nb]	errors [nb] statistical	experimental		theoretical	
[-4.6, -3.9]	0.90	±0.11	+0.26	−0.15	+0.04	−0.02
[-3.9, -3.6]	1.26	±0.24	+0.29	−0.24	+0.03	−0.05
[-3.6, -3.3]	1.65	±0.23	+0.36	−0.32	+0.06	−0.04
[-3.3, -3.0]	1.62	±0.23	+0.31	−0.30	+0.04	−0.05
[-3.0, -2.8]	1.61	±0.28	+0.46	−0.21	+0.05	−0.04
[-2.8, -1.7]	0.43	±0.06	+0.08	−0.09	+0.01	−0.01

Table A.4: *The results of the single differential D^{*+} production cross section measurements are given. The D^{*+} tagged D^0 signals used for the measurement are reconstructed with the CST and fulfill life time tagging requirements. Beside of the statistical errors from the signal extraction, the systematical errors arising from the experimental method and the theoretical errors are quoted, where the latter includes the uncertainties of the decay's branching ratio and the model dependencies of the acceptance determination.*

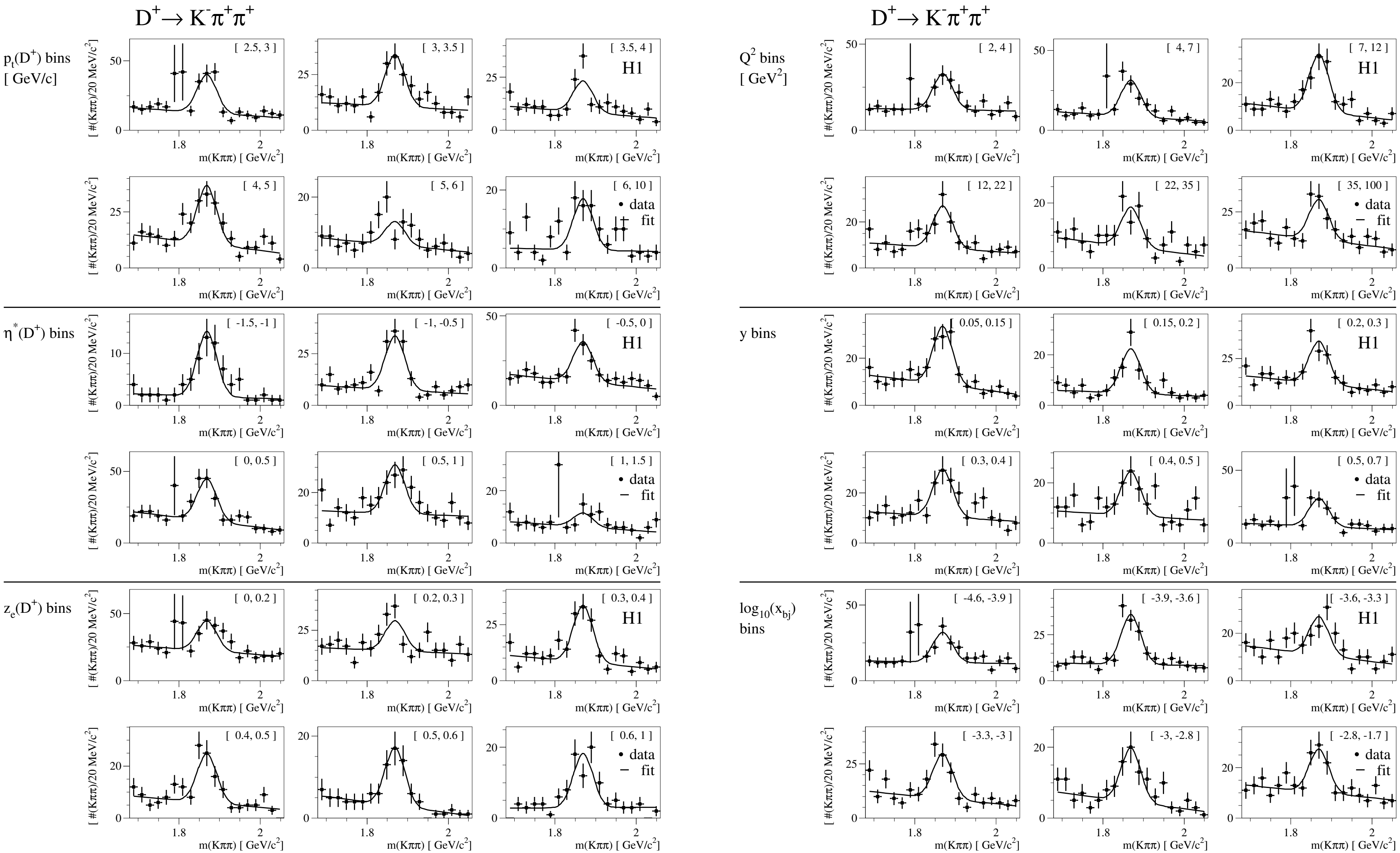

Figure A.3: *The bin wise $m(K\pi\pi)$ mass spectra of the selected D^+ candidates are shown. The bin ranges are given in the upper right corner of the histograms. The large statistical errors of data points just below the nominal D^+ mass origin from two events with event weight 20. The fitted curves are the results of the signal extraction which are used to determine the central values of the differential cross section measurements. The numerical fit results are listed in table 7.2.*

Bin wise fit results in the D^+ channel

$p_t(D^+)$ [GeV/c]	χ^2 / ndf	$N(D^+)$	$B_{2\sigma}$	$N_D/B_{2\sigma}$
[2.5, 3.0]	17.3 / 14	82.8 ± 13.4	60.1 ± 5.0	1.38 ± 0.25
[3.0, 3.5]	16.2 / 14	69.9 ± 12.0	51.0 ± 4.2	1.37 ± 0.26
[3.5, 4.0]	17.8 / 14	44.2 ± 10.2	40.7 ± 3.8	1.09 ± 0.27
[4.0, 5.0]	16.3 / 14	78.2 ± 12.0	51.1 ± 4.2	1.53 ± 0.27
[5.0, 6.0]	14.6 / 14	19.9 ± 7.3	30.8 ± 3.2	0.64 ± 0.24
[6.0, 10.0]	25.8 / 14	39.3 ± 8.5	21.9 ± 2.8	1.79 ± 0.45

Q^2 [GeV^2]	χ^2 / ndf	$N(D^+)$	$B_{2\sigma}$	$N_D/B_{2\sigma}$
[2, 4]	7.9 / 14	62.5 ± 11.8	56.9 ± 4.6	1.10 ± 0.22
[4, 7]	11.0 / 14	68.2 ± 11.2	41.4 ± 3.9	1.65 ± 0.31
[7, 12]	10.2 / 14	72.8 ± 11.2	37.4 ± 3.6	1.95 ± 0.35
[12, 22]	14.4 / 14	55.0 ± 10.7	41.3 ± 3.8	1.33 ± 0.29
[22, 35]	18.9 / 14	36.7 ± 8.8	30.9 ± 3.3	1.19 ± 0.31
[35, 100]	11.7 / 14	53.9 ± 11.7	60.0 ± 4.6	0.90 ± 0.21

$\eta(D^+)$	χ^2 / ndf	$N(D^+)$	$B_{2\sigma}$	$N_D/B_{2\sigma}$
[-1.50, -1.00]	6.8 / 14	37.3 ± 7.0	8.3 ± 1.7	4.51 ± 1.25
[-1.00, -0.50]	21.4 / 14	78.2 ± 11.9	36.1 ± 3.7	2.17 ± 0.39
[-0.50, 0.00]	12.9 / 14	67.3 ± 12.4	63.1 ± 4.7	1.07 ± 0.21
[0.00, 0.50]	10.3 / 14	87.7 ± 13.8	73.9 ± 5.2	1.19 ± 0.20
[0.50, 1.00]	15.1 / 14	57.9 ± 11.3	55.7 ± 4.4	1.04 ± 0.22
[1.00, 1.50]	13.1 / 14	16.0 ± 7.6	29.5 ± 3.3	0.54 ± 0.26

y	χ^2 / ndf	$N(D^+)$	$B_{2\sigma}$	$N_D/B_{2\sigma}$
[0.05, 0.15]	6.7 / 14	73.6 ± 11.5	42.0 ± 3.8	1.76 ± 0.32
[0.15, 0.20]	10.1 / 14	53.0 ± 9.3	22.8 ± 2.8	2.33 ± 0.50
[0.20, 0.30]	10.0 / 14	68.2 ± 11.9	55.3 ± 4.4	1.23 ± 0.24
[0.30, 0.40]	14.0 / 14	56.6 ± 11.3	50.1 ± 4.2	1.13 ± 0.24
[0.40, 0.50]	17.9 / 14	44.2 ± 10.1	43.6 ± 3.9	1.01 ± 0.25
[0.50, 0.70]	9.7 / 14	57.6 ± 11.7	54.1 ± 4.6	1.06 ± 0.23

$z_e(D^+)$	χ^2 / ndf	$N(D^+)$	$B_{2\sigma}$	$N_D/B_{2\sigma}$
[0.00, 0.20]	9.9 / 14	67.3 ± 14.5	105.9 ± 6.4	0.63 ± 0.14
[0.20, 0.30]	20.3 / 14	44.8 ± 11.9	70.7 ± 4.9	0.63 ± 0.17
[0.30, 0.40]	16.7 / 14	76.2 ± 11.6	39.4 ± 3.7	1.93 ± 0.35
[0.40, 0.50]	14.0 / 13	56.7 ± 10.0	28.6 ± 3.3	1.98 ± 0.42
[0.50, 0.60]	2.4 / 13	42.8 ± 8.1	14.5 ± 2.3	2.96 ± 0.73
[0.60, 1.00]	12.8 / 12	45.8 ± 8.1	14.2 ± 2.4	3.24 ± 0.78

$\log_{10}(x_{Bj})$	χ^2 / ndf	$N(D^+)$	$B_{2\sigma}$	$N_D/B_{2\sigma}$
[-4.6, -3.9]	11.0 / 14	59.7 ± 11.7	57.6 ± 4.7	1.04 ± 0.22
[-3.9, -3.6]	11.4 / 14	81.6 ± 12.0	42.3 ± 3.9	1.93 ± 0.33
[-3.6, -3.3]	18.3 / 14	48.4 ± 10.8	51.6 ± 4.2	0.94 ± 0.22
[-3.3, -3.0]	18.4 / 14	62.2 ± 11.2	42.9 ± 3.9	1.45 ± 0.29
[-3.0, -2.8]	13.8 / 14	45.9 ± 8.7	22.0 ± 2.8	2.09 ± 0.47
[-2.8, -1.7]	9.6 / 14	51.5 ± 11.0	48.7 ± 4.1	1.06 ± 0.24

Table A.5: *The results of the bin wise D^+ signal extraction are given which are obtained from the fits to the mass spectra shown in figure A.3. The mean and the width used in the fit are fixed to the values determined with the inclusive signal: $m(D^+) = 1869.0 \pm 2.2$ GeV/c^2 and $\sigma_m = 23.9 \pm 2.2$ GeV/c^2 (cf. tab. 115).*

$\sigma_{vis}(ep \to eD^+X)$: single differential results

$p_t(D^+)$	$d\sigma/dp_t$	errors [nb/GeV/c]				
[GeV/c]	[nb/GeV/c]	statistical	experimental		theoretical	
[2.5, 3.0]	1.953	±0.316	+0.412	−0.343	+0.134	−0.144
[3.0, 3.5]	1.053	±0.180	+0.215	−0.170	+0.071	−0.080
[3.5, 4.0]	0.556	±0.128	+0.121	−0.090	+0.039	−0.039
[4.0, 5.0]	0.353	±0.054	+0.104	−0.054	+0.026	−0.024
[5.0, 6.0]	0.063	±0.023	+0.072	−0.010	+0.004	−0.005
[6.0, 10.0]	0.025	±0.005	+0.005	−0.004	+0.002	−0.002

Q^2	$d\sigma/dQ^2$	errors [nb/GeV^2]				
[GeV^2]	[nb/GeV^2]	statistical	experimental		theoretical	
[2, 4]	0.2000	±0.0377	+0.0467	−0.0332	+0.0141	−0.0148
[4, 7]	0.1551	±0.0254	+0.0341	−0.0245	+0.0109	−0.0107
[7, 12]	0.0950	±0.0145	+0.0213	−0.0140	+0.0077	−0.0065
[12, 22]	0.0373	±0.0072	+0.0105	−0.0060	+0.0025	−0.0027
[22, 35]	0.0153	±0.0036	+0.0033	−0.0026	+0.0010	−0.0012
[35, 100]	0.0042	±0.0009	+0.0009	−0.0007	+0.0003	−0.0003

$\eta(D^+)$	$d\sigma/d\eta$	errors [nb]				
	[nb]	statistical	experimental		theoretical	
[-1.50, -1.00]	0.84	±0.16	+0.25	−0.12	+0.06	−0.08
[-1.00, -0.50]	0.97	±0.15	+0.20	−0.14	+0.07	−0.07
[-0.50, 0.00]	0.66	±0.12	+0.14	−0.10	+0.05	−0.04
[0.00, 0.50]	0.83	±0.13	+0.18	−0.13	+0.06	−0.06
[0.50, 1.00]	0.76	±0.15	+0.36	−0.22	+0.06	−0.05
[1.00, 1.50]	0.28	±0.13	+0.15	−0.09	+0.02	−0.03

y	$d\sigma/dy$	errors [nb]				
	[nb]	statistical	experimental		theoretical	
[0.05, 0.15]	5.69	±0.89	+1.21	−1.66	+0.41	−0.38
[0.15, 0.20]	5.50	±0.96	+1.41	−1.02	+0.39	−0.40
[0.20, 0.30]	3.70	±0.64	+1.02	−0.75	+0.26	−0.25
[0.30, 0.40]	3.33	±0.66	+0.94	−0.74	+0.23	−0.25
[0.40, 0.50]	2.44	±0.55	+0.76	−0.47	+0.17	−0.20
[0.50, 0.70]	1.68	±0.34	+0.40	−0.29	+0.12	−0.14

$z_e(D^+)$	$d\sigma/dz_e$	errors [nb]				
	[nb]	statistical	experimental		theoretical	
[0.00, 0.20]	2.22	±0.48	+0.64	−0.31	+0.18	−0.17
[0.20, 0.30]	2.87	±0.76	+0.96	−0.55	+0.22	−0.21
[0.30, 0.40]	4.78	±0.73	+1.00	−0.69	+0.34	−0.34
[0.40, 0.50]	3.47	±0.61	+0.71	−0.53	+0.24	−0.25
[0.50, 0.60]	2.86	±0.54	+0.61	−0.53	+0.21	−0.20
[0.60, 1.00]	0.64	±0.11	+0.18	−0.13	+0.04	−0.04

$\log_{10}(x_{Bj})$	$d\sigma/dx_{Bj}$	errors [nb]				
	[nb]	statistical	experimental		theoretical	
[-4.6, -3.9]	0.47	±0.09	+0.14	−0.07	+0.03	−0.03
[-3.9, -3.6]	1.82	±0.27	+0.47	−0.42	+0.15	−0.13
[-3.6, -3.3]	1.00	±0.22	+0.35	−0.18	+0.07	−0.07
[-3.3, -3.0]	1.30	±0.23	+0.31	−0.19	+0.09	−0.09
[-3.0, -2.8]	1.44	±0.27	+0.40	−0.40	+0.10	−0.12
[-2.8, -1.7]	0.28	±0.06	+0.06	−0.05	+0.02	−0.02

Table A.6: *The results of the single differential D^+ production cross section measurements are given. Beside of the statistical errors from the signal extraction, the systematical errors arising from the experimental method and the theoretical errors are quoted, where the latter includes the uncertainties of the decay's branching ratio and the model dependencies of the acceptance determination.*

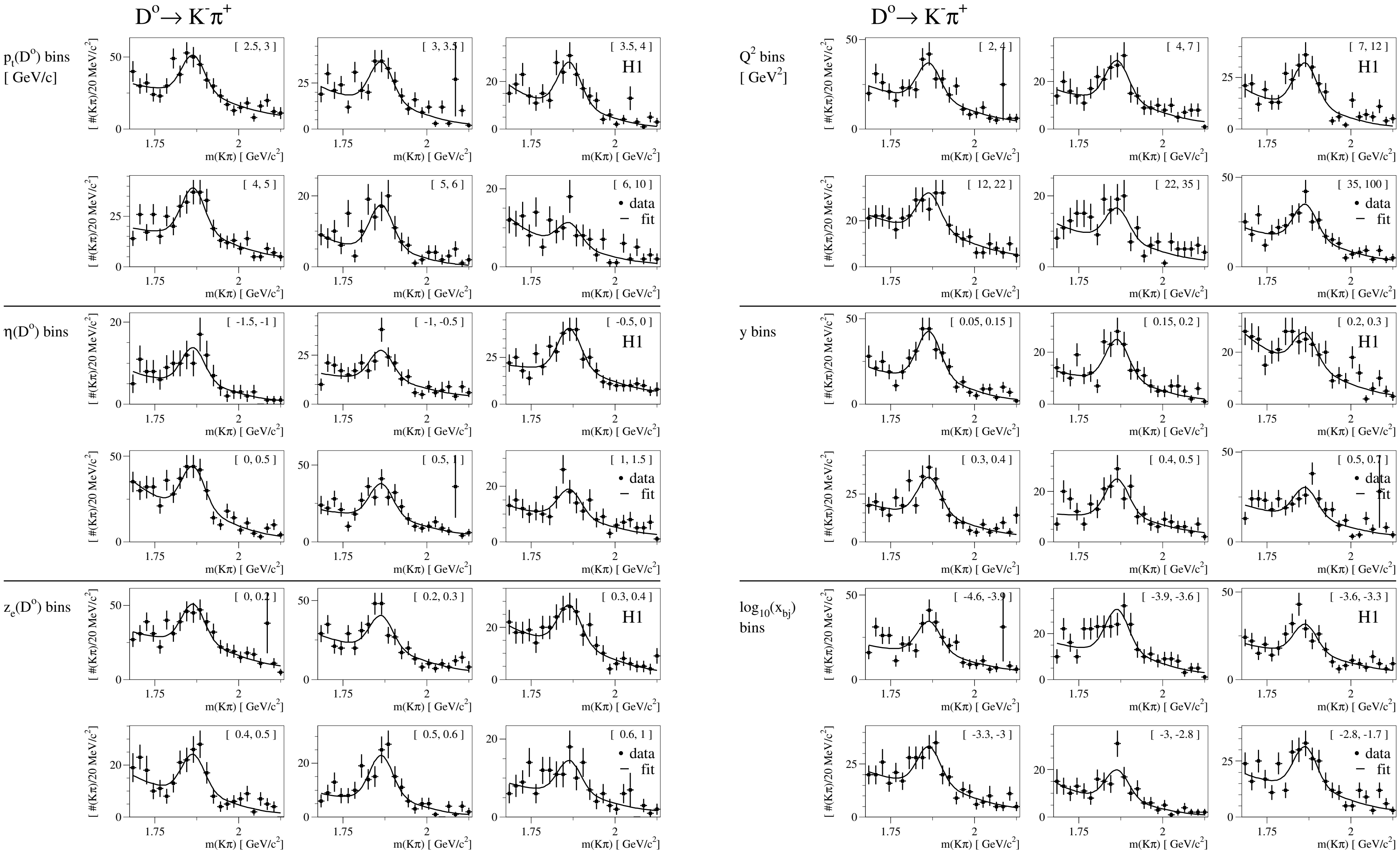

Figure A.4: *The bin wise $m(K\pi)$ mass spectra of the untagged D^0 candidates are shown. The bin ranges are given in the upper right corner of the histograms. The fitted curves are the results of the signal extraction which are used to determine the central values of the differential cross section measurements. The numerical fit results are listed in table A.7.*

Bin wise fit results in the D^0 channel

$p_t(D^0)$ [GeV/c]	χ^2 / ndf	$N(D^0)$	$B_{2\sigma}$	$N_D/B_{2\sigma}$
[2.5, 3.0]	19.5 / 18	107 ± 15	126 ± 10	0.85 ± 0.13
[3.0, 3.5]	30.9 / 18	89 ± 12	63 ± 8	1.42 ± 0.26
[3.5, 4.0]	20.5 / 18	75 ± 11	36 ± 8	2.07 ± 0.53
[4.0, 5.0]	15.5 / 18	93 ± 12	72 ± 7	1.29 ± 0.21
[5.0, 6.0]	27.3 / 18	50 ± 12	14 ± 13	3.63 ± 3.58
[6.0, 10.0]	22.2 / 18	24 ± 8	27 ± 6	0.87 ± 0.34

Q^2 [GeV^2]	χ^2 / ndf	$N(D^0)$	$B_{2\sigma}$	$N_D/B_{2\sigma}$
[2, 4]	15.8 / 18	82 ± 12	80 ± 8	1.02 ± 0.18
[4, 7]	16.9 / 18	68 ± 10	54 ± 6	1.27 ± 0.24
[7, 12]	41.8 / 18	85 ± 14	42 ± 10	2.01 ± 0.57
[12, 22]	11.5 / 18	65 ± 11	81 ± 8	0.80 ± 0.16
[22, 35]	33.3 / 18	36 ± 9	37 ± 6	1.00 ± 0.28
[35, 100]	18.1 / 18	81 ± 12	69 ± 7	1.18 ± 0.21

$\eta(D^0)$	χ^2 / ndf	$N(D^0)$	$B_{2\sigma}$	$N_D/B_{2\sigma}$
[-1.50, -1.00]	9.2 / 17	35 ± 7	21 ± 5	1.65 ± 0.49
[-1.00, -0.50]	20.3 / 18	60 ± 11	60 ± 7	1.00 ± 0.21
[-0.50, 0.00]	10.0 / 18	91 ± 13	86 ± 8	1.05 ± 0.17
[0.00, 0.50]	20.6 / 18	103 ± 14	87 ± 9	1.17 ± 0.20
[0.50, 1.00]	21.2 / 18	87 ± 12	75 ± 8	1.15 ± 0.20
[1.00, 1.50]	17.8 / 18	40 ± 9	44 ± 6	0.92 ± 0.23

y	χ^2 / ndf	$N(D^0)$	$B_{2\sigma}$	$N_D/B_{2\sigma}$
[0.05, 0.15]	19.5 / 18	111 ± 13	59 ± 8	1.87 ± 0.33
[0.15, 0.20]	17.7 / 18	63 ± 10	38 ± 6	1.65 ± 0.36
[0.20, 0.30]	25.3 / 18	52 ± 11	78 ± 7	0.67 ± 0.15
[0.30, 0.40]	21.8 / 18	79 ± 12	65 ± 8	1.21 ± 0.23
[0.40, 0.50]	19.1 / 18	59 ± 9	45 ± 6	1.31 ± 0.27
[0.50, 0.70]	32.4 / 18	66 ± 11	68 ± 7	0.98 ± 0.19

$z_e(D^0)$	χ^2 / ndf	$N(D^0)$	$B_{2\sigma}$	$N_D/B_{2\sigma}$
[0.00, 0.20]	15.8 / 18	105 ± 14	126 ± 9	0.84 ± 0.13
[0.20, 0.30]	21.8 / 18	86 ± 13	96 ± 9	0.90 ± 0.16
[0.30, 0.40]	11.8 / 18	62 ± 11	66 ± 7	0.94 ± 0.19
[0.40, 0.50]	22.3 / 17	60 ± 12	39 ± 9	1.52 ± 0.46
[0.50, 0.60]	18.9 / 17	65 ± 9	21 ± 5	3.08 ± 0.91
[0.60, 1.00]	14.5 / 17	34 ± 7	28 ± 5	1.20 ± 0.34

$\log_{10}(x_{Bj})$	χ^2 / ndf	$N(D^0)$	$B_{2\sigma}$	$N_D/B_{2\sigma}$
[-4.6, -3.9]	25.7 / 18	75 ± 12	77 ± 8	0.97 ± 0.18
[-3.9, -3.6]	24.6 / 18	75 ± 10	51 ± 6	1.48 ± 0.26
[-3.6, -3.3]	22.2 / 18	67 ± 12	76 ± 8	0.88 ± 0.18
[-3.3, -3.0]	12.7 / 18	74 ± 12	73 ± 8	1.00 ± 0.19
[-3.0, -2.8]	14.5 / 18	51 ± 9	30 ± 6	1.71 ± 0.49
[-2.8, -1.7]	26.0 / 18	73 ± 11	61 ± 7	1.20 ± 0.23

Table A.7: *The results of the bin wise untagged D^0 signal extraction are given which are obtained from the fits to the mass spectra shown in figure A.4. Beside the exponential background quoted the wrong charge background is subtracted for the extraction. The size of the latter in a 2-σ window of the fitted signal Gaussian is about 43% of the total signal size. The mean and the width used in the fit for the signal Gaussian are fixed to the values determined with the inclusive signal: $m(D^0) = 1863.9 \pm 3.5$ GeV/c^2 and $\sigma_m = 33.6 \pm 3.0$ GeV/c^2 (cf. fig. 7.2).*

$\sigma_{vis}(ep \to eD^0X)$: single differential results

$p_t(D^0)$ [GeV/c]	$d\sigma/dp_t$ [nb/GeV/c]	errors [nb/GeV/c] statistical	experimental		theoretical	
[2.5, 3.0]	5.291	$\pm$0.718	$+$1.112	$-$0.891	$+$0.134	$-$0.183
[3.0, 3.5]	3.038	$\pm$0.409	$+$0.497	$-$0.780	$+$0.127	$-$0.079
[3.5, 4.0]	2.286	$\pm$0.340	$+$0.812	$-$0.620	$+$0.085	$-$0.062
[4.0, 5.0]	1.130	$\pm$0.146	$+$0.187	$-$0.209	$+$0.031	$-$0.043
[5.0, 6.0]	0.516	$\pm$0.120	$+$0.139	$-$0.129	$+$0.018	$-$0.015
[6.0, 10.0]	0.056	$\pm$0.018	$+$0.016	$-$0.021	$+$0.002	$-$0.003

Q^2 [GeV^2]	$d\sigma/dQ^2$ [nb/GeV^2]	errors [nb/GeV^2] statistical	experimental		theoretical	
[2, 4]	0.6625	$\pm$0.0990	$+$0.1132	$-$0.1614	$+$0.0238	$-$0.0190
[4, 7]	0.3859	$\pm$0.0578	$+$0.0787	$-$0.0884	$+$0.0195	$-$0.0103
[7, 12]	0.2669	$\pm$0.0432	$+$0.0663	$-$0.0573	$+$0.0084	$-$0.0073
[12, 22]	0.1025	$\pm$0.0179	$+$0.0211	$-$0.0230	$+$0.0029	$-$0.0030
[22, 35]	0.0474	$\pm$0.0113	$+$0.0096	$-$0.0107	$+$0.0013	$-$0.0013
[35, 100]	0.0186	$\pm$0.0027	$+$0.0032	$-$0.0038	$+$0.0005	$-$0.0007

$\eta(D^0)$	$d\sigma/d\eta$ [nb]	errors [nb] statistical	experimental		theoretical	
[-1.50, -1.00]	1.85	$\pm$0.38	$+$0.34	$-$0.46	$+$0.09	$-$0.05
[-1.00, -0.50]	1.74	$\pm$0.30	$+$0.28	$-$0.28	$+$0.04	$-$0.07
[-0.50, 0.00]	2.43	$\pm$0.34	$+$0.42	$-$0.36	$+$0.06	$-$0.11
[0.00, 0.50]	2.88	$\pm$0.39	$+$0.53	$-$0.87	$+$0.10	$-$0.07
[0.50, 1.00]	2.67	$\pm$0.37	$+$0.52	$-$0.87	$+$0.10	$-$0.07
[1.00, 1.50]	1.91	$\pm$0.41	$+$0.70	$-$0.77	$+$0.07	$-$0.08

y	$d\sigma/dy$ [nb]	errors [nb] statistical	experimental		theoretical	
[0.05, 0.15]	22.72	$\pm$2.65	$+$3.99	$-$6.35	$+$0.76	$-$0.64
[0.15, 0.20]	20.35	$\pm$3.12	$+$4.29	$-$4.46	$+$0.56	$-$0.69
[0.20, 0.30]	7.07	$\pm$1.43	$+$2.05	$-$2.51	$+$0.19	$-$0.20
[0.30, 0.40]	10.29	$\pm$1.55	$+$2.60	$-$2.60	$+$0.28	$-$0.39
[0.40, 0.50]	9.26	$\pm$1.48	$+$2.24	$-$1.57	$+$0.40	$-$0.27
[0.50, 0.70]	4.95	$\pm$0.83	$+$1.26	$-$1.21	$+$0.24	$-$0.14

$z_e(D^0)$	$d\sigma/dz_e$ [nb]	errors [nb] statistical	experimental		theoretical	
[0.00, 0.20]	7.99	$\pm$1.07	$+$1.59	$-$1.62	$+$0.35	$-$0.22
[0.20, 0.30]	12.53	$\pm$1.92	$+$2.92	$-$2.34	$+$0.50	$-$0.43
[0.30, 0.40]	9.39	$\pm$1.64	$+$1.74	$-$2.08	$+$0.26	$-$0.31
[0.40, 0.50]	9.96	$\pm$2.00	$+$2.12	$-$2.22	$+$0.27	$-$0.26
[0.50, 0.60]	11.60	$\pm$1.65	$+$2.10	$-$2.43	$+$0.32	$-$0.44
[0.60, 1.00]	1.47	$\pm$0.32	$+$0.29	$-$0.41	$+$0.06	$-$0.05

$\log_{10}(x_{Bj})$	$d\sigma/dx_{Bj}$ [nb]	errors [nb] statistical	experimental		theoretical	
[-4.6, -3.9]	1.55	$\pm$0.25	$+$0.39	$-$0.27	$+$0.06	$-$0.04
[-3.9, -3.6]	3.71	$\pm$0.50	$+$1.36	$-$1.02	$+$0.14	$-$0.10
[-3.6, -3.3]	3.44	$\pm$0.60	$+$0.71	$-$0.70	$+$0.11	$-$0.09
[-3.3, -3.0]	3.93	$\pm$0.62	$+$0.88	$-$0.94	$+$0.11	$-$0.15
[-3.0, -2.8]	4.29	$\pm$0.79	$+$1.43	$-$1.16	$+$0.15	$-$0.12
[-2.8, -1.7]	1.18	$\pm$0.18	$+$0.23	$-$0.27	$+$0.03	$-$0.04

Table A.8: *The results of the single differential D^0 production cross section measurements are given. Beside of the statistical errors from the signal extraction, the systematical errors arising from the experimental method and the theoretical errors are quoted, where the latter includes the uncertainties of the decay's branching ratio and the model dependencies of the acceptance determination.*

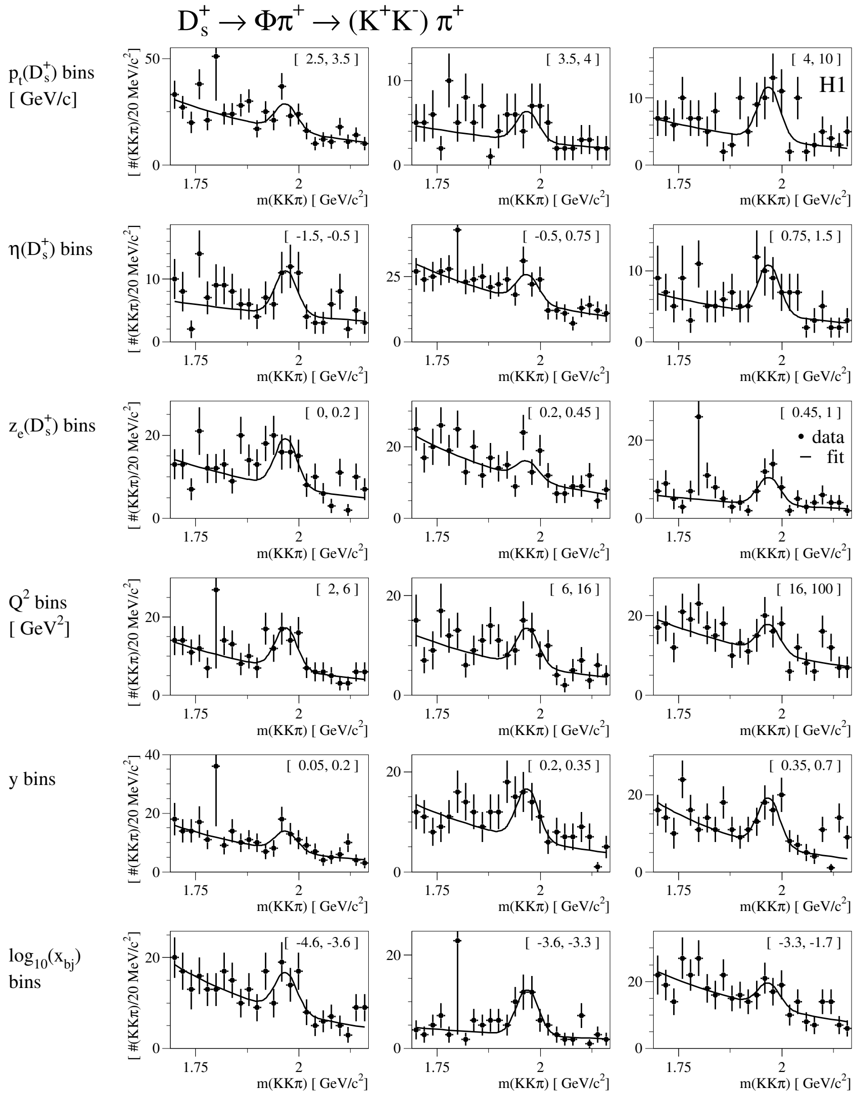

Bin wise fit results in the D_s^+ channel

$p_t(D_s^+)$ [GeV/c]	χ^2 / ndf	$N(D_s^+)$	$B_{2\sigma}$	$N_D/B_{2\sigma}$
[2.5, 3.5]	20.3 / 19	40.4 ± 12.4	86.9 ± 5.6	0.46 ± 0.15
[3.5, 4.0]	19.4 / 19	11.7 ± 5.4	14.9 ± 2.3	0.78 ± 0.38
[4.0, 10.0]	21.4 / 19	26.3 ± 7.7	20.0 ± 2.9	1.31 ± 0.43
$\eta(D_s^+)$	χ^2 / ndf	$N(D_s^+)$	$B_{2\sigma}$	$N_D/B_{2\sigma}$
[-1.50, -0.50]	24.3 / 19	23.2 ± 7.4	22.9 ± 2.8	1.01 ± 0.34
[-0.50, 0.75]	13.1 / 19	34.2 ± 11.8	81.7 ± 5.4	0.42 ± 0.15
[0.75, 1.50]	12.3 / 19	23.2 ± 7.3	20.5 ± 2.7	1.13 ± 0.38
$z_e(D_s^+)$	χ^2 / ndf	$N(D_s^+)$	$B_{2\sigma}$	$N_D/B_{2\sigma}$
[0.00, 0.20]	33.1 / 19	38.6 ± 9.5	40.0 ± 3.6	0.96 ± 0.25
[0.20, 0.45]	19.4 / 19	16.3 ± 9.5	58.5 ± 4.6	0.28 ± 0.16
[0.45, 1.00]	20.8 / 19	23.3 ± 7.6	18.6 ± 2.8	1.25 ± 0.45
Q^2 [GeV^2]	χ^2 / ndf	$N(D_s^+)$	$B_{2\sigma}$	$N_D/B_{2\sigma}$
[2, 6]	12.8 / 19	35.3 ± 9.0	35.2 ± 3.6	1.00 ± 0.27
[6, 16]	19.1 / 19	25.2 ± 8.2	31.2 ± 3.3	0.81 ± 0.27
[16, 100]	19.0 / 19	23.5 ± 10.1	56.5 ± 4.5	0.41 ± 0.18
y	χ^2 / ndf	$N(D_s^+)$	$B_{2\sigma}$	$N_D/B_{2\sigma}$
[0.05, 0.20]	10.8 / 19	22.4 ± 8.6	37.8 ± 3.8	0.59 ± 0.24
[0.20, 0.35]	26.7 / 19	33.8 ± 8.8	34.1 ± 3.3	0.99 ± 0.27
[0.35, 0.70]	35.1 / 19	41.3 ± 9.5	36.0 ± 3.6	1.15 ± 0.29
$\log_{10}(x_{Bj})$	χ^2 / ndf	$N(D_s^+)$	$B_{2\sigma}$	$N_D/B_{2\sigma}$
[-4.6, -3.6]	13.9 / 19	28.0 ± 9.2	43.6 ± 4.0	0.64 ± 0.22
[-3.6, -3.3]	13.0 / 19	32.3 ± 7.5	15.1 ± 2.3	2.15 ± 0.59
[-3.3, -1.7]	16.3 / 19	23.9 ± 10.3	65.0 ± 4.7	0.37 ± 0.16

Figure A.5: *The bin wise $m(KK\pi)$ mass spectra of the selected D_s^+ candidates are shown and the results of the signal extraction used to determine the central values of the differential cross section measurements are given. The mean and the width used in the fit are fixed to the values determined with the inclusive signal: $m(D_s^+) = 1968.6 \pm 6.7$ GeV/c^2 and $\sigma_m = 26.2 \pm 6.3$ GeV/c^2 (cf. fig. 7.2).*

$\sigma_{vis}(ep \to eD_s^+X)$: single differential results

$p_t(D_s^+)$ [GeV/c]	$d\sigma/dp_t$ [nb/GeV/c]	errors [nb/GeV/c] statistical	experimental		theoretical	
[2.5, 3.5]	1.088	$\pm$0.333	+0.221	$-$0.265	+0.270	$-$0.270
[3.5, 4.0]	0.444	$\pm$0.204	+0.162	$-$0.090	+0.111	$-$0.111
[4.0, 10.0]	0.071	$\pm$0.021	+0.016	$-$0.012	+0.018	$-$0.018

Q^2 [GeV^2]	$d\sigma/dQ^2$ [nb/GeV^2]	errors [nb/GeV^2] statistical	experimental		theoretical	
[2, 6]	0.1718	$\pm$0.0435	+0.0480	$-$0.0378	+0.0429	$-$0.0431
[6, 16]	0.0531	$\pm$0.0171	+0.0115	$-$0.0115	+0.0133	$-$0.0134
[16, 100]	0.0065	$\pm$0.0028	+0.0014	$-$0.0013	+0.0016	$-$0.0016

$\eta(D_s^+)$	$d\sigma/d\eta$ [nb]	errors [nb] statistical	experimental		theoretical	
[-1.50, -0.50]	0.59	$\pm$0.19	+0.12	$-$0.10	+0.15	$-$0.15
[-0.50, 0.75]	0.50	$\pm$0.17	+0.10	$-$0.12	+0.12	$-$0.12
[0.75, 1.50]	0.81	$\pm$0.25	+0.43	$-$0.29	+0.20	$-$0.21

y	$d\sigma/dy$ [nb]	errors [nb] statistical	experimental		theoretical	
[0.05, 0.20]	3.49	$\pm$1.34	+0.74	$-$0.85	+0.87	$-$0.88
[0.20, 0.35]	4.52	$\pm$1.17	+2.81	$-$1.92	+1.13	$-$1.12
[0.35, 1.00]	2.34	$\pm$0.54	+0.68	$-$0.58	+0.58	$-$0.58

$z_e(D_s^+)$	$d\sigma/dz_e$ [nb]	errors [nb] statistical	experimental		theoretical	
[0.00, 0.20]	4.05	$\pm$0.99	+2.58	$-$0.97	+1.04	$-$1.01
[0.20, 0.45]	1.36	$\pm$0.79	+0.39	$-$0.41	+0.34	$-$0.34
[0.45, 1.00]	0.94	$\pm$0.31	+0.22	$-$0.18	+0.23	$-$0.23

$\log_{10}(x_{Bj})$	$d\sigma/dx_{Bj}$ [nb]	errors [nb] statistical	experimental		theoretical	
[-4.6, -3.6]	0.54	$\pm$0.18	+0.16	$-$0.14	+0.13	$-$0.13
[-3.6, -3.3]	2.14	$\pm$0.50	+0.48	$-$0.40	+0.53	$-$0.54
[-3.3, -1.7]	0.36	$\pm$0.16	+0.07	$-$0.08	+0.09	$-$0.09

Table A.9: *The results of the single differential D_s^+ production cross section measurements are given. Beside of the statistical errors from the signal extraction, the systematical errors arising from the experimental method and the theoretical errors are quoted, where the latter includes the uncertainties of the decay's branching ratio and the model dependencies of the acceptance determination.*

Appendix B

Subtrigger Efficiencies

The method of measuring the subtrigger efficiencies has been discussed in detail in section 4.3. The table shown on the next page summarizes the measured efficiencies in the trigger elements of subtrigger 61. The results found in data and simulated D-meson samples are compared and a good agreement is found.

D^+	reference	Efficiency of trigger element		$\Delta\varepsilon$ [%]
trigger element	trigger	ε_{data} [%]	ε_{sim} [%]	$(\varepsilon_{sim} - \varepsilon_{data})$
`DCRPh_THig`	035	98.74 ± 0.03	98.05 ± 0.10	-0.69 ± 0.10
`zVtx_sig`	035	93.08 ± 0.07	93.61 ± 0.18	0.53 ± 0.19
`SPCLe_IET`	071	99.96 ± 0.01	100.00 ± 0.00	0.04 ± 0.01
`(v:8)`	039	99.95 ± 0.01	(100.00)	0.05 ± 0.01
`(d:0)&&(f:0)`	112	99.95 ± 0.02	(100.00)	0.05 ± 0.02
subtrigger efficiency		91.78 ± 0.08	91.78 ± 0.20	0.01 ± 0.21

D_s^+	reference	Efficiency of trigger element		$\Delta\varepsilon$ [%]
trigger element	trigger	ε_{data} [%]	ε_{sim} [%]	$(\varepsilon_{sim} - \varepsilon_{data})$
`DCRPh_THig`	035	98.65 ± 0.09	97.87 ± 0.20	-0.78 ± 0.22
`zVtx_sig`	035	94.42 ± 0.18	94.78 ± 0.32	0.36 ± 0.37
`SPCLe_IET`	071	99.96 ± 0.01	100.00 ± 0.00	0.04 ± 0.01
`(v:8)`	039	99.94 ± 0.02	(100.00)	0.06 ± 0.02
`(d:0)&&(f:0)`	112	99.95 ± 0.03	(100.00)	0.05 ± 0.03
subtrigger efficiency		93.01 ± 0.20	92.76 ± 0.37	-0.24 ± 0.42

D^0	reference	Efficiency of trigger element		$\Delta\varepsilon$ [%]
trigger element	trigger	ε_{data} [%]	ε_{sim} [%]	$(\varepsilon_{sim} - \varepsilon_{data})$
`DCRPh_THig`	035	98.69 ± 0.05	97.75 ± 0.10	-0.94 ± 0.11
`zVtx_sig`	035	91.91 ± 0.13	91.80 ± 0.19	-0.11 ± 0.23
`SPCLe_IET`	071	99.96 ± 0.01	100.00 ± 0.00	0.04 ± 0.01
`(v:8)`	039	99.93 ± 0.02	(100.00)	0.07 ± 0.02
`(d:0)&&(f:0)`	112	99.90 ± 0.04	(100.00)	0.10 ± 0.04
subtrigger efficiency		90.52 ± 0.14	89.73 ± 0.21	-0.78 ± 0.25

D^{*+}	reference	Efficiency of trigger element		$\Delta\varepsilon$ [%]
trigger element	trigger	ε_{data} [%]	ε_{sim} [%]	$(\varepsilon_{sim} - \varepsilon_{data})$
`DCRPh_THig`	035	98.93 ± 0.32	98.25 ± 0.41	-0.68 ± 0.52
`zVtx_sig`	035	93.60 ± 0.76	94.47 ± 0.71	0.87 ± 1.04
`SPCLe_IET`	071	99.96 ± 0.01	100.00 ± 0.00	0.04 ± 0.01
`(v:8)`	039	99.93 ± 0.02	(100.00)	0.07 ± 0.02
`(d:0)&&(f:0)`	112	99.90 ± 0.04	(100.00)	0.10 ± 0.04
subtrigger efficiency		92.40 ± 0.81	92.82 ± 0.80	0.41 ± 1.14

Table B.1: *The table summarizes the channel wise trigger element efficiencies of ST 61 measured in data and simulated event samples.*

Appendix C

Track Extrapolation with `CSTCOR`

The lifetime tag relies crucially on using the best estimate of the decay particles' track parameter at their production point, i.e. inside the beam pipe, and on an accurate description of their resolution. But the tracking detectors, herein the CJC and CST, measure the tracks inside their volumes only.

In the following the `CSTCOR` algorithm is discussed which extrapolates tracks from these volumes through the detector materials to the interaction region. Beside of correcting the track parameters themselves according to the particle's energy loss in the materials and the inhomogeneities of the magnetic field, it also estimates the deterioration in their resolution which arises dominantly from multiple scattering (MS).

Detector materials

The materials in the central region of the H1 experiment and their properties are listed in table C.1. Their extentions are approximated by cylinders centered at the z-axis with an inner radii R_i and thicknesses d_i. The materials are characterized by their atomic numbers Z_i and masses A_i, their densities ρ_i and their radiation lengths X_0^i.

These materials are summarized to detector volumes to minimize the computation time needed for the track extrapolation. The volumes have been chosen according to the tasks performed by the reconstruction chain and are indicated in the second row of table C.1.

In table C.2 the properties of these detector volumes are listed. Beside of the radius R_c of the volume's center and its total thickness $d = \sum_i d_i$, the material properties averaged with the formulas for mixtures and compounds given in [17],

$$\begin{aligned} \tfrac{1}{A} = \tfrac{\sum_i \rho_i \cdot d_i / A_i}{\sum_i \rho_i \cdot d_i} \ , \quad Z = \tfrac{\sum_i Z_i \cdot \rho_i \cdot d_i / A_i}{\sum_i \rho_i \cdot d_i / A_i} \ , \\ \rho = \tfrac{\sum_i \rho_i \cdot d_i}{\sum_i d_i} \quad \text{and} \quad \tfrac{1}{X_0} = \tfrac{\sum_i d_i / X_0^i}{\sum_i d_i} \ , \end{aligned} \tag{C.1}$$

where the sums run over all materials i included in the detector volume, are quoted.

Material description	volume	R_i [cm]	thickness d_i [cm]	atomic number Z_i	weight A_i [g/mol]	density ρ_i [g/cm^3]	rad. length X_0^i [cm]
beam pipe 1998-2000 (Al)	1	4.50	0.020	13.0	27.0	2.700	8.90
beam pipe 1998-2000 (CFK)	1	4.52	0.070	6.0	12.0	1.500	23.00
Air	2,3,4	4.59	1.110	7.0	14.6	0.001	30420.00
electrical shield (CST)	2,3,4	5.35	0.005	13.0	27.0	2.700	8.90
mechanical shield (CST)	2,3,4	5.36	0.010	6.0	12.0	1.500	23.00
silicon sensors (inner layer)	2	5.70	0.030	14.0	28.1	2.330	9.40
hybrid (inner layer)	3,4	5.67	0.064	13.0	27.0	2.700	8.90
Air (inner layer)	2,3,4	5.73	2.000	7.0	14.6	0.001	30420.00
Air (outer layer)	9,10,11	7.73	1.970	7.0	14.6	0.001	30420.00
cooling pipes (Cu)	7,8	7.90	0.060	29.0	63.5	8.960	1.40
silicon sensors (outer layer)	9	9.70	0.030	14.0	28.1	2.330	9.40
hybrid (outer layer)	10,11	9.67	0.064	13.0	27.0	2.700	8.90
Air	9,10,11	9.73	2.250	7.0	14.6	0.001	30420.00
voltage cables (Cu)	9,10,11	11.60	0.002	29.0	63.5	8.960	1.40
mechanical shield (CST)	9,10,11	11.98	0.005	6.0	12.0	1.500	23.00
electrical shield (CST)	9,10,11	11.99	0.010	13.0	27.0	2.700	8.90
Air	14	12.00	3.200	7.0	14.6	0.001	30420.00
CIP inner wall	14	15.20	0.200	10.9	22.3	0.064	431.00
Argon gas	14	15.40	0.300	18.0	40.0	0.002	34035.00
Ethane gas (C_2H_6)	14	15.70	0.300	18.0	30.0	0.001	10980.00
CIP middle wall	14	16.00	0.300	10.9	22.3	0.064	431.00
Argon gas	14	16.30	0.300	18.0	40.0	0.002	34035.00
Ethane gas (C_2H_6)	14	16.60	0.300	18.0	30.0	0.001	10980.00
CIP outer wall	14	16.90	0.200	10.9	22.3	0.064	431.00
Air	14	17.10	0.250	7.0	14.6	0.001	30420.00
CIZ inner wall	14	17.35	0.180	21.9	47.5	0.143	114.00
Argon gas	14	17.53	1.070	18.0	40.0	0.002	34035.00
Ethane gas (C_2H_6)	14	18.60	1.070	18.0	30.0	0.001	10980.00
CIZ outer wall	14	19.67	0.180	21.9	47.5	0.143	114.00
Air	14	19.85	0.450	7.0	14.6	0.001	30420.00
CJC1 inner wall	14	20.30	0.150	6.0	12.0	1.500	23.00
Argon gas	15	20.45	12.250	18.0	40.0	0.002	34035.00
CJC1 wires	15	32.70	0.006	74.0	184.0	19.300	0.35
Ethane gas (C_2H_6)	15	32.71	12.240	18.0	30.0	0.001	10980.00
CJC1 outer wall	16	44.95	0.150	6.0	12.0	1.500	23.00
COZ inner wall	16	45.50	0.160	21.9	47.5	0.143	114.00
Argon gas	16	45.66	1.320	18.0	40.0	0.002	34035.00
Ethane gas (C_2H_6)	16	46.98	1.330	18.0	30.0	0.001	10980.00
COZ outer wall	16	48.31	0.490	21.9	47.5	0.143	114.00
Air	16	48.80	0.550	7.0	14.6	0.001	30420.00
COP inner wall	16	49.35	0.400	10.9	22.3	0.064	431.00
Argon gas	16	49.75	0.400	18.0	40.0	0.002	34035.00
Ethane gas (C_2H_6)	16	50.15	0.400	18.0	30.0	0.001	10980.00
COP middle wall	16	50.55	0.500	10.9	22.3	0.064	431.00
Argon gas	16	51.05	0.400	18.0	40.0	0.002	34035.00
Ethane gas (C_2H_6)	16	51.45	0.400	18.0	30.0	0.001	10980.00
COP outer wall	16	51.85	0.500	10.9	22.3	0.064	431.00
Air	16	52.35	0.650	7.0	14.6	0.001	30420.00
CJC2 inner wall	16	53.00	0.150	6.0	12.0	1.500	23.00
Argon gas	17	53.15	15.420	18.0	40.0	0.002	34035.00
CJC2 wires	17	68.57	0.006	74.0	184.0	19.300	0.35
Ethane gas (C_2H_6)	17	68.58	15.420	18.0	30.0	0.001	10980.00
CJC2 outer wall	18	84.00	0.400	13.0	27.0	2.700	8.90

Table C.1: *The radial extention and properties (see text) of the materials in the central region of the H1 detector are given. They are summarized to the detector volumes given in table C.2.*

Nr	volume description	R_c [cm]	thickness d [cm]	z-range [cm]	atomic number Z	weight A [g/mol]	density ρ [g/cm^3]	rad. length X_0 [cm]
1	beam pipe 1998-2000	4.5	0.090	[-400.0, 400.0]	7.3	14.8	1.767	17.0
2	inner CST layer (Si)	6.2	3.075	[-17.8, 17.8]	11.3	22.8	0.033	717.2
3	inner hybrid ($+z$)	6.2	3.075	[17.8, 23.0]	11.8	24.4	0.066	375.2
4	inner hybrid ($-z$)	6.2	3.075	[-23.0, -17.8]	11.8	24.4	0.066	375.2
5	inner air ($+z$)	6.2	3.075	[23.0, 400.0]	7.0	14.6	0.001	30420.0
6	inner air ($-z$)	6.2	3.075	[-400.0, -23.0]	7.0	14.6	0.001	30420.0
7	cooling pipes ($+z$)	7.9	0.060	[20.4, 23.0]	29.0	63.5	8.960	1.4
8	cooling pipes ($-z$)	7.9	0.060	[-23.0, -20.4]	29.0	63.5	8.960	1.4
9	outer CST layer (Si)	9.9	4.270	[-17.8, 17.8]	12.3	25.1	0.028	741.9
10	outer hybrid ($+z$)	9.9	4.270	[17.8, 23.0]	12.3	25.6	0.052	441.2
11	outer hybrid ($-z$)	9.9	4.270	[-23.0, -17.8]	12.3	25.6	0.052	441.2
12	outer air ($+z$)	9.9	4.270	[23.0, 400.0]	7.0	14.6	0.001	30420.0
13	outer air ($-z$)	9.9	4.270	[-400.0, -23.0]	7.0	14.6	0.001	30420.0
14	CIZ/CIP	16.3	8.550	[-112.5, 106.5]	7.5	15.3	0.040	683.4
15	CJC1 gas/wires	32.7	24.500	[-112.5, 107.5]	39.4	92.5	0.006	1315.9
16	COP/COZ	48.9	7.900	[-110.5, 105.5]	7.2	14.6	0.081	354.4
17	CJC2 gas/wires	68.6	30.850	[-112.5, 107.5]	36.4	84.7	0.005	1623.6
18	outer CJC2 wall	84.2	0.400	[-112.5, 107.5]	13.0	27.0	2.700	8.9

Table C.2: *The summarized detector volumes implemented in* CSTCOR *are given for the data taking period 1998-2000: the R_c values denote the radii of the volumes' centers, d their radial thicknesses and their extentions in z are given. The properties of the materials included in a volume are averaged according to the formulas in equation C.1.*

Energy loss corrections

The track parameters $(\kappa, \phi_0, \theta, d_{ca}, z_0)$ denoting the measured track parameters with respect to the origin have been introduced in section 5.1. The transverse and total momenta p_t and p of the particle in the magnetic field B and its energy E are derived from the curvature κ by

$$p_t\,[\,\mathrm{GeV}\,] = \frac{0.003 \cdot B\,[\,\mathrm{T}\,]}{|\kappa\,[\,\mathrm{cm}^{-1}\,]\,|}\,, \quad p = \frac{p_t}{\sin\theta} \quad \text{and} \quad E = \sqrt{m^2 + p^2}, \tag{C.2}$$

where the mass m of the particle has to be supplied by the user. The speed of light is set to one for the discussion. The Lorentz factors used in the following are defined by $\beta = p/E$ and $\gamma = E/m$.

In the calculations the energy loss and MS are treated as if they happen only at the center of the volume, i.e. as if all the material is concentrated in this point. Thereto the crossing $\vec{x}_c$ of the track with a cylinder centered at the z-axis with radius R_c is calculated. The effective length L_{eff} in the material which is crossed by the particle is estimated in a linear approximation by

$$L_{\text{eff}} = d \cdot \sqrt{1 + \tan^2\phi_{\text{inc}} + \cot^2\theta}, \tag{C.3}$$

where d denotes the thickness of the volume, ϕ_{inc} the particle's incidence angle in $r\phi$ with respect to normal vector on the cylinder surface and θ is the track's measured polar angle.

The mean energy loss of the particle in the detector volume is calculated with the Bethe-Bloch formula [17]

$$-\frac{dE}{dx} = K \cdot \frac{Z}{A} \cdot \frac{1}{\beta^2} \cdot \left[\frac{1}{2} \cdot \ln\left(\frac{2 \cdot m_e \cdot \beta^2 \cdot \gamma^2 \cdot T_{\max}}{I^2}\right) - \beta^2 - \frac{\delta}{2}\right], \tag{C.4}$$

with $K = 0.307\ \mathrm{MeV} \cdot \mathrm{cm}^2/\mathrm{mol}$. m_e denotes the electron mass and the maximal kinetic energy $T_{\max}$ which can be imparted to a free electron in a single collision is given by

$$T_{\max} = \frac{2 \cdot m_e \cdot \beta^2 \cdot \gamma^2}{1 + 2 \cdot \gamma \cdot m_e/m + (m_e/m)^2}\ . \tag{C.5}$$

For the mean excitation energy the approximation $I\,[\,\mathrm{eV}\,] = 16 \cdot Z^{0.9}$ [71] is used, where Z denotes the averaged atomic number. The relativistic density effect is not considered, i.e. $\delta = 0$. The mean energy ΔE lost by the particle in the material is then given by

$$\Delta E = -\frac{dE}{dx} \cdot \rho \cdot L_{\mathrm{eff}} > 0. \tag{C.6}$$

Because the particle's momentum is measured after this energy loss, its curvature κ' in front of the material towards the interaction region can be estimated with

$$\kappa' = \kappa \cdot \frac{p}{p'} = \kappa \cdot \frac{p}{\sqrt{(E + \Delta E)^2 - m^2}}. \tag{C.7}$$

Equation C.6 denotes the mean energy loss only. Its fluctuations, the energy straggling, are a measure for the accuracy of the energy loss correction made: in thin layers the energy loss follows a Landau distribution, where the tails arise from large energy transfers in single collisions, while it approaches a Gaussian in thick layers. In `CSTCOR` the accuracy of the energy loss correction is estimated by

$$\sigma(\Delta E) = \frac{4.02 \cdot \xi}{2 \cdot \sqrt{\ln 4}}, \quad \xi = 1.534 \cdot 10^{-4} \cdot \frac{Z \cdot \rho \cdot L_{\mathrm{eff}}}{A \cdot \beta^2}, \tag{C.8}$$

where $(4.02 \cdot \xi)$ denotes the full width half maximum of the Landau distribution [72] which is transformed under the assumption of a Gaussian shape into one standard deviation. This estimated fluctuation is then propagated with equation C.7 into the error in the curvature $\sigma(\kappa')$.

Multiple scattering corrections

The distortions of the particle's flight direction by multiple scattering in the material are treated in `CSTCOR` as errors in the radial incident angle ϕ_{inc} and the polar angle θ at the particle's crossing point $\vec{x}_c$. The mean planar scattering angle θ_{MS} is estimated in the Gaussian approximation [17] by

$$\theta_{\mathrm{MS}} = \frac{13.6\ \mathrm{MeV}}{\beta \cdot p} \cdot \sqrt{\frac{L_{\mathrm{eff}}}{X_0}} \cdot \left[1 + 0.038 \cdot \ln\left(\frac{L_{\mathrm{eff}}}{X_0}\right)\right], \tag{C.9}$$

where the notation introduced above has been used. While θ_{MS} is used directly as the estimated error in the polar angle, $\sigma(\theta) = \theta_{\mathrm{MS}}$, the scattering angle is enlarge by the $r\phi$-projection and the error in the radial incident angle is given by

$$\sigma(\phi_{\mathrm{inc}}) = \phi_{\mathrm{MS}} = \theta_{\mathrm{MS}} / \sin(\theta). \tag{C.10}$$

This treatment does not describe the effect of multiple scattering on the $r\phi$ track parameters measured in the CJC. Instead the formulas derived in [59] are used in the volumes of the two CJC rings to estimate the errors in κ' and ϕ_{inc}:

$$\begin{aligned} \sigma^2(\kappa') &= 1.430 \cdot \phi_{\mathrm{MS}}^2 / L_{CJC}^2 \\ \sigma^2(\phi_{\mathrm{inc}}) &= 0.229 \cdot \phi_{\mathrm{MS}}^2 \end{aligned} \tag{C.11}$$

and in addition a negative correlation $cor(\kappa', \phi_{\mathrm{inc}}) = -0.374$ between them is introduced. Therein L_{CJC} denotes the radial distance between the inner- and outermost points measured on the track, the track length (cf. chap. 5).

Track corrections

CSTCOR is steered by supplying the radii R_{out} and R_{in} which denote from where to where the track has to be extrapolated: the CJC track parameters in the CST volume needed for the CJC-CST track fit are obtained by $R_{\mathrm{out}} = R_{\mathrm{end}}$ and $R_{\mathrm{in}} = 7.75$ cm, where R_{end} is the radius of the outermost measured CJC hit, and the extrapolation of CST tracks to the interaction region is steered by $R_{\mathrm{out}} = 7.75$ cm and $R_{\mathrm{in}} = 0$.

Starting from the outer radius the algorithm loops over the detector volumes and tests which are traversed by the track, where for volumes only partially crossed their thickness d is corrected accordingly.

For each volume the particle's crossing point $\vec{x}_c$ and incidence angle ϕ_{inc} are calculated and the corrected curvature κ' and the covariance matrix $cov(\kappa', \phi_{\mathrm{inc}}, \theta)$ of the parameters at $\vec{x}_c$ are determined. The parameters with respect to the origin corrected for the material in the respective volume $(\hat{\kappa}, \hat{\phi}_0, \hat{\theta}, \hat{d}_{ca}, \hat{z}_0)$ and their covariance matrix corrections are calculated with $\vec{x}_c$, $(\kappa', \phi_{\mathrm{inc}}, \theta)$ and $cov(\kappa', \phi_{\mathrm{inc}}, \theta)$. The magnetic field B averaged along the track in the volume is used for the extrapolation from $\vec{x}_c$ to the origin.

To calculate x_c^{i+1} in the $(i+1)$-th volume the track parameters corrected for the material in the previous i-th volume and the average magnetic field B_i in the i-th volume are used. The curvature is corrected for the inhomogeneities of the magnetic field according to $\kappa' = \kappa \cdot B_{i+1}/B_i$ not until the track is extrapolated from x_c^{i+1} back to the origin.

The track parameters corrected for all requested materials are then given with respect to the average magnetic field in the volume at R_{in}, respectively B at the origin for $R_{\mathrm{in}} = 0$. The calculated covariance matrix corrections of all volumes are summed and have to be added to the covariance matrix of the original track parameters by the user.

Appendix D

Constrained Vertex Fitter `VFit2dc`

In the following the mathematical model of the two dimensional track-vertex fit `VFit2dc` is discussed. The program fits a set of N tracks to the most probable common point of origin, the secondary vertex. It includes a constraint which forces the separation of the primary and secondary vertices to be conform with the momentum direction of the mother particle, where the latter is determined by the sum over the decay particles' momenta. The measured position of the event's primary vertex has to be supplied as input.

Such an additional constraint can be included in the fit model by direct substitution. This method usually provides fast algorithms, but the basic track-vertex fit model has to be adapted according to the substitution.

Inhere the directional constraint is added to the unconstrained `VFit2du` fitter by the means of Lagrange multipliers. This method has the advantage that the solution can be factorized: At first the unconstrained problem is solved in each fit iteration. This solution is then corrected to meet in addition the required constraint.

The method of Lagrange multipliers is equivalent to a direct substitution of the constraint, but the basic track-vertex fit model is unchanged by it. Because any desired condition can be added in a similar way at the end of the fit iteration loop, the approach is by far more general than the substitution method.

The implementation closely follows the CLEO note [73] which gives a general introduction into least square fitting theory. The unconstrained fitter `VFit2du` is based on the fast global method described in [74] which is formulated with the notation introduced in [75].

Variable definition

The flight trajectory of a charged particle in the $r\phi$-plane is described by the track parameters introduced in chapter 5. The vector $\vec{T}_i = (\kappa_i, \phi_i, d_i)^t$ gives the curvature, azimuthal angle and d_{ca} parameter of the i-th track with respect to the origin and their 3x3 covariance matrix is denoted with V_i. The index i runs over the N input tracks: $i = 1, \ldots, N$. The measured radial position of the primary vertex is denoted with $\vec{r}_{pv} = (x_{pv}, y_{pv})^t$ and

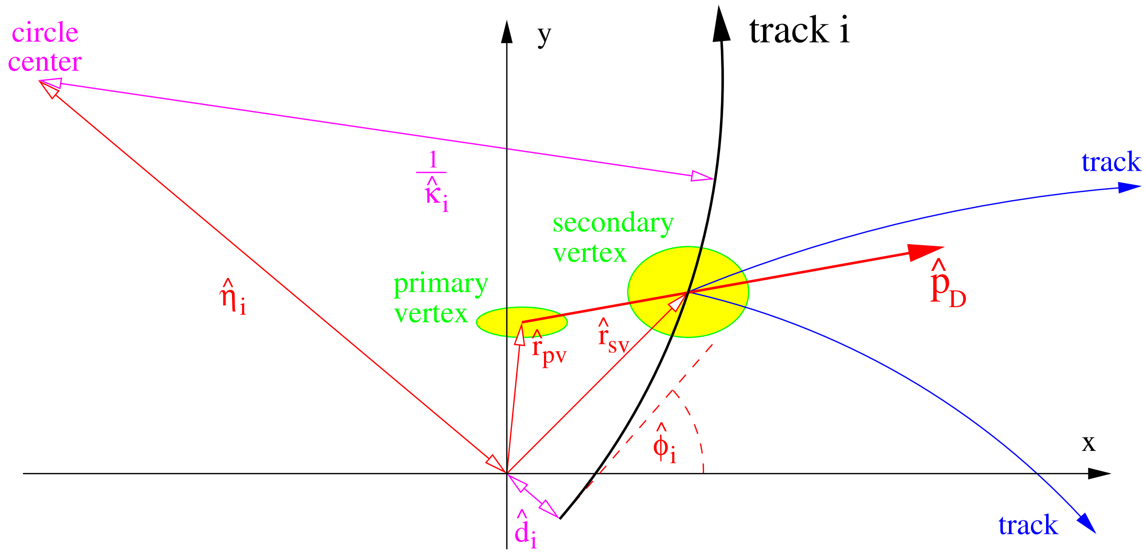

Figure D.1: *The fit parameters used in the constrained track-vertex fitter* VFit2dc *are schematically drawn. Their exact definition is given in the text.*

V_{pv} stands for its 2x2 covariance matrix. These measurements are the input to the fitter and they are summarized in the vector y and the covariance matrix V_y as follows:

$$y = \begin{pmatrix} \vec{T}_1 \\ \vdots \\ \vec{T}_N \\ \vec{r}_{pv} \end{pmatrix} \qquad \text{and} \qquad V_y = \begin{pmatrix} V_1 & & & \emptyset \\ & \ddots & & \\ & & V_N & \\ \emptyset & & & V_{pv} \end{pmatrix}. \tag{D.1}$$

The fit determines the most probable common origin $\hat{r}_{sv} = (\hat{x}_{sv}, \hat{y}_{sv})^t$, the secondary vertex, of the N input tracks. The particle trajectories are forced through the secondary vertex and they are therefore defined by their transverse momentum vectors alone. Internally the momentum of the i-th particle is parameterized by the vector $\hat{Q}_i = (\hat{\eta}_i, \hat{\phi}_i)^t$, $i = 1, \ldots, N$. The signed distance $\hat{\eta}_i$ of the circle center from the origin is related to the fitted track parameters by $\hat{\eta}_i = 1/\hat{\kappa}_i - \hat{d}_i$ (cf. fig. D.1). The fitted azimuthal angle $\hat{\phi}_i$ of the particle is defined at the point of closest approach to the origin.

In addition the constraint applied on the decay direction alters the position of the primary vertex to the fitted value $\hat{r}_{pv} = (\hat{x}_{pv}, \hat{y}_{pv})^t$. The fit parameters are summarized in the vector $\hat{x}$ and their covariance matrix is given by $V_{\hat{x}}$. They are defined by

$$\hat{x} = \begin{pmatrix} \hat{r}_{sv} \\ \hat{Q}_1 \\ \vdots \\ \hat{Q}_N \\ \hat{r}_{pv} \end{pmatrix} \qquad \text{and} \qquad V_{\hat{x}} = \begin{pmatrix} C_{0,0} & C_{0,1} & \cdots & C_{0,N} & C_{0,N+1} \\ C_{0,1}^t & C_{1,1} & \cdots & C_{1,N} & C_{1,N+1} \\ \vdots & \vdots & \ddots & \vdots & \vdots \\ C_{0,N}^t & C_{1,N}^t & \cdots & C_{N,N} & C_{N,N+1} \\ C_{0,N+1}^t & C_{1,N+1}^t & \cdots & C_{N,N+1}^t & C_{N+1,N+1} \end{pmatrix}. \tag{D.2}$$

The covariance matrix has been split into 2x2 matrices $C_{i,j}$ as follows:

$$\left.\begin{array}{l} C_{0,0} \\ C_{i,i} \\ C_{N+1,N+1} \end{array}\right\} \text{ covariances of } \left\{\begin{array}{l} \text{the secondary vertex position} \\ \text{the } i\text{-th track momentum } \hat{Q}_i,\ i=1,\dots,N \\ \text{the primary vertex position} \end{array}\right.$$

$$\left.\begin{array}{l} C_{0,i} \\ C_{0,N+1} \\ C_{i,j} \\ C_{i,N+1} \end{array}\right\} \text{correlations between} \left\{\begin{array}{l} \text{the secondary vertex and the } i\text{-th track momentum} \\ \text{the secondary and the primary vertices} \\ i\text{-th and } j\text{-th track momenta} \\ \text{the } i\text{-th track momentum and the primary vertex.} \end{array}\right.$$

The transformation of the fit parameters to the fitted track parameters is given by

$$\hat{y}(\hat{x}) = (\hat{T}_1(\hat{x}), \dots, \hat{T}_N(\hat{x}), \hat{r}_{pv}), \tag{D.3}$$

where the functions $\hat{T}_i(\hat{x})$, $i = 1, \dots, N$ are defined by

$$\hat{T}_i(\hat{x}) = \hat{T}_i(\hat{r}_{sv}, \hat{Q}_i) = \begin{pmatrix} \hat{\kappa}_i(\hat{r}_{sv}, \hat{Q}_i) \\ \hat{\phi}_i(\hat{r}_{sv}, \hat{Q}_i) \\ \hat{d}_i(\hat{r}_{sv}, \hat{Q}_i) \end{pmatrix} = \begin{pmatrix} \frac{\mathrm{sign}(\hat{\eta}_i)}{\sqrt{(\hat{x}_{sv}+\hat{\eta}_i\cdot\sin\hat{\phi}_i)^2+(\hat{y}_{sv}-\hat{\eta}_i\cdot\cos\hat{\phi}_i)^2}} \\ \hat{\phi}_i \\ \frac{1}{\hat{\kappa}_i(\hat{r}_{sv},\hat{Q}_i)} - \hat{\eta}_i \end{pmatrix}. \tag{D.4}$$

Unconstrained fitter `VFit2du`

The unconstrained fitter `VFit2du` minimizes the χ^2_u function

$$\chi^2_u(\hat{x}) = (y - \hat{y}(\hat{x}))^t \, V_y^{-1}(y - \hat{y}(\hat{x})). \tag{D.5}$$

To obtain the minimum in the (k+1)-th fit iteration the χ^2_u function is linearized. Therefore the function $\hat{y}(\hat{x})$ is evolved around the solution of the previous iteration $\hat{x}_k$:

$$\hat{y}(\hat{x}) \approx \hat{y}(\hat{x}_k) + \left.\frac{\partial \hat{y}}{\partial \hat{x}}\right|_{\hat{x}_k} (\hat{x} - \hat{x}_k) = \hat{y}_k + \mathcal{A}_k \Delta\hat{x}_k \tag{D.6}$$

Because the functions $\hat{T}_i(\hat{x})$ depend only on the secondary vertex position and the fit parameters $\hat{Q}_i$, the Jacobian $\mathcal{A}_k$ is a sparse matrix which can be written as

$$\mathcal{A}_k = \left.\frac{\partial \hat{y}}{\partial \hat{x}}\right|_{\hat{x}_k} = \begin{pmatrix} A_{k_1} & B_{k_1} & & \emptyset & \emptyset \\ \vdots & & \ddots & & \vdots \\ A_{k_N} & \emptyset & & B_{k_N} & \emptyset \\ \emptyset & \cdots & \cdots & \emptyset & \mathbb{I} \end{pmatrix}, \tag{D.7}$$

where the matrices A_{k_i} and B_{k_i} are given by

$$A_{k_i} = \left.\frac{\partial \hat{T}_i}{\partial \hat{r}_{sv}}\right|_{\hat{x}_k}, \quad B_{k_i} = \left.\frac{\partial \hat{T}_i}{\partial \hat{Q}_i}\right|_{\hat{x}_k}, \quad i = 1, \ldots, N. \tag{D.8}$$

The linearized χ^2_u function of the (k+1)-th iteration can then be written as

$$\chi^2_u(\hat{x}) \approx (\Delta\hat{y}_k - \mathcal{A}_k \Delta\hat{x}_k)^t \; V_y^{-1}(\Delta\hat{y}_k - \mathcal{A}_k \Delta\hat{x}_k), \tag{D.9}$$

where $\Delta\hat{y}_k = y - \hat{y}_k$ has been introduced.

The solution x_{k+1} of the (k+1)-th iteration is then given by

$$\hat{x}_{k+1} = \hat{x}_k + V_{\mathcal{A}_k} \; \mathcal{A}_k^t \; V_y^{-1} \Delta\hat{y}_k, \tag{D.10}$$

where the Hesse matrix $V_{\mathcal{A}_k}$, defined by

$$V_{\mathcal{A}_k} = (\mathcal{A}_k^t \; V_y^{-1} \mathcal{A}_k)^{-1} \tag{D.11}$$

gives also the covariance matrix $V_{\hat{x}_{k+1}}$ of the solution.

The Hesse matrix is the inverse of the symmetric $(2N{+}2)$-dimensional matrix $(\mathcal{A}_k^t \; V_y^{-1} \mathcal{A}_k)$. The number of arithmetical operation necessary for a matrix inversion is proportional to the third power of its dimension. Because $\mathcal{A}_k$ and V_y are sparse matrices, the inversion can be done with fewer computations and thus faster by partitioning the matrix [74]. Therefore the matrix product is written as

$$\mathcal{A}_k^t \; V_y^{-1} \; \mathcal{A}_k = \begin{pmatrix} D_{k_0} & D_{k_1} & & D_{k_N} & \emptyset \\ D_{k_1}^t & E_{k_1} & & \emptyset & \vdots \\ \vdots & & \ddots & & \vdots \\ D_{k_N}^t & \emptyset & & E_{k_N} & \emptyset \\ \emptyset & \cdots & \cdots & \emptyset & V_{pv}^{-1} \end{pmatrix}, \tag{D.12}$$

where the 2x2 matrices D_{k_i} and E_{k_i} can be calculated to be

$$\begin{aligned} D_{k_0} &= \textstyle\sum_{i=1}^{N} A_{k_i}^t V_i^{-1} A_{k_i} & \\ D_{k_i} &= A_{k_i}^t V_i^{-1} B_{k_i} & i = 1, \ldots, N. \\ E_{k_i} &= B_{k_i}^t V_i^{-1} B_{k_i} & \end{aligned} \tag{D.13}$$

Using the notation introduced in equation D.2 the Hesse matrix $V_{\mathcal{A}_k}$ is then given by

$$\begin{aligned} C_{0,0} &= (D_{k_0} - \textstyle\sum_{i=1}^{N} D_{k_i} E_i^{-1} D_{k_i}^t)^{-1} & \\ C_{0,i} &= C_{0,0} D_{k_i} E_i^{-1} & j = 1, \ldots, N \\ C_{i,j} &= \delta_{ij} E_i^{-1} + E_i^{-1} D_{k_i}^t C_{0,0} D_{k_j} E_j^{-1} & i, j = 1, \ldots, N. \end{aligned} \tag{D.14}$$

Thus only N+1 inversions of 2x2 matrices have to be calculated.

Constrained fitter `VFit2dc`

The direction between the production and decay vertices of a D-meson, referred to as decay direction, is equivalent to the direction of the D-meson's momentum, i.e. its flight direction. In background events the two directions are not correlated and therefore such a pointing condition can be used to distinguish signal and background.

The selected D-meson candidates decay at a secondary vertex which is separated by some $100\,\mu m$ from the primary vertex. Due to this small leverage arm the decay direction is only poorly resolved. The D-meson's flight direction is known more accurately, because it is reconstructed from the momenta of its decay particles. The directions of the latter can be measured precisely over the large radial extent of the drift chamber.

Thus a constrained fit requiring the flight and decay direction to be equivalent yields a more accurate description of the event topology and the minimal χ^2 value, respectively the fit probability $\mathcal{P}_{\mathrm{vf}}$, can be used to suppress background events.

The directional constraint is formulated with the fit parameters introduced in equation D.2 as follows:

$$f_c(\hat{x}) = (\hat{r}_{sv} - \hat{r}_{pv}) \wedge \hat{p}_D(\hat{x}) = (\hat{x}_{sv} - \hat{x}_{pv}) \cdot \hat{p}_y(\hat{x}) - (\hat{y}_{sv} - \hat{y}_{pv}) \cdot \hat{p}_x(\hat{x}) \stackrel{!}{=} 0, \qquad \text{(D.15)}$$

where $\hat{p}_D$ is calculated with the sum over the decay particles' fitted momenta:

$$\hat{p}_D(\hat{x}) = \begin{pmatrix} \hat{p}_x(\hat{x}) \\ \hat{p}_y(\hat{x}) \end{pmatrix} = \sum_{i=1}^{N} \mathrm{sign}(\hat{\eta}_i) \cdot \begin{pmatrix} -\hat{y}_{sv} + \hat{\eta}_i \cdot \cos\hat{\phi}_i \\ +\hat{x}_{sv} + \hat{\eta}_i \cdot \sin\hat{\phi}_i \end{pmatrix}. \qquad \text{(D.16)}$$

In D-meson decays $\hat{p}_D$ corresponds to the D-meson's transverse momentum vector. Equivalent to equation D.6 $f_c(\hat{x})$ is evolved around the solution of the previous iteration $\hat{x}_k$:

$$f_c(\hat{x}) \approx f_c(\hat{x}_k) + \left.\frac{\partial f_c}{\partial \hat{x}}\right|_{\hat{x}_k} (\hat{x} - \hat{x}_k) = \gamma_k + \Gamma_k \Delta\hat{x}_k \qquad \text{(D.17)}$$

The constraint is added to the χ^2 function by introducing Lagrange multipliers λ as follows:

$$\chi^2(\hat{x}) = (\Delta\hat{y}_k - \mathcal{A}_k\Delta\hat{x}_k)^t\, V_y^{-1}(\Delta\hat{y}_k - \mathcal{A}_k\Delta\hat{x}_k) + 2\lambda^t(\gamma_k + \Gamma_k\Delta\hat{x}_k). \qquad \text{(D.18)}$$

The minimum of the χ^2 function is then calculated not only with respect to the fit parameters $\hat{x}$, but also with respect to the Lagrange multipliers λ, because the condition $\partial\chi^2/\partial\lambda = 0$ required for the minimum correspond to the constraint equation D.15.

The solution $\hat{x}_{k+1}$ of the $(k+1)$-th fit iteration, which satisfy the constraint, is derived from the solution $\hat{x}'_{k+1}$ of the unconstrained fit (cf. eq. D.10) which minimize the χ^2_u function.

The validity of this treatment can be proven by a little manipulation of the total χ^2 function defined by equation D.18. This is achieved by rewriting

$$\Delta\hat{x}_k = (\hat{x} - \hat{x}_k) = (\hat{x}'_{k+1} - \hat{x}_k) - (\hat{x}'_{k+1} - \hat{x}) \qquad \text{(D.19)}$$

and using equation D.10 to prove the relation

$$V_y^{-1}(\Delta\hat{y}_k - \mathcal{A}_k(\hat{x}'_{k+1} - \hat{x}_k)) = 0, \tag{D.20}$$

which corresponds to the requirement that $\hat{x}'_{k+1}$ is the minimum of the unconstrained χ^2_u function. Using this last two equations, the total χ^2 function of equation D.18 can be written as

$$\begin{aligned}\chi^2(\hat{x}) &= +(\Delta\hat{y}_k - \mathcal{A}_k(\hat{x}'_{k+1} - \hat{x}_k))^t\ V_y^{-1}(\Delta\hat{y}_k - \mathcal{A}_k(\hat{x}'_{k+1} - \hat{x}_k)) \\ &\quad +(\hat{x}'_{k+1} - \hat{x})^t\ V^{-1}_{x'_{k+1}}(\hat{x}'_{k+1} - \hat{x}) + 2\lambda^t(\gamma_k + \Gamma_k\Delta\hat{x}_k) \\ &= \chi^2_u(\hat{x}'_{k+1}) + \chi^2_c(\hat{x}).\end{aligned} \tag{D.21}$$

The first term is constant and it gives the minimal χ^2_u value which has been determined with the unconstrained fit. The second term is a constrained χ^2_c function in the fit parameters determined by the unconstrained fit which forces the solution to satisfy the constraint equation. The solution $(\hat{x}_{k+1}, \lambda)$ which minimizes this function is given by

$$\begin{aligned}\hat{x}_{k+1} &= \hat{x}'_{k+1} + V^{-1}_{\hat{x}'_{k+1}}\Gamma^t_k\lambda \\ \lambda &= V_\Gamma(\gamma_k + \Gamma_k\hat{x}'_{k+1}),\end{aligned} \tag{D.22}$$

where the Hesse matrix V_Γ, which denotes also the covariance matrix of the Lagrange multipliers λ, is defined as

$$V_\Gamma = (\Gamma_k V_{\hat{x}'_{k+1}}\Gamma^t_k)^{-1}. \tag{D.23}$$

The covariance matrix of solution $\hat{x}_{k+1}$ is given by

$$V_{\hat{x}_{k+1}} = V_{\hat{x}'_{k+1}} - V_{\hat{x}'_{k+1}}\Gamma^t_k V_\Gamma \Gamma_k V_{\hat{x}'_{k+1}}. \tag{D.24}$$

To determine the solution which minimizes the total χ^2 function, the fit is iterated until the minimal χ^2 value is changes by less than a certain cutoff value ε by the last iteration step: $\chi^2(\hat{x}_{k+1}) - \chi^2(\hat{x}_k) < \varepsilon$.

Appendix E

Signal efficiency error calculation

The D-meson signal efficiency ε_D is needed to calibrate the simulated CST D^0 efficiency with data (see chap. 5) and to compare the efficiencies of the lifetime tagging cuts measured in data and simulated D-meson samples (see chap. 6). An error calculation for ε_D is necessary to judge the degree of agreement. The estimate for $\sigma(\varepsilon_D)$ used inhere is discussed in the following.

The signal efficiency is measured with the D-meson's mass spectrum M_r used as reference sample and the mass spectrum M_c of candidates which meet a certain condition. The numbers of signal events in the two samples, N_r and N_c, is determined by fits to the mass spectra necessary for the background subtraction.

Because M_c is a subset of M_r, N_r and N_c are correlated which has to be considered in the error calculation for the signal efficiency $\varepsilon_D = N_c/N_r$:

$$\left(\frac{\sigma(\varepsilon_D)}{\varepsilon_D}\right)^2 = \left(-\frac{\sigma(N_r)}{N_r}\right)^2 - 2\cdot\frac{\sigma(N_r)}{N_r}\cdot\frac{\sigma(N_c)}{N_c}\cdot cor(N_r, N_c) + \left(\frac{\sigma(N_c)}{N_c}\right)^2. \qquad \text{(E.1)}$$

Because the signals are extracted independently the correlation $cor(N_r, N_c)$ is a priori unknown.

Due to the background subtraction the errors in the extracted signal numbers are not Poisson like, i.e. $\sigma(N_r) \neq \sqrt{N_r}$ and $\sigma(N_c) \neq \sqrt{N_c}$. Therefore the well known formula for the error calculation of efficiencies based simply on event counting,

$$\sigma(\varepsilon) = \sqrt{\frac{\varepsilon\cdot(1-\varepsilon)}{N_r}} \qquad \text{(E.2)}$$

which considers the correlation between N_r and N_c, can not be applied. The correlation $cor(N_r, N_c)$ is therefore estimated otherwise.

If the number of signal events N_u in the subset of candidates which do not meet the requirement is known, the signal efficiency can be written as $\varepsilon_D = N_c/(N_c + N_u)$. N_c and

N_u are uncorrelated, because the two sample have no candidates in common. Thus the error of ε_D can simply be written as

$$\left(\frac{\sigma(\varepsilon_D)}{\varepsilon_D}\right)^2 = \left(-\frac{\sigma(N_u)}{(N_c+N_u)}\right)^2 + \left(\frac{N_u \cdot \sigma(N_c)}{N_c \cdot (N_c+N_u)}\right)^2, \tag{E.3}$$

where $\sigma(N_u)$ denotes the error on N_u.

But a bad signal-to-noise ratio in the sample of candidates which do not meet the requirement usually does not allow the determination of N_u. Therefore it is estimated by $N_u = N_r - N_c$ and its error can be approximated by $\sigma^2(N_u) = \sigma^2(N_r) - \sigma^2(N_c)$. Inserting these relations into equation E.3 results in

$$\left(\frac{\sigma(\varepsilon_D)}{\varepsilon_D}\right)^2 = \left(-\frac{\sigma(N_r)}{N_r}\right)^2 + (1 - 2 \cdot \varepsilon_D)\left(\frac{\sigma(N_c)}{N_c}\right)^2, \tag{E.4}$$

where $\sigma(N_r)$ and $\sigma(N_c)$ denote the errors evaluated by the fits to the mass spectra. The correlation $cor(N_r, N_c)$ found by comparing equations E.4 and E.1 is then given by

$$cor(N_r, N_c) = \frac{\sigma(N_c)}{\sigma(N_r)}. \tag{E.5}$$

If the errors in N_r and N_c are Poisson like, i.e. $\sigma(N_r) = \sqrt{N_r}$ and $\sigma(N_c) = \sqrt{N_c}$ equation E.2 can be directly derived from equation E.4.

Appendix F

The H1 Silicon Vertex Detector

In the following the ETH internal report `ETHZ-IPP PR-2000-1` is reproduced. The references cited inside are given at the end of the report. The report has been published in [1].

ETH IPP
Institute for Particle Physics

ETHZ-IPP PR-2000-1
February 15, 2000

The H1 silicon vertex detector

D. Pitzl[a], O. Behnke[d], M. Biddulph[b], K. Bösiger[c], R. Eichler[a], W. Erdmann[a], K. Gabathuler[b], J. Gassner[b], W.J. Haynes[e], R. Horisberger[b], M. Kausch[d], M. Lindström[f], H. Niggli[a,b], G. Noyes[e], P. Pollet[a], S. Steiner[c], S. Streuli[a], K. Szeker[a], P. Truöl[c]

[a] Institute for Particle Physics, ETH Zürich, Switzerland
[b] Paul Scherrer Institute, Villigen, Switzerland
[c] Physics Institute, University Zürich, Switzerland
[d] DESY, Hamburg, Germany
[e] Rutherford Appleton Laboratory, Chilton, didcot, UK
[f] Physics Department, Univeristy of Lund, Sweden

December 11, 2001

Abstract

The design, construction and performance of the H1 silicon vertex detector is described. It consists of two cylindrical layers of double sided, double metal silicon sensors read out by a custom designed analog pipeline chip. The analog signals are transmitted by optical fibers to a custom designed ADC board and are reduced on PowerPC processors. Details of the design and construction are given and performance figures from the first data taking periods are presented.

1 Introduction

The Central Silicon Tracker (CST) of the H1 experiment at the HERA electron-proton collider of DESY has been built to provide vertex information from precision measurements of charged particle tracks close to the interaction point. It consists of two concentric cylindrical layers of silicon sensors with two-coordinate readout allowing the identification of heavy-flavour particles with decay lengths of a few hundred micrometers [2]. The production cross section for charmed quark pairs at HERA is of order 1 μb which offers a rich field of physics topics [3] that can be exploited once a large number of charm events are tagged by the vertex detector. In addition, the production of b-quarks can be studied. The b cross section is smaller by about two orders of magnitude but the longer lifetimes of B-mesons lead to a more efficient tagging. The bulk of the heavy quarks are produced close to threshold such that their decay products have an average transverse momentum around 0.7 GeV/c. The vertex resolution is dominated by multiple scattering and the amount of material in front of the second silicon layer must be kept at a minimum. This led to a design with all readout electronics arranged at the ends and a central region consisting essentially only of active sensor material.

Space for the installation of the CST was obtained by reducing the beam pipe radius from 95 mm to 45 mm, which was the minimum radius required to protect the vertex detector from the direct and backscattered synchrotron radiation emitted by the electron beam.

The CST has been fully operational since the beginning of the 1997 running period. It complements the original central tracking detectors of H1, which consist of the main jet-cell drift chamber extending from 20.3 cm to 84.4 cm in radius, interspersed by a drift chamber for z-coordinate measurement between 46 cm and 48.5 cm radius, and an inner z-drift chamber between 17.35 cm and 20 cm radius. A superconducting coil provides a uniform magnetic field of 1.16 T. Further details can be found in [1]. Simultaneously to the implementation of the CST the tracking of electrons scattered at small deflection angles was made possible with the installation of initially four and, since 1998, eight disks of silicon sensors in the Backward Silicon Tracker (BST). The BST [4] uses the same frontend ASICs and the same readout electronics as the CST.

In the following section the layout and mechanics of the CST are described. Section 3 covers the frontend components, i.e. the sensors, the readout and control chips, the hybrid and the optical link. The on-line data processing and monitoring of slow control data is covered in section 4. The off-line track linking and the alignment procedure are explained in section 5. The performance numbers achieved so far are presented in section 6.

2 Layout

2.1 Geometry

The radial space available for upgrading the H1 experiment with a vertex detector was limited on the outside by the first MWPC trigger chamber starting at 15 cm radius. On the inside the space was restricted by a beam pipe radius of 4.5 cm as required by the synchrotron radiation environment, and by an additional 7 mm wide gap for cooling of the

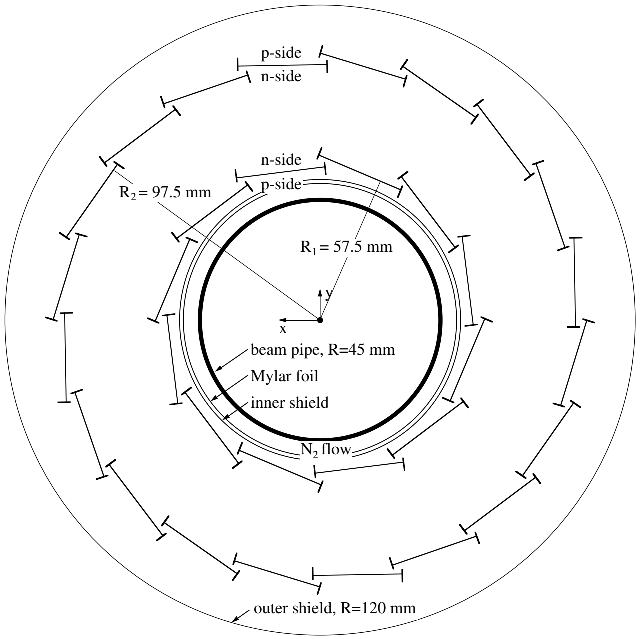

Figure 1: CST geometry in the r-ϕ-plane.

beam pipe with nitrogen gas flowing inside of a Mylar foil. The beampipe was initially made of aluminium with a wall thickness of 1.7 mm. It was replaced in early 1998 by a beam pipe made of 0.15 mm aluminium and 0.9 mm carbon fiber.

The two layers of the CST are formed from 12 and 20 faces at radii of 5.75 cm and 9.75 cm, respectively, as shown in figure 1. One face or 'laddder' consists of six silicon sensors and aluminium nitride hybrids at each end (see figure 2). A double layer of carbon fiber strips with a total thickness of 700 μm and a height of 4.4 mm is glued to the edges. The carbon fiber strips were specified with a Young's modulus of at least 400 000 N/mm^2. The gravitational sag of a full ladder when supported at the outer ends was measured to be less than 6 μm.

The positions of the ladders in a layer are shifted tangentially to ensure an overlap in r-ϕ of adjacent active areas, which amounts to 1.5% in the inner layer and 2.1% in the outer layer. The active length in z is 35.6 cm for both layers, see figure 2, to be compared to the length of the luminous region at HERA with an rms width of 10 cm. The coverage of the outer layer extends over ± 1.35 units in pseudorapidity for tracks emerging from the origin. The length is a compromise between rapidity coverage and preamplifier noise which is proportional to the length.

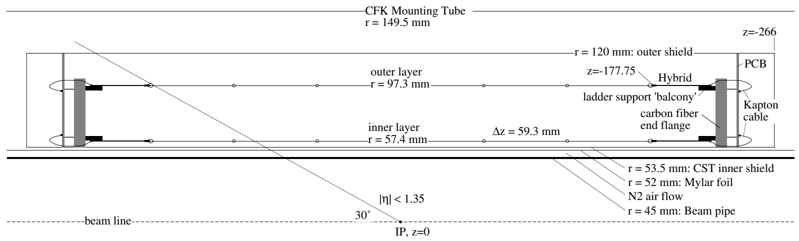

Figure 2: Side view of the upper half of the CST.

2.2 Mechanical Frame and Installation

The ladders are mounted on small balconies extending from carbon fiber endflanges (see figure 3). These balconies contain a high precision metal pin used to position the hybrids at laser-cut holes. Two small screws on each hybrid are used for fixation. The carbon fiber endflanges house a circular cooling water pipe for each layer with copper-tin sheets attached which reach into the balconies and thus provide thermal contact with the hybrids. The power dissipation of the CST is 50 W [11]. This power is removed with 12^{o}C cold water at a total flow rate of 2ℓ/min. The equilibrium temperature rises from 19^{o}C for the unpowered detector to 28^{o}C during operation.

The endflanges are split in the horizontal plane (see figure 3) allowing for the installation around the beam pipe. The lower half of the CST rests on three carbon fiber legs in a carbon fiber support tube (see figure 4) which is attached to the innermost tracking chamber of H1. The upper half of the CST rests on the lower half.

Upon installation the two halves of the CST are first mounted on rail extensions around the beam pipe about 2 m from the final position. A split service tube enclosing power leads, optical fibers and cooling pipes is equally mounted behind the CST and connections between the CST and the service tube are made. Then the CST and the service tube slide on straight carbon fiber rails, integrated in the support tube, into the final position, which is defined by spring-loaded end stops.

The service tube, depicted in figure 4, has a radial width of only 2 mm and surrounds the backward silicon tracker [4]. The wall of the service tube is made of a sandwich of 20 μm aluminium foil, 2 mm Rohacell [18] with grooves for the aluminium power leads and another 20 μm aluminium foil. At the edges of the half-shells flat cooling pipes of 2 mm height are incorporated. Cable connectors and voltage regulators are integrated in the service tube endflange facing away from the CST.

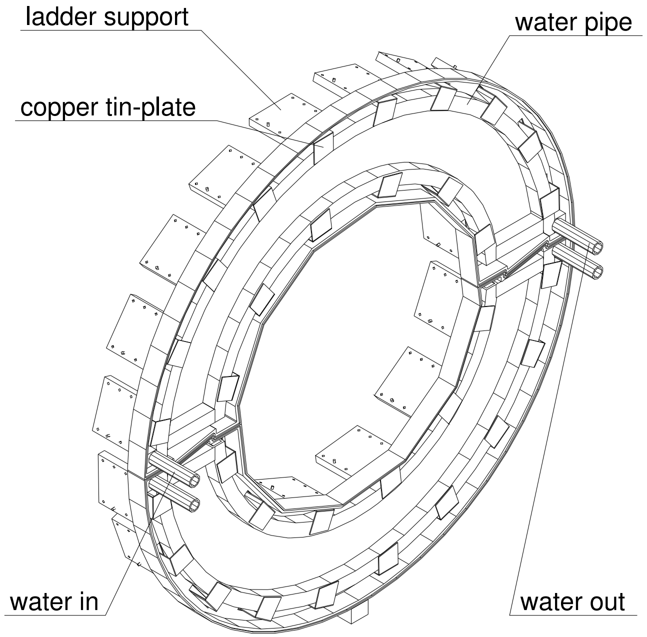

Figure 3: Carbon-fiber endflange. The cover is removed to display the integrated cooling pipe. Copper-tin sheets provide thermal contact to each balcony where the hybrids are mounted.

3 Frontend Components

Each ladder consists of two electrical units, called half-ladders. A half-ladder consists of three silicon sensors of $300\,\mu$m thickness, and a ceramic hybrid of $635\,\mu$m thickness carrying the front-end electronics, see figure 5.

The silicon sensors have $12\,\mu$m wide strip implants on both sides. The strips on the p-side, where holes are collected, are oriented parallel to the beam direction and have a pitch of $25\,\mu$m. Every second strip is read out for a measurement of the ϕ-coordinate at a known radius. The intermediate strips contribute to the signal by capacitive coupling and improve the position resolution . The implants on the n-side, where electrons are collected, are rotated by 90^o with respect to the p-side strips and have a pitch of $88\,\mu$m for a measurement of the z-coordinate. Every n-strip is read out by means of a second metal layer integrated on the sensors. There are 640 readout lines on each side of a sensor, which are daisy-chained by aluminium wire bonds between sensors, and connected to preamplifier ASICs on the hybrid. This arrangement leads to an effective strip length of 17.3 cm on the p-side and to a three-fold ambiguity for the z-coordinate on the n-side. The insensitive region at each end of the sensors and a gap of $300\,\mu$m between the sensors lead to a coverage in the z-direction of 97 % on the p-side and 95 % on the n-side. In total, the CST contains 64 half-ladders with 192 silicon sensors and 81 920 readout channels.

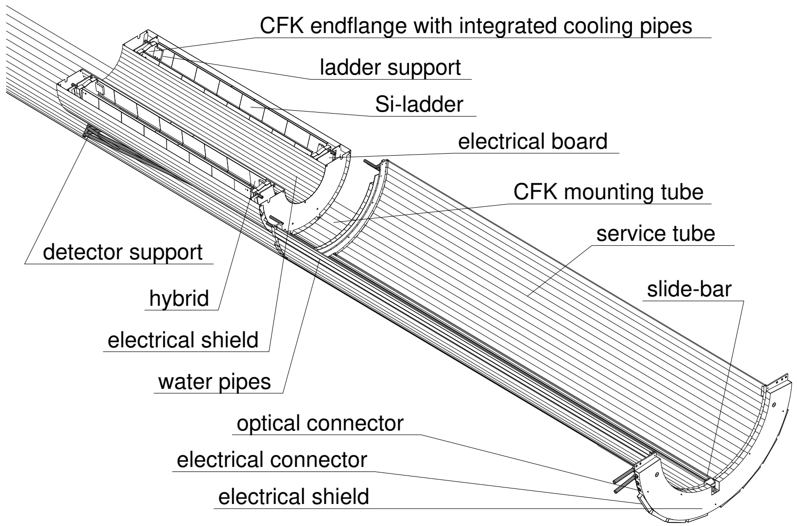

Figure 4: View of the lower half of the CST and the service tube which surrounds the BST and contains the supply cables, the optical fibers and pipes for cooling water. Both are supported by the carbon fiber support tube which contains a carbon fiber sliding rail for insertion. The beam pipe is not shown.

3.1 Silicon Sensors

High resistivity n-type silicon ($\rho > 6\,\text{k}\Omega\text{cm}$) was obtained as a 100 mm diameter boule from Wacker Chemitronic [7]. Cutting of $300\,\mu$m wafers and polishing of both sides was performed by Siltronix [9]. The wafer processing was performed at CSEM [8], where the basic double sided process was extended to provide a second metal layer over a $5\,\mu$m thick deposited oxide on the n-side. The contact vias between metal-1 and metal-2 have a drawn opening of $12 \times 24\,\mu\text{m}^2$ and proved to be very reliable. Using contact chain test structures a failure rate of less than 10^{-4} was determined (all CST sensors together contain $1.2 \cdot 10^5$ vias). The masks for the 14 layers in this process were designed by the collaboration.

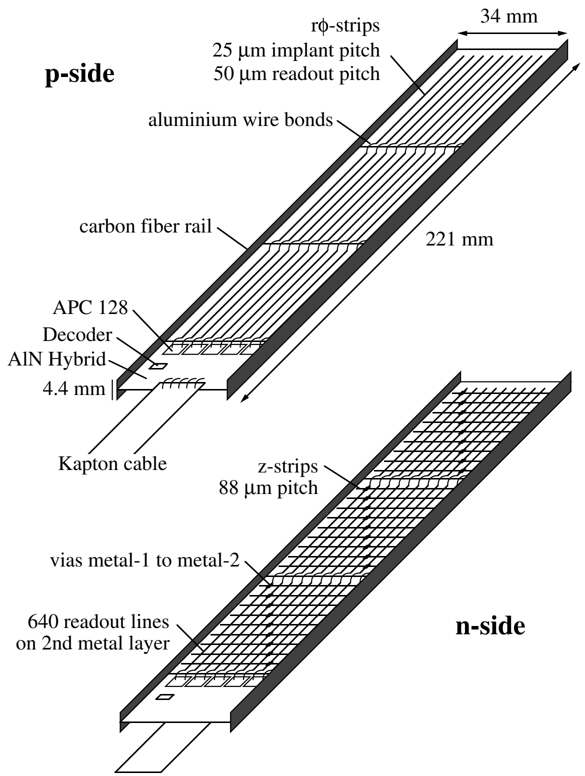

Figure 5: Schematic view of a half ladder. The upper part shows the p-side, the lower part the n-side.

The CST sensors have a full size of $5.9 \times 3.4\,\mathrm{cm}^2$, such that two sensors can be produced on a 100 mm diameter wafer. The strip implants are DC coupled to the metal-1 layer on both sides. Early prototypes were AC coupled but showed [6] a defect rate for the coupling capacitors on the n-side that led us to resort to DC coupling. The intermediate strips on the p-side are biased from a common guard ring across a punch-through gap covered by a FOXFET gate. With gate and guard at ground potential and positive bias voltage applied to the n-side the intermediate strips float at 4 V, with a uniformity of about 1 V on individual detectors and also between different wafers and different production lots. We are currently not supplying a dedicated gate voltage, although this option is available in the cabling scheme. The active area on the p-side (the junction side) is surrounded by a multi-ring guard structure with floating gates, that leads to a gradual increase of the surface potential from 0 V at the innermost guard ring to the full bias voltage at the edge. The carbon fiber strips glued to the sides of the sensors are floating at bias potential.

Each strip on the n-side is surrounded by a narrow ring of p-implant to provide the necessary interstrip insulation. The n-side can only be operated at full depletion, which requires between 30 V and 50 V for the installed sensors. Although the strips are DC coupled to the metal-1 layer and all n-side strips are read out we kept the accumulation channel structure which provides a high resistance connection to a common guard ring [6]. The sensors can then be fully depleted for a measurement of the total leakage current with only 2 test probe contacts, instead of having to contact 640 strips on each side.

Detectors with less than 6 μA of leakage current at 50 V bias where selected. Further tests prior to assembly included sparse measurements of the punch-through voltage on the p-side and the conductivity of the metal-1 to metal-2 vias on the n-side. The depletion voltage was determined at several positions on each sensor by a measurement of the interstrip resistance on the n-side. Finally, each sensor was scanned under a microscope for shorts or interrupts in the metallization. Sensors with more than 6 defective strips on either side were rejected. The final yield of accepted sensors was 62 % for 9 production lots.

The interstrip capacitance of one strip with respect to its six closest readout neighbours was measured as 1.5 pF/cm on the p-side, for 50 μm pitch and 12 μm implant width. On the n-side a value of 19 pF was measured for the capacitance of one strip with respect to the other 639 strips on a sensor. It is dominated by the overlap capacitance between metal-1 and metal-2 lines across the 5 μm oxide layer.

3.2 Analog Pipeline Chip

The time between bunch crossings at HERA is 96 ns while the H1 level-1 trigger decision arrives after 2.4 μs. Therefore all front-end readout systems have to store the signals from at least 25 beam crossings in a pipeline. For the H1 silicon detectors an integrated preamplifier and pipeline chip with multiplexed readout for 128 channels has been developed [15] and fabricated in 1.2 μm CMOS technology [16]. Figure 6 shows the schematics of the APC128 readout chip. The various external signals, internal switches and circuit components are explained in the following sections.

3.2.1 Preamplifier

The charge sensitive input amplifier consists of a single push-pull inverter stage which offers minimal noise for a given power dissipation. The open loop gain is about 150, which, together with a (parasitic) feedback capacitance $C_1 = 0.45\,\mathrm{pF}$, leads to a Miller

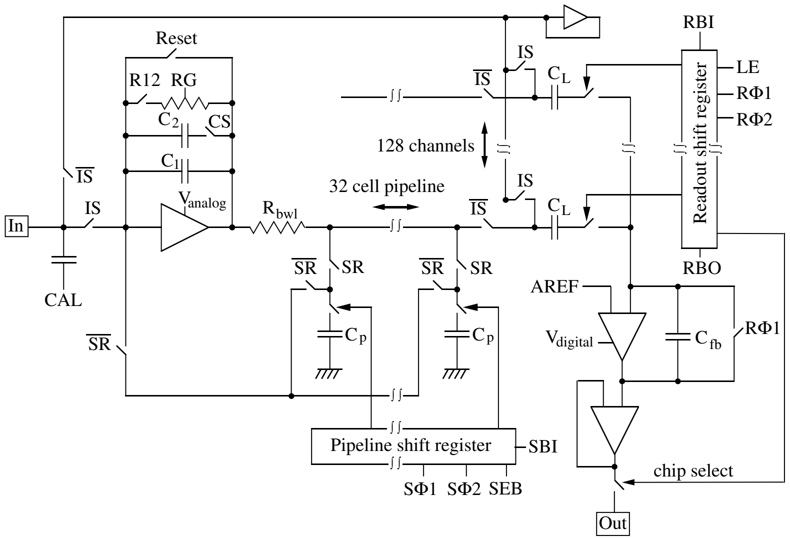

Figure 6: Schematic drawing of the APC128 chip showing one channel and all peripheral blocks.

capacitance $C_M = (A+1)C_1$ that is not much larger than the input load capacitance, especially on the n-side. The equivalent noise charge was measured as

$$\mathrm{ENC} = 700\,e + C_L \cdot 50\,e/\mathrm{pF}$$

at 0.3 mW power dissipation and sampling at 10 MHz [17]. The risetime of the amplifier with the detector load was measured to be 100 ns for the p-side and 150 ns for the n-side. Due to DC coupling between sensor and chip the preamplifier must absorb the strip leakage current through its feedback resistor (RG), which is adjustable by an external voltage and set to a value of about 1 MΩ. Consequently the signal decay time is 450 ns which is sufficient to avoid pile-up at HERA. Leakage currents of up to several hundred nA per strip can be tolerated before the preamplifier runs into saturation.

Several switches are used to control the preamplifier. During data taking the input select switch IS is closed, connecting the preamplifier input to a strip. The Reset switch is open and the switch R12 is closed, activating the feedback resistor RG. By closing switch CS a second feedback capacitor C_2 can be added, which can be used for analog signal processing [15] and calibration purposes. At H1, however, this feature is not used during regular data taking. The sample/read switch SR connects the preamplifier output to the switched capacitor analog pipeline. The preamplifier can be tested by applying a voltage step to the CAL input. The CAL pulse is reduced internally by about a factor 35 (not shown in figure 6). The CAL capacitors of four neighbouring channels have nominal values of 40, 80, 120 and 160 fF, which leads to a charge injection corresponding to one to four minimum ionizing particles in 300 μm of silicon for a 3 V external test pulse.

3.2.2 Pipeline

The output voltage of the preamplifier is captured on one of 32 capacitors ($C_p = 1$ pF) that form the analog pipeline for each channel. The capacitors are cyclically switched under the control of a common shift register operating at the HERA frequency of 10.4 MHz. A sample clock made from two signals ($S\Phi1$ and $S\Phi2$), phase shifted by 50%, with flat tops and common low periods of at least several ns is required. The shift register is cleared by setting both clock signals high and requires a couple of nanoseconds per cell. The sample bit (SBI) must be refreshed externally every 32 cycles.

3.2.3 Re-read and offset subtraction

The pipeline is stopped externally at a level-1 trigger signal. The H1 second level trigger may reject an event after a decision time of 22 μs, upon which the sampling phase is resumed. An L2 accept decision starts the readout, for which the APC must be put into a different mode. First, the input is disconnected from the silicon sensor by opening the input select switch IS. This automatically closes the switches $\overline{\mathrm{IS}}$ which connects all 128 strips to an extra preamplifier in auto-feedback configuration to absorb the leakage current during the readout phase. Secondly, the sample/read switch SR is opened, and the switches $\overline{\mathrm{SR}}$ are closed, which disconnects the write lines to the pipeline capacitors and prepares the read lines. Thirdly, the reset switch is closed for a few μs to bring the preamplifier into a well-defined state.

The APC employs a self-re-reading architecture where the pipeline capacitors are read back by the same preamplifier that wrote them. The pipeline cell associated with the triggered event is reached by advancing the sample bit in the shift register from the stopped position, refreshing it externally, if necessary. The sample enable bar switch SEB is open during this phase in order not to discharge the pipeline capacitors while advancing the sample bit. The selected capacitor is then read back through the preamplifier by closing SEB. The charge stored is amplified by a factor $C_p/C_1 \approx 2.1$ and copied to the latch capacitor C_L. A second and a third sample of the pulse stored in the pipeline is also read back and added to the charge on C_L, which improves the signal-to-noise ratio by effectively increasing the integration time.

The latch capacitors are necessary to separate the preamplifier section of the APC, which operates at a voltage of about 2 V (V_{analog}), from the readout section, that operates at 5 V ($V_{digital}$). They also provide intermediate storage of the signals during the serial readout. Thirdly, they are used to perform an on-chip pedestal subtraction. During sampling and up to this point the right plate of the latch capacitor C_L was connected to the readout amplifier by closing the latch enable switch LE and permanently filling the readout shift register. Switch LE is now opened, which captures the signal charge on the right plate. The left plate is cleared by resetting the preamplifier. The pedestal is taken from three pipeline capacitors just before the event occurred and read back with the same procedure as the signal. With the R12 and Reset switches open, the preamplifier maintains the pedestal potential, including any shift of the operating point due to leakage current, at the left plate of C_L. When the readout amplifier is connected to C_L again the difference between pedestal and signal is transferred.

3.2.4 Serial readout

The serial readout is controlled by a shift register which again requires a two-phased clock signal (RΦ1 and RΦ2) and a readout bit RBI. The right plates of the latch capacitors C_L are sequentially connected to the readout amplifier having a feedback capacitance C_{fb}, which provides an amplification of about 10. A readout speed of 4 MHz can be reached, if the analog output of the APC is immediateley followed by a driver amplifier. For the CST it is limited to 1.6 MHz by the trace capacitance on the ceramic hybrid carrying the APC. The readout of 10 APCs is multiplexed by feeding the readout bit appearing at RBO to the RBI input of the next chip. A chip select mechanism ensures that only one APC at a time connects to the common readout line. The full serial readout cycle for 1280 channels requires 1.1 ms, which is just sufficient in H1.

3.2.5 Decoder Chip

The APC requires 13 external signals, of which only the clock and sample bit signals are fast, while the others change only when switching from sampling to readout mode. The number of external clock and control signals that need to be brought to the front end can be reduced to four by using a dedicated Decoder chip [11]. The desired state of all APC switches is first loaded serially into registers on the Decoder chip and then applied to the APC. The fast clock and data signals are passed directly either to the pipeline or the readout shift register. Further functionalities have been added to the Decoder Chip: It can generate a test pulse for the CAL signal at any of the 32 pipeline buffer positions. It has a 7-bit DAC which drives a current source for the APC preamplifiers allowing to define the operating point externally. Finally, two stabilized and one temperature dependent voltage can be connected to the readout line, which allows a gain calibration and temperature monitoring. The Decoder chip was also fabricated in 1.2 μm SACMOS technology [16].

3.3 Hybrid and Optical Readout

Aluminium nitride was chosen as the substrate of the ceramic hybrid for its excellent heat conductivity $\lambda_{AlN} = 160\,W/Km$, compared to $\lambda_{Al_2O_3} = 25\,W/Km$ for aluminium oxide. The hybrids have a size of $34 \times 43\,mm^2$ and have two conductor layers on each side. Connecting vias and holes for fixing screws are cut by laser [10]. One side contains a blank area of $20 \times 16\,mm^2$ for heat contact with the mechanical support structure. Five APCs and one Decoder are mounted on each side of the hybrid and connected by aluminium wire bonds. The hybrid carries current sources for the APC preamplifiers, a voltage reference for gain calibration, a temperature monitor and drivers for the analog output signal. The back side of the hybrid, which supplies the n-side of the silicon sensors, is floating at bias voltage potential. The digital input signals are transferred across small capacitors which separate the DC levels. A thin Kapton cable with 20 lines is glued and wire bonded to the hybrid and connects to a ring-shaped printed circuit board (endring print) mounted on the CST endflanges.

The digital control signals and the analog readout are transferred by optical fibers [11] over 34 m between the detector and the electronics trailer, which minimizes the amount of cable material introduced into the center of H1 and prevents electromagnetic interference. Receivers for a set of four digital control signals are mounted on four endring prints, each serving one quarter of the CST. The analog signals are transmitted by a total of 64 LEDs, which are connected to sockets located on the endring print. One LED transmits the serial readout of either 1280 p-side channels or 1280 n-side channels from two neighbouring half ladders. The LEDs for the n-side are floating at the bias voltage potential.

4 Readout and Monitoring

The frontend system is connected via 34 m optical fibers and electrical cables to the readout electronics in the electronics trailer. The fibers and cables are interrupted twice by connector boards allowing the installation of the CST and access to other H1 detector components.

4.1 Readout and on-line Data Processing

Figure 7 shows schematically the components of the readout and monitoring system. All electrical and optical leads arrive at a converter card located in the electronics trailer. It contains LED drivers for the digital control signals and PIN diode receivers for the analog optical signals. It also provides passive filtering for the frontend supply voltages and the detector bias voltage. The supply voltages are further stabilized by active voltage regulators placed on the service tube about 1 m from the detector. These regulators can

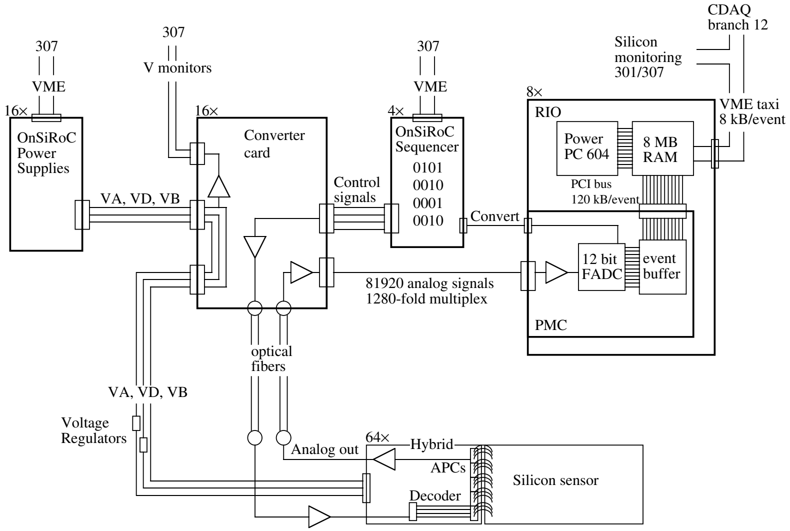

Figure 7: Schematic drawing of the CST readout components.

be adjusted from the converter cards allowing to optimize the working points individually for units consisting of pairs of ladders (four half-ladders). Finally, the converter cards include circuits for monitoring temperatures, voltages and detector leakage currents. If a given temperature limit is exceeded or if the cooling system fails, the converter card autonomously operates relays switching off the supply voltages to the frontend.

The frontend voltages are generated in VME modules called OnSiRoC [12]. The bias voltages are programmable in the range 0 V to 108 V. The OnSiRoC is interfaced to the H1 central trigger and generates the control sequences required to run the APC128 chips. A typical sequence occupies 32 kB in memory and is loaded through VME. A fast compiler was developed on a Macintosh platform which allows to generate the sequences from higher level building blocks.

The digitisation of the analog signals is performed on a custom-built PCI-bus mezzanine card [13] using 12 bit FADCs. The CST creates about 1 MB of raw data per event, which is transferred via PCI bus into 8 MB memories on RIO2 VME cards [14]. A hit-finding and zero-suppression algorithm is executed on PowerPC 604 RISC processors operating at 96 MHz. The algorithm first determines and subtracts an average baseline for groups of 128 channels located on individual frontend chips. The event-to-event variation of this common baseline is comparable to the single-channel RMS noise. In a second loop over the data the individual pedestals are subtracted and hit searching is performed. A hit is defined as a contiguous group of channels, each with an amplitude greater than its RMS noise, and with an integrated pulse height of at least four times the average single channel noise. The hits are copied to an output buffer. In a third loop the pedestals are updated, using a running average for each channel and each APC pipeline buffer, and variances for individual noise determination are accumulated, except for those channels contributing to a hit. Further counters are used to identify 'hot' channels which are included in the noise determination even if they contribute to hits, which eventually results in a higher calculated RMS noise value with a corresponding reduction of efficiency. The hit finding algorithm executes in about 7 ms with 10240 channels served by one processor, while the pedestal updating requires 10 ms but is executed only every fourth event. The formatted hit data are sent via a VME-taxi optical link to the central data acquisition system of H1.

4.2 Radiation Monitor

The APC128 chip has been tested for radiation sensitivity in a Co^{60} source. A single chip can tolerate about 1 kGy before the analog output saturates due to internal leakage currents. This limit is lower and depends on the readout speed when several chips are daisy-chained. All other front-end components have been selected for similar radiation tolerance.

A set of silicon PIN-diodes are attached to the outer shield of the CST [20]. They are continously read out, independent of the H1 data acquisition system. The counting rate is monitored as a function of time and displayed in the H1 and HERA control rooms. Counting rates above a certain threshold require beam tuning or optimisation of collimator settings. If the conditions cannot be improved within a few minutes the beams have to be dumped. This occurs a few times per year, mainly at the beginning of a running period. The dose determined by dosimeters attached to the CST was 50 Gy per year in 1996 and 1997 when HERA stored positrons. During the electron running in 1998 a dose of up to 250 Gy was accumulated which led to severe base-line shifts in the APCs in the inner layer. In the 1999 shutdown the affected ladders were moved to the outer layer and the readout ordering was changed to be fully efficient for the 1999-2000 running period.

4.3 Temperature and Leakage Current Monitor

Temperature dependent solid state current sources (AD590) are mounted on the CST endflanges. They are directly monitored in the converter card which operates relays to cut off all supply voltages to the CST, should the temperature exceed a value of 60°C. This hard wired safety circuit is independent of the H1 slow control system. Furthermore the temperature reading is digitized and displayed by a LabView application in the control room.

Each hybrid houses a voltage divider driven by a 2.5 V voltage reference, one element being an NTC resistor for temperature measurement. Furthermore a second reference voltage for gain calibration is derived from the same reference. The readout sequence directs the Decoder chip to transfer these voltages over the analog readout chain at the end of each event readout. A monitoring program with access to the data stream samples and displays the temperatures and reference voltages and records their history. It also provides on-line hit-maps and pulse height distributions for immediate data quality control.

5 Offline reconstruction

5.1 Track Linking

Tracks from the central tracking chambers are extrapolated to the CST half-ladders where the search region is limited to five units of the track extrapolation error. Ambiguities due to multiple track fit hypotheses in the chambers are resolved by selecting the best combination of hits in the inner and outer CST layer. If several tracks cross one half-ladder they are sorted according to their extrapolation error and the best track is linked first. Tracks are linked down to a separation of $150\,\mu$m.

The linking of n-side hits must resolve the three-fold ambiguity created by the daisy-chained readout with a spacing of 5.93 cm. Tracks which have been measured in both z-chambers have extrapolation errors below 1 mm in z and are linked unambiguously. If only CJC information is available the resolution can be above 1 cm. For these cases the linking exploits the correlation between the inner and outer layer and uses the event vertex as a further constraint.

5.2 CST tracks

The position and direction of a track can be determined from the hits in both projections and in both layers of the CST. Together with the curvature measured in the CJC a so-called CST track can be defined. These tracks are used in the CST alignment and they provide a largely unbiased reference for a re-calibration of the CJC and the z-chambers.

6 Alignment

In order to profit from the high intrinsic position resolution of the CST the position of each sensor in space must be known with comparable precision. The alignment procedure consists of three steps: An optical survey for the three sensors on a half-ladder, an internal software alignment of the 64 half-ladders relative to each other and a software alignment of the entire CST relative to the rest of the H1 tracking system.

6.1 Optical Survey

Each half-ladder was surveyed using a microscope and a step-motor controlled x-y stage with $1\,\mu$m resolution. A z-coordinate perpendicular to the sensor plane was measured using the focal adjustment coupled to a digital micrometer. Each sensor has 12 alignment marks on the metallization layer whose positions relative to the strip implants are known from the mask design and within processing tolerances of less than $3\,\mu$m. The survey was analyzed in terms of the relative displacements and rotations of the three sensors on a half-ladder to an accuracy of $3\,\mu$m and 0.1 mrad. It was observed that the individual sensors are not perfectly flat but are curved with a sagitta of about $30\,\mu$m over a diagonal. A common average curvature is used for all sensors in alignment and reconstruction. The original wafers were flat within $5\,\mu$m after cutting and polishing. The curvature is probably caused by the thick oxide layer deposited on the n-side.

6.2 Internal Alignment

The positions of the ladders are defined by the balconies on the carbon fiber endflanges. The mechanical precision of the balconies and the assembly procedure assure that no forces which may deform the ladders are exerted. The placement in space is accurate to a few hundred micrometers. After applying the alignment corrections from the optical survey the 64 half-ladders are treated as rigid bodies, which require 384 alignment parameters. These are determined in a software alignment procedure using three sets of tracking data.

6.2.1 Cosmic rays

Cosmic ray data are taken regularly during breaks in the HERA machine operation. Penetrating tracks with 4 hits in the CST are selected. The parameters of the 'upper' and the 'lower' track must agree within errors, which leads to four constraint equations. As an example figure 8 shows the distribution of the difference of the track positions at their closest approach to the origin of the H1 coordinate system — the so-called muon miss-distance. After alignment the standard deviation of the Gaussian is $52\,\mu$m, which corresponds to a single-track impact parameter resolution of $38\,\mu$m for tracks with a transverse momentum above 4 GeV/c. The corresponding impact parameter resolution in the z-projection is $74\,\mu m$. Several million cosmic ray triggers are required for a sufficient illumination of all half-ladders.

6.2.2 Overlaps

Cosmic tracks mainly constrain the relative positions of half-ladders in the inner and outer layer and in the upper and lower half of the CST. The position of neighbouring

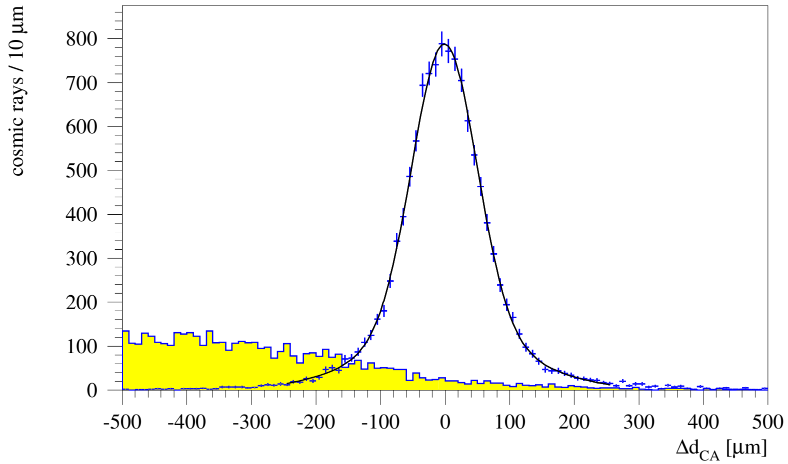

Figure 8: Muon miss distance for 4-hit cosmic ray tracks with $p_t > 4$ GeV/c and $|d_{CA}| < 2$ cm before and after alignment

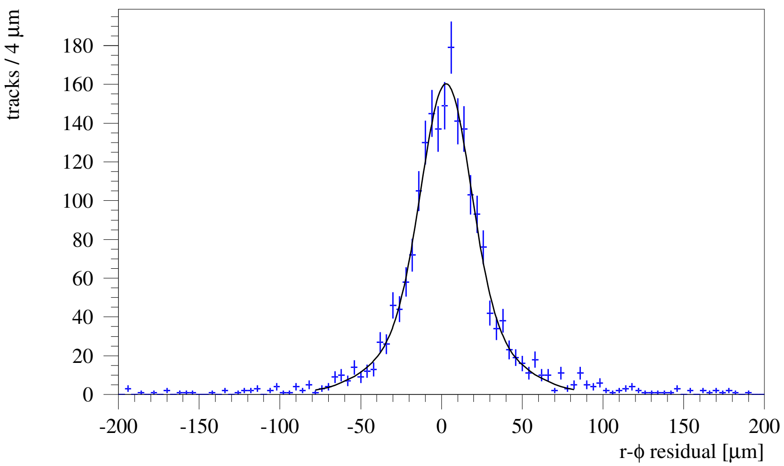

Figure 9: Distance between tracks and hits in overlap regions in the $r-\phi$ projection after alignment.

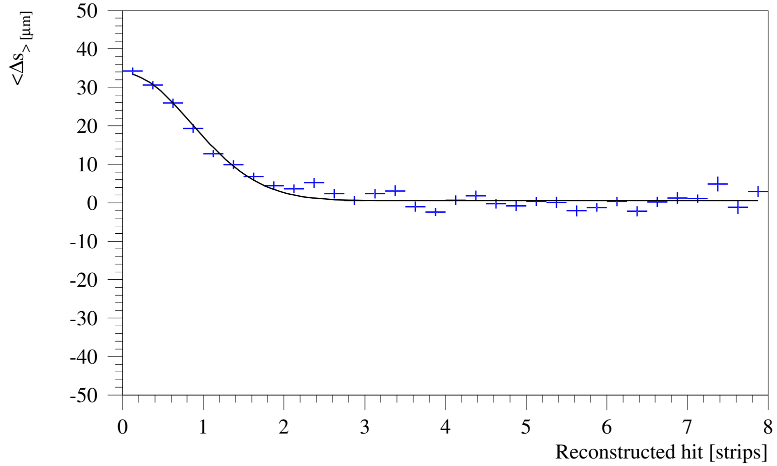

Figure 10: Mean overlap residuals versus the reconstructed cluster position in units of strip numbers on the p-side (50μm pitch). Strip 0 is next to the guard ring. The curve is a fit to a semi-Gaussian with a width of 0.85 pitch units.

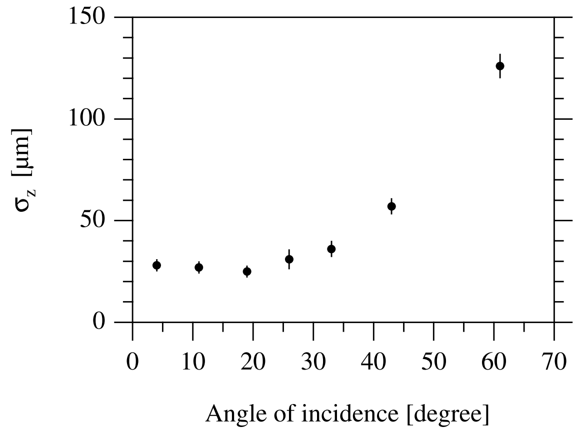

Figure 11: Intrinsic resolution in z inferred from overlap residuals as a function of incident angle in the r-z projection.

half-ladders are constrained by tracks passing through the overlap regions. Tracks with 3 hits are selected from normal ep luminosity data and are used to formulate two constraint equations, one in each readout coordinate. Two hits are used to define the track and to predict the hit in the overlap region. A distribution of residuals in the $r-\phi$ projection is shown in figure 9 from which an intrinsic point resolution of $12\,\mu$m is inferred.

Close to the guard ring region of the sensors a systematic shift of the overlap residuals is observed. In figure 10 the mean of the residual distribution is shown as a function of the distance of the reconstructed cluster position from the guard ring. The shift is well described by a semi-Gaussian with an amplitude of $33\,\mu$m and a width of 0.85 pitch units. The shift is attributed to charge collected on the guard ring. A correction is made and overlaps on the first two strips are not used in the alignment procedure.

The angles of incidence do not deviate by more than 22^o from the normal in the $r-\phi$ projection while much larger angles occur in the $r-z$ projection. The dependence of the intrinsic z-resolution (measured on the n-side) on the angle of incidence is shown in figure 11. It is well described by a parabola and reaches a minimum of $22\,\mu$m at 15^o from normal incidence [19].

6.2.3 Vertex Fits

Multi-track events from ep data are selected and a common 3D event vertex fit is performed. The sum of the χ^2 values over several ten thousand events is included in the overall minimization with respect to the alignment parameters. This method alone does not lead to a robust estimation of the internal alignment parameters but together with cosmic rays and overlap tracks it provides a uniformly distributed track sample of high statistics that improves the quality of the combined alignment.

6.2.4 Alignment Procedure

The alignment is performed using the three data sets simultaneously. A common χ^2 is accumulated and minimized iteratively with respect to the 384 local alignment parameters. The sparseness of the corresponding Hessian matrix is exploited for a fast solution of the linearized equations [21]. Two sets of alignment parameters were determined for 1997, using alignment data sets taken several months apart. The parameters are made comparable by applying six overall constraints, that correspond to a displacements or rotation of the entire CST. It is found that the internal alignment parameters agree with RMS spreads of $6\,\mu$m and 0.1 mrad. Compared to the intrinsic silicon resolution this reproducibility and long-term stability is sufficient.

6.2.5 Global alignment

The global alignment determines the displacements and tilts of the entire CST with respect to the CJC and the z-chambers. Six parameters are determined by minimizing the differences between CST and CJC tracks, using ep events and cosmic rays.

7 Performance

7.1 Occupancy

The on-line zero-suppression on average finds 60 p-side clusters and 200 n-side clusters, corresponding to channel occupancies of 0.8% and 2%, respectively. The higher occupancy on the n-side is due to larger non-Gaussian tails in the noise distribution. The occupancies are stable in time. The average number of linked hits is 14 for each projection which represents the track-related occupancy.

7.2 Signal to Noise Ratio

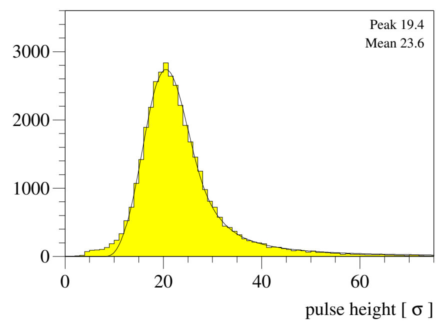

Figure 12: p-side cluster pulse height divided by the average single channel noise for minimum ionizing tracks at vertical incidence. A best-fit Landau curve convoluted with a Gaussian is also shown.

Minimum ionizing particles have a most probable energy loss of 84 keV in $300\,\mu$m of silicon, which leads to a signal of about 23 000 electron-hole pairs. The thermal noise level is determined by the preamplifier design, its operating conditions and the detector load capacitance. For three daisy-chained sensors the capacitance of one strip to all neighbours amounts to 27 pF on the p-side and 57 pF on the n-side, where the contribution from the

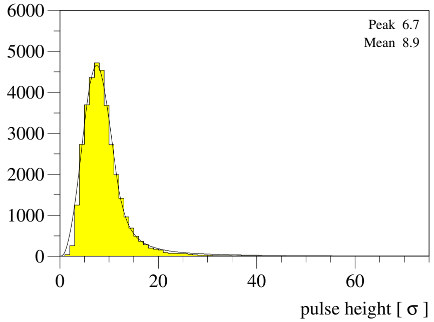

Figure 13: n-side cluster pulse height divided by the average single channel noise for minimum ionizing tracks at vertical incidence. The line is a Landau curve convoluted with a Gaussian.

double metallization dominates. The APC is routinely operated in a triple sampling mode and with a power dissipation of 0.3 mW per channel.

Figure 12 shows the distribution of cluster pulse heights divided by the average single-channel noise for cosmic muon tracks, normalized to vertical incidence. The shape is well described by a Landau energy loss distribution with a most probable signal-to-noise ratio of 19 for the p-side and 6.7 for the n-side, see figure 13. The difference is due to the strip capacitance loading the preamplifier which is a factor of two larger on the n-side, and due to the incomplete charge amplification caused by the limited gain of the preamplifier.

7.3 Efficiency

The CST hit efficiencies are most accurately determined with cosmic tracks passing through four CST half-ladders. Using three linked hits and the curvature from the CJC the track parameters are determined in a fit and the intersection with the fourth half-ladder is calculated. Figure 14 shows for a sample of 20000 muon tracks with transverse momentum above 2 GeV the distance between the intersection point and all hits in the test layer in the z-projection. The central peak at zero contains the signal hits while the noise hits create a flat background distribution. The central peak can be described by two gaussians with widths of 33 μm and 64 μm for test half-ladders in the inner and outer layer, respectively. By comparing the number of hits in the peak with the number of passing tracks one can determine the hit-efficiencies. Fig. 15 shows the results for p- and n-side hits for all 64 half-ladders. Besides some fluctuations, which can be associated with specific hardware problems for the selected data runs, the efficiencies are in agreement with being the same

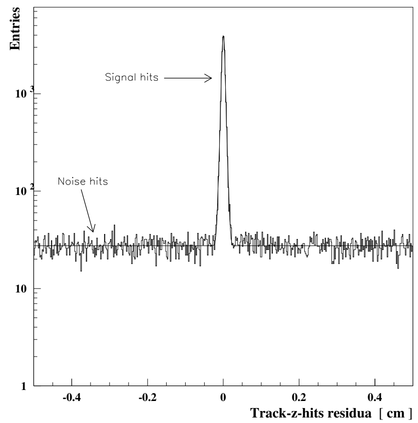

Figure 14: Distance between cosmic track intersect points and all hits on a half-ladder in the z-projection.

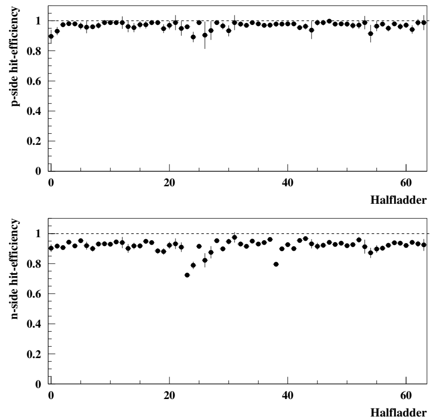

Figure 15: Hit efficiencies for p-side (top) and n-side (bottom) for all 64 half-ladders as measured from cosmic ray tracks

for all half-ladders. For the p-side the average efficiency is 97%, while it is 92% for the n-side. The inefficiencies is caused by silicon defects, dead or noisy readout channels, the hit finding algorithm and the linking procedure. The lower efficiency for n-side is due to the lower signal-to-noise ratio.

7.4 Beam Line Reconstruction

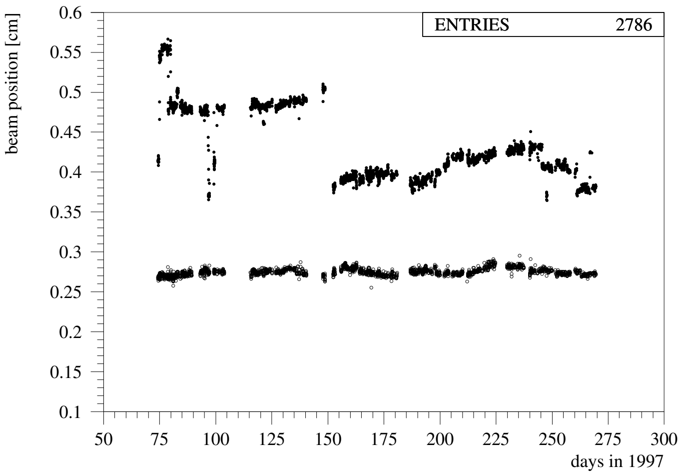

Figure 16: HERA beam position during 1997 as determined by the CST. The lower band of symbols shows the vertical beam position (stable at 0.27 cm), the upper band with a step around day 150 shows the horizontal beam position.

A precise knowledge of the beam position as a function of time is required for many decay-length or impact parameter studies. The beam position and tilt is determined by accumulating CST tracks over typically 30 minutes and minimizing the closest approach to a line in space. Figure 16 shows the horizontal and vertical beam position determined for the 1997 luminosity period. The horizontal beam movements reflect adjustments to the HERA optics.

The remaining distribution of the closest approach to the beam line (d_{CA}) has a central Gaussian part with contributions from the CST intrinsic resolution, from multiple scattering in the beam pipe and the first silicon layer and from the beam spot size. The decays of long-lived particles contribute to the non-Gaussian tails. From the HERA machine optics an elliptical beam spot with a horizontal-to-vertical aspect ratio of 5 to 1 is expected. This allows to separate the different contributions by measuring the width of the central Gaussian of the d_{CA} distribution as a function of the track direction around the beam. The result is shown in figure 17 for tracks with high momentum where the multiple scattering contribution can be neglected. A fit of the form

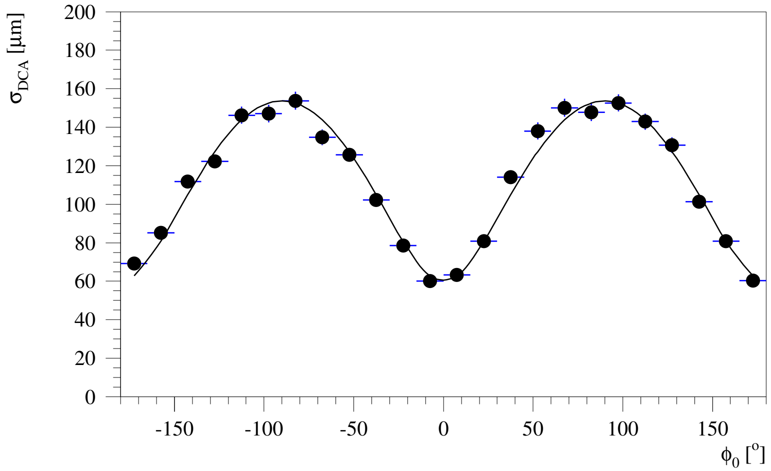

Figure 17: Width of the CST impact parameter distribution versus the track direction ϕ_0 around the beam spot for transverse momenta above 4 GeV/c. The curve is discussed in the text.

$$\sigma^2 = \sigma_0^2 + \sigma_x^2 \sin^2\phi + \sigma_y^2 \cos^2\phi$$

is used to extract the CST intrinsic d_{CA} resolution of $\sigma_0 = 54\,\mu$m and a horizontal beam spot size of $\sigma_x = 155\,\mu$m, which agrees with the HERA optics. A ratio $\sigma_y/\sigma_x = 1/5$ as given by the optics was assumed in the fit to unfold the CST intrinsic resolution.

7.5 Impact Parameter Resolution

The multiple scattering contribution to the width of the d_{CA} can be measured as a function of momentum by unfolding the contribution of the beam spot size. This contribution is minimal for horizontal tracks. The result is shown in figure 18 for data from 1997 and from 1999. A fit according to

$$\sigma^2 = \sigma_0^2 + (A/p_t)^2$$

leads to asymptotic values σ_0 of 57 μm and 59 μm for the two years while the parameter $A \sim \sqrt{d/X_0}$ improves by a factor 1.55, as expected for the change from an aluminium beam pipe ($d = 1.9\%\,X_0$) to a carbon fiber beam pipe ($d = 0.6\%\,X_0$), when adding the constant contribution of $d = 0.6\%\,X_0$ the first silicon layer and the CSt inner shield.

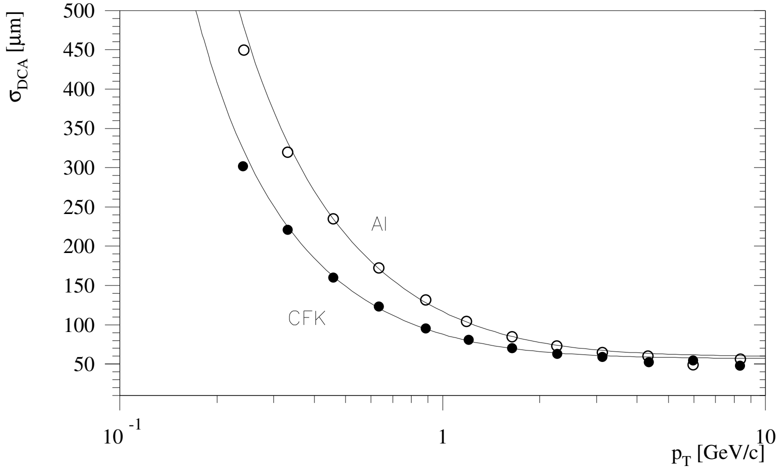

Figure 18: CST impact parameter resolution as a function of transverse momentum for horizontal tracks (within $\pm 15^{o}$). The open symbols are from 1997 (Al beam pipe), the filled symbols from 1999 (carbon fiber beam pipe). The curves are discussed in the text.

8 Summary

The H1 silicon vertex detector CST has been operated successfully at HERA since the beginning of 1997. The sensors, the readout electronics and the optical signal transmission are functioning reliably and efficienctly. A point resolution of $12\,\mu$m with a signal-to-noise ratio of 19 has been achieved for the $r-\phi$ coordinate, while the minimal point resolution in z is $22\,\mu$m with a signal-to-noise ratio of 7. An impact parameter resolution of $37\,\mu$m in the $r-\phi$ plane has been achieved for high momentum tracks, which opens a wide range of physics topics in the field of heavy quark production in electron-proton collisions.

References

[1] I. Abt et al., Nucl. Instr. and Meth. A386 (1997) 310 and A386 (1997) 348

[2] H1 Collaboration, Technical proposal to build silicon tracking detectors for H1, DESY PRC 92/01, July 1992; R. Horisberger, Proc. Int. Europhysics Conf. on High Energy Physics, Marseille, July 1993

[3] R. Eichler and S. Frixione, Proceedings *Future Physics at HERA*, Hamburg 1996, G. Ingelmann, A. DeRoeck, R. Klanner (editors)

[4] W. Eick et al., Nucl. Instr. and Meth. A386(1997) 81

[5] M. Biddulph, PhD thesis No ETH-12331, (1997)

[6] D. Pitzl et al., Nucl. Instr. and Meth. A348(1994) 454

[7] Wacker Chemitronics, Burgdorf, Germany

[8] C.S.E.M. SA, CH 2007 Neuchâtel, Maladière 71, Switzerland

[9] Siltronix SA, CH-1214 Vernier Geneva, Switzerland

[10] Radeberger Hybridelektronik GmbH, D-01454 Radeberg, Germany

[11] W. Erdmann et al., Nucl. Instr. and Meth. A372(1996) 188

[12] J. Buerger et al., Nucl. Instr. and Meth.A386(1997) 269

[13] W.J. Haynes et al., Nucl. Instr. and Meth. A403(1998) 313

[14] CES 8320 RIO2, Creative Electronic Systems, Geneva

[15] A prototyp version with 12 channels has been described in: R. Horisberger and D. Pitzl, Nucl. Instr. and Meth. A326(1993) 92

[16] Faselec AG, Philips Semiconductor, Binzstr. 44, CH-8045 Zürich, Switzerland.

[17] G. Klaiber, Diplomathesis ETH-Zurich 1996, unpublished

[18] Rohacell from Roehm AG, Switzerland

[19] J. Gassner, Diplomathesis ETH-Zurich 1996, unpublished

[20] L Jönsson, B. Lundberg, U. Mjörnmark, Lund University, Sweden

[21] V. Blobel, private commuinication. See also http://www.desy.de/~blobel/

Danksagung

Eine Doktorarbeit in einer so grossen Kollaboration wie H1 benötigt viel Mithilfe, welche ich reichlich und bereitwillig von zahlreichen Menschen in Villigen, Hamburg und Zürich erfahren habe. Euch allen sei herzlichst für Euren Beitrag zum Gelingen dieser Arbeit gedankt. Besonders hervorheben möchte ich Ralph Eichler, der mir in diesen Jahren teurer Mentor und Doktorvater war, ich danke Dir, dass Du mir diese Erfahrung ermöglicht und sie mitgeprägt hast.

Ohne Wolfram Erdmann, der mich in die Feinheiten des Vertexing initiert hat und immer die richtigen, wenn teilweise auch unangenehmen Fragen gestellt hat, wäre diese Arbeit um Einiges bescheidener ausgefallen. Daniel Pitzl hat mich in den CST Detektor eingewiesen und meine Leidenschaft für dieses Projekt geweckt, besonders die langen Nächte in Halle Nord werden mir unvergesslich bleiben. Chris Grab wurde in meiner Zeit hier in Zürich nie müde, meine zahlreichen Fragen bereitwillig zu beantworten, und seine detailierten Englischkorrekturen machen diese Arbeit erst lesbar. André Rubbia möchte ich für seine Bereitschaft danken, diese Arbeit zu begutachten. Marta Sekolec und Rosa Bächli gebührt besonderer Dank, Sie haben mir bereitwillig in allen administrativen Belangen geholfen.

Die letzen Jahre waren nicht nur im Rahmen der Physik lehrreich, sondern sie haben mich auch als Mensch geprägt. Dafür gebührt vielen Menschen Dank, welche mich auf diesem Weg begleitet haben und mir ans Herz gewachsen sind. Hervorheben möchte ich Martina Krotthammer, die mir seit vielen Jahren beste Freundin ist und mich immer wieder auf den rechten Weg gewiesen hat. Tina, Stefan und Nea Lüders bereichern mein Leben hoffentlich noch lange mit Ihre wundervolle Freundschaft, ich danke Euch aus tiefstem Herzen dafür. Christian Konstanty hat meine Zeit in Hamburg wertvoll gemacht, Du warst und bleibst hoffentlich weiterhin eine Stütze in meinem Leben. Stefan Hengstmann hat mich mit seinem Enthusiasmus für den Segelsport angesteckt, ich danke Dir für die vielen schönen Stunden auf dem Wasser. Caro, Fred und Leon Schwendrat, Ihr seid die erste Adresse für obdachlose Österreicher in Hamburg, ich freue mich schon auf unseren nächsten Grillabend mit Blick auf den Michl. Stephanie Heinzelmann, weltbesten Kinoberaterin und mehr, danke ich für die Bereicherung meiner Zeit in Zürich. Meinen Eltern und meinen Schwestern Katharina und Therese gebührt ein besonderer Dank, Sie haben in all den Jahren immer hinter mir gestanden und haben mich in meinen Entscheidungen durchwegs unterstützt.

Curriculum Vitae

Personal Data

Full Name	Johannes Nikolaus Konrad Gassner
Date of Birth	February 10, 1973
Place of Birth	Graz (Austria)
Nationality	Austrian

Education

1979 – 1983	Volksschule Obdorf, Bludenz (Austria)
1983 – 1991	Neusprachliches Privatgymnasium Mehrerau, Bregenz (Austria)
1991	"Matura mit gutem Erfolg"
1991 – 1996	Studies of physics at the Swiss Federal Institute of Technology (ETH) in Zurich
1996	Diploma in physics at the ETH Zurich. Title of the thesis: "Measurement of the Spatial Resolution of the H1 Silicon Vertex Detector"
1997	Military service
1997 – 2002	Graduate education in experimental particle physics at the ETH Zurich